Nanowires and Surface Tuning
Electrocatalysis at the nanoscale

Dissertation
zur Erlangung des Doktorgrades Dr. rer. nat.
der Fakultät für Naturwissenschaftender
Universitäat Ulm

vorgelegt von

Germán José Soldano

Supervisor: Prof. Wolfgang Schmickler

2011

Amtierender Dekan: Prof. Dr. Axel Groß

1. Gutachter: Herr Prof. Dr. Wolfgang Schmickler
2. Gutachter: Herr Prof. Dr. Axel Groß

Tag der Promotion: 31.10.2011

Contents

Part I

Introduction and calculation method

1
Introduction

This thesis is divided in four parts. The introductions and conclusions of the last three will be given in the corresponding chapters. In the current part, we give the fundamental background of theory which the further chapters are based on: density functional theory and Schmickler-Santos theory. The second part corresponds to the main topic of this thesis: free-standing atomic wires. In the third part, we examine more stable wires, which are attached to highly oriented pyrolytic graphite steps. Both free-standing and graphite-supported wires are characterized and examined from an electrochemical perspective. Finally, we explore two wholly different systems which are nevertheless analyzed with the same electrochemical perspective: modified metal surfaces. There, we explore the catalytic enhancement of rhodium overlayers on gold and palladium, and several aspects of the cyanide-modified platinum surface.

2

Background theories

An ocean traveler has even more vividly the impression that the ocean is made of waves than that it is made of water.

Arthur S. Eddington
Astronomer and physicist.

2.1   Quantum chemistry theories

To provide a detailed description of Hartree-Fock and density functional theory (DFT) is beyond the scope of this thesis. Instead, their basic foundations are given. An excellent introduction particularly applied to surfaces is given in [1], which this section is based on.

The Hamiltonian

It is interesting that despite of the complexity and richness of the equations that have radically changed the human perspective of the universe, these equations are usually expressed in a very innocent form. The equations that describe atomic systems are not an exception:

$$H\psi \;=\; E\psi \tag{2.1}$$

$$H\psi \;=\; i\hbar\frac{\partial\psi}{\partial t} \tag{2.2}$$

These are the time-independent and time-dependent Schrödinger equations, respectively. As Paul Dirac claimed when he published the relativistic equation for the electron, most of the physics and all the chemistry is explained by these equations [2]. If we neglect the relativistic and the magnetic effects, the Hamiltonian H that describes the nuclei and electrons is given by

$$H = T_{nucl} + T_{el} + V_{nucl-nucl} + V_{el-el} + T_{nucl-el} \tag{2.3}$$

where T and V are the kinetic and electrostatic interaction, respectively, both referring to electrons (el) and nuclei ($nucl$). The corresponding explicit terms are given by

$$T_{nucl} \;=\; \sum_{I=1}^{L}\frac{P_I^2}{2M_I} \tag{2.4}$$

$$T_{el} \;=\; \sum_{i=1}^{N}\frac{p_i^2}{2m} \tag{2.5}$$

$$V_{nucl-nucl} \;=\; \frac{1}{2}\sum_{I\neq J}\frac{Z_I Z_J e^2}{|R_I - R_J|} \tag{2.6}$$

$$V_{el-el} \;=\; \frac{1}{2}\sum_{i\neq j}\frac{e^2}{|r_i - r_j|} \tag{2.7}$$

$$V_{nucl-el} \;=\; -\sum_{i,I}\frac{Z_I e^2}{|r_i - R_I|} \tag{2.8}$$

where capital and lower case letters stand for nuclei and electron parameters, respectively: p and P are the momentum, Z the charge, r and R the coordinates, m and M the masses, and $e = 1.6\exp{-19}C$.

The Born-Oppenheimer approximation

Since the exact solution of the Schrödinger equation 2.1 is not possible, several approximations are made, the first of which takes advantage of the fact that m/M is very small. This entails that the electrons are generally 10^2 to 10^3 times faster

than the nuclei, which in turn allows the assumption that the electrons instanta-
neously *find* their ground state for any configuration of the nuclei. This is the
Born-Oppenheimer approximation. Since it is the configuration of the electron that
determines at which potential the nuclei move, one can calculate this potential sep-
arately by a Hamiltonian for fixed nuclear coordinates:

$$H_{el}(\circledR) = T_{el} + V_{nucl-nucl} + T_{nucl-el} + V_{el-el} \tag{2.9}$$

where $\circledR$ stresses the fact that the coordinates of the nuclei are fixed. The cor-
responding Schrödinger equation is then

$$H_{el}(\circledR)\psi(r, \circledR) = E_{el}(\circledR)\psi(r, \circledR) \tag{2.10}$$

Finally, the equation of motion can be calculated classically

$$M_I \frac{\partial^2}{\partial t^2} R_I = -\frac{\partial}{\partial R_I} E_{el}(\circledR) \tag{2.11}$$

and the force acting on the atoms can be evaluated by

$$F_I = -\frac{\partial}{\partial R_I} E_{el}(\circledR) = \langle \psi(r, \circledR)| \frac{\partial}{\partial R_I} H_{el}(\circledR)|\psi(r, \circledR)\rangle \tag{2.12}$$

Generalities of the Hartree-Fock theory

One particular feature of the Hamiltonian is that its expectation value in any state
Ψ will never give an energy value lower than the ground state energy E_0.

$$\frac{\langle \Psi|H|\Psi\rangle}{\langle \Psi|\Psi\rangle} \geq E_0 \tag{2.13}$$

Hence, if we start with a guess for $|\Psi\rangle$ and improve it systematically, we will
get closer to the ground state energy. A first crude guess for the wave function can
simply be the normalized product of one-particle functions ψ_i. This is the essence of
the Hartree equations, in which the expectation value is minimized with respect to
ψ_i. The Hartree equations can therefore be solved in a self-consistent way. The most
important shortcoming of the Hartree *ansatz* is that it does not take into account the
anti-symmetry of the wave function. This is solved by the Hartree-Fock equations.
The solution of the expectation value for the Hartree and the Hartree-Fock equations
differ by one term, the exchange energy E_x, which can be interpreted as follows:
Since the Coulomb repulsion among electrons of the same spin is already avoided by
the anti-symmetry of the wave function, E_0 from the Hartree-Fock method is lower
than E_0 from the Hartree method by an amount equal to E_x. However, the electrons
of opposite spin are still not correlated and the energy can be reduced further by
preventing these electrons to always avoid each other.

Density functional theory

The most important variable in density functional theory (DFT) is the electronic density $n(\mathbf{r})$, which can be expressed as a sum over single-particle states

$$n(\mathbf{r}) = \sum_{i=1}^{N} |\psi_i(\mathbf{r})|^2 \qquad (2.14)$$

The major attainment of DFT is that all the properties that can be derived from the Hamiltonian are uniquely related to $n(\mathbf{r})$. This is simply demonstrated by the *Thomas-Fermi theory*, according to which the chemical potential μ of free electrons (non-interacting) in a *weakly varying* effective potential v_{eff} is given by

$$\mu = \frac{\hbar^2}{2m}(3\pi^2 n(\mathbf{r}))^{2/3} + v_{eff}(\mathbf{r}) \qquad (2.15)$$

Since $n(\mathbf{r})$ is uniquely related to the effective potential and the number of electrons N via $N = \int n(\mathbf{r})d^3r$, it determines the full Hamiltonian. The effective one-electron potential is a sum of three potentials: the external potential ($v_{ext}(\mathbf{r})$), the Hartree potential ($v_H(\mathbf{r})$), and the exchange-correlation potential ($v_{xc}(\mathbf{r})$), defined as

$$v_{ext}(\mathbf{r}) = -\sum_{I} \frac{Z_I e^2}{|\mathbf{r} - \mathbf{R_I}|} \qquad (2.16)$$

$$v_H(\mathbf{r}) = \int d^3r' n(\mathbf{r}') \frac{e^2}{|\mathbf{r} - \mathbf{r}'|} \qquad (2.17)$$

$$v_{xc}(\mathbf{r}) = \frac{\delta E_{xc}[n]}{\delta n} \qquad (2.18)$$

where $E_{xc}[n]$ is a *functional* – a function of another function. Although $E_{xc}[n]$ is not known, it depends *only* on the the electron density n, and therefore is independent of any specific system or element. The most commonly used functionals in DFT are based on two approximations: the *local density approximation* (LDA) and the *General gradient approximation* (GGA), given by

$$E_{xc}^{LDA}[n] = \int d^3r n(\mathbf{r}) \varepsilon_{xc}^{LDA}(n(\mathbf{r})) \qquad (2.19)$$

$$E_{xc}^{GGA}[n] = \int d^3r n(\mathbf{r}) \varepsilon_{xc}^{GGA}(n(\mathbf{r}), |\nabla n(\mathbf{r})|) \qquad (2.20)$$

For the LDA functional, the exchange-correlation energy ε_{xc} used corresponds to the homogeneous electron gas. The LDA functional describes unexpectedly well

features of bulks and surfaces. However, as far as absolute energies are concerned, LDA is not sufficiently accurate. This shortcoming is tracked down to the fact that LDA overestimates the bonds. A remarkable improvement was achieved with the GGA functional, in which the gradient of the density is also included in ε_{xc}. For many chemical reactions the associated DFT error using GGA is ≤ 0.1 eV.

With these functions the so-called Kohn-Sham equations can be formulated:

$$\left\{ -\frac{\hbar^2}{2m}\nabla^2 + \upsilon_{eff}(\mathbf{r}) \right\} \psi_i(\mathbf{r}) = \varepsilon_i \psi_i(\mathbf{r}) \qquad (2.21)$$

Just like in the case of the Hartree equations, the Kohn-Sham equations can be solved iteratively in a self-consistent procedure. In fact, the Hamiltonian of Hartree and Kohn-Sham differ only by υ_{xc}, which is absent in the former case.

We need only one more term to have the complete equation of energy according to density functional theory, and that is the Hartree energy:

$$V_H = \frac{1}{2} \int d^3r d^3r' \frac{e^2 n(\mathbf{r})n(\mathbf{r}')}{|\mathbf{r} - \mathbf{r}'|} \qquad (2.22)$$

V_H is the classical electrostatic energy of the electronic charge distribution. Since it is implicitly contained twice in the Kohn-Sham eigenvalue ε_i, it has to be subtracted once. The ground state energy can now be expressed as

$$E = \sum_{i=1}^{N} \varepsilon_i + E_{xc}[n] - \int \varepsilon_{xc}(\mathbf{r})n(\mathbf{r})d^3r - V_H + V_{nucl-nucl} \qquad (2.23)$$

ε_i	Single particle energy obtained from the Kohn-Sham equations (2.21)	$E_{xc}[n]$	Exchange-correlation functional, equation (2.19 or 2.20)
ε_{xc}	Exchange-correlation potential, equation (2.18)	$n(\mathbf{r})$	Electronic density, equation (2.14)
V_H	Hartree energy, equation (2.22)	$V_{nucl-nucl}$	Electrostatic interaction between the nuclei, equation (2.7)

The computational effort that implies to solve equation 2.21 increases significantly with the number of electrons in the system. Solving it for metal surfaces such as Pt or Pd, whose electrocatalytic properties are worth being examined in an atomic level, would require alien super-computers or, even more rare, super-human patience. However, it is well-known that only the valence electrons are involved in most chemical reactions. If the influence of the core electrons is negligible, their effect can be replaced by an effective potential *independent* of the valence electrons and only dependent on the nature of the atom. These are the *pseudo-potentials*.

Since this reduces the number of electrons that has to be considered to the number of valence electrons, pseudopotentials lead to an enormous saving of computer time.

2.2   Santos-Schmickler theory

Despite of the accelerating progress in the understanding of electrocatalysis due to the parallel evolution of computational science, there has been no major progress in reaction theory. The latter is a crucial issue since DFT itself can not perform electron transfer reactions, which involves collective solvent fluctuations. The major achievement of the Santos-Schmickler theory is the possibility to calculate the activation energy of simple electrochemical reactions by combining Anderson-Newns-type theories with DFT calculations.

The topic of this section is to give the basic understanding of the Santos-Schmickler theory and to present the implications of the corresponding equations, their derivation has been given elsewhere [3, 4]. The theory has different approximations for different electrochemical reactions, the following corresponds to the adsorption of a proton from the solution onto the surface of a metal electrode:

$$H^+ + e^- \rightarrow H_{ad} \tag{2.24}$$

which is the rate-determining step in the hydrogen evolution reaction on several transition metal surfaces (Volmer reaction).

Electron-transfer reactions

Before treating the Santos-Schmickler theory, it is useful to refresh the basics of the electron-transfer reactions. As the name suggests, these are chemical processes in which charge is transferred from one species to another. The numerous reactions of this type are classified according to their mechanism in *outer-sphere* and *inner-sphere* electron transfer reactions: In the first case, the species is not chemically adsorbed on the substrate, the catalyst plays no role and the mechanism does not imply bond breaking or bond forming. In this case the electron simply "hops" between the substrate and the non-adsorbed species. In the second case, at least one of the conditions above is not fulfilled. The reaction is accompanied by a reorganization of the species (inner-sphere) and the solvation shell (outer-sphere). The Volmer reaction (see 2.24) is an inner-sphere electron transfer reaction: in the final state hydrogen is specifically adsorbed on the surface (a bond is formed) and the nature of the metal (catalyst) plays an important role. The reaction coordinate of the process is schematized in figure 2.1.

At the initial state, the proton is surrounded by its solvation shell and very close, down to a few Ångstroms, to the metal surface. At such short distances the electron
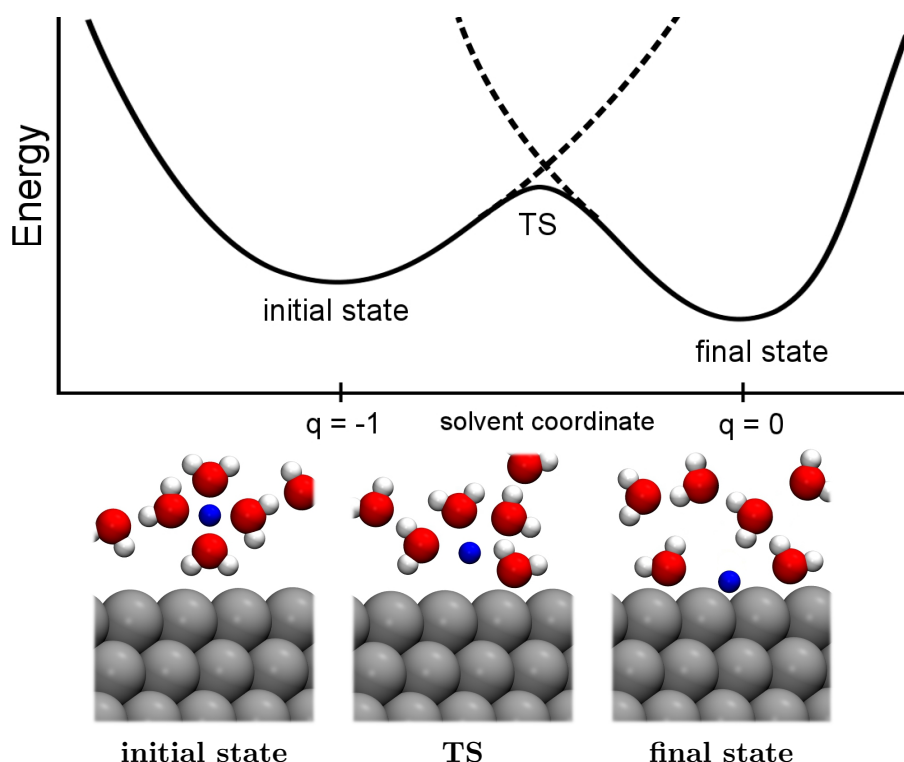
Figure 2.1: Schematic diagram of a one-dimensional potential energy surface for a proton adsorption on a metal electrode. The three stages of the reaction are represented below: initial state, transition state (TS), and final state.

from the metal could simply transfer to the proton by tunnel effect in an unsolvated system and the reaction would be very fast. However, the proton is strongly solvated, the motion of the solvent molecules produces an oscillation around the equilibrium energy (minimum of the initial state). These molecules *slow down* the reaction since this will only occur when they adopt a configuration that resembles the solvation shell of the uncharged and surface-adsorbed hydrogen (transition state), which requires thermal activation. At this state the electron transfer occurs, the proton adsorbs on the metal surface and the system reorganizes into its new equilibrium configuration (final state). In this scenario, the rate determining step is given by the activation energy required to reorganize the solvent from the initial state to the transition state. The surface-proton electron exchange is much faster in comparison. This is the case of an *adiabatic* reaction. In figure 2.1, an adiabatic reaction implies the isoenergetical crossing of the curves at the transition state. However, it could also be that the electron exchange between the substrate and the adsorbate is no longer faster than the solvent motion. Therefore, even if the solvent is in a configuration suitable as an intermediate state, the reaction does not occur because the

interaction between the adsorbate and the metal is weak and the electron simply does not tunnel. In this case we speak of a *nonadiabatic* reaction. In figure 2.1, a nonadiabatic reaction implies that the system can pass the saddle point and return to its initial state without crossing to the other curve.

Anderson-Newns approximation

A general model for the calculation of the total energy in an electrochemical environment must take into account the energy contribution from the solvent and the energy corresponding to the electronic part of the system (energy level of the $1s$ state of hydrogen and of the k states of the metal).

$$E_{Tot} = E_{sol} + E_{el} \tag{2.25}$$

• *Solvation energy* (E_{sol}): According to the Marcus theory, the energy involved in the process of electron transfer for a solvent interacting with a species A is well described by a one-dimensional harmonic oscillator model. The initial state of the solvent is represented by a parabola λq^2, where q is the *solvent coordinate* and λ is the reorganization energy. The variable λ is the energy gain due to the interaction with the species A and is proportional to the square of the corresponding coupling constant. The reaction coordinate q describes the state of the solvent, we will get a better idea of its meaning in a few lines. If we denote n_a as the occupation of the state a of the species A with a nucleus charge of $Z = 1$, then the charge of A is simply $(1 - n_a)$. When the species A is ionized, its interaction with the solvent is to first order, proportional to the charge on the ion: $2\lambda q(1 - n_a)$. Thus the energy of the solvent is:

$$E_{sol} = \lambda q^2 + 2\lambda q(1 - n_a) \tag{2.26}$$

$$n_a = \int_{-\infty}^{0} \rho_a(\varepsilon) d\varepsilon \tag{2.27}$$

The integral 2.27 is made over all the *occupied* states of A. This implies to consider all the states below the Fermi level E_F, which for convenience is our reference level: $E_F = 0$. In the initial state the charge of A is equal to one and E_{sol} is a parabola whose minimum is at $q = -1$. At the final state the charge of A is equal to zero and E_{sol} is a parabola with its minimum at $q = 0$. We can now interpret the solvent coordinate: If the state of the solvent is well described by q, then it would be in equilibrium with a species of charge $-q$.

Equation 2.26 describes the slow solvent modes, which correspond to the motion of the nuclei. Their fluctuations shift the electronic level of the reactant and induce electron transfer. In the adiabatic scenario the fast electronic mode *follows* the slow one instantaneously and only renormalize the electronic energy. For the sake of

simplicity, we keep the solvation equation as it is and we will come back to the fast modes later.

• *Electronic reactant energy* (E_{el}): The calculations are performed at hydrogen-surface distances lower than 2.4 Å, where the spin does not play a direct role. In this case the electronic Hamiltonian can be written as

$$H_{el} = \varepsilon_a n_a + \sum_k \varepsilon_k n_k + \sum_k (V_k c_k^+ c_a + V_k^* c_a^+ c_k) \tag{2.28}$$

The $1s$ state of hydrogen is denote by a, the states of the metal by k, the state occupation by n, and its energy level by ε. The first two terms indicate that the energy level is proportional to their occupation. The last term effects the electron exchange between the metal and hydrogen; V_k is the coupling constant, c^+ denotes a creator and c an annihilation operator. The term $V_k c_k^+ c_a$ corresponds to the electron transfer from the metal to the adsorbate and the term $V_k c_a^+ c_k$ corresponds to the exchange from the metal surface to the adsorbate. This can be solved exactly within the Green function formalism, giving

$$E_{el} = \int_{-\infty}^{0} \varepsilon \rho_a(\varepsilon) d\varepsilon \tag{2.29}$$

where ρ_a is none other than the density of states projected on the a state of the species A (the state $1s$ of hydrogen):

$$\rho_a(\varepsilon) = \frac{1}{\pi} \frac{\Delta(\varepsilon)}{[\varepsilon - \varepsilon_a - 2\lambda q - \Lambda(\varepsilon)]^2 + \Delta(\varepsilon)^2} \tag{2.30}$$

There are two important parameters, the *broadening* (Δ) and the *shift* (Λ). These are the so-called chemisorption functions. Δ determines the width of ρ_a and it has a simple interpretation: an electron in the state a decays with a lifetime of $\tau = \hbar/\Delta$ into empty states of the metal. Λ is the energy difference between the electronic state of the species A interacting with the metal and the electronic state of the species A isolated. This shift can be obtained in terms of Δ:

$$\Delta(\varepsilon) = \pi \sum_k |V_k|^2 \delta(\varepsilon - \varepsilon_k) \tag{2.31}$$

$$\Lambda(\varepsilon) = \frac{P}{\pi} \int \frac{\Delta(\varepsilon)}{\varepsilon - \varepsilon'} d\varepsilon' \tag{2.32}$$

where P denotes the Cauchy principal value.

• *Total energy* (E_{Tot}): Summing the solvent and electronic contributions, the total energy for the electron transfer reaction is given by

$$E_{Tot}(q) = \lambda q^2 + 2\lambda q Z_H + \int_{-\infty}^{0} \varepsilon \rho_a(\varepsilon) d\varepsilon + V_f \tag{2.33}$$

So far, we have neglected the correlation and the exchange between the electrons on the metal and on the hydrogen atom, which are the well-known shortcomings of the Anderson-Newns-type theories.

Santos-Schmickler theory

In order to correct the electronic terms, we shall analyze the situation at the final and the initial states of the Volmer reaction. At the final state ($q = 0$), E_{sol} is zero and the therefore $E_{Tot}(0) = E_{el}$. In order to obtain the electronic term E_{el}, we proceed as follows:

We calculate the DOS projected on to the $1s$ state of hydrogen (ρ_a);

we fit it into a function (ρ_a^{fit}) of the form of equation 2.30 from where we obtain the chemisorption functions;

Finally, we solve equation 2.29, where instead of using ρ_a we use the fitted density ρ_a^{fit}. We denote this energy by E_{el}^{fit}. Naturally, this is not exact since the fit is not perfect. We can also obtain the electronic energy of the adsorbed hydrogen at the equilibrium *directly* from DFT.[1] We will call this energy E_{el}^{DFT}. The associated error is only related to the error of DFT itself, but for the formalism of the Santos-Schmickler theory E_{el}^{DFT} is exact. Thus, we can calculate the latter theory error ΔE at $q = 0$:

$$\Delta E_{Tot}(0) = E_{el}^{fit}(0) - E_{el}^{DFT} \tag{2.34}$$

The correlation and exchange corrections are somehow contained in ΔE. Now let us see how we can extrapolate it for other values of q. At the initial stage of the Volmer reaction ($q = -1$), the electronic state of hydrogen is empty ($n_a = 0$), which entails that there is no correlation or exchange with the metal to correct for and that the total energy is simply E_{sol}. Since the electronic energy is fundamental at $n_a = 1$ and zero at $n_a = 0$, it is reasonable to assume that the error for other values of q are proportional to n_a:

$$\Delta E_{Tot}(q) = \Delta E_{Tot}(0)n_a(q) \tag{2.35}$$

This allow us to extrapolate the DFT results to other values in the range $-1 \leq q \leq 0$.

The last term to consider is the energy of the proton in solution V_f. According to equation 2.26, the energy corresponding to the proton ($E_{Tot}(-1)$) is simply $-\lambda$, but here only the interaction with the slow modes of the solvent is considered. In order to include the fast ones, the image force of the proton, and the electrostatic potential, we make use of the fact that at the equilibrium potential the free energy

---

[1]As long as the occupation n_a does not change, the $1s$ state of H_{ad} is fully occupied ($n_a = 1$) because of its high ionization energy on the metals considered in this thesis. Therefore, solvent fluctuations should have no effect on the total energy, which allows use to ascribe the electronic energy use of DFT to calculate E_{el} and the error of the model for $q = 0$.

of the proton must be equal to half of the free energy G_i of the hydrogen molecule. If we assume a linear dependency with the charge of hydrogen $(1 - n_a)$, we can write

$$V_f = (1 - n_a) \left(\frac{G_i}{2} + \lambda - e_0 \eta \right) \tag{2.36}$$

where η is the overpotential and G_i is the free energy of H_2.

The final expression for the energy of the hydrogen adsorption from the solution onto the metal surface as a function of the solvent coordinate q is

$$E(q) = E_{sol} + E_{el}^{fit}(q) + \Delta E_{Tot}(q) \tag{2.37}$$

E_{sol}	Solvation energy $(\lambda q^2 + 2\lambda q + V_f)$, equations 2.26 and 2.36.
$E_{el}^{fit}(q)$	Electronic energy, equations 2.30 and 2.29.
$\Delta E_{Tot}(q)$	Correction term, equation 2.35.

The free energy for hydrogen adsorption as a function of the solvent coordinate q and the hydrogen distance from the surface z can be obtained by the above equation. As an example, the free energy surfaces for the Volmer reaction on Au and Pt surfaces are shown in figure 2.2.
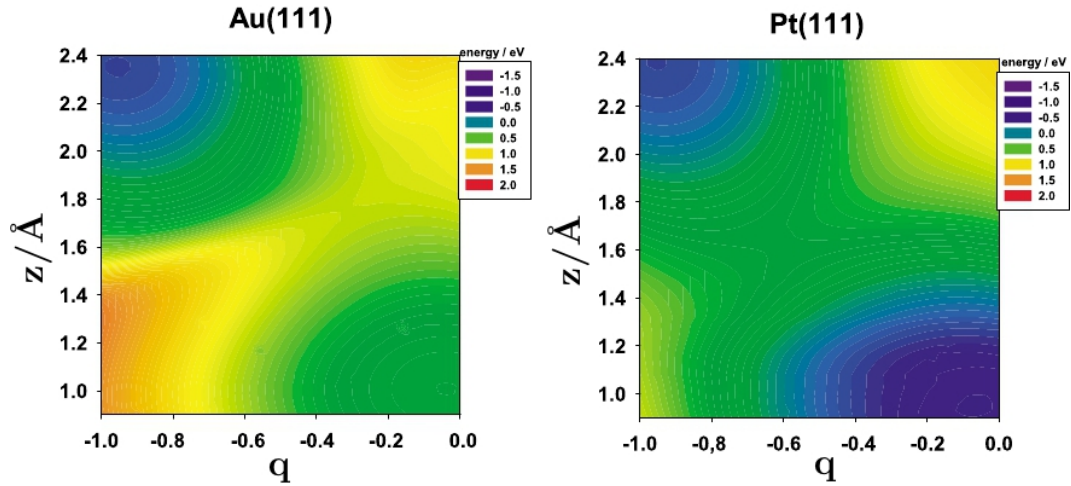
Figure 2.2: Free energy surface for hydrogen adsorption on Au(111) and Pt(111) surfaces, respectively, in aqueous media as function of the hydrogen distance z from the surface and the solvent coordinate q [5].

In accord with experimental findings, the Santos-Schmickler theory appplied to the Volmer reaction predicts a high activation energy for Cd, medium values for the three coin metals, and very low values for Pt surfaces [5].

3

Technicalities

When you see something that is technically sweet, you go ahead and do it and you argue about what to do about it only after you have had your technical success. That is the way it was with the atomic bomb.

J. Robert Oppenheimer
Theoretical physicist.

Unless mentioned, all the calculations presented in this work were performed with DACAPO [6], a density functional theory (DFT) code. The electron-ion interactions were accounted through ultrasoft pseudopotentials [7], while the valence electrons were treated within the generalized gradient approximation (GGA) in the version of Perdew and Wang [8,9] (if other exchange correlation functionals were used, they will be indicated in the corresponding section).

The molecular and atomic orbitals shown are plotted within the Wannier formalism [10]. Special care was taken for the parametrization of the energy cutoff (pwco) and the k-points sampling of the Brillouin zone (kpts) based on the Monkhorst-Pack grid [11]. Both parameters were optimized for each metal and each structure (wire, slab, bulk) in such a way that the increase by 1 k-point, or by 50 eV in the energy cutoff, led to a negligible change in energy (from 5 to 20 meV depending on the systems).

The majority of the systems described in this part of the thesis are related to free-standing wires and fcc(111) surfaces. To avoid redundancy, their technicalities are described here although they will be given when necessary in the corresponding sections.

3.1   Nanowires

First-principle calculations

The systematic increase of kpts and plane waves cutt-off (*pwco*) with respect to the change in energy for monometallic nanowires is shown in figure 3.1.
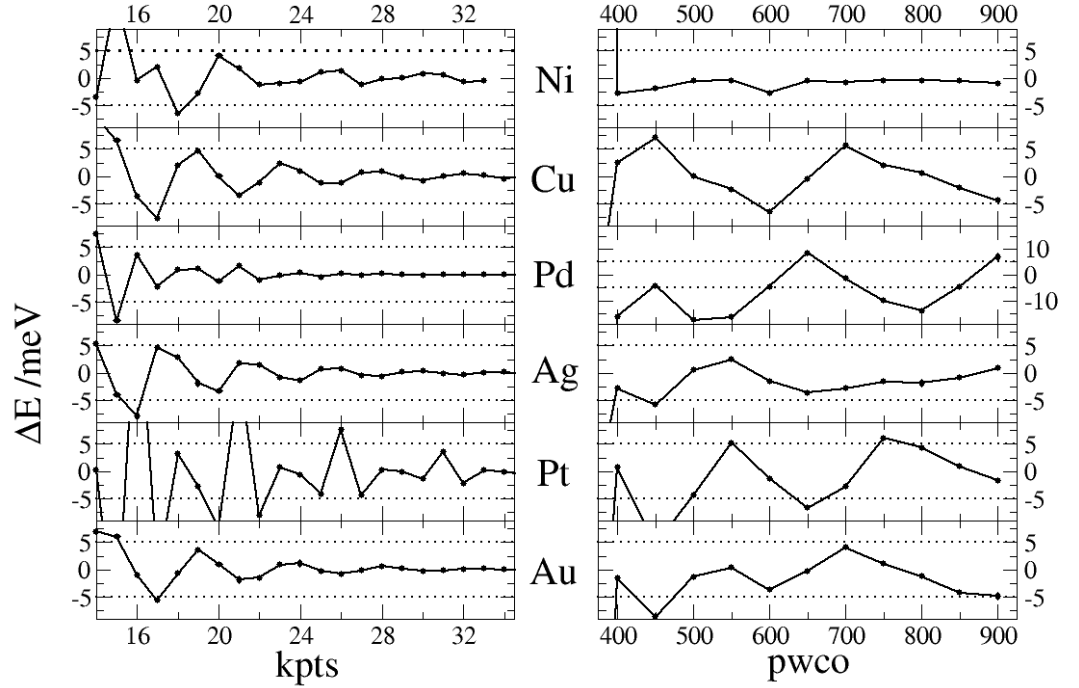
Figure 3.1: Energy difference with respect to the previous value (ΔE) of k-points (*kpts*) and plane wave cutoff (*pwco*) for monometallic nanowires. The dotted lines capture the ΔE values between ± 5 meV.

Taking advantage of the relatively low computationally demanding 1-dimensional systems and to be on the safe side, the parameters chosen are higher than the minimum needed for convergence: *pwco*=500 eV and *kpts*=28×1×1. These parameters entail an absolute error of 5 meV for all the metals studied with the exception of Pd, where the error is 10 meV. The spin polarization was considered, but only Ni and Pd wires show spin dependency. The energy difference between the magnetic

and the non-magnetic system ($E_{spin} = E_{spinON} - E_{spinOFF}$) is -0.153 eV for Ni and -0.015 eV for Pd nanowires. A magnetic moment of 1.15 μB was found for Ni and 0.54 μB for Pd. We will detail this phenomenon on page 38.

Modeling

The nanowires were modeled by one-atom-thick linear free-standing wires placed in a rectangular cell. Periodic boundary conditions were used. The size of the cell is given by the vector ($L_x; L_y; L_z$) sketched in figure 3.2, where $L_y = L_z = 11$ Å. Since the axis x is the axis of the wire, L_x depends on the wire metals and has to be optimized. A quadratic relation between the total energy and the length of the wire (L_x) was obtained. The length corresponding to the equilibrium energy was determined with an accuracy of 0.001 Å. The resulting length of the cell is the bond distance between the wire atoms (see table 3.4)
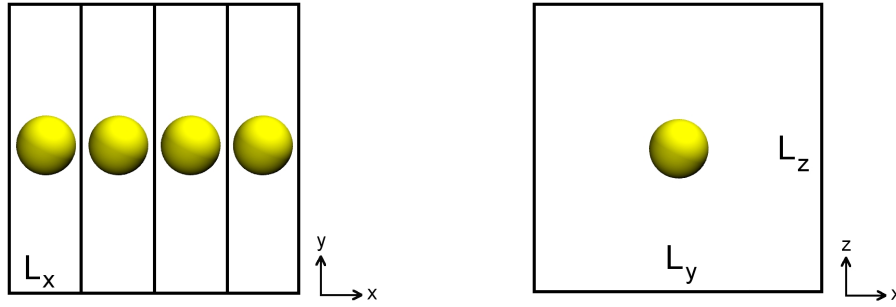
Figure 3.2: Nanowire unit cell dimensions: L_x, L_y, and L_z. In the left panel L_x is repeated 4 times.

It has long been recognized that atomic chains can adopt a zigzag configuration. In order to consider this arrangement, we used the same procedure as for the linear wires, but with a unit cell containing two atoms, one fixed and the other relaxed perpendicular to the wire axis. For the relaxations computed, the convergence was achieved when the total forces were less than 0.01 eV/Å.

3.2   Slab and bulk metal

First-principle calculations

For consistency, the same *pwco* used for nanowires were computed for bulk and slabs. After optimization of the Monkhorst-Pack grid, the kpts chosen are 8×8×8 for the bulk and thus 8×8×1 for slabs.

Modeling

The fcc bulk unitary cell was computed. The lattice constant (a_0) was changed until the minimum in energy was achieved with an uncertainty of 0.002 Å. Some parameters obtained by the latter calculations are compared with those of the literature in table 3.1.

	source	**Ni**	**Pd**	**Pt**	**Cu**	**Ag**	**Au**
a_0	exp.[1]	3.52	3.88	3.92	3.61	4.08	4.07
	this work	3.528	3.985	4.004	3.660	4.138	4.179
E_{coh}	exp.[1]	-4.435	-3.936	-5.852	-3.50	-2.96	-3.78
	this work	-4.92	-3.74	-5.69	-3.61	-2.72	-3.13

Table 3.1: Equilibrium lattice constant (a_0) and cohesive energy (E_{coh}) for some fcc transition metal bulk structures.[1] [12]

For slabs, an fcc-(111) surface was computed with one atom per layer and a five interlayer distance of vacuum along the z axis (sketched in figure 3.3).
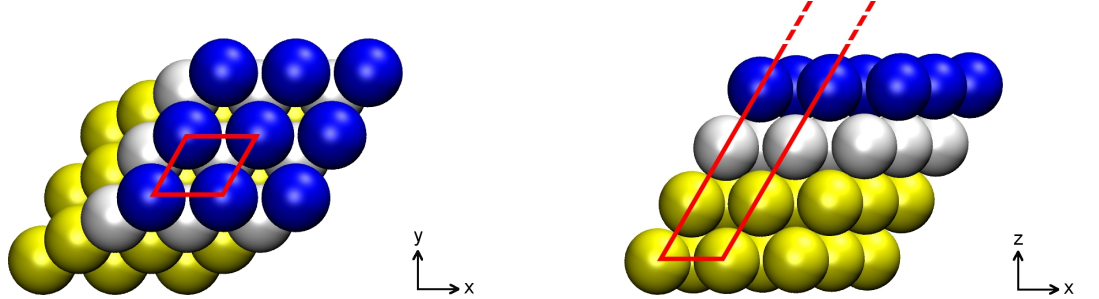
Figure 3.3: Top and side view of a four-layer slab. The unit cell is colored red. The top two layers, which are allowed to relax, are colored white and blue.

In order to determine the number of layers, the surface energy[1] (σ) and the percentage change in the top two interlayer distances (Δd_{12} and Δd_{23}) were calculated for an increasing number of layers as shown in figure 3.4. In each case the two-top layers were fully relaxed and the rest was fixed at the nearest-neighbor distance corresponding to the bulk.

---

[1] $\sigma = (E_{slab(N)} - NE_{bulk})/2$ where $E_{slab(N)}$ is the energy of an N-layer 1x1 surface unit slab and E_{bulk} is the bulk energy per atom. Since the slab has actually *two* surfaces, the slab-bulk energy difference has to be divided by a factor of 2.
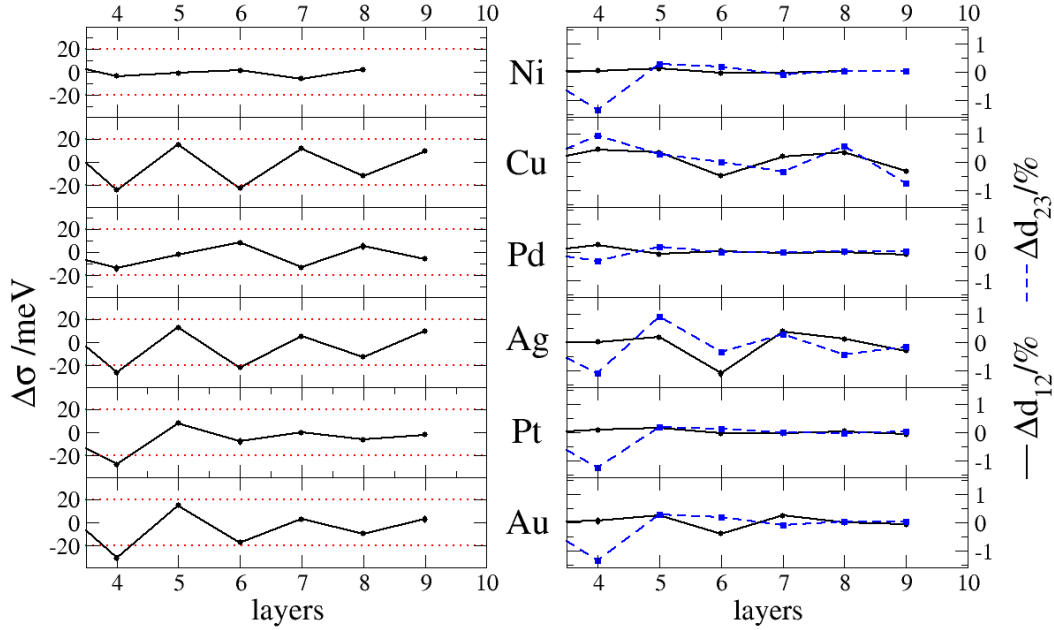
Figure 3.4: Surface energy (σ) and lattice spacing convergence with respect to the number of layers. Δd_{12} and Δd_{23} are the change in the lattice spacing between the first and second layer, and between the second and third layer, respectively. Red dotted lines capture values of ± 20 meV for σ.

As can be seen in the figure, five layers are more than sufficient to achieve convergence of σ and interplane distances. The final results are compared with experimental values in table 3.2.

	source	**Ni**	**Pd**	**Pt**	**Cu**	**Ag**	**Au**
σ [eV]	this work	0.64	0.49	0.63	0.46	0.37	0.37
	exp.[1]	0.70	1.16	1.00	0.71	0.55	0.61
Φ [eV]	this work	5.16	5.32	5.76	4.77	4.49	5.23
	exp.[2]	5.15	5.12	5.65	4.65	4.26	5.10

Table 3.2: Surface energy (σ), lattice spacing (Δd_{12} and Δd_{23}) and work function (Φ) of some transition metals. When found, these results are compared with experimental values. [1] [13], [2] http://environmentalchemistry.com/yogi/periodic

Many experimental values are derived from surface tension measurements made in the liquid phase and extrapolated to zero temperature, which are not related to any particular crystal face. In this case, the DFT values are more reliable than the

experimental ones [1]. For the relaxations computed, the convergence was achieved when the total forces were less than 0.01 eV/Å.

Part II

Free-standing atomic nanowires

4
Introduction

Metal nanowires are amongst the smallest devices that can be constructed. They have already been used for high chemical sensing [14–19], nanoelectronics and as probe microscopy tips [20], however, these applications are just a starting point. Due to their versatile properties, such as quantized conduction [21, 22] and photonic adjustability [23], nanowires promise to play an important role in nanotechnology. The new microelectronic era requires more components per chip, faster operations, lower costs, and less power consumption. In this sense the International Technology Roadmap for Semiconductors (ITRS) has predicted that the expected feature size should be around 32 nm by 2012. At this scale, electron transport through the wires is ballistic and quantized. The current is carried by quantum channels where electrons are partly transmitted and partly reflected. If perfectly transmitting, each (spin degenerate) channel contributes to the conductance with one quantum unit $G_0 = 2e^2/h$. Thus, measuring the conductance gives information about the width of the wires.

The large number of techniques available for the fabrication of nanowires can be classified as *mechanical* and *nonmechanical*.
Mechanical: Involves the mechanical breaking of a fine metal wire [24–26], or sepa-

25

rating two metal electrodes in contact [27–29]. This technique has several disadvantages: the wires fabricated in this way are not removable from their substrate (which makes them unsuitable for many applications), they are not long-term stable, and finally, this procedure cannot be used to produce an array of nanowires.

**Nonmechanical**: Atomic force microscopy (AFM) and scanning tunneling microscopy (STM) have been used to fabricate wires [30, 31], however, they cannot be applied for mass production; besides the AFM method is not reversible, i.e., the wire chain cannot be reconstructed. These disadvantages are overcome by the employment of an *electrochemical etching/deposition* method [32, 33], sketched in figure 4.1a. The nanowires fabricated in this manner are immune to *destructive* environmental vibration, which makes them long-term stable (seconds to hours), they can be integrated into conventional electronic circuits and even an array of wires can be obtained. Furthermore, the nanowire width can be flexibly controlled by etching atoms away or depositing atoms back onto the wire with the electrochemical potential while its conductance is monitored, as shown in figure 4.1b.

(a)   **(b)**
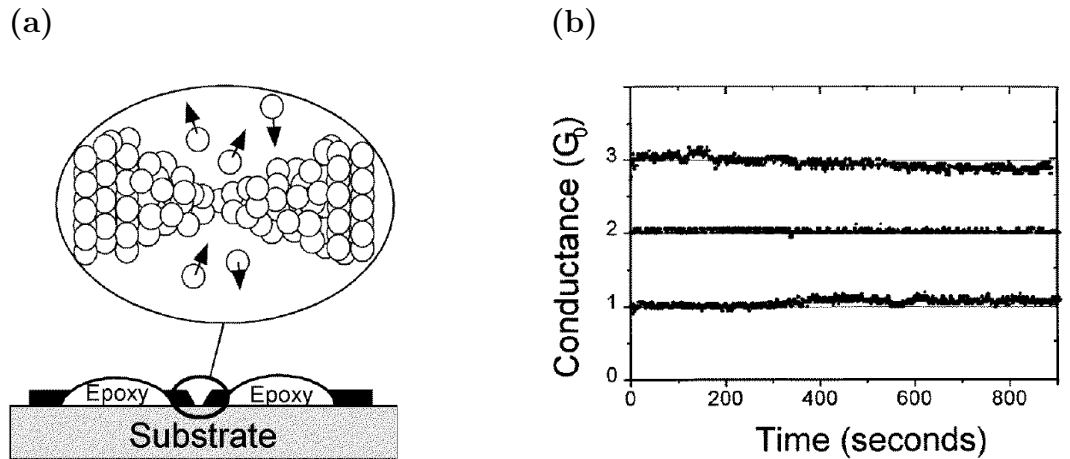
Figure 4.1: (a) A schematic drawing of the experimental set-up. A single or an array of metal wires is supported on a glass substrate. Each wire is covered with a layer of insulator except the central portion which is then etched electrochemically until the conductance quantization appears. **(b)** Cu nanowires with conductances multiple of G_0 fabricated by stopping the etching process at the selected steps with an automatic switch. Adapted from Ref. [32].

A similar method was later developed by Bohn and Shi et al. [34] in which the controllability of the etching stop-point is enhanced. In this case atomic scale junctions (ASJs) are built. The nanogap substrate of these structures is the working electrode, which is kept open during the electrochemical process and is not specifically wired into the potentiostat circuit. This leads to extremely slow charge transfer and to an enhanced control of the electrode kinetics. Stable Au ASJs on silicon were

obtained by either electrodeposition of Au in prefabricated Au nanogaps or electrodissolution of an overgrown Au junction. Perhaps the only disadvantage of this method concerns its regenerabilty: The repeated fabrication of Au ASJs results in irreparable damage to the Au nanogaps as shown in figure 4.2b, preventing the formation of new ASJs.

(a)   **(b)**
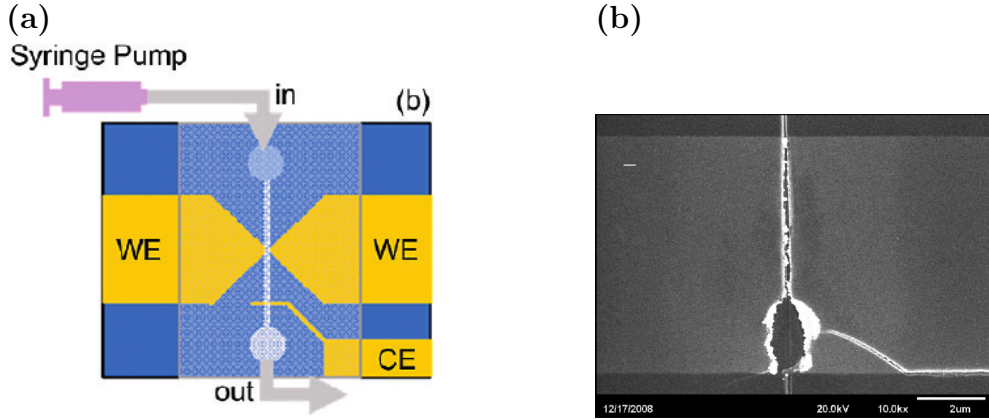
Figure 4.2: (a) Schematic diagram of the sample used for fabrication of ASJs in microfluidic channels. **(b)** SEM image of an overgrown Au junction after electrodissolution. Damage to the structure is clearly evident near the bottom of the nanogap. Adapted from Ref. [35].

This problem was solved by keeping the Au nanogap but incorporating a second metal (Cu or Ag), which dissolves at a potential at which Au does not [35]. The Au-Cu and Au-Ag bimetallic ASJs obtained show remarkable stability, exhibiting steady conductance values for over 3 hours in favorable cases.

The amount of difficulties that the experimentalists have to overcome for the fabrication and the measuring of such small structures is readily noticed. On the other hand, in the theoretical world, the size of nanowires is actually an advantage: it allows to perform high precision DFT calculations. In the following chapters metallic nanowires will be described from a theoretical perspective. As a starting point, we study the electronic properties and the structural stability of mono- and bimetallic wires in chapters 5 and 6, respectively. Then, from chapter 7 to chapter 10 we focus on a still unexplored application for nanowires: fuel cell catalysts. The thermodynamics and kinetics of atomic hydrogen adsorption and hydrogen molecule dissociation on nanowires is addressed in chapters 7 and 9, respectively. There, we test the suitability of nanowires as a catalyst for the hydrogen evolution reaction. A similar study is performed for the adsorption of atomic oxygen in chapter 10, where we analyze the possibility of using nanowires for the catalysis of the oxygen reduction reaction. Finally, the dissociation of a single water molecule is analyzed in

chapter 11. The results obtained in this first part are summarized in chapter 12. At the end, we shall answer a central question: *How does the nanowire structure affect the chemical and catalytic properties of the metals?*

5
Monometallic nanowires

And computers are getting smarter all the time: scientists tell us that soon they will be able to talk to us. (By they I mean computers: I doubt scientists will ever be able to talk to us.)

Dave Barry Humorist writer.

In this chapter we introduce and discuss intrinsic properties of bare free-standing nanowires. There are a few theoretical papers on their basic physical properties. It has been shown that the interfacial capacity per area of such wires is much larger than that of bulk electrodes, transport is enhanced by several orders of magnitude, and the potential of zero charge is shifted to substantially higher values, so that under normal electrochemical working potentials nanowire electrodes carry a sizable negative charge [36]. Other studies concern ionic adsorption [37] and outer-sphere electron transfer [38]. From the ongoing research, one unresolved problem emerges: the *intrinsic stability*. Nanowires made of Au, Ag, or their combinations, are stable for hours [34, 35] while wires made of Cu, Pt or Pd show a mean lifetime of the order of seconds only; however, they can be stabilized at the potential of the hydrogen evolution region [35, 39–44]. The explanations given for the differing stabilities are contradictory: On the one hand, the reactivity of such wires to small species (which could ultimately break the chain) should make Au wires as unstable as Cu

wires since both have a similar affinity for hydrogen [45]. On the other hand, if it is assumed that hydrogen adsorption is the process that actually stabilizes the wire [46], then Ag wires should be unstable since in this case the adsorption is endergonic [45]. It has also been suggested that the cohesive energy could explain the differing stabilities [35]. Unfortunately, the measurements of quantities that could help to unravel these mysteries, are almost impossible to perform experimentally. However, the reduced size of these systems makes them perfectly suitable to be examined with precise DFT calculations.

In this work, physical quantities such as cohesive and surface energy are calculated for several transition metal wires. An explanation for the experimental instability of Cu wires in contrast to the stability of Au and Ag wires is given, which relies on the higher surface energy of the former. A detailed description of the electronic structures of nanowires is also given. An unexpected similitude with the charge density distribution of planar surfaces was found for nanowires as well as a remarkable shift in the position of the d band.

5.1   Stability

The cohesive energies for monometallic wires and slabs are calculated by subtracting the isolated atom energy:

$$
\begin{aligned}
E_{coh}^{wire} &= E_{wire} - E_{at} & (5.1) \\
E_{coh}^{bulk} &= E_{bulk} - E_{at} & (5.2)
\end{aligned}
$$

It has been proposed that this quantity itself could explain the differing stabilities for nanowires [35]. In disagreement with this assumption, the cohesive energy for Cu wires (unstable) is lower than for Ag wires (stable) and almost the same as Au wires (stable). If we examine table 5.1 in greater detail we will see that the low E_{coh} values of wires are associated with much lower values for the corresponding bulk metals. This is because a bulk atom is coordinated by 12 atoms while wires have only 2 neighbors per atom. Therefore, even if the wire bond is strong, like in the case of Pt, there is a stronger driving force that tends to break the wire in order to reorganize the atoms in a more coordinated structure. Naturally, this force exists for all monostrand wires, but for some metals it can be sufficiently small so that the wire is relatively stable. One way to take this into account is by simply calculating the difference in the cohesive energy between a wire and the corresponding bulk metal:

$$\Delta E_{coh} = E_{coh}^{wire} - E_{coh}^{bulk} \tag{5.3}$$
$$= (E_{wire} - E_{at}) - (E_{bulk} - E_{at}) \tag{5.4}$$
$$= E_{wire} - E_{bulk} = \sigma_{wire} \tag{5.5}$$

Equation 5.5 is none other than the wire surface energy (σ_{wire}): the lower this is, the smaller the force that tends to break the nanowire.

	system	**Ni**	**Pd**	**Pt**	**Cu**	**Ag**	**Au**
E_{coh} (wire) [eV]	wire	-2.09	-1.15	-3.04	-1.68	-1.32	-1.63
	bulk	-4.92	-3.74	-5.69	-3.61	-2.72	-3.13
d_{nn} (wire) [Å]	wire	2.18	2.51	2.39	2.32	2.64	2.61
	bulk	2.49	2.82	2.83	2.59	2.93	2.89
σ (wire) [eV]	wire	2.83	2.57	2.67	1.93	1.39	1.51
	slab	0.63	0.53	0.64	0.46	0.35	0.34
γ (wire)[meV/Å^2]	wire	95	65	74	57	32	35
	slab	116	77	92	79	48	45
Φ (wire) [eV]	wire	5.07	5.43	6.17	5.24	5.12	6.43
	slab	5.16	5.32	5.76	4.77	4.49	5.23

Table 5.1: Cohesive energy (E_{coh}), nearest-neighbors distance (d_{nn}), surface energy (in eV per atom for σ and in meV/Å^2 for γ, see text) and work function (Φ) for Ni, Pd, Pt, Cu, Ag, and Au monometallic wires. E_{coh} and d_{nn} are compared with those of bulk metals and the surface energies are compared with those of fcc(111) slabs.

This quantity is in much better agreement with the experimental facts than the cohesive energy: for the unstable wires (Cu, Ni, Pd, and Pt) $\sigma \geq 2$ eV, while for the stable wires (Ag and Au) $\sigma \leq 1.5$ eV. This difference becomes larger if the area A of such structures is considered. For this purpose γ is defined as σ/A and the area of wires is obtained by considering them as cylinders with length and radius equal to the wire bond distance (L_x), which gives $A_{wire} = 2\pi L_x^2$. As table 5.1 shows, γ is almost twice as large for Cu as compared to Au and Ag wires. In order to have a reference for these values, the surface energies (σ and γ) for fcc(111) slabs were also calculated.

$$\sigma_{slab} = (E_{slab} - E_{bulk})/2 \tag{5.6}$$

$$\gamma_{slab} = \sigma_{slab}/A \tag{5.7}$$

For σ, the factor of two in the denominator takes account of the *two* surfaces of the slab (one at the top and the other one at the bottom). As we can see from table 5.1, σ for wires is at least four times bigger than for the close-packed metal surfaces. It may look surprising that γ is larger for slab surfaces than for wires, but this is because the wires expose more surface per atom than the two fcc(111) slab faces. These results suggest that the driving force for the chain breaking could be simply the minimization of the metal surface energy, a force which is larger for Cu wires making them unstable in comparison with the other metals of the same periodic column. The electrochemical annealing observed in wires made of Cu [32, 35] improves the crystallinity of the structures and makes them more stable (the spontaneous breaking takes minutes instead of seconds). This is in agreement with our interpretation since the improvement of cristallinity decreases the surface energy. It has been reported that the high surface stress of thicker Cu nanowires is also the driving force for the so-called *shape memory effect*, which is much larger than those of most bulk shape memory alloys [47]. The fact that Cu wires can be stabilized at sufficiently negative bias where hydrogen adsorption seems to occur, is also consistent with this theory since hydrogen can decrease the surface energy [46]. The same phenomenon should occur in Ni, Pd, and Pt wires, whose surface energies are even higher than those of Cu wires. This hypothesis successfully explains the experimental facts through thermodynamics, but to have a final answer, the kinetics of wire breaking should be addressed. The study of dynamics and mechanics of the wire breaking is a wide and complex issue itself [48] and therefore is left for a future work.

The work functions of nanowires and slabs are also compared in table 5.1. In general, $\Phi_{wire} > \Phi_{slab}$, this difference being particularly large for gold wires. These results confirm earlier findings for Au and Ag nanowires by Leiva et al. [36]; as noted by these authors, the large shift in the work function implies a shift in the potential of zero charge (pzc), which in turn means that the wires carry a negative charge excess in the hydrogen evolution region.

5.2   Stress

When the linear monoatomic wires are compressed along their axis, the chain adopts a zigzag configuration in order to avoid repulsion. Zigzag and linear nanowires were studied separately, although it is obvious that the string tension of the former leads

ultimately to the latter one. The potential energy and the stress of such wires is represented in figure 5.1.
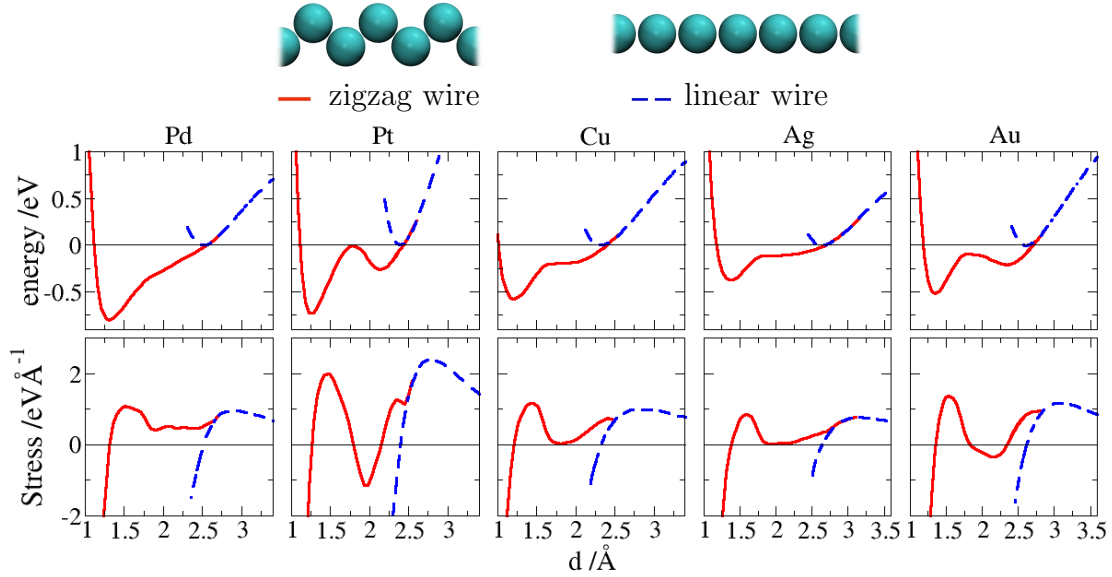
Figure 5.1: Potential energy per atom and stress for zigzag and linear nanowires as a function of the distance d. For the linear configuration, d corresponds to the intermetallic distance, while for the zigzag wires d corresponds to half the unit cell along the x axis (wire axis). The energy is referred to the equilibrium energy of the linear configuration.

The advantage of discriminating both configurations is that we can point out at which state of the elongation the linear configuration sets in. All the wires of the figure present a global minimum in the zigzag form, which corresponds to a nearest-three-atom angle close to 60°.[1] The equilibrium energy of the zigzag wires is around 0.5 eV lower than that of linear ones for the three coin metals, and around 0.75 eV lower for Pd and Pt. Interestingly, Pt and Au wires show a second minimum, which corresponds to a nearest-three-atom angle close to 120°. The wire stress at distances d corresponding to the equilibrium of the linear configuration is close to 1 eV/Å. In almost all the cases studied, the stress reaches a maximum there, the exception being Pd, where it grows to more than 2 eV/Å. Considering the stretch to which the nanowires are subjected in the experiments, it is more reasonable to assume that their configuration is linear, or close to linearity, as has been pointed out in other theoretical works [49]. However, it is important to keep in mind that

---

[1]The increasing energy at $d < 1.2$ Å is a consequence of the repulsion between the two-atoms unit cell, and therefore is artificial. In reality, at such short distances the wire would simply become wider, and the energy would actually decrease, but we would not be dealing with one-atom-thick wires anymore.

the zigzag arrangement lowers the energy of the linear wires considerably.

5.3 Charge density distribution

As we shall see in further sections, the extension of the orbitals over a metal surface or around a nanowire has crucial consequences on the adsorption of species. One way to study this extension is by analysing the electronic density (ρ). To start with, let us compare the radial charge density of several nanowires. As shown in figure 5.2a, the total electronic density contained in a cylindrical tube of width dr was integrated and assigned to the corresponding r (radial distance from the wire). This sum for different radial distances is plotted in figure 5.2b.
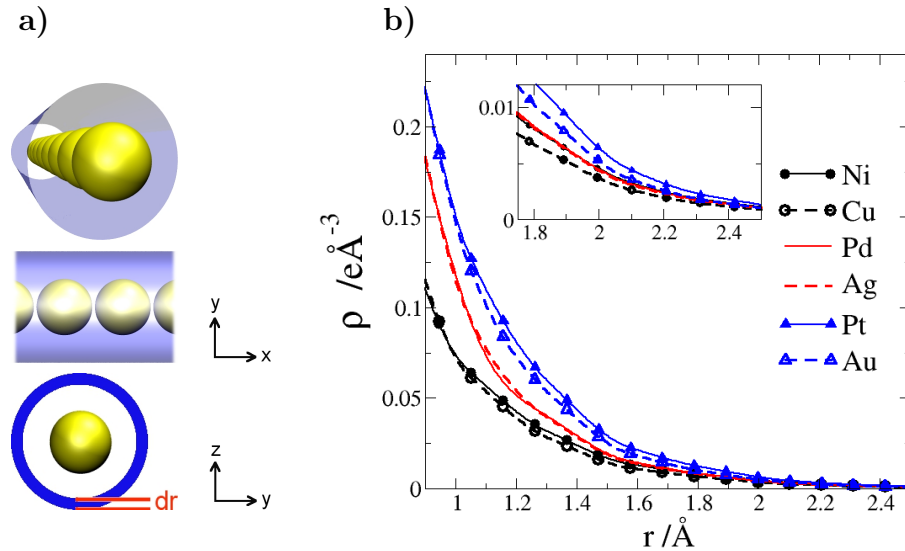
Figure 5.2: a) Perspective views of the charge surrounding a nanowire. The axial length of the axis (L_x) and the cylindrical shell of width dr is shown. **b)** Electronic charge density (ρ) as a function of the distance from nanowire axis.

As it was expected, the electronic density of the metal wires reaches further distances as we go down in the periodic table while metals of the same periodic row have similar ρ.

How different is the charge density experienced by a species approaching a nanowire from that on a metal surface? On fcc(111) slabs, a surface atom is coordinated to nine closer neighbors, while on monostrand wires, each atom is coordinated to only two others. Besides, the interatomic distances are shorter for wires (see table 5.1). On such different structures, one would expect that the charge density at a distance z from the wire would be quite different from the charge at distance z on a slab

surface regardless of the site at which we measure it (one would expect that the differences would be beyond localization effects). In order to look into this intuitive idea, the total charge density of xy planes at distance z from the surface or the wire axis was calculated (illustrated in figure 5.3a). We call this the charge density ρ_z which is plotted in figure 5.3b.

As we can see, for slabs and wires of the same metal ρ_z is the same. This may be against our predictions, but it is important to remember that the charge density can mask important chemical information *hidden* in the first or even second decimal place. To get to that order of values, we can calculate the charge density difference ($\Delta\rho$) defined as the difference between the charge density of the substrate ρ^{sub} (slabs or wires) and that of the isolated atoms ρ^{atom}:

$$\Delta\rho = \rho^{sub}(N) - \sum_{i=1}^{N} \rho^{atom}(i) \tag{5.8}$$

Once $\Delta\rho$ is obtained, we proceed as we did before calculating the total sum at xy planes (illustrated in figure 5.3c). By doing this, the *charge density difference sub-zeta* $\Delta\rho_z$ is acquired which is plotted in figure 5.3d.

To our surprise, even $\Delta\rho_z$ is quite similar for slabs and wires of the same metal. This teaches us that despite of the large geometrical differences between slabs and wires, the average charge density at a certain distance from the structures is rather similar. This also indicates that differences in the charge distribution are site dependent, e.g., the localization effect is important. Looking at figure 5.3d in greater detail, it can be observed that Cu and Pd wires have slightly more charge than surfaces for distances between 1 and 2 Å. Gold wires, on the other hand show a meager retraction of the electronic tail. For silver, these differences are negligible. Interestingly, Cu and Ag wires show a small charge depletion at $z >1.5$ Å which is not seen on Au and Pd wires.

5.4   The wire bond

The bond distance between the wire atoms was compared with the nearest-neighbor distance of bulk metals in table 5.1. As expected, the bond distance is shorter for wires due to the bond order conservation: The less coordinated the atom is the stronger becomes each bond, which in turn reduces the bond length. To explore the matter further, we analyze again the charge density difference (equation 5.8) but this time we focus our attention in the bond regions of the wires, that is, in-between the atoms. Therefore, the $\Delta\rho$ at each yz plane (planes perpendicular to the wire axis) were added. The resulting $\Delta\rho_x$ is shown in figure 5.4 for several nanowires.

The region $0 < x < 1$ corresponds to the wire bond region. Since for $\Delta\rho$ the charge density of atoms is taken as a reference, it is consistent to relate these results

a)

b)

ρ **slab**

ρ **wire**

c)

Δρ **slab**

Δρ **wire**

d)
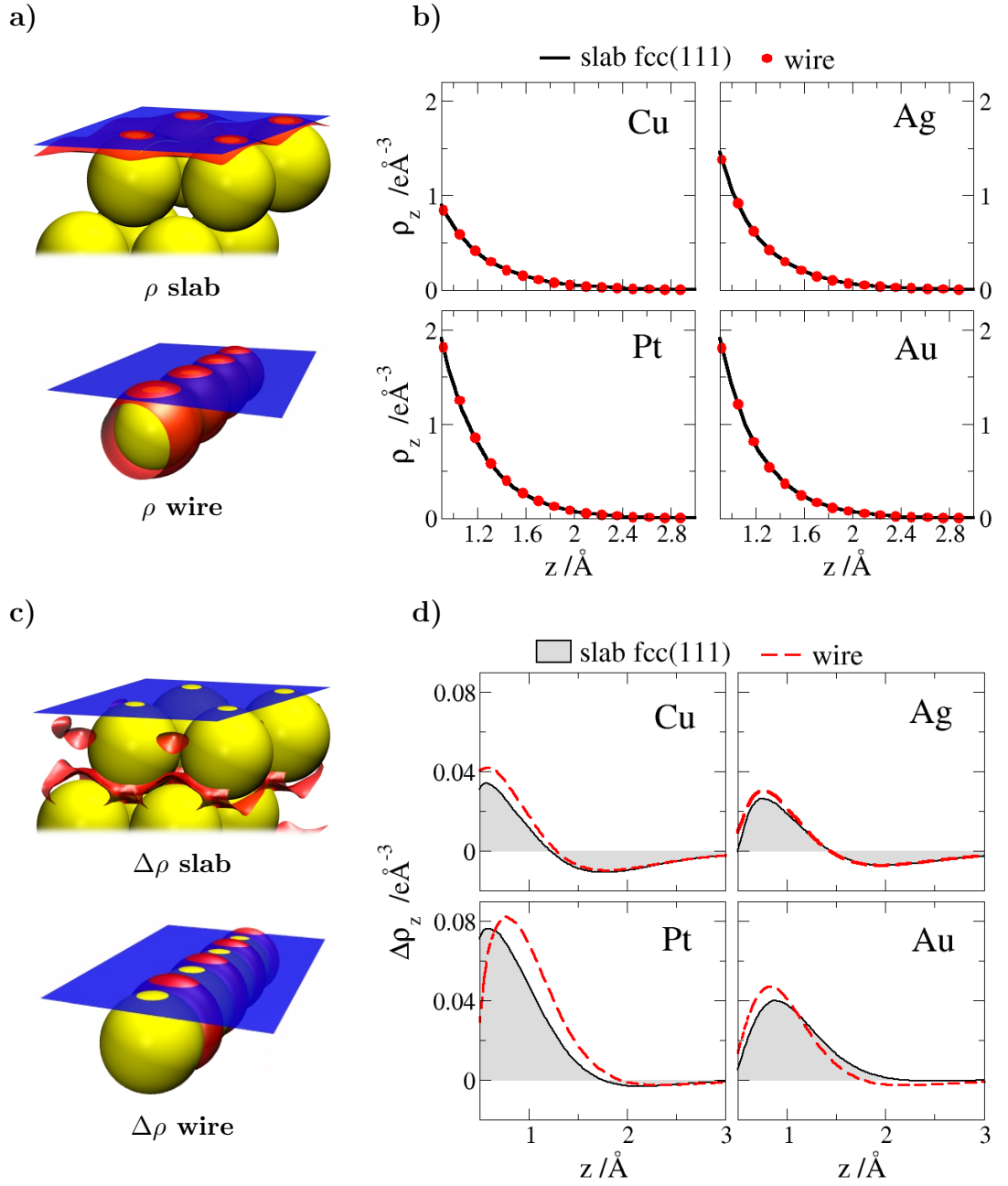
Figure 5.3: a) Perspective views of the charge density (ρ) on a slab and on a wire for an isovalue of 0.12 e/Å^3. A light blue xy plane is also shown. **b)** Charge density sub-zeta (ρ_z) as a function of the distance from the substrates (slab or wire). For the slab $z = 0$ corresponds to the surface atom center and for the nanowire to its axis. **c-d)** Same as **a** and **b** correspondingly but for the charge density difference $\Delta\rho_z$.

a)

b)
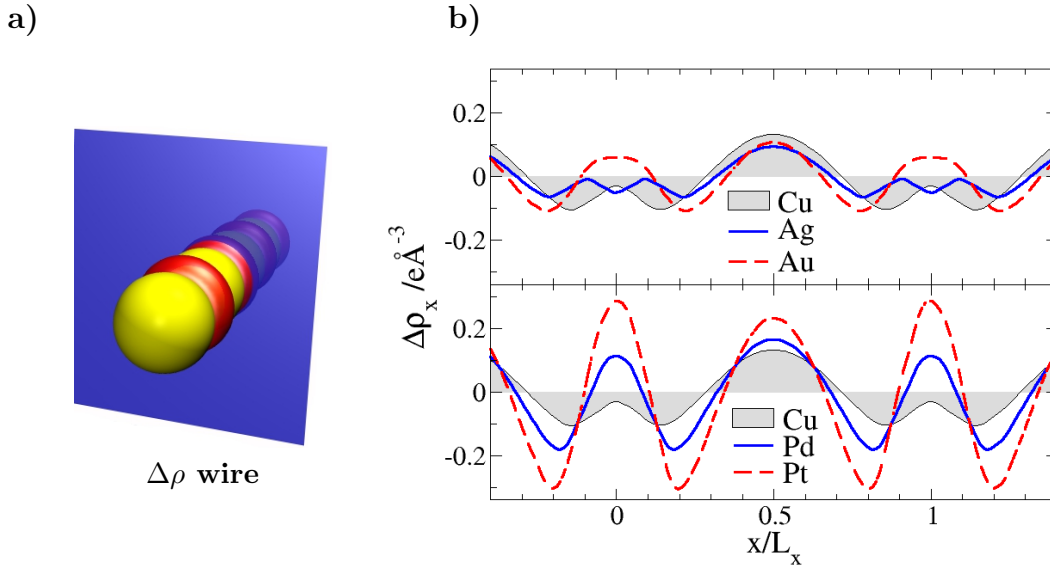
Figure 5.4: a) Perspective view of the charge density difference ($\Delta\rho$) on a nanowire. The red lobes correspond to electron accumulation (isovalue of 0.12 e/Å^3). A yz plane is also shown in the figure. **b)** Sum of the charge density difference at each yz plane ($\Delta\rho_x$) for several nanowires. To facilitate the comparison the distance along the wire axis has been normalized (dividing it to the wire bond distance L_x). A Cu nanowire is used for comparison in both panels.

to the cohesive energy of wires shown in table 5.1. The largest electron charge accumulation was found for Pt nanowires in agreement with its E_{coh}, which is the most negative among the nanowires studied. In general, the bigger the electronic accumulation in the bond-region, the stronger is the bond and therefore the lower is E_{coh}. However, it seems that the charge accumulation *at* the atoms ($x = 0, 1, ...$) observed in Au, Pd, and Pt wires is also related to a lowering of the total energy.

The shape and the orientation of the atomic orbitals are important to gain a geometrical idea of chemical bonds and their symmetry. Figure 5.5a shows the most relevant orbitals for nanowires.

Judging by their symmetry and their overlap, one can already predict that some states will be degenerate: d_{xy} with d_{xz} and d_{z^2} with $d_{x^2y^2}$, which is confirmed in figure 5.5b where the band structure and the density of states of a gold monostrand wire are plotted.

The orbitals are differentiated by their energy width: The larger the overlap of orbitals along the wire axis, the broader is the corresponding density of states. The band structure of all the monometallic nanowires studied in this thesis are shown in figure 5.6.

Note the spin split of some bands for Ni and Pd nanowires. The magnetization of

a)   b)
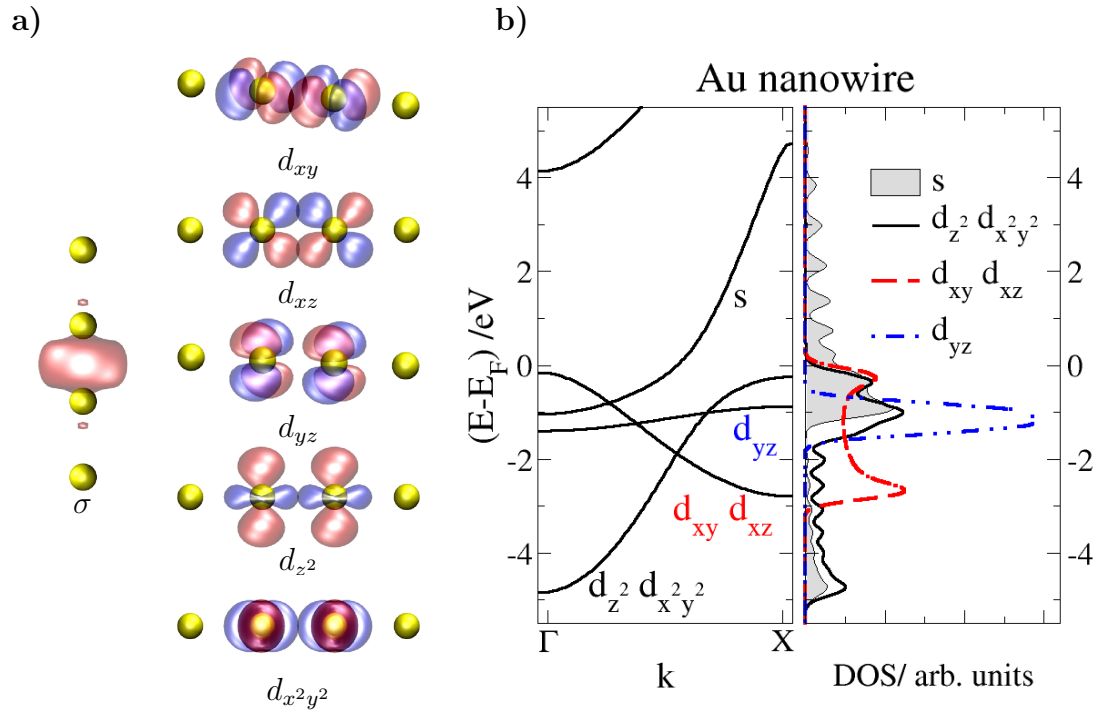
**Figure 5.5: a)** Side view of the most relevant orbitals for an infinite one-atom-thick gold wire. One molecular orbital (σ) and all the atomic d orbitals (shown by pairs) are represented. **b)** Band structure and density of states (DOS) for a gold monostrand nanowire. The Fermi energy (E_F) is used as a reference.
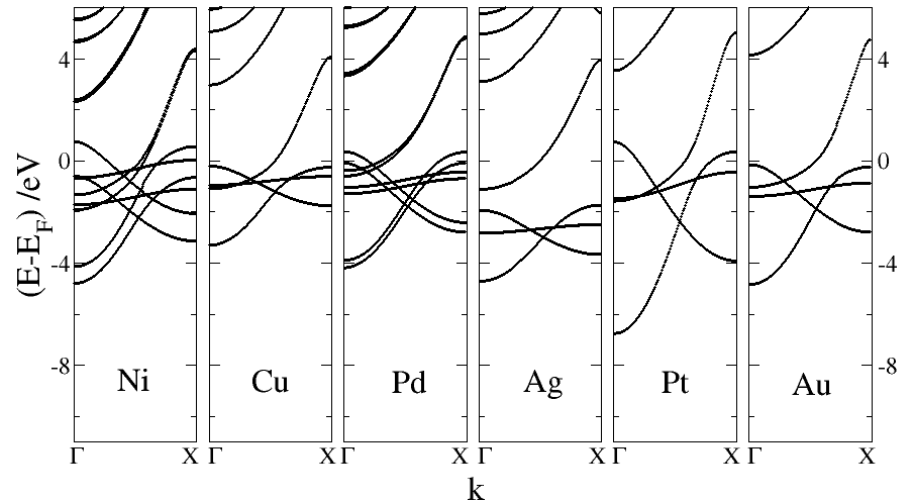
Figure 5.6: Band structure of some one-atom-thick linear metal nanowires.

the latter has been observed experimentally [50] and called the attention of several groups since neither bulk Pd nor the isolated atom are magnetic. Studies based on DFT show that Pd wires magnetize for a wire bond range from 2.3 to 3.4 Å with a polarization maximum of $\sim 0.5\mu_B$ [49]. Our results are in excellent agreement with these findings. The reason for this striking phenomenon can be explained in a first attempt by the increase of the interatomic hybridization, which causes the valence d band to become partially unfilled due to charge donation to the s state. However, some authors claim that the latter picture could be too simple to explain the large magnetic moment of Pd and that the one-dimensionality of the system is the determinant of such behavior [49].
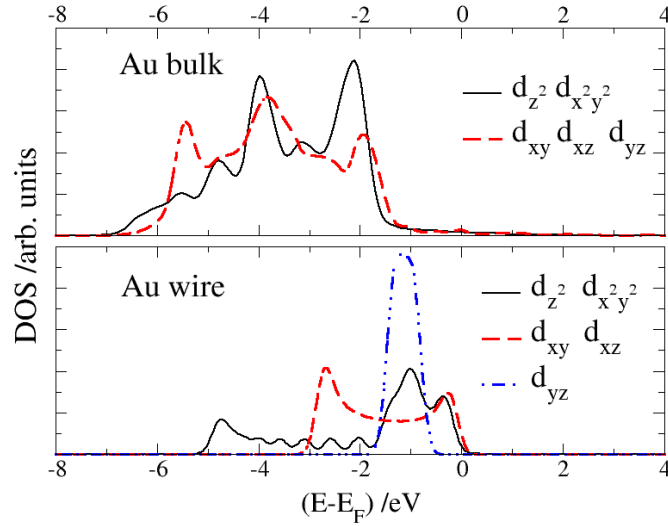

Figure 5.7: Comparison between the projected density of states (DOS) of the d band of bulk gold and a gold monostrand nanowire. For the wire, the DOS is reduced by a factor of three.

As compared with bulk metals, on nanowires the symmetry of the d states is broken as we can see in figure 5.7. In fact, the DOS of the bulk projected in the d orbitals are represented by only two groups: (d_{xy}, d_{xz}, d_{yz}) and $(d_{x^2y^2}, d_{z^2})$. Due to the different orientations of the wire atoms with respect to the bulk, comparisons between projected d orbitals should not be made band by band. It is only important to compare the differences in their width separately.

5.5 d band shift

From the chemical point of view, the most remarkable difference between fcc(111) surfaces and monostrand nanowires is the position of the d band center. Figure 5.8

shows the DOS projected on to the d band of several slabs and nanowires.
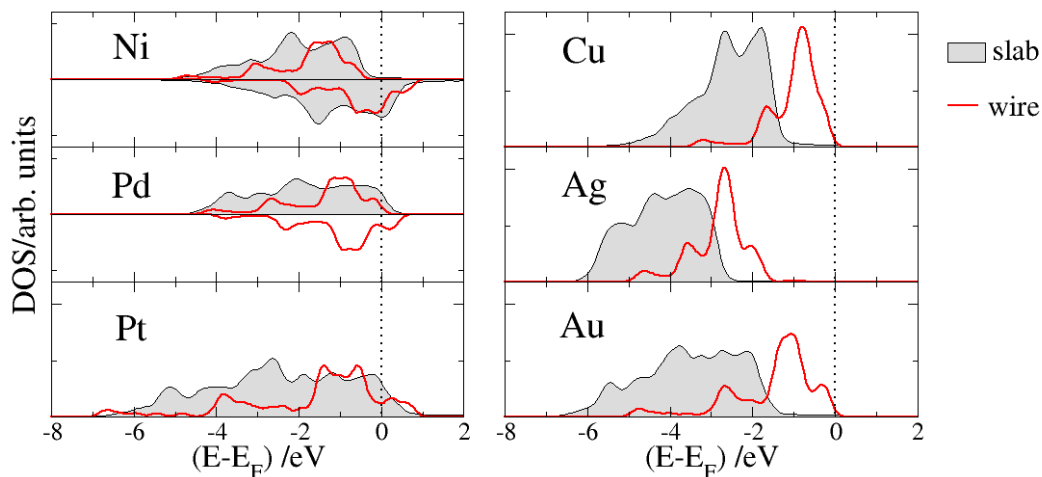
Figure 5.8: Density of states (DOS) projected on the d band states for fcc(111) surfaces and nanowires. Two curves are shown for spin polarized systems; for the rest, both curves are symmetric. The DOS for nanowires has been reduced by a factor of two.

For the three coin metals the d band of nanowires is clearly upshifted in energy in comparison with their respective surfaces. Since the total number of d electrons has to be conserved, their d band cannot pass through the Fermi level. For Ni, Pd, and Pt, this shift is not so important but the narrowing of the states is still evident which in turn pushes up the d band center. As we will see in section 7.2 this shifts are the key to understanding the large hydrogen affinity of Cu and Au nanowires.

5.6   Conclusions

In this chapter a physical and chemical description of monometallic wires was addressed. It was found that the surface energy of Cu, Pd, and Pt wires was considerably larger than that of Ag and Au wires, which explains the experimentally observed instability of the former group. We have also shown that the cohesive energy itself is not sufficient to explain these tendencies. The atomic chain is more stable in the zigzag configuration than in the linear one by at least 0.5 eV. In general, the stress of the wire at the linear equilibrium (which corresponds better to the experimental nanowires) is of the order of 1 eV/Å.

As far as the electronic density distribution is concerned, the electronic decay as a function of the distance from the wire is similar for elements of the same periodic row, and they extend as we go down in the periodic table. The average charge density of wires was found to be similar to that of the fcc(111) surfaces despite of

their great geometrical differences. However, these differences can be substantial in a *local-site* comparison. In general, wires with lower cohesive energies have a larger electron accumulation in the bond region.

Some remarkable differences with respect to the close-packed surfaces were found, such as larger work functions, magnetization of Pd, and the breaking of the d band symmetry. Nevertheless, from a practical point of view the most important finding is the d band shift towards higher energy values, particularly for Cu and Au wires. We will come back to this phenomenon in section 7.2, where the adsorption of hydrogen on monometallic wires is inspected.

6

Bimetallic nanowires

In these days, a man who says a
thing cannot be done is quite apt to
be interrupted by some idiot doing it.

Elbert Green Hubbard Writer
and philosopher.

For industrial applications, it is of paramount importance to control the chemical
doping or alloying of materials in order to enhance their electrical or mechanical
properties. At the nanoscale, this poses challenge that has not been undertaken yet.
Due to their small size, predictions based on bulk metallic alloys cannot be applied to
nanowires. These facts have encouraged several research groups to create bimetallic
wires in innovative ways. In page 25 a non-mechanical electrochemical technique to
produce bimetallic wires was described [35]. Despite the fact that effectively only
Au-Ag and Au-Cu bimetallic wires were obtained by this method, it should be
applicable to any α-β system where α is stable at potentials at which β dissolves.
Another method to create bimetallic wires consists in irradiating two closely spaced
spots in an alloy metal film of 3 to 5 nm thickness with the high-intensity electron
beam of an electron microscope. The two holes created grow spontaneously and
the metal bridge in between thins down, forming a nanowire [51, 52]. By the latter
technique, atomic chains can be generated from different alloy compositions, as
shown in figure 6.1.

When these bimetallic nanowires narrow down to single atom-width, they are
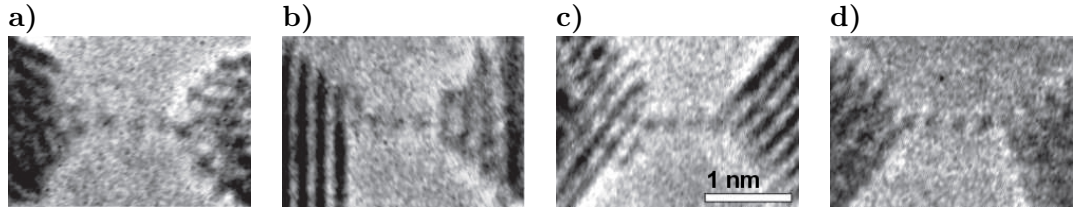
Figure 6.1: Atom-resolved high-resolution transmission electron microscopy (HRTEM) snapshots of suspended atomic chains, generated from different alloy compositions $Au_{1-x}Ag_x$. **a-d)** x=(0.2, 0.4, 0.6, 0.8), respectively [52].

frequently formed as three hanging atoms, one of whose show a stronger signal than the others in high-resolution transmission electron microscopy (HRTEM), as we can see in figure 6.1d. Independent experiments and molecular dynamics show unambiguously that the latter result corresponds to three Ag atoms and a single Au atom at the end of the chain [52]. As the authors of the latter experiments concluded, *"detailed experimental and theoretical work would still be necessary to understand and predict the properties of such bimetallic systems at the nanoscale."*
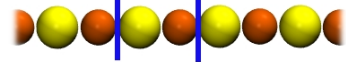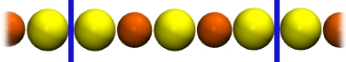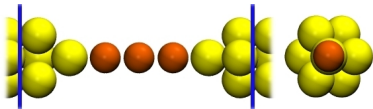
In this chapter, the stability of atomic bimetallic wires of the configuration $\alpha_1\beta_1$ with $(\alpha \neq \beta)$=(Ni, Pd, Pt, Cu, Ag, Au), so-called intercalated wires, are studied. By this analysis we can predict which are the most stable combinations and also if intercalation is preferred over segregation at the one-dimensional nanoscale. The metal combinations used by Shi et al. [35] (Au-Cu and Au-Ag) and Galvão et al. [52] (Au-Ag), are studied in greater detail and in several configurations.

6.1   Technicalities

Modeling

To describe a representative set of one-atom thick bimetallic wires, more than 40 $Au\beta$ wires were computed and 15 $\alpha_1\beta_1$ that result from combining all the atoms from Ni and Cu periodic columns. They are distinguished by their *composition*, and their *mixture index* (MI). The composition is denoted by the chemical formula $\alpha_m\beta_n$ where m and n are the numbers of α and β atoms in the unit cell, respectively. The MI is used for wires with the same chemical composition and indicates the *intercalation* grade. MI counts the number of inter-metal bonds. In order to make MI independent of the number of atoms, the *relative mixture index* (RMI) is used, and is defined as $RMI=MI/N$ where N is the number of atoms in the unit cell. For quantitative comparisons the *fractional composition* $(\chi=n/N)$ is used. Examples are given in table 6.1.

In order to compare these monostrand wires with others closer to the experimen-

| Bimetallic wire	formula	MI	RMI	χ
	Au_1Cu_1	2	1.0	0.50
	Au_3Cu_2	4	0.8	0.40
	Au_3Cu_2	2	0.4	0.40
	Au_TCu_3	2	0.4	0.60

Table 6.1: Example of Au_mCu_n wires with their chemical formula, mixture index (MI), relative mixture index (RMI) and fractional composition (χ). Note that the highest RMI possible is 1. The length of the unit cells are sketched within blue lines.

tal setup, the $Au_T\beta$ wires were computed (see bottom of figure 6.1). They consist of cluster-like terminated wires formed by two layers of three equidistant atoms each, the wire being perpendicular to them. For this case, MI, RMI and χ are taken without considering the layer atoms. The size of the cell is given by the vector $(L_x; L_y; L_z)$ where $L_y=L_z=11$ Å. Since the x axis is the axis of the wire, L_x depends on the metal mixture and has to be optimized. For each bimetallic wire several values of L_x were selected; at each of these lengths the atoms were allowed to relax along the wire axis. For the $Au_T\beta$ wires, the layer atoms were fully relaxed. A quadratic relation between the total energy and L_x was obtained, the minimum was achieved with an accuracy of 2 meV. Convergence was achieved when the total forces were less than 0.01 eV/Å.

First principles parameters

Special care was taken for the parametrization of the energy cutoff and the k-points sampling of the Brillouin zone based on the Monkhorst-Pack grid [11]. Both parameters were increased systematically until the change in the absolute energy was less than 10 meV. The systematical increase of k-points and plane wave cutoff were tested for Cu_1Au_1 and Ag_1Au_1 wires.

As shown in figure 6.2, 400 eV energy cutoff and a grid of $5 \times 1 \times 1$ seem to be enough to satisfy the energy accuracy, but to be on the safe side, the calculations were performed with 450 eV cutoff and a $8 \times 1 \times 1$ Monkhorst Pack grid. This choice minimizes the *relative* error that results from the comparison of bimetallic
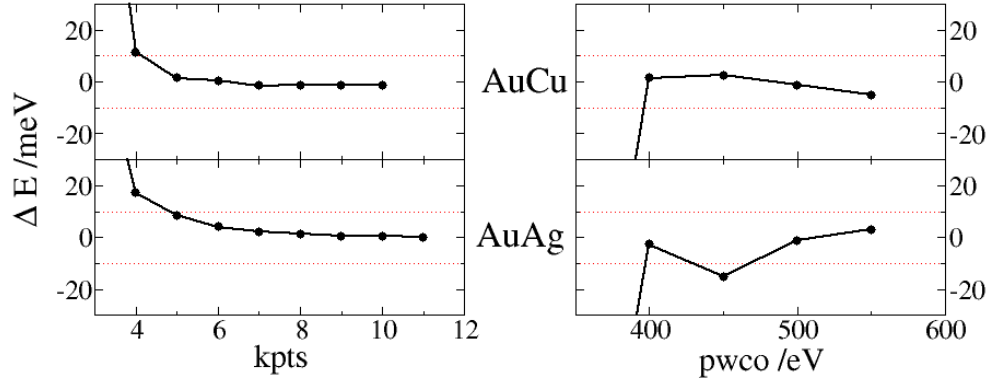
Figure 6.2: Energy difference with respect to the previous value (ΔE) of k-points (*kpts*) and plane wave cutoff (*pwco*) for AuCu and AuAg bimetallic wires.

wires of different composition with corresponding different cell sizes (explained in detail later). Spin considerations were included for some representative systems. As shown in the previous chapter, Ni and Pd monometallic wires are spin polarized. All the bimetallic wires containing Ni or Pd also presented magnetic moments with the exception of PtPd bimetallic wires. In all cases the magnetization of chains with Ni were bigger than those with Pd wires.

Cohesive, surface and combination energy equations

The cohesive and the surface energy were calculated in reference to the isolated atoms and the bulk systems, respectively, as shown in equations 6.1 and 6.2. Another important parameter to compare is the change in the wire energy due to the inter-metal interaction, e.g., the energy gain by breaking a monometallic wire bond and making an inter-metal one. This is the so-called *combination energy* E_{comb}, defined in equation 6.3

$$E_{coh} = \frac{E_{wire}(\alpha_m \beta_n) - m E_{at}(\alpha) - n E_{at}(\beta)}{m + n} \tag{6.1}$$

$$\sigma = \frac{E_{wire}(\alpha_m \beta_n) - m E_{bulk}(\alpha) - n E_{bulk}(\beta)}{m + n} \tag{6.2}$$

$$E_{comb} = \frac{E_{wire}(\alpha_m \beta_n) - m E_{wire}(\alpha) - n E_{wire}(\beta)}{MI} \tag{6.3}$$

where $E_{wire}(\alpha)$ and $E_{wire}(\beta)$ are the energy per atom of α and β monometallic wires, respectively. Negative values of E_{comb} indicates good inter-metal affinity and preference for intercalation while positive values indicate energetically unfavourable

inter-metal interactions and preference for segregation. To start with, we study these parameters for the highest grade of intercalation ($RMI=1$).

6.2   Intercalated $\alpha_1\beta_1$ wires

Both the relative stability of bimetallic wires with respect to the monometallic ones, and the trend for intercalation/segregation, can be studied by means of the combination energy (equation 6.3). Negative values of E_{comb} indicate good inter-metal affinity and preference for intercalation while positive values indicate unfavorable inter-metal interactions and preference for segregation. The combination energy E_{comb}, cohesive energy E_{coh}, surface energy σ, and the inter-metal bond distance (d_{nn}) for several bimetallic wires are presented in table 6.2.

	E_{comb} [eV/at]					E_{coh} [eV/at]				
	Ni	**Au**	**Ag**	**Cu**	**Pt**	**Ni**	**Au**	**Ag**	**Cu**	**Pt**
Pd	-0.09	-0.07	0.12	-0.01	-0.01	-1.71	-1.46	-1.12	-1.42	-2.09
Pt	-0.08	0.26	0.41	0.20		-2.63	-2.07	-1.76	-2.15	
Cu	0.14	-0.15	0.01			-1.75	-1.80	-1.49		
Ag	0.14	-0.14				-1.45	-1.61			
Au	-0.06					-1.92				

|	σ [eV/at]					d_{nn} [Å]				
	Ni	**Au**	**Ag**	**Cu**	**Pt**	**Ni**	**Au**	**Ag**	**Cu**	**Pt**
Pd	2.61	1.97	2.09	2.24	2.62	2.33	2.56	2.64	2.40	2.43
Pt	2.68	2.36	2.44	2.51		2.30	2.50	2.56	2.36	
Cu	2.52	1.57	1.67			2.28	2.46	2.48		
Ag	2.36	1.31				2.46	2.62			
Au	2.11					2.40				

Table 6.2: Combination energy (E_{comb}), cohesive energy (E_{coh}), surface energy (σ) and inter-metal bond distance (d_{nn}) for several $\alpha_1\beta_1$ bimetallic wires. Particularly low E_{comb} and σ are highlighted in red.

The best inter-metal affinity and lowest surface energy among the 15 combinations of metals correspond to Au_1Cu_1 and Au_1Ag_1 wires. This is in agreement with the fact that Au-Cu and Au-Ag bimetallic wires were indeed obtained experimentally [35,52]. Au_1Pd_1 has the fourth lowest surface energy and shows good inter-metal affinity. Ag_1Cu_1 has a negligible energy gain due to the inter-metal interaction but its surface energy is the third lowest in table 6.2. Thus, we predict that the combination of Au-Pd and Ag-Cu should also lead to stable bimetallic wires. Despite of the lower combination energy of $Ni\beta_n$ wires, their surface energy is among the highest

found. It is, however, relatively small for Ni_1Au_1 wires which is therefore the only stable bimetallic wire predicted for Ni. Gold is by far the metal that combines best with the transition metals studied here, while platinum is the worst. In the next section, the two most stable bimetallic wires from table 6.2 are studied in greater detail for $RMI \leq 1$.

6.3 Au_mCu_n and Au_mAg_n wires

As table 6.1 shows, two different bimetallic wires can have the same fractional composition χ but they can still be distinguished by the relative mixture index RMI. It is instructive to compare the cohesive and the surface energy in such cases since this gives a more general idea of the inter-metal affinity. Figure 6.3 shows E_{coh} and σ with respect to the fractional composition χ.
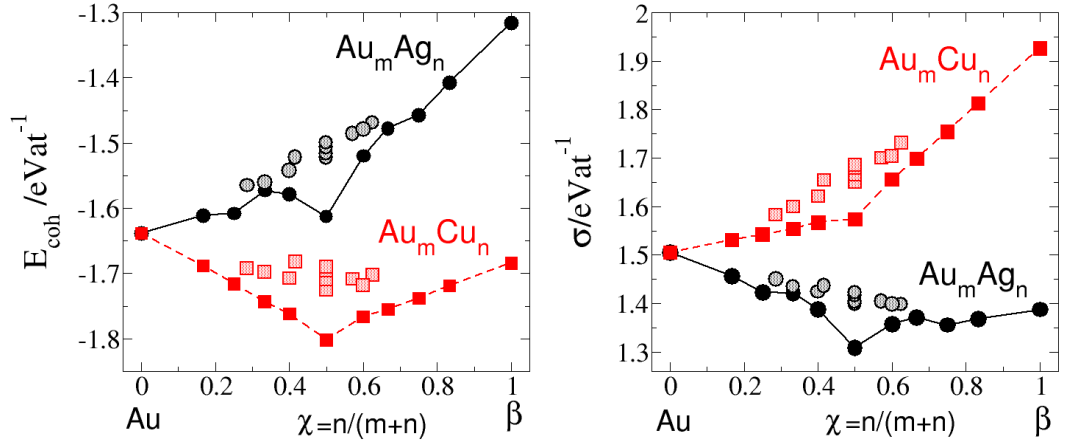
Figure 6.3: Cohesive (E_{coh}) and surface (σ) energy as a function of the fractional composition (χ) of Auβ wires. $\chi = 0$ corresponds to a Au monometallic wire and $\chi = 1$ to a β monometallic wire (Ag or Cu). The isolated points correspond to wires with RMI values lower than the maximum RMI possible for its composition. The lines are only an aid to the eyes.

Among the points with the same χ in figure 6.3, those with the bigger RMI are connected with a line. As we can see, this line is in all cases below the rest of the points, which means that for a given composition, the more mixed the different metals are, the more stable is the wire. Another important result is that at $\chi=0.5$ for $RMI=1$, both bimetallic wires have a global energy minimum either in the cohesive energy or in the surface energy. In addition, these wires have the largest entropy possible for their configuration. Thus, the most stable configuration for Au_mCu_n and Au_mAg_n wires is that with $m = n = 1$.

In the experimental Au-Ag wires of Galvão et al. [52], the lower surface energy of Ag with respect to Au leads to a lower amount of the latter in the atomic chain. On the other hand, in the experimental Au-Cu and Au-Ag wires of Shi et al. [35], Au does not dissolve at the potential at which the atomic chains are formed. Therefore, for both cases, $\chi \approx 1$. These results agree with the natural assumption that at $\chi \approx 1$, bimetallic and β pure wires have similar stability.

6.4   The inter-metal bond

On an average, E_{comb} (see page 46) is -0.11 eV for Au_mAg_n wires and -0.14 eV for Au_mCu_n wires. In order to reveal the reason of this stabilization, the electronic distribution in mono- and bimetallic wires was studied by comparing their charge density difference ($\Delta\rho$) defined as usual

$$\Delta\rho = \rho_{wire}(\alpha_m\beta_n) - m\rho_{at}(\alpha) - n\rho_{at}(\beta) \tag{6.4}$$

For a given position along the wire axis (x), a total sum over $\Delta\rho$ on the yz plane is made and denoted by $\Delta\rho_x$. Regions along the wire axis with $\Delta\rho_x > 0$ correspond to electron accumulation (bond region) while regions with $\Delta\rho_x < 0$ correspond to electron depletion. The results for $Au_3\beta_2$ wires for $\beta=(Cu,Ag)$ are shown in figure 6.4.

There is a larger depletion around the β atoms of the bimetallic wires than in β monometallic wires. Correspondingly, there is a larger charge accumulation on the Au side of the former than on Au monometallic wires (figure 6.4 down). This charge redistribution is due to the larger electronegativity of Au compared to Ag and Cu. Alternatively we can compare the work functions (Φ) of the monometallic wires which follow the same trend, as shown in table 6.3.

	X [53]	Φ [eV]
Cu	1.93	5.24
Ag	1.90	5.12
Au	2.54	6.44

Table 6.3: Atomic electronegativities (X) in Pauling units [54] and work functions of monometallic wires.

The charge depletion for Au_3Cu_2 does not involve a change in the Cu-Cu bond region, while for Au_3Ag_2 the charge accumulation is lower than in the Ag monometallic wire. This can be interpreted as a Ag-Ag bond weakening due to the presence of Au, which is not observed in the Cu-Cu bond. The same tendency is observed for all the other $Au_m\beta_n$ wires studied, including the $Au_T\beta_n$ wires. The only case where
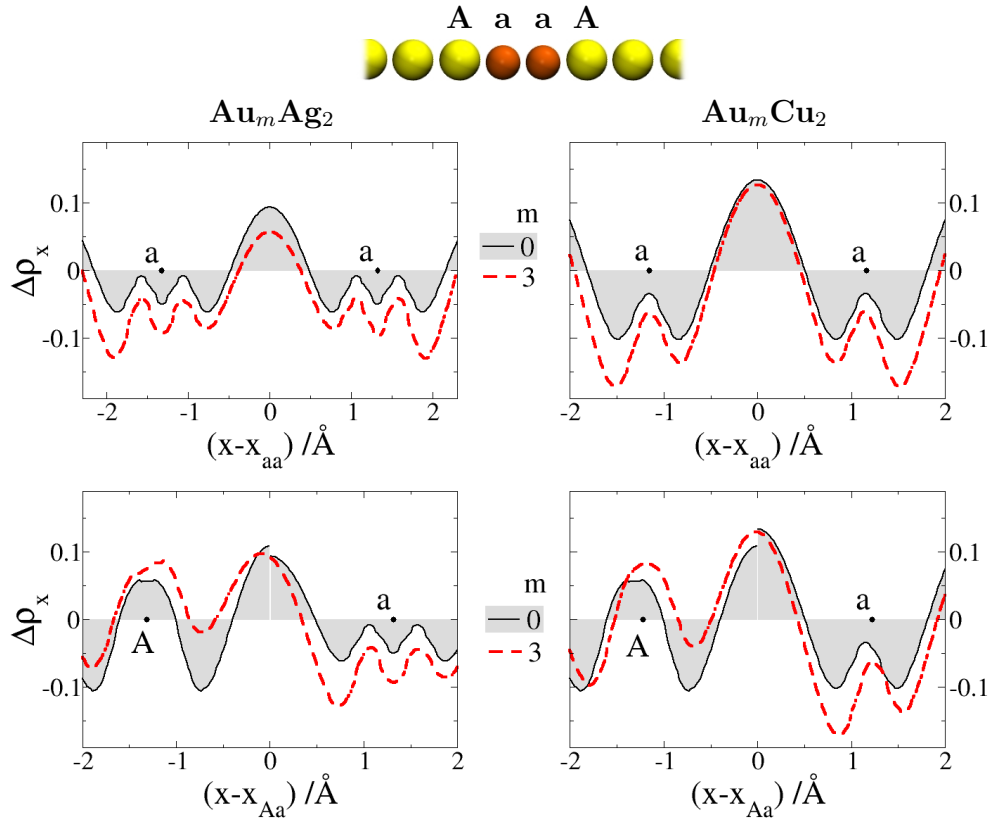
Figure 6.4: Charge redistribution in $Au_m\beta_2$ and β monometallic wires. Au atoms are labeled with capital letters and β atoms with lower case letters. The Au-β region is shown above and the β-β region below. x_{aa} and x_{Aa} are the positions along the wire axis at half the a-a and A-a atom distances respectively. The shaded area corresponds to $\Delta\rho$ of the monometallic wires. For the top panels the shaded area in each plot corresponds to a single monometallic wire. For the bottom panels, the shaded area in each plot corresponds to two monometallic wires, note the discontinuity at $(x$-$x_{Aa}) = 0$.

$\Delta\rho(x)$ is clearly different is in $Au_1\beta_1$ wires. Still, the difference is only quantitative: such wires have a larger accumulation in the Au atoms region and a larger depletion in the β atoms region than other $Au_m\beta_n$ chains.

6.5   Conclusions

From the 15 possible combinations to form wires between elements of Ni and Cu periodic columns, those containing gold were found to be the most stable ones. The best inter-metal affinity corresponds to gold-copper and gold-silver. In agreement with these results, experimental wires have been obtained combining these metals [35]. Due to their low surface energy and favorable combination energy, we predict that Au-Pd, Ag-Cu, and Au-Ni combinations should also lead to stable bimetallic wires.

Giving their particular stability, $Au_m\beta_n$ wires with $\beta=(Cu, Ag)$ were studied in greater detail. The inter-metal bond was found to be stronger than the bond of the pure wires due to a charge redistribution toward the Au atoms, which strengthens the polar character of the covalent bond.

One still unexplored topic is the electronic effect caused by the inter-metal interactions, which may have a strong influence in the chemisorption properties of nanowires. We will address this issue in chapter 8, where the adsorption of hydrogen on bimetallic wires is examined.

7

Atomic hydrogen adsorption on monometallic wires

There is an abundant literature about metal nanowires in the vacuum or in air, but relatively little about wires in an electrochemical environment. Pioneering experimental work in this area has been performed by the groups of Tao [32] and Kiguchi et al. [55,56]. They have examined the conductivity of monoatomic wires composed of the three coinage metals. It is well-known that as long as the wires get thinner the conductance drops until it becomes quantized and its value is ideally a multiple of $2e^2/h$ (G_0). Tao and Kiguchi found a deviation from this phenomenon. As shown in figure 7.1, Cu and Au wires show *integral conductance* (multiple of G_0) at potentials higher than the potential of the hydrogen evolution region (φ_{HER}). However, at potentials below φ_{HER}, Cu and Au exhibit *fractional* conductance. On the other hand, this conductance dependency on the potential is not observed on Ag wires, for which the conductance is always integral [56].
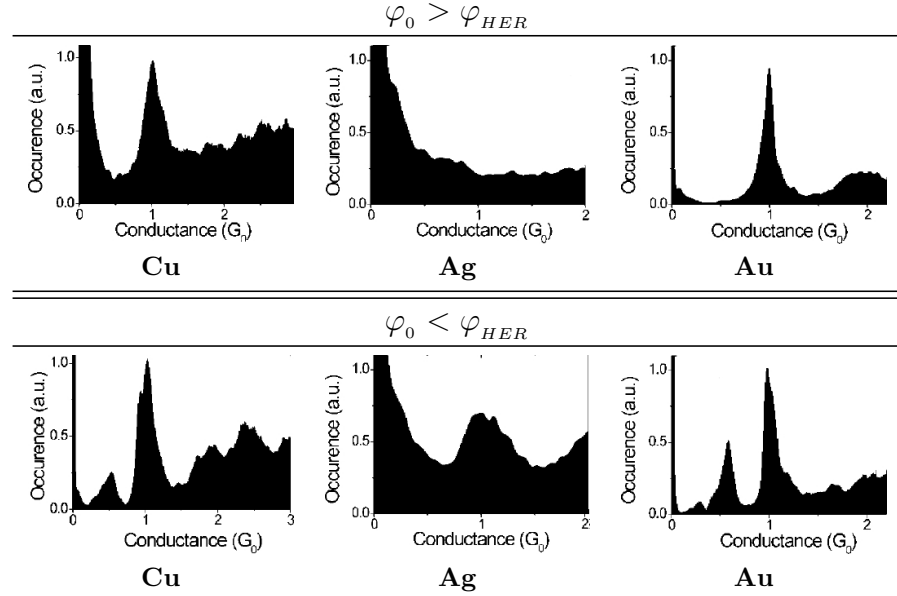
Figure 7.1: Experimental conductance histogram for coinage metal nanowires at higher (top panels) and lower (bottom panels) potentials than the potential of the hydrogen evolution reaction (HER). Adapted from [56].

The authors ascribed this phenomenon to the adsorption of hydrogen. There is, however, a problem with this idea: at least on the planar surfaces of the three coin metals, hydrogen does not adsorb. Is the adsorption of hydrogen favorable on nanowires?

In this section the free energy of adsorption (ΔG_{ads}) of hydrogen on several metal wires is calculated. Using hydrogen as a microscopic probe, the reactivity of monometallic wires and surfaces is compared. The hydrogen-substrate bond is described in detail, for which the low-coverage case is considered. Then, the adsorption energy at increasing hydrogen coverages on the wire is presented. Later on, kinetic considerations are addressed: The activation barrier for the process of proton adsorption in an aqueous solution is calculated using Santos-Schmickler theory. Finally, the highlights of this research are reviewed in the conclusions.

7.1   Technicalities

Modeling

The initial set up for hydrogen adsorption on wires and slabs correspond to the one described in section 3.2.

Hydrogen on wires: The relaxed configurations of the monometallic bare wires were used (so-called pre-relaxed wires) and a hydrogen atom was added on top and bridge sites. At low hydrogen coverages ($\theta \leq 1/6$), the adsorption energy difference between relaxed and fixed-pre-relaxed wires is negligible (< 0.03 eV). Thus, pre-relaxed wires were used. The wire axis length (L_x) has to be sufficiently large to avoid interactions with its images. Convergence was reached when the increase of one atom changed the hydrogen adsorption energy for less than 20 meV as shown in figure 7.2; results are summarized in table 7.1.

	Ni	Cu	Pd	Ag	Pt	Au
L_x /atoms	7	8	6	10	9	6

Table 7.1: Length of the unit cell (L_x) needed to avoid self-interaction for a single hydrogen adsorption process on several monometallic wires.
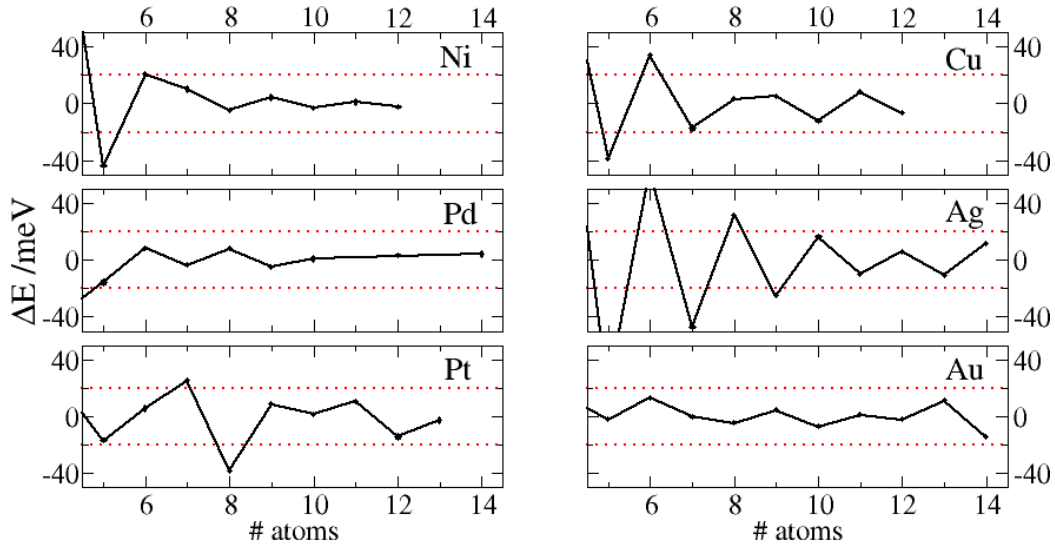
Figure 7.2: Change in the adsorption energy with respect to the length of the wire for the *bridge* position.

At high hydrogen coverages ($\theta \geq 1$), the adsorption energy difference between relaxed and fixed-pre-relaxed wires is at least 0.05 eV. Therefore, at high coverages the atoms were relaxed in different wire bond distances until the equilibrium energy was found (achieved with an accuracy of 2 meV).

Hydrogen on surfaces: Hydrogen was adsorbed on the pre-relaxed four-layer slabs described in section 3.2. Two coverages were studied, $\theta = 1$ and $\theta = 1/4$, for which

1×1 and 2×2 lateral unit cells were used, respectively. Hydrogen was deposited on high-symmetry sites. The first two layers of the slab were fixed and the rest (top two layers and hydrogens) was fully relaxed.

First-principle parameters

Hydrogen on wires: The k-points and the plain-wave cutoff energy were taken from the parametrization for monometallic wires (see page 18). For kinetic considerations, single point calculations of hydrogen at several distances from the wire or the surface (d_{HW}) are needed. When the adsorbate is at sufficient distance, spin polarization sets in. Therefore, spin is contemplated at $d_{HW} \geq 2.4$ Å. At closer distances, the spin was considered only for Ni and Pd wires since only they show magnetic properties.

Hydrogen on surfaces: The same parameters used for the bare surfaces (see page 19) were computed here. The spin was only considered for Ni systems since the rest of the slabs did not present spin polarizations.

ΔG$_{ads}$ determination

In order to determine if hydrogen adsorption is thermodynamically favored, the free energy of adsorption (ΔG_{ads}) has to be calculated, for which the entropic term has to be considered:

$$\Delta E_{ads} = E_{Subs+H} - \left(E_{Subs} + \frac{E_{H_2}}{2} \right) \tag{7.1}$$

$$\Delta G_{ads} = \Delta E_{ads} + \Delta E_{ZPE} - T\Delta S_{ads} \tag{7.2}$$

$$= \Delta E_{ads} + \Delta E_{ZPE} - \frac{TS_{H_2}^0}{2} \tag{7.3}$$

$$= \Delta E_{ads} + 0.23 \tag{7.4}$$

ΔE_{ads} is the enthalpy of adsorption which is easily calculated with DFT by subtracting half the energy of the bare substrate (E_{Subs}) and the energy of a hydrogen molecule in the gas phase($E_{H_2}/2$) from the energy of the substrate *with* the hydrogen atom adsorbed E_{Subs+H}. The subindex $Subs$ refers to a wire or a slab. ΔE_{ZPE} is the difference in zero point energy between the adsorbed and the gas phase hydrogen and ΔS_{ads} is half the entropy of adsorption of H$_2$. The same procedure as Nørskov is used [57] where the vibrational entropy of the adsorbed hydrogen is considered negligible and therefore $\Delta S_H \approx S_{H_2}^0/2$ where $S_{H_2}^0 = 0.41$ eV [58] is the entropy of H$_2$ in the gas phase at standard conditions. ΔE_{ZPE} was calculated for all the monometallic wires. The values were always around (0.02 ± 0.01) eV which is in line

with the finding that vibrational frequencies depend much less on the metal than the bond strength [59]. This leads to a constant entropic term of 0.23 eV.

7.2   Wire enhanced reactivity

Hydrogen adsorption energy on fcc(111) surfaces

The fcc(111) surface presents more high-symmetry sites than the linear wires. The former are illustrated in figure 7.3.

fcc-hollow   **hcp-hollow**   **bridge**   **top**
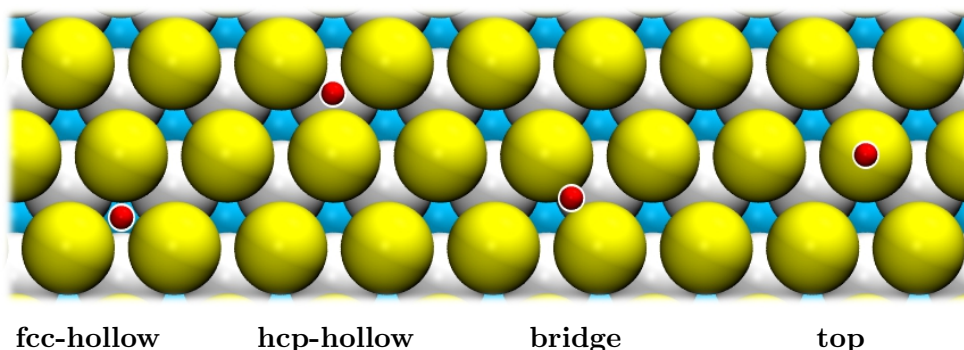
Figure 7.3: High-symmetry points at which atomic (left panel) and molecular (right panel) adsorption on fcc(111) surfaces occurs. The top, second and third surface layers are colored yellow, white and light blue, respectively. Hydrogen is colored red.

The corresponding adsorption energies (ΔE_{ads}) are summarized and compared with literature values in table 7.2.

Two relevant conclusions can be deduced from the analysis of table 7.2. First, the hollow-fcc adsorption site is the most stable configuration for all cases; and second, the adsorption is endothermic only for Ag and Au surfaces (later we will see that by adding the entropic term, hydrogen adsorption on Cu surfaces is not favored either). Our results are in general agreement with related published studies.

Hydrogen adsorption energy on monometallic wires

The adsorption of hydrogen on linear wires has only two high-symmetry sites: bridge and top. The corresponding energies are summarized in table 7.3.

In all cases, hydrogen on the bridge site is the most stable configuration. In order to facilitate the comparison, the hydrogen free energy of adsorption (ΔG_{ads}, section 7.1) of the most stable adsorption site for fcc(111) surfaces and linear wires is shown in table 7.4

position	source	**Ni**	**Pd**	**Pt**	**Cu**	**Ag**	**Au**
fcc-hollow	exp.	-0.51[a]	-0.45[b]	-0.47[c]	-0.13[d]	-	-
fcc-hollow	this work	-0.58	-0.62	-0.49	-0.20	0.16	0.15
	theory	-0.60[e]	-0.51[f]	-0.48[g]	-0.18[h]	0.20[i]	0.11[j]
hcp-hollow	this work	-0.56	-0.59	-0.45	-0.18	0.18	0.20
	theory	-0.59[e]	-0.45[f]	-0.45[g]	-0.17[h]	0.23[i]	0.15[j]
bridge	this work	-0.43	-0.48	-0.43	-0.04	0.30	0.25
	theory	-0.46[e]	-0.32[f]	-0.44[g]	-0.03[h]	0.27[i]	0.19[j]
top	this work	0.02	-0.01	-0.41	0.45	0.69	0.43
	theory	0.00[e]	0.04[f]	-0.45[g]	0.43[h]	0.64[i]	0.35[j]

Table 7.2: Adsorption energy in eV of H$_{at}$ on fcc(111) surfaces at 1/4 coverage, top two layers fully relaxed. Experimental values are compared with literature values. [a] [60], [b] [61]$(\theta < 1/4)$, [c] [62], [d] [63]$(\theta = 2/3)$, [e] [64] [f] [65]$(\theta = 1)$, [g] [66], [h] [67], [i] [68], [j] [69]

		Ni	**Pd**	**Pt**	**Cu**	**Ag**	**Au**
E_{ads} [eV]	(bridge)	-0.428	-0.550	-0.594	-0.486	0.002	-0.665
	(top)	0.005	-0.400	-0.528	0.298	0.748	-0.109
dH_{nn} [Å]	(bridge)	1.60	1.74	1.75	1.58	1.73	1.71
	(top)	1.44	1.55	1.54	1.46	1.60	1.54

Table 7.3: Hydrogen adsorption energies (E_{ads}) and hydrogen distances from its nearest neighbors (dH_{nn}) on monometallic wires.

| ΔG_{ads} [eV] at SHE	**Ni**	**Pd**	**Pt**	**Cu**	**Ag**	**Au**
slab	-0.35	-0.28	-0.26	0.03	0.39	0.38
wire	-0.20	-0.32	-0.36	-0.26	0.23	-0.44

Table 7.4: Free energy of adsorption (ΔG_{ads}) of hydrogen atom on the hollow-fcc site for fcc(111) surfaces and on the bridge site for monometallic wires.

In comparison with the process on surfaces, hydrogen adsorption on wires is generally enhanced. Moreover, in the case of Au and Cu the hydrogen free energy of

adsorption becomes negative. On the other hand, this enhancement is not observed on silver, whose free energy of adsorption remains endergonic. These results support the idea that the fractional conductance observed on Cu and Au nanowires are due to hydrogen adsorption. Accordingly, this would also explain why this phenomenon is not observed on Ag wires. Why are nanowires more reactive than fcc(111) surfaces?

7.3   The hydrogen-substrate bond

Before turning to the explanation of the reactivity of nanowires, let us recapitulate our understanding of hydrogen adsorption on surfaces. The hydrogen $1s$ state interacts with both the valence sp and d band states of the metals. In each case, the overlap between the states results in bonding and antibonding contributions. As shown in figure 7.4, for surfaces the DOS of the sp band is wide and flat. The interaction with hydrogen leads to a broad DOS in which the antibonding states are above the Fermi level (empty), and therefore the sp orbitals contribute favorably to the hydrogen-surface bond.
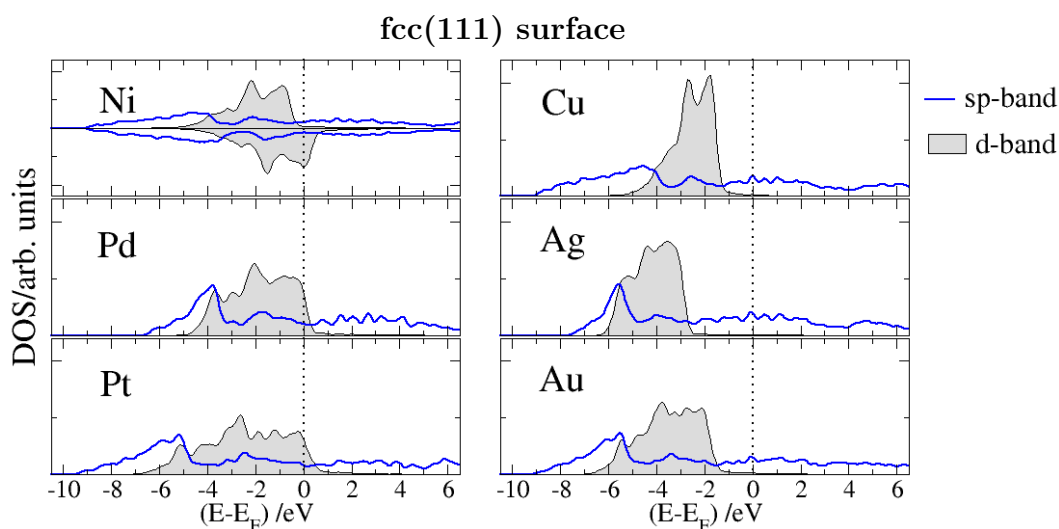
Figure 7.4: Density of states (DOS) projected on the sp and the d band of several fcc(111) surfaces. Two curves are shown for spin polarized systems; for the rest, both curves are symmetric.

The d band of surfaces instead is narrow and sharp. The so-called σ bonding and σ^* antibonding, that result from its interaction with hydrogen, tend to appear right below and above the metal d band, respectively. This entails that when the d band reaches or even crosses the Fermi level (Ni, Pd, and Pt surfaces), σ^* is practically unoccupied. Nevertheless, the d band can also be far below the Fermi

level (coin metal surfaces) and therefore σ^* can be partially or totally occupied. If the antibonding state is occupied, the overlap between the d band and the hydrogen orbital weakens the bond because of Pauli repulsion. The bigger the radius of the metal, the larger the repulsion, thus, the adsorption is stronger for Cu and weaker for Au at the surfaces. The Pauli repulsion determines the strength of the bond, which explains the values of ΔG_{ads} for the surfaces in table 7.4. At wires, however, the d band is shifted to higher energy values as we can see in figure 7.5. Regardless of the magnitude of the shift, the occupation of the d band has to be conserved.
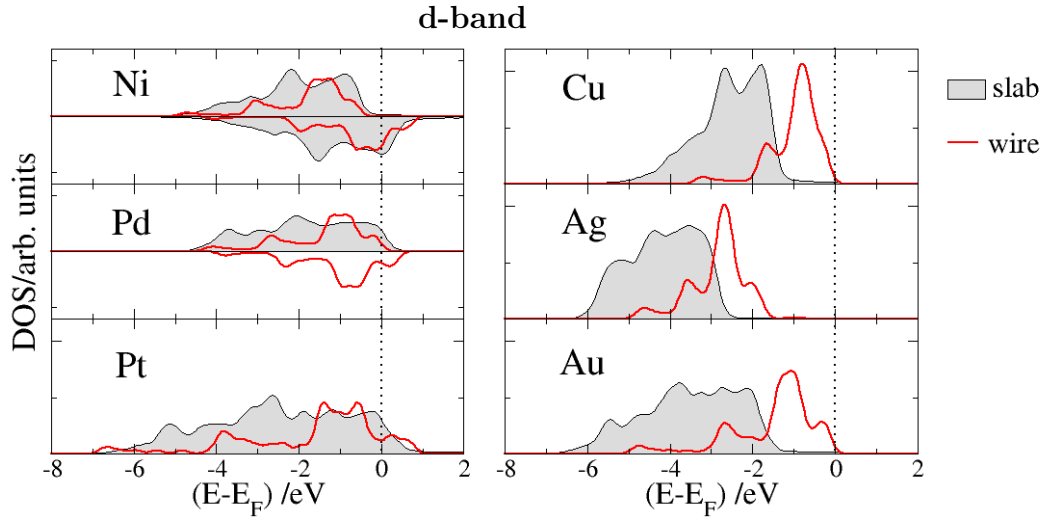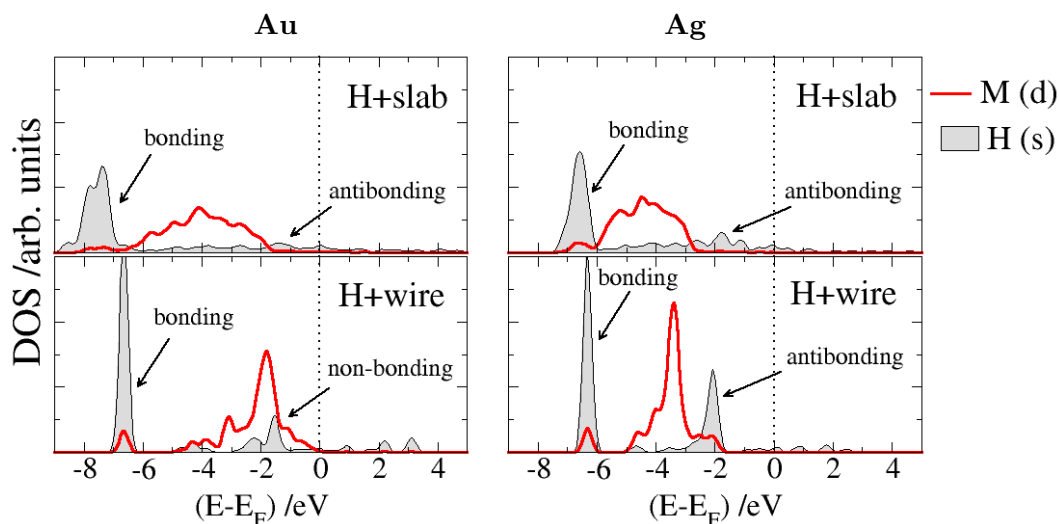

Figure 7.5: Density of states (DOS) projected on the d band of several fcc(111) surfaces (slab) and monometallic nanowires. Two curves are shown for spin polarized systems; for the rest, both curves are symmetric. The DOS for nanowires has been reduced by a factor of two.

This implies that for nickel, palladium, and platinum wires, there is no significant shift. Accordingly, ΔG_{ads} on such wires and surfaces is similar. In the case of silver nanowires, the d band is up-shifted, but it remains far below the Fermi level, so, like in the surface case, σ^* is mostly occupied. For copper and gold, the shift is so important, that their d bands reach the Fermi level, leaving σ^* almost completely unfilled. Because of the contribution of the d band to the hydrogen-wire bond, and in contrast to their surfaces, Au and Cu nanowires have a negative ΔG_{ads}. The effect is more pronounced for Au, which has a bigger orbital radius and then interacts more strongly with hydrogen.

In order to confirm that σ^* is occupied in the case of Ag and empty in the case of Au, their DOS are compared in figure 7.6.

Since the assignment of non-bonding and antibonding states by just looking at the DOS is not trivial, the examination must be checked by other technique. With

Figure 7.6: Density of states (DOS) projected on the s state of hydrogen and the d band of Au and Ag surfaces (top panel) compared to that of wires (bottom panel).

Wannier orbitals [10] for example, the shape of the *occupied* molecular orbitals can be plotted as shown in figure 7.7.

Au σ bonding   Ag σ bonding   Ag σ^* antibonding
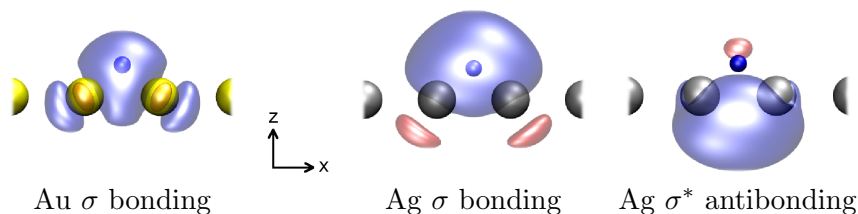
Figure 7.7: Bonding (σ) and antibonding (σ^*) states that result from the overlap of hydrogen with the d band of Au and Ag wires. Note the node that separates hydrogen from the wire in the antibonding case.

As can be seen in figure 7.6, at the surface the hydrogen-wire antibonding (σ^*) is occupied for both Au and Ag. At the wire, however, the shift of the d band in the case of Au is so large that σ^* gets emptied. In the case of the Ag wire σ^* remains filled. To have a general comparison, the DOS projected on to the hydrogen $1s$ state and the d band for all the monometallic wires studied are shown in figure 7.8.

Among all the wires examined in the figure, Ag is the only one in which hydrogen adsorption implies the filling of antibonding states. Accordingly, its ΔG_{ads} is the highest among wires of table 7.4. For the rest of the metals of the table, the bigger the metal orbital the stronger is the hydrogen adsorption, i.e., ΔG_{ads} is more exergonic for Pt and Au than for Ni and Cu.
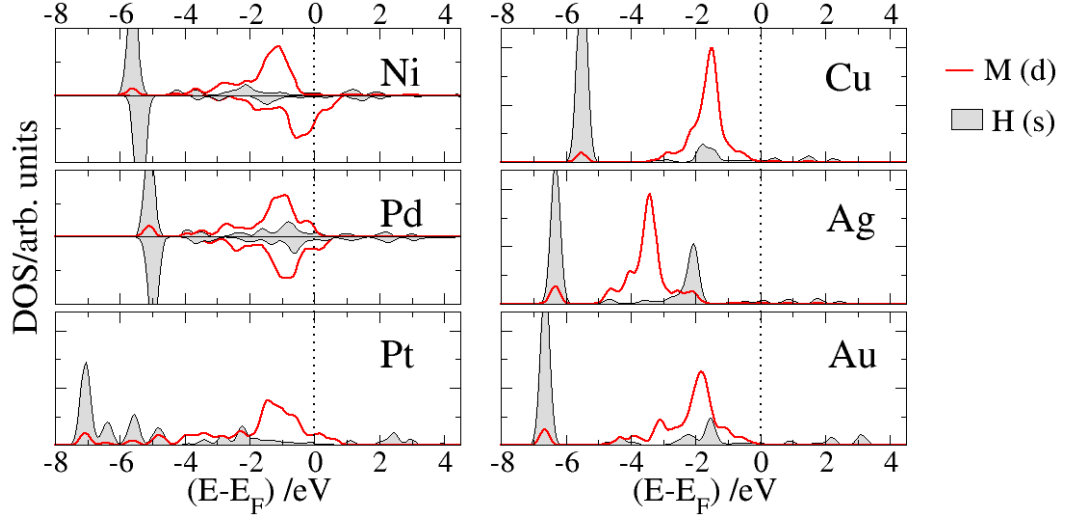
Figure 7.8: DOS projected on hydrogen (bridge) for all the monometallic nanowires studied. The s state of hydrogen and the d band of the metal are plotted.

Using the DOS projected on to the different orbitals of the d band (PDOS), it is possible to determine which orbitals make the larger contribution to the hydrogen-wire bond. The latter are sketched in figure 7.9. We can intuit that hydrogen will overlap efficiently with the σ_w, d_{xz} and $d_{x^2y^2}$ orbitals of the wire. This is confirmed in figure 7.9 where the corresponding DOS in the presence and in the absence of hydrogen for a Au wire are plotted.

The peak at around -6.5 eV, which is absent in the bare wire case, corresponds to the hydrogen $1s$ state (see figure 7.8). The energy down-shift of the d orbitals is a consequence of the increase of the Fermi level due to hydrogen adsorption.

Charge density

The charge density difference for hydrogen adsorbed wires was calculated according to

$$\Delta\rho = \rho_{H+wire} - (\rho_H - \rho_{wire}) \tag{7.5}$$

Some examples are given in figure 7.10. Only hydrogen and its first neighbors are shown. Blue regions correspond to electron depletion and red regions to electron accumulation.
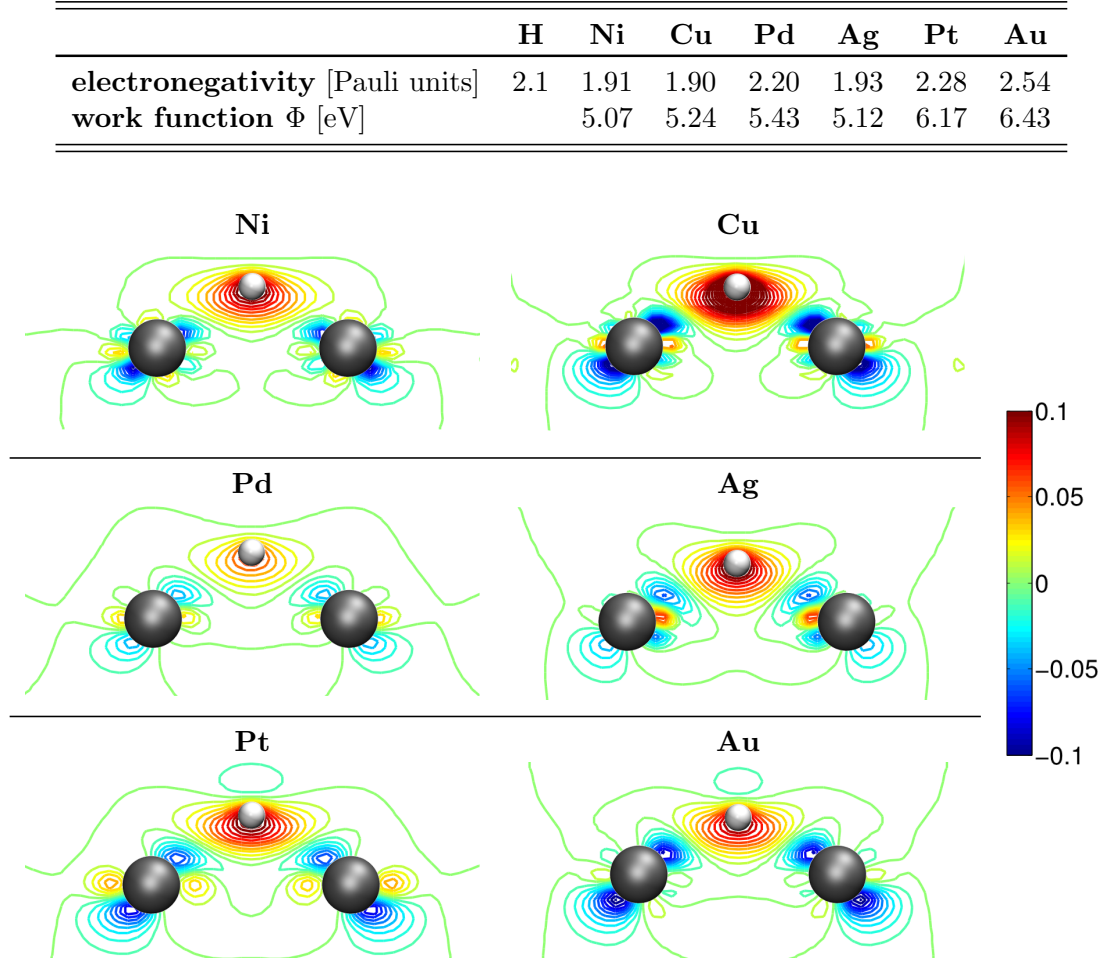
Hydrogen carries an excess of charge which is greater on Cu and Ag wires due to their smaller electronegativity in comparison with hydrogen. Since electronegativity is more suited for charge comparisons of isolated atoms, the work functions of the clean wires are also tabulated in figure 7.10 which are in line with the previous
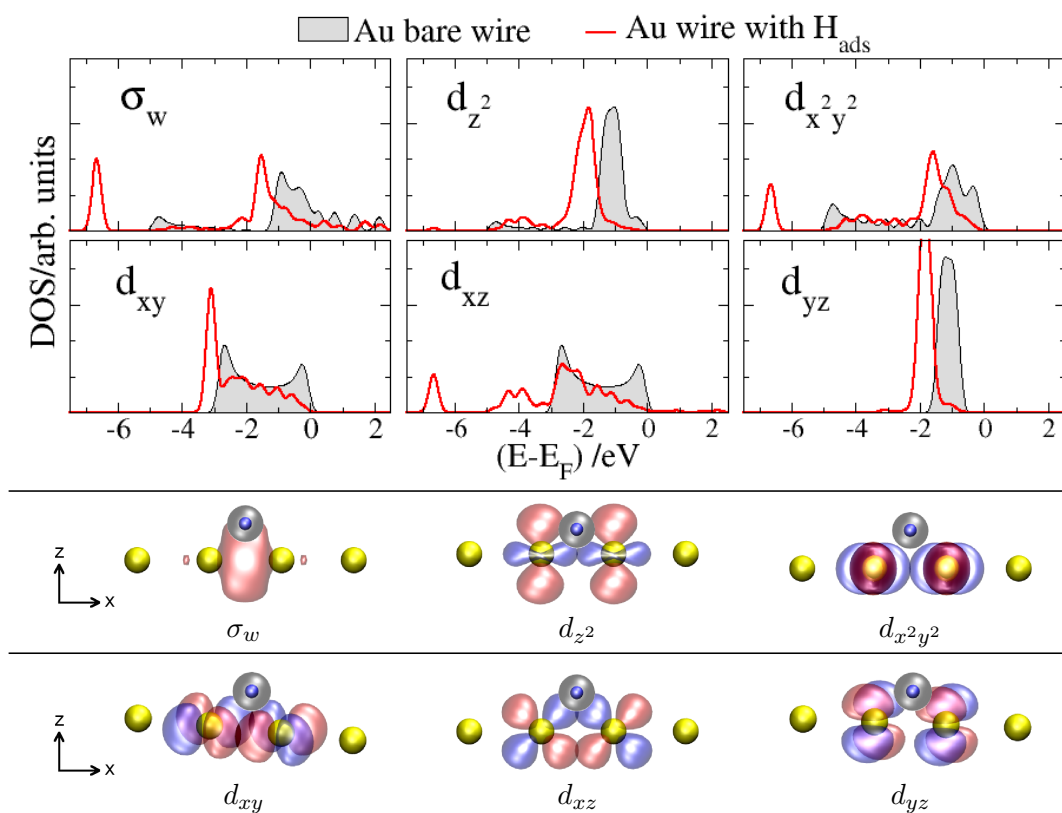
Figure 7.9: top: DOS projected on some relevant states of a Au nanowire with and without hydrogen adsorbed. **bottom:** Bare wire orbitals superimposed with H $1s$ orbital. The predicted most favorable overlaps come from $sigma$, d_{xz} and $d_{x^2y^2}$.

statement. Note that the shape of the blue regions around the metals resemble one of the lobes of the d_{xz} orbital, which is to be expected since part of the charge is actually *coming* from that orbital.

	H	Ni	Cu	Pd	Ag	Pt	Au
electronegativity [Pauli units]	2.1	1.91	1.90	2.20	1.93	2.28	2.54
work function Φ [eV]		5.07	5.24	5.43	5.12	6.17	6.43

Figure 7.10: Contour plot of the charge density difference ($\Delta\rho$) of hydrogen on some transition metal nanowires. The charge spacing between contour lines is 0.01 $e/\text{Å}^3$. The electronegativity of the atoms and the work function of the metal nanowires are given above.

7.4 Hydrogen coverages

In the previous section the *isolated* hydrogen adsorption ($\theta \ll 1$) was studied. This was chosen in order to make the hydrogen-hydrogen interaction of the unit cell images negligible, and to focus in the *unperturbed* hydrogen-wire bond. In this section the situation at higher hydrogen coverages is studied. The adsorption energy is calculated according to

$$E_{ads}(n) = \frac{E_{(nH+wire)} - \left(\frac{n}{2}E_{H_2} + E_{wire}\right)}{n} \tag{7.6}$$

Hydrogen adsorption energies as a function of the coverage (θ) are examined in figure 7.11.
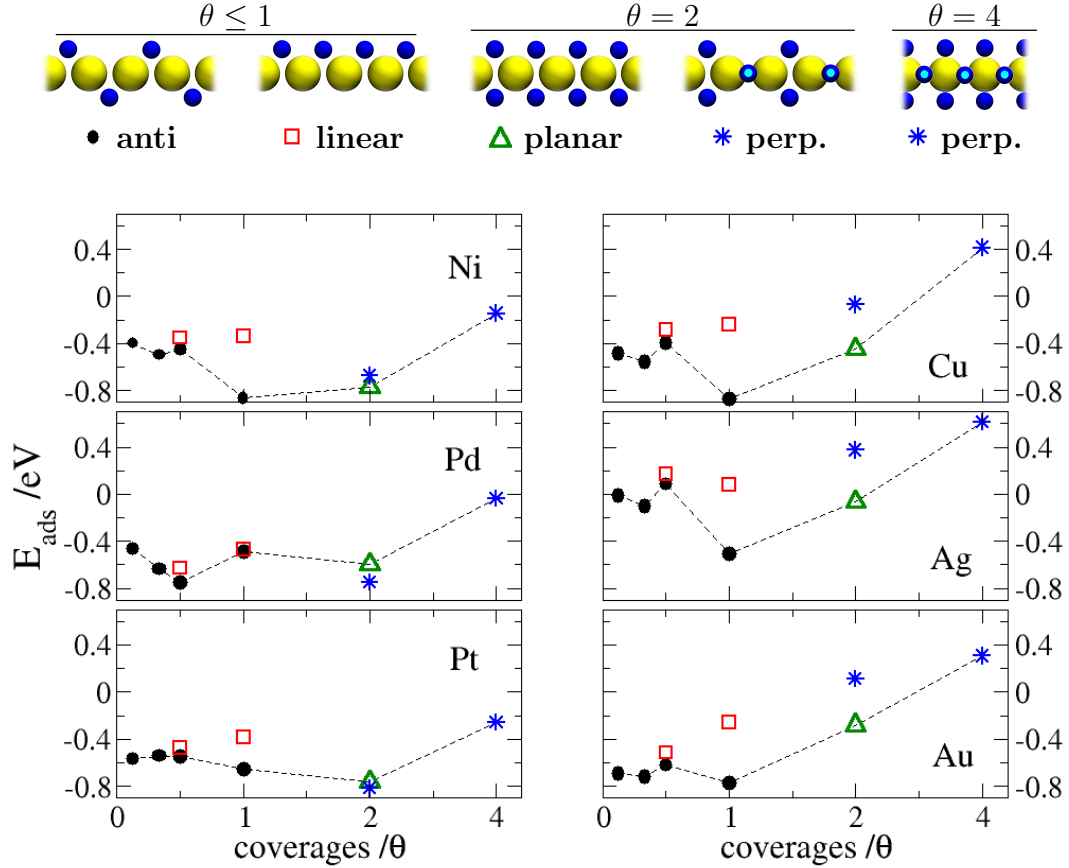
Figure 7.11: top) Side view of the configurations of hydrogen at different coverages. Gold is colored yellow and hydrogen blue; eclipsed hydrogens are depicted with lightblue centers. **bottom)** Adsorption energy (E_{ads}) as a function of the hydrogen coverage on nanowires. The energy of the *line* configuration for $\theta < 1/2$ is not shown since they are the same as the *anti* configuration. The dashed line is only an aid to the eyes.

At coverages of $\theta \leq 1$ hydrogen takes two configurations on the wire, the *anti* and the *linear* configuration. At coverages lower than $\theta = 1/2$ the energy difference between these two is negligible, but from then on the *anti* arrangement is favored since the hydrogen nuclear repulsion is avoided. Surprisingly, at $\theta = 1$ the adsorption energy is even smaller than at lower coverages, only on Pd wires it is higher. Another unexpected feature is observed at $\theta = 2$. Comparing the *planar* and the *perpendicular* arrangements, the chemical intuition favors the latter one since it has lower hydrogen-hydrogen repulsion. On the contrary, the *planar* arrangement is around 0.4 eV more stable for the three coin metals. For Ni, Pd, and Pt both

configurations are similar in stability.

At coverages $\theta < 2$, the adsorption of hydrogen is lower than -0.4 eV for all the wires studied here except for Ag. At coverages $\theta \geq 2$, the adsorption is more favorable on Ni, Pd, and Pt than on the three coin metals. In fact, in the former case even at $\theta = 4$ the process is exothermic.

The repulsion between the adsorbed hydrogen atoms can be understood as dipole-dipole a repulsion. Although the latter cannot be calculated without a certain ambiguity (it is hard to determine where the adsorbate molecule/atom ends), the dipole moment is proportional to the change in the work function, whose calculation is straightforward by DFT:

$$\Delta\Phi = \Phi_{nH+wire} - \Phi_{wire} \tag{7.7}$$

where $\Phi_{nH+wire}$ is the work function of the hydrogenated wire and Φ_{wire} is the work function of the bare wire. The change in the work function for coverages $\theta \leq 1$ are shown in figure 7.12.
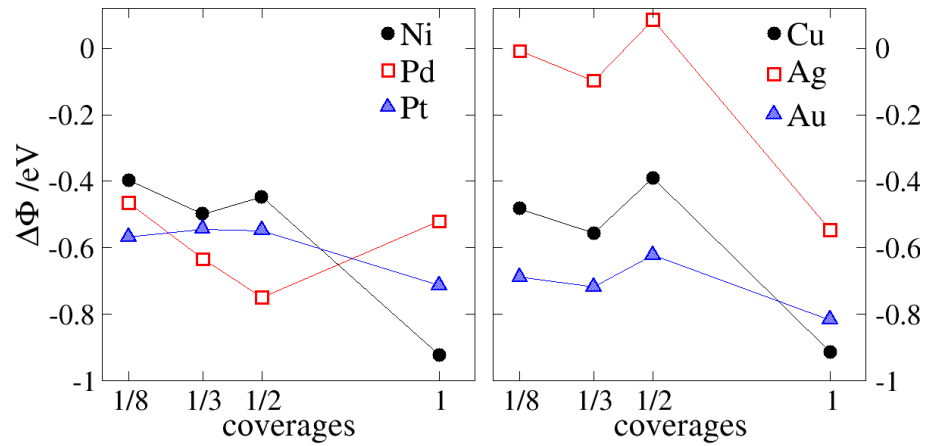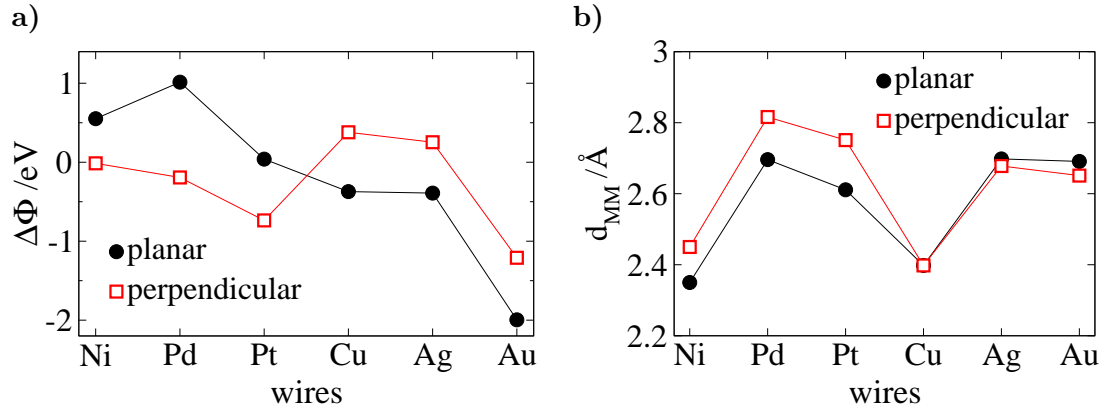

Figure 7.12: Change in the work function ($\Delta\Phi$) of hydrogenated wires with respect to the clean wires for *planar* and *perpendicular* configurations at coverages lower than one hydrogen atom per metal ($\theta \leq 1$).

Surprisingly, the dipole repulsion is smaller at one hydrogen per metal atom than at lower coverages with the solely exception of Pd, in perfect correspondence with the trends of the adsorption energies shown in figure 7.11 for $\theta \leq 1$.

In order to explain the unexpected trend at $\theta = 2$ for the three coin metals, the change in the work function was also obtained for the latter coverage. Results are shown in figure 7.13a.

As we can see from the figure, in the perpendicular configuration the dipole moment is lower for Ni, Pd, and Pt. Interestingly enough, this is not the case for

Figure 7.13: a) Change in the work function ($\Delta\Phi$) of hydrogenated wires with respect to the clean wires for several metals and configurations at a coverage of two hydrogen atoms per metal ($\theta = 2$). **b)** Intermetallic distance (d_{MM}) corresponding to the wires examined in **a**. The lines connecting the data points in the plots are just an aid to the eye.

the three coin metals, in which the planar configuration is more stable –look at the intercrossing of lines in figure 7.13a. These results are not directly related to the intermetallic distance d_{MM} (shown in figure 7.13b), since for instance, $\Delta\Phi$ is not larger for Ni and Cu, for which the intermetallic distance is the smallest. However, the lower energies for $\theta = 1$ and the unexpected lower energy of the *parallel* configuration at $\theta = 2$ may be explained by a dellocalization effect. The adsorption energies at $\theta = 1$ could be lower than at $\theta < 1$ due the fact that in the former case the states of hydrogen are in an extended resonance with the s and d band of the metals than at lower coverages, as shown in the DOS of figure 7.14.
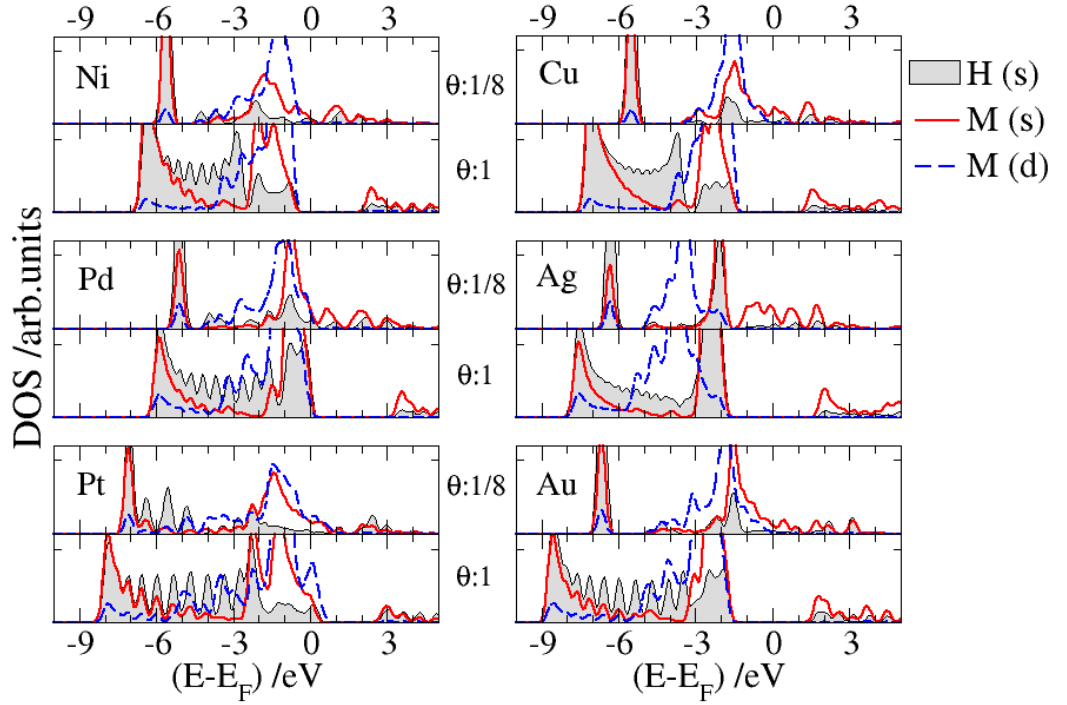
Figure 7.14: DOS projected on the hydrogen s orbital at low hydrogen coverages ($\theta = 1/8$) and at $\theta = 1$ (in the *anti* configuration). For Ni and Pd, only the DOS of one spin is plotted, for the other one the DOS is shifted around 0.5 eV to higher energies.

Figure 7.15 shows a similar study at $\theta = 2$ where the DOS of the *parallel* and the *perpendicular* configurations are compared. Apparently the hydrogen-metal states are more extended in energy than in the *parallel* arrangement (note the energy nodes in the *perpendicular* case at -5.5 and -1.5 eV). In addition, in the *planar* configuration the HOMO is a non-bonding band (d_{xz} of the wire atoms) while in the *perpendicular* case the HOMO is an antibonding band (the shape of the lobes around the hydrogens atoms point away from the wire and are separated by a node). These results allowed us to conclude that at the wires, hydrogen repulsion is not always the driving force that governs the geometrical organization of the atoms; the delocalization effect and the stability of the HOMO may play a crucial role.
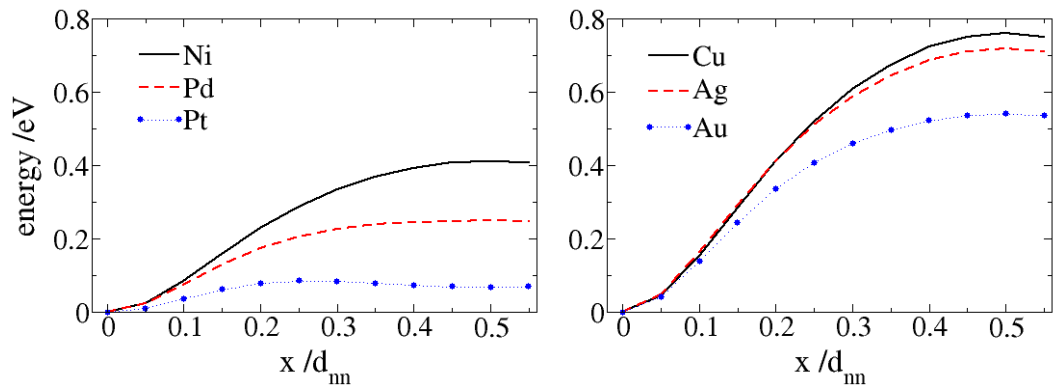
Perpendicular
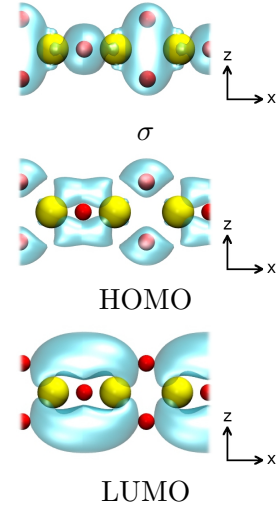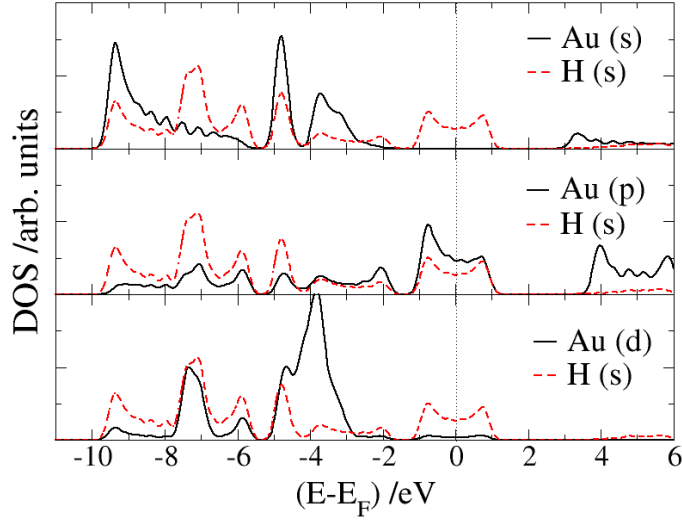
Planar
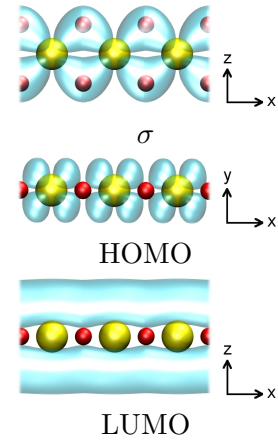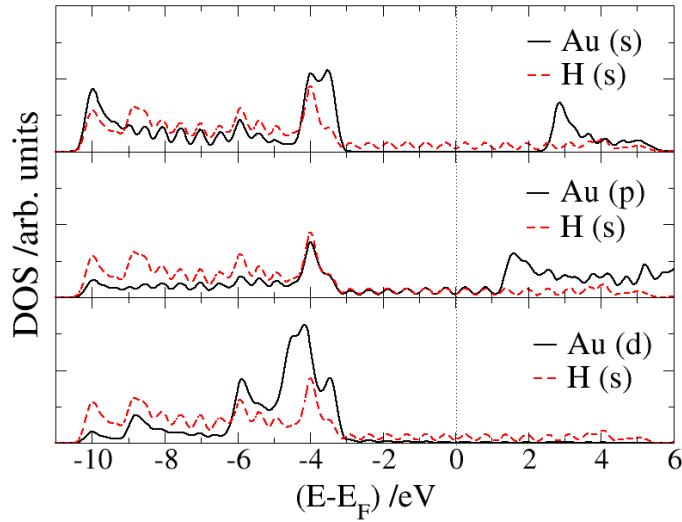
Figure 7.15: DOS of hydrogen on a Au wire at coverage $\theta = 2$ in the *perpendicular* and *planar* configuration. All the valence orbitals of the metal are compared with the hydrogen $1s$ orbital. At right, the lowest bonding molecular orbital and the HOMO are sketched for each case.

7.5   Kinetics of the hydrogen reaction

Diffusion

The activation energy E_a for the hydrogen atom diffusion along the wire was calculated by relaxing the atom along the z axis at several fixed x positions (the wire and the y component of hydrogen were always kept fixed). The reaction coordinates are presented in figure 7.16 and the corresponding activation energies are shown in table 7.5.

Figure 7.16: Potential energy of a hydrogen atom moving along the wire axis on several nanowires. The adsorbate was relaxed along the perpendicular wire axis. The displacement (x) is referred to the bridge position and in units of the inter-metal atom distance (d_{nn}).

Note that in the case of Pt there is a local minimum in the *top* position which entails a subtle higher activation barrier than the one predicted by $E_{ads}^{top} - E_{ads}^{bridge}$.

	Ni	**Pd**	**Pt**	**Cu**	**Ag**	**Au**
E_a (eV)	0.41	0.25	0.09	0.76	0.72	0.54
Δz (Å)	0.27	0.35	0.27	0.39	0.49	0.44

Table 7.5: Hydrogen diffusion activation energy (E_a) and hydrogen total displacement in the perpendicular axis to the wire (Δz) on several nanowires.

Once again, there is a clear difference between Ni and Cu periodic columns. The barrier for diffusion is smaller on the former ones with the notorious case of Pt where hydrogen diffuses with an activation barrier of 0.09 eV. The second lowest E_a corresponds to Pd with 0.25 eV. For the rest of the cases and particularly for the three coin metal wires, hydrogen diffusion is slow. It can be also observed that the

activation for hydrogen diffusion is lower for metals with more extended d orbitals, such as Pt and Au. This is because for the latter wires the interaction constant for hydrogen does not decay so rapidly as for wires with less extended d-orbitals [70].

The Volmer reaction

The DFT results have shown that Cu and Au nanowires have a much stronger affinity for hydrogen than their (111) surfaces. From the thermodynamical point of view, this makes them promising electrocatalysts. However, the final answer is given by the activation barrier of the process. Using the Schmickler-Santos theory, we have evaluated the first step of hydrogen evolution, the Volmer reaction (page 10), on both the (111) surfaces and the nanowires. We focus on the activation energy at the standard hydrogen potential NHE, which is a good indicator of the reactivity. At this potential, the free energy for the Volmer reaction is given by the adsorption energies reported above plus an entropy term, which is of the order of 0.2 eV [57]. Thus, to obtain the free energies of adsorption at NHE, a value of 0.2 eV has to be added. Results are summarized in figure 7.17.

These plots show the free energy of the system as a function of two coordinates: the solvent coordinate q (page 12) and the distance from the surface. The initial state is a proton at $q = -1$ and far from the surface or the wire, the final state an adsorbed hydrogen atom at $q = 0$. These two states are separated by an energy barrier of 0.7 eV for the surfaces, 0.5 eV for Cu nanowires, and only 0.1 eV for Au nanowires. In the latter case, the saddle point is localted at more negative values of q, which entails that the hydrogen species is more strongly solvated at the transition state, lowering the activation energy of the Volmer reaction. This indicates that the reaction is very fast on Au nanowires. The high rate is caused both by the favorable position of the d band and its strong interaction with hydrogen.

The reaction is not as fast on Cu nanowires due to its smaller valence orbitals, which weakens the metal-hydrogen interaction. Indeed, its coupling constant near the transition state is smaller than that of gold by a factor of two. Still, at room temperature the Volmer reaction rate is three orders of magnitude larger than on Cu(111) surfaces.

7.6   Conclusions

At low coverages ($\theta \le 1/6$), hydrogen adsorption on Cu and Au wires is 0.3 and 0.8 eV more stable than on their fcc(111) surfaces, respectively, turning the process exergonic. Hydrogen adsorption on Ag wires, like on its surface, is an endergonic reaction. Examination of the DOS reveals that the reason for the differing reactivities is the d band energy up-shift: In the case of Cu and Au, this shift is so large that the
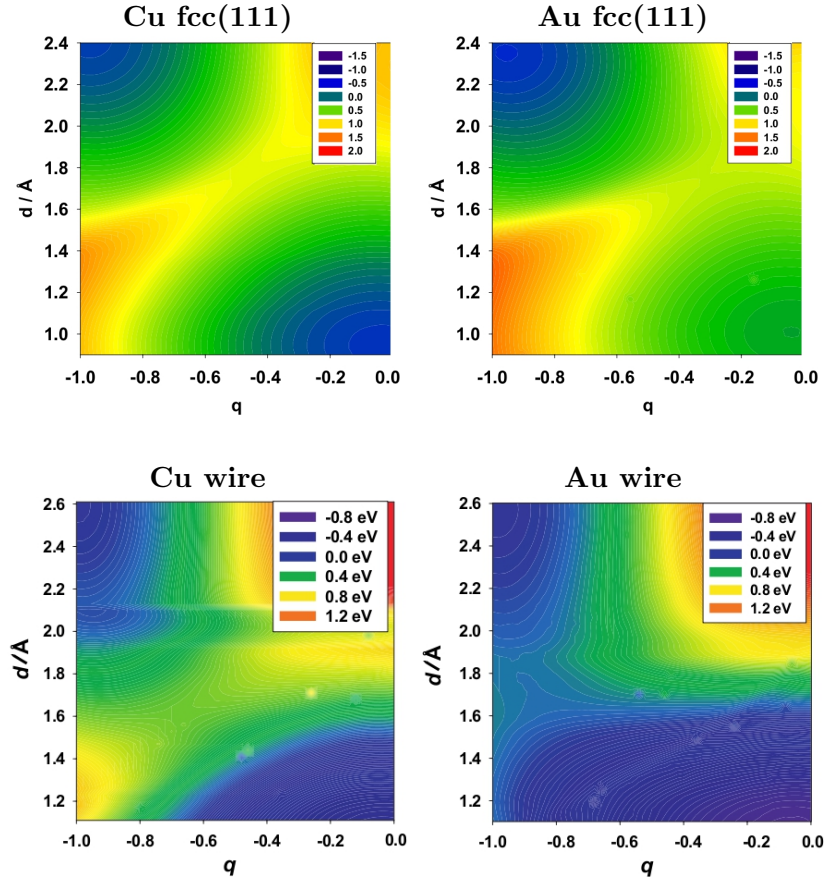
Figure 7.17: Potential energy surface for the reduction of H$^+$ on Cu and Au wires as a function of hydrogen distance from the substrate (d) and the solvent coordinate q.

d band reaches the Fermi level. On Ag wires on the other hand, the shift is smaller and does not change the chemisorption strength significantly. Accordingly, only in the latter case occupied hydrogen-wire antibonding states were found. These results support the hypothesis of Kiguchi et al. [55, 56], who suggest that the fractional conductance observed on Cu and Au wires, but not on Ag ones, is due to hydrogen adsorption. On Ni, Pd, and Pt wires, the hydrogen free energies of adsorption were found to be similar than on their fcc(111) surfaces (exergonic), which is expected since there the d band up-shift is rather small.

For the three coin metal wires at the hydrogen coverage of $\theta = 1$, the adsorption energy is significantly lower than at lower coverages. This unexpected result is attributed to an increase of the resonance between the states of hydrogen and those of the metal wire. It was found that hydrogen-hydrogen repulsion is not the driving force that determines the location of the adsorbates: At the coverage of $\theta = 2$ for the three coin metals, the more stable configuration (*planar*) has a larger hydrogen-

hydrogen repulsion than the *perpendicular* one. However, this difference is overcompensated by the *planar* arrangement due to its larger resonance of hydrogen-wire states and due to its more stable HOMO. At coverages $\theta < 2$, hydrogen adsorption is favored on all the metal wires studied here, with the exception of Ag. At coverages $\theta \geq 2$, the adsorption is more favorable on Ni, Pd, and Pt.

Hydrogen diffusion on the wire would occur rapidly on Pt, slower on Pd, and very slowly on the other metals studied. The activation energy (E_a) for the adsorption of a proton in an aqueous medium (H^+) on a Au wire is 0.1 eV, while on Au fcc(111) surface it is 0.7 eV. On Cu wires E_a is 0.5 eV in contrast to 0.7 eV for the planar surface. The process is lower on copper wires since, despite of having the d band tail right at the Fermi level, its valence orbitals are much tighter than those of gold and hence the hydrogen-wire interaction is weaker.

8

Atomic hydrogen on bimetallic wires

Anything you dream is fiction, and
anrything you accomplish is science,
the whole history of mankind is
nothing but science fiction.

Ray Bradbury Writer.

In chapter 6 we observed that a few metallic combinations forming atomic wires were more stable than the corresponding monometallic ones, suggesting a tendency for mixing. The most favorable combinations obtained correspond to Au-Cu and Au-Ag chains. In this chapter, the reactivity and the electronic effect induced by the foreign metal are investigated. In order to study the *strength* of the electronic perturbation that Au produces on the β atoms, $Au_m\beta_2$ are studied with β=(Cu, Ag) and $m = 0, 1, 2..., 7$. On the other hand, to study the *extent* of the electronic effect, $Au_m\beta_5$ are examined. Given their particular properties, $Au_1\beta_1$ wires are addressed separately. An interesting question emerges from the comparison of mono- and bimetallic wires. As it was explained in the previous chapter, Au and Cu monometallic chains have a large affinity for hydrogen, while for Ag wires the interaction with hydrogen is repulsive. If Ag wires are inert while Cu and Au wires are reactive, how is their reactivity when these metals combine?

8.1   Technicalities

Modeling

The starting point for these systems was the optimized bimetallic wires described in chapter 6. In this case, those systems with less than four metal atoms per unit cell had to be replicated along the x axis sufficient times so that the unit cell images avoid hydrogen-hydrogen interaction. Adsorptions at different non-equivalent high-symmetry sites were calculated. The wire was kept fixed and hydrogen was allowed to relax so that the latter would have the function of a microscopic probe as has been performed on surfaces [71].

First-principle parameters

The k-points and the plain-wave cutoff energy were taken from the parametrization for bimetallic wires (see page 45).

8.2   The electronic effect

The free energy of adsorption ΔG_{ads} (described on page 56) at the standard equilibrium potential ϕ_0 (SHE) for several positions of hydrogen on Au$_m\beta_2$ wires is shown in figure 8.1. The sites are distinguished by capital letters for Au atoms and lower case letters for β atoms.

For hydrogen adsorbed on top(A) and bridge(Aa) sites, the adsorption becomes more stable with increasing m, but is always less stable than on Au monometallic wires. For hydrogen adsorbed on top(a) and bridge(aa) sites, the adsorption energy is around 0.3 eV more stable than on β monometallic wires. The reason for these differences can be explained in terms of the position of the d band. The density of states (DOS) of the isolated bimetallic wires are shown in figure 8.2.

The position of the d band of the Au atoms at the *A-a* interface is sensitive to the total number of Au atoms: The fewer Au atoms the wire contains, the more shifted is the d band to lower energies and, consequently, the more unfavorable is the adsorption. This explains why the adsorption on top(A) and bridge(Aa) sites is less stable than on Au monometallic wires. Simultaneously, Au induces a subtle *up*-shift of the d band on its β neighbors, which explains why the adsorption of hydrogen on top (a) and bridge(aa) is better than on β monometallic wires.

In order to determine if the change in the β-β bond distance is related to the change in the adsorption energies shown in figure 8.1, the adsorption of hydrogen on β monometallic wires was calculated taking the β-β bond distance of each Au$_m\beta_2$ wire examined. It is found that the change in the adsorption energy due to the
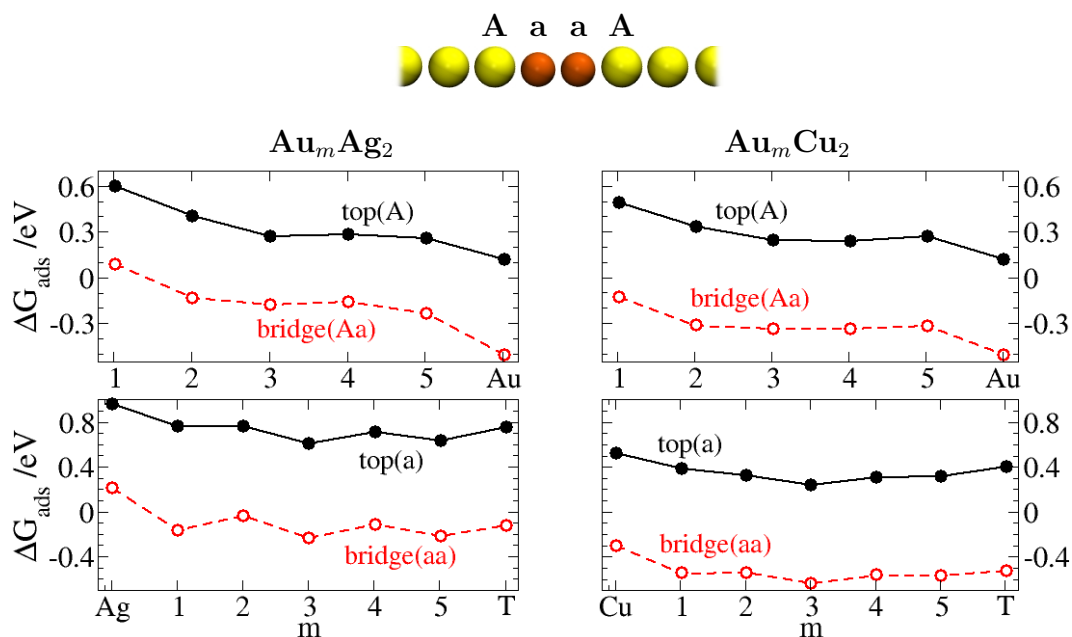
Figure 8.1: Free adsorption energy of hydrogen (ΔG_{ads}) on $Au_m\beta_2$ and monometallic wires for several *top* and *bridge* positions. Au atoms are labeled with capital letters and β atoms with lower case ones. Adsorption on monometallic wires is denoted by Au, Ag, or Cu, correspondingly.

differing β-β bond distances was negligible (± 0.04 eV). Thus, the d-band shift is only caused by the electronic effect.

We have learnt so far that Au induces an upward shift of the d band center of its β neighbors, which increases their reactivity. Now we will inspect the extension of such an effect along the β atoms of a bimetallic wire. For that matter we examine bimetallic wires with a relatively long β chain (five atoms long) interacting with Au atoms: $Au_m\beta_5$ with m=(0,1,2...,7). Results are given in figure 8.3.

As we can see in the figure, ΔG_{ads} of hydrogen top(c) and bridge(bc) on $Au_m\beta_5$ wires is already very close to that of β monometallic wires. All the adsorptions on Au_mCu_5 wires are exergonic like on Cu monometallic wires. For the Au_mAg_5 wires, at the bridge(ab) position, $\Delta G \approx 0$, but at top(b) and bridge(bc) (further away from Au) it is endergonic like on Ag monometallic wires. These results indicate that the electronic perturbation induced by Au does not go further than to its second β neighbor.

A a a A
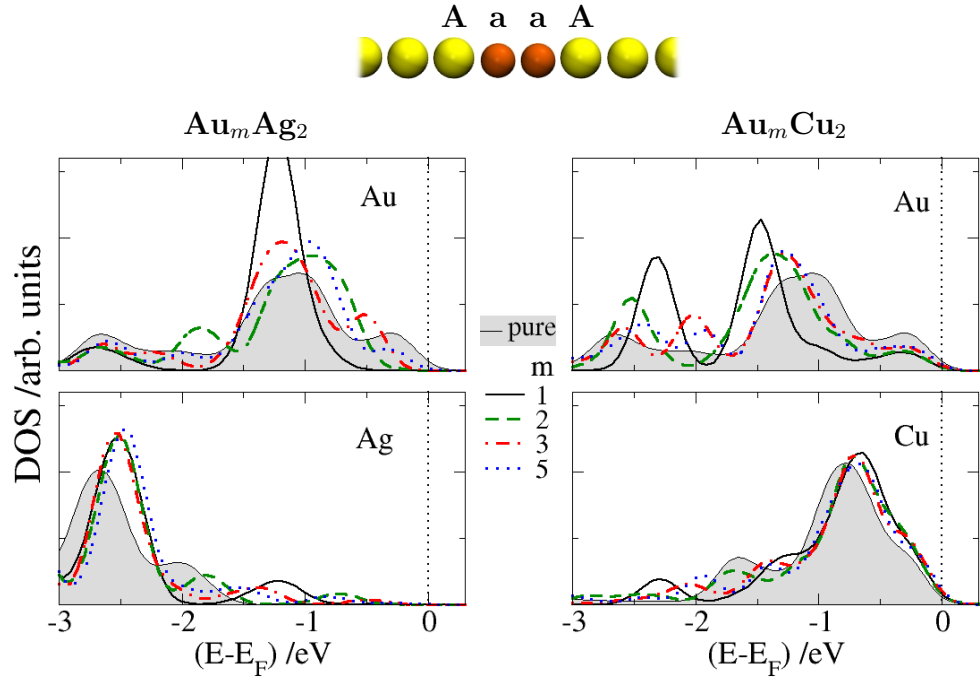
Figure 8.2: DOS of monometallic (shaded surface) and $Au_m\beta_2$ (lines) wires. Au atoms are labeled with capital letters and β atoms with lower case ones. The d band of A and a atoms is plotted.

## 8.3   Intercalated Au_1Cu_1 and Au_1Ag_1 wires

The electronic effect in this configuration is pushed to its limit: each atom has two foreign metal neighbors. This leads to a natural question: Which metal determines the reactivity of the wire? Values of ΔG_{ads} for mono- and bimetallic wires are compared in table 8.1.

wire	**bridge**	**top**
Au	-0.44	0.12
Ag	0.21	0.98
Cu	-0.30	0.53

$Au\beta$ wires	**bridge**	**top** (Au)	**top** (β)
Au_1Ag_1	0.23	0.82	1.09
Au_1Cu_1	-0.21	0.49	0.40

**Table 8.1:** ΔG_{ads} for monometallic and $Au_1\beta_1$ wires.

For the Au_1Ag_1 wire, the electronic effect induced by Au makes no significant contribution to ΔG_{ads}. It is actually the other way around: Ag neutralizes the large reactivity of Au! On the other hand, Au_1Cu_1 chains are as reactive as Cu and Au monometallic wires. The DOS of hydrogen on $Au_1\beta_1$ and on the corresponding
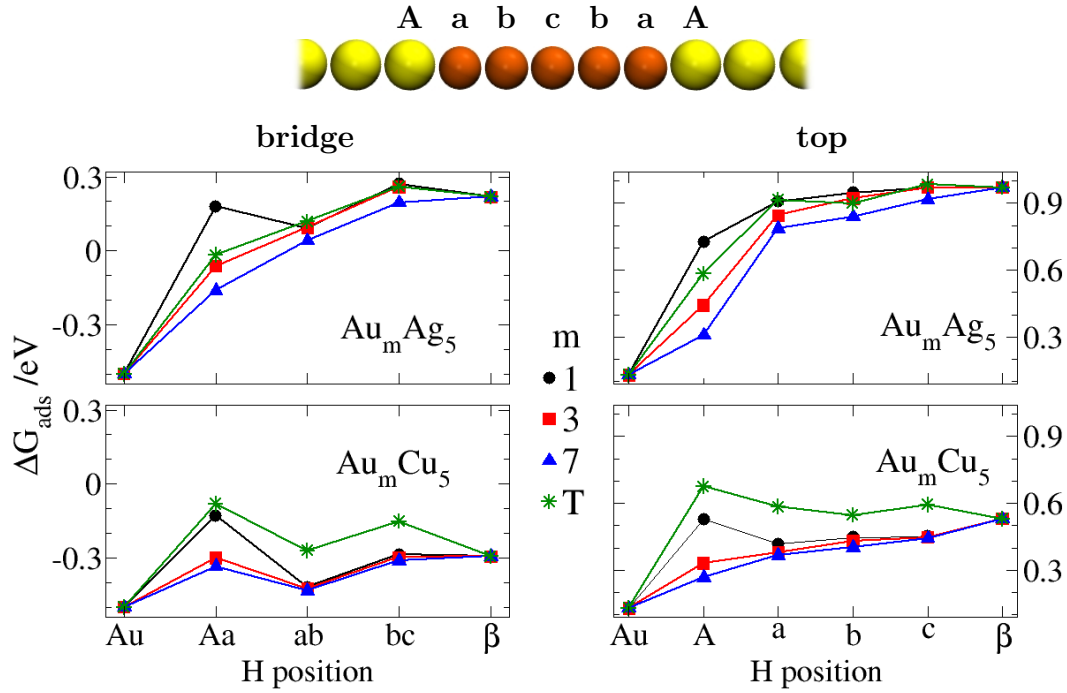
Figure 8.3: Hydrogen free energy of adsorption (ΔG_{ads}) on monometallic and on $Au_m\beta_5$ wires for several bridge (left plots) and top (right plots) positions. Au atoms are labeled with capital letters and β atoms with lower case ones. The adsorption on monometallic wires is denoted by Au and β in the abscissas.

three monometallic wires are compared in figure 8.4. There are two clear regions for hydrogen $1s$ states: One region with a narrow and strong peak at lower energy values, which corresponds to the *bonding* states of hydrogen with the wire; and one region with smaller and wider peaks at around -2 eV. An examination of the shape of $Wanniers$ orbitals [10] confirms that if the latter peaks are above (in energy) the d band region, they correspond to *antibonding* states, as it is the case for hydrogen on Ag monometallic wires; otherwise they correspond to *non-bonding* states, as it is the case for hydrogen on Cu and Au monometallic wires. The presence of antibonding states explains the high values of ΔG_{ads} for hydrogen on Ag wires. For Au_1Ag_1 wires, the small peak of the $1s$ hydrogen state is above the d band of Ag and therefore the antibonding state observed in Ag monometallic wires remains. For Au_1Cu_1 wires on the other hand, the small peaks corresponding to hydrogen are not above the d band of any of the metals, which confirms that they are *non-bonding* states. This explains why hydrogen on $Au_1\beta_1$ wires behaves like on the corresponding β monometallic wires.
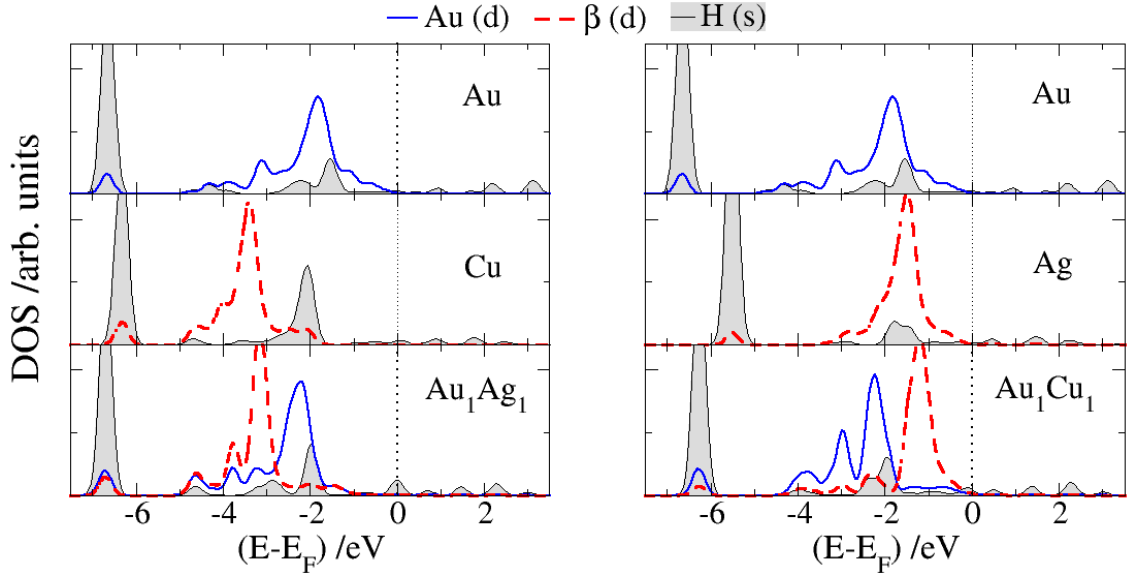
Figure 8.4: DOS of hydrogen on bridge positions over monometallic (top two plots) and bimetallic wires (bottom plot). Hydrogen s state and the d band of its first metal neighbors are shown.

8.4   Conclusions

Using hydrogen as a microscopic probe, the reactivity of $Au_m\beta_n$ bimetallic wires with $\beta=(Cu,Ag)$ was studied. The combination of Cu and Ag with Au produces shifts in the d band of the β atoms, which is solely attributed to the electronic effect, since the bond expansion effect is negligible. When combined with Ag or Cu, Au reactivity depends on the number of other Au neighbors: the fewer they are, the more inert it becomes. This is due to a downward shift of the d band center induced by the β atoms, which is stronger when Au has fewer Au neighbors. Correspondingly, the reactivity of the β atoms increase in comparison with monometallic wires due to an upward shift of the d band center induced by Au. In this case, the reactivity is rather insensitive to the number of Au atoms m. The extension of this electronic effect induced by Au reaches no further than to its second β neighbor, from then on the reactivity resembles that of monometallic β wires. For the particular case of the most stable bimetallic wires studied, the $Au_1\beta_1$ wires, it was found that its reactivity is close to that of the corresponding pure β wires. Consequently, the large affinity that Au has for hydrogen is neutralized by its Ag neighbors.

9

H_2 dissociation/recombination

Often the second step of hydrogen evolution is the chemical recombination of two adsorbed hydrogen atoms, known as the Tafel reaction.

$$2H_{ad} \rightarrow H_2 \tag{9.1}$$

Strictly, this topic should be a subsection of the *Kinetics of the hydrogen reaction* (page 70), but due to its broad content, it is discussed in this chapter.

It is actually simpler to work with the reverse reaction, the dissociation of H_2, since in this case the initial state is the same for all substrates – the molecule far away from the electrode. Gohda et al. [72] have recently shown that the presence of water on the surface have a negligible effect on the Tafel reaction. Therefore, its energetics are very similar to the corresponding reaction in the vacuum, where it is well studied. Besides, the Tafel reaction does not involve electron transfer. Thus it can be described by pure DFT.

9.1   Technicalities

Modeling

In figure 9.1, the four high-symmetry orientations considered for the approximation of the hydrogen molecule to the wire is illustrated. They are distinguished by three letters which indicate the position of the first hydrogen atom, the molecule center-of-mass, and the position of the second hydrogen atom, respectively.
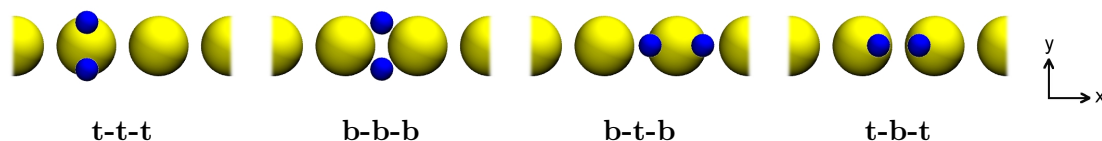
Figure 9.1: Top view of the four orientations at which H$_2$ approaches the wires. **t** refers to *top* and **b** to *bridge* positions

In order to determine which of the four pathways of figure 9.1 would lead to the lower barrier, one-dimensional approximations were used. The wire was pre-relaxed and fixed. The molecule was relaxed laterally at fixed distances from the wire. The energetically favored pathway was later studied in greater detail through potential energy surface (PES) representations and compared with that of one-dimensional approximations. For each PES scan approximately 200 total energy points were calculated. The height of H$_2$ varied between 0.8 Å and 4 Å in steps of 0.2 Å. The hydrogen-hydrogen distance was expanded at each height from 0.5 Å to about 3 Å in steps of 0.2 Å. The 2D energy surface was interpolated by quadratic approximations for which a fortran code was written.

First-principle parameters

The k-points and the plain-wave cutoff energy were taken from the parametrization for monometallic wires (see page 18).

9.2   Dissociation pathway selection

At this level of calculation, the hydrogen molecule was relaxed along its axis at fixed different distances from the wire. This is the so-called one-dimensional approximation. The potential energy of those H$_2$ orientations that lead to dissociation are shown in figure 9.2.

As can be seen in the figure, the barrier is higher for the three coin metals than for the Ni periodic column, regardless of the pathway. In the latter case the
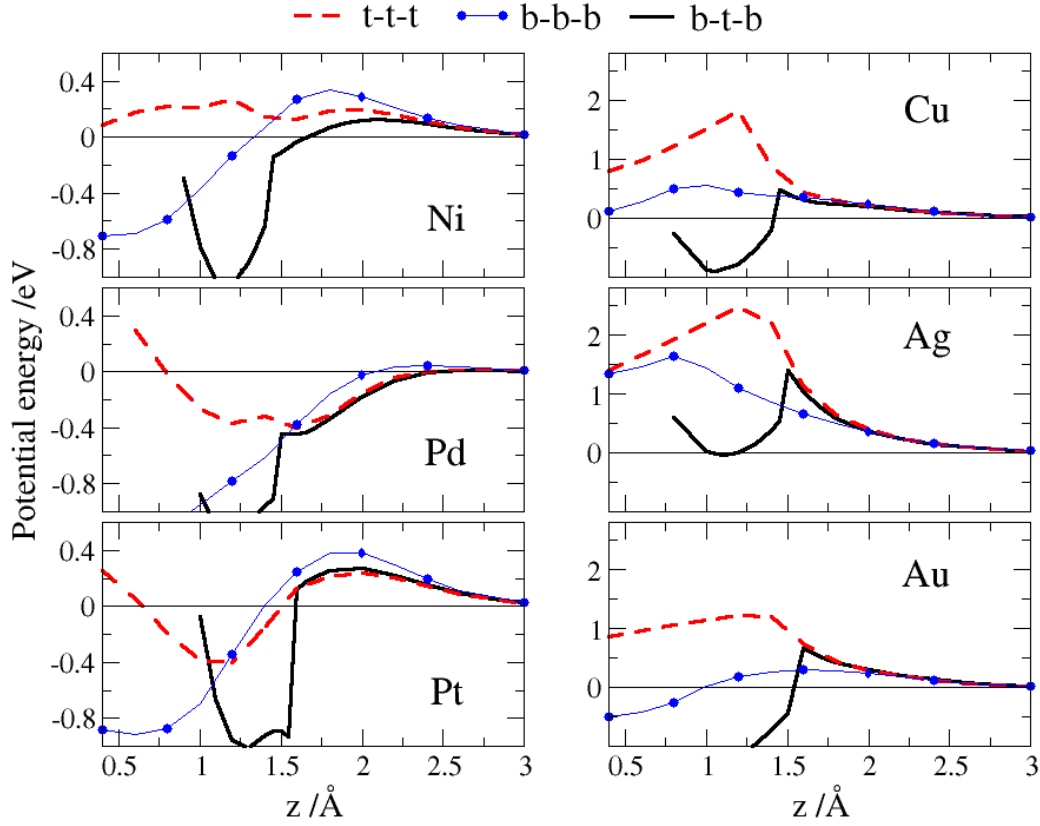
Figure 9.2: Potential energy of H_2 at different distances from the wire (z) in three configurations. The molecule was allowed to relax along its axis and the wire was kept fixed. Note the different energy scale.

activation barriers for each metal are rather similar. For the Cu periodic column instead, the t-t-t pathway is higher than the others by almost 1 eV. In general, the b-t-b configuration has the lowest activation energy. The sudden breaks in the potential curves for this configuration correspond to the breaking of the hydrogen bond. This is an artifact of the relaxation that has to be interpreted with care since it does not necessarily mean that the molecule breaking occurs suddenly as well. In contrast, the potential for the b-b-b path is smooth. The relaxation in this case does not involve the sudden hydrogen bond breaking. The H_2 t-b-t orientation was ruled out for the rest of the calculations since it does not lead to hydrogen dissociation. Instead, the molecule experiences an exponential repulsion as shown in figure 9.3.

The values of E_a for hydrogen dissociation are summarized in table 9.1.
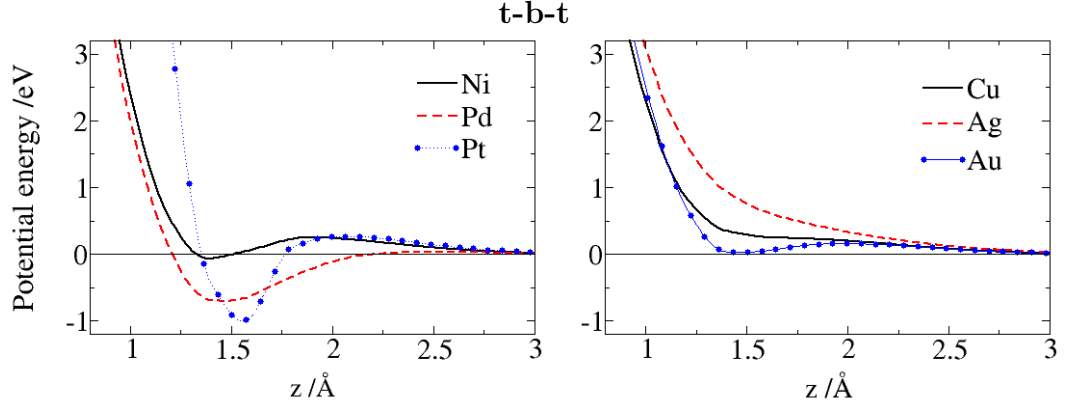
Figure 9.3: Adiabatic one-dimensional approximation. Potential energy of H$_2$ for the t-b-t configuration as a function of its distance from the wire (z). The molecule was allowed to relax along its axis and the wire was kept fixed.

	Ni	Pd	Pt	Cu	Ag	Au
b-t-b	0.14	0.01	0.28	0.48	1.40	0.67
t-t-t	0.27	0.01	0.24	1.80	2.48	1.22
b-b-b	0.34	0.05	0.38	0.54	1.64	0.30

Table 9.1: Activation energy (E_a) of H$_2$ dissociative adsorption on wires for all the configurations considered according to the adiabatic one-dimensional approximation.

9.3   Activation energy determination

In this section, the b-t-b orientation will be studied in detail. We start by giving another one-dimensional approximation for the calculation of the barrier for hydrogen dissociation. Later we will compare the results obtained so far with those acquired from the most accurate procedure to determine activation energies, the PES calculation.

One-dimensional diabatic and adiabatic approximations

Perhaps the easiest way to determine the activation energy of a dissociation process is to calculate a one-dimensional potential energy surface (PES) within the Lennard-Jones formalism [73]: First we calculate the potential energy of a fixed hydrogen molecule (in its equilibrium bond distance) approaching the wire, and then we do the same for two widely separated hydrogen atoms. As an example, this is shown in figure 9.4 for hydrogen molecule in the b-t-b orientation approaching a gold wire.

Far from the wire the energy difference between H$_2$ and $2H_{at}$ (shown as D in the
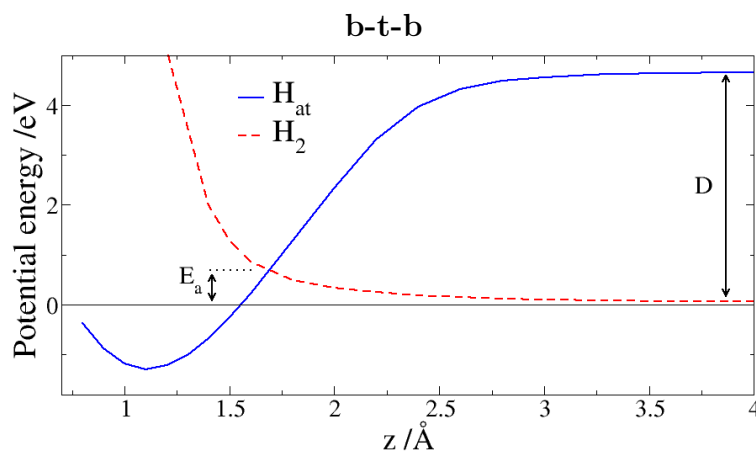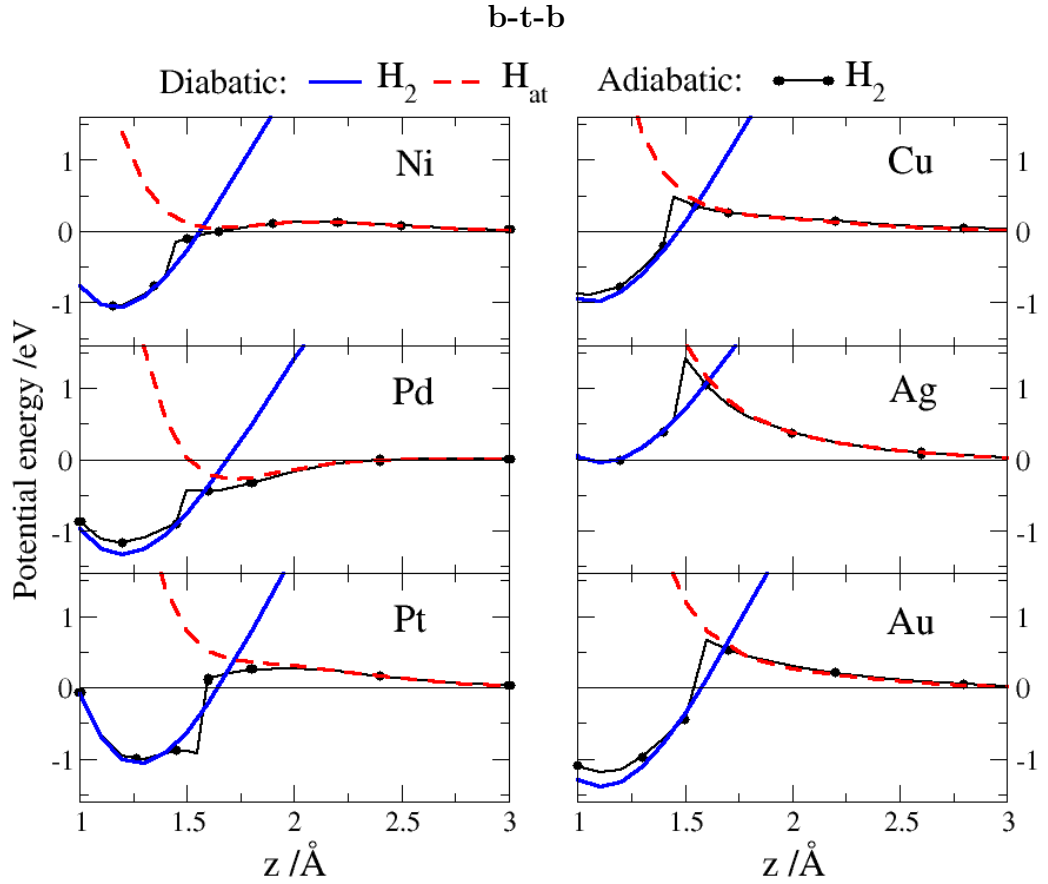
Figure 9.4: Diabatic one-dimensional approximation. Potential energy curves of the hydrogen molecule dissociative adsorption for the b-t-b pathway in the Lennard-Jones formalism.

figure) corresponds to the dissociation energy of a hydrogen molecule in the vacuum. The minimum of the atomic curve (at around 1.1 Å) is the adsorption energy of two widely separated hydrogen atoms, and as we have seen above, is exothermic. In the Lennard-Jones formalism, the crossing point between H_2 and H_{at} curves determines whether there is a barrier for dissociative adsorption of the molecule or not. In this example this would lead to a *diabatic* activation energy of 0.67 eV. This procedure is a helpful tool to gain information about the energetics of the adsorption and since it is performed with a few single point calculations, is not computationally demanding. The diabatic scenario for all the metals studied here is presented in figure 9.5.

It can be seen already at this approximation level that the dissociation on Pd is non-activated, on Ni almost non-activated and for the rest clearly activated. It is instructive to disentangle the contributions that both potential curves make to the final activation energy: The atomic energy curves are rather similar among all the metals studied, but in the case of Ag it is substantially up-shifted in energy, which leads to a higher energy curve crossing. However, the most remarkable difference between the hydrogen molecule curves, is the one of Ni and Cu periodic columns. In the latter case the potential grows exponentially as long as the molecule approaches the wire, while in the Ni periodic column the potential only grows exponentially *after* crossing the atomic potential curve. Moreover, in the case of Pd and Ni the H_2 curves have a local minimum, i.e. a molecular adsorption energy of around -0.25 eV and 0.05 eV, respectively. These studies show that Ni, Pd, and Pt wires have a better affinity towards the hydrogen molecule than the three coin metal wires, and that this has an important influence on the dissociation activation energy.

Now let us compare this diabatic scenario with the adiabatic one described in

Figure 9.5: Comparison of the diabatic and adiabatic one-dimensional potential energies for the dissociation of H$_2$ on several nanowires.

section 9.2, which is also shown in figure 9.5. For the Ni periodic column it is clear that the Lennard-Jones approximation is accurate. Due to the relaxation of H$_2$ the adiabatic approximation is lower in energy than the fixed molecule case. In this scenario we can certify that hydrogen dissociation on Pd wires is non-activated. Interestingly, on Ni and Pt the activation barrier occurs at relatively far distances from the wire ($\sim$2 Å), distances at which the molecule has not been broken yet! In principle, a lower E_a should be obtained in the adiabatic scenario since we allow the crossing of the curves by relaxing the H$_2$ molecule while it approaches the wire. Nevertheless, in the case of the three coin metals the activation energies obtained in the adiabatic case are higher than those predicted by the Lennard-Jones approximation. This may seem unexpected, but we will see later that is a consequence of solving a multi-dimensional problem with a one-dimensional representation.

Potential energy surfaces

The most accurate procedure to calculate the activation energy of hydrogen dissociation along the b-t-b configuration is by determining the potential energy surface (PES) of the molecule approaching the wires. The contour plots along two-dimensional cuts through the six-dimensional coordinate space of H_2 interacting with the wires are shown in figure 9.6. These coordinates are the H-H distance (d_{HH}) and the molecule center-of-mass distance from the wire (z). These 2D potentials have an elbow shape so that they are usually called *elbow-plots*.

The barriers obtained by the three procedures described so far are compared in table 9.2.

	Ni	**Pd**	**Pt**	**Cu**	**Ag**	**Au**
E_a/eV (LJ)	0.14	0.01	0.40	0.42	1.11	0.62
E_a/eV (RLX)	0.14	0.01	0.28	0.48	1.40	0.67
E/eV (PES)	0.13	0.01	0.36	0.48	1.50	0.78

Table 9.2: Activation energy (E_a) of H_2 dissociative adsorption on wires in the b-t-b configuration according to three procedures: Lennard-Jones (LJ-diabatic scenario), axial relaxation of the hydrogen molecule at fixed distances from the wire (RLX-adiabatic scenario) and contour plot from the potential energy surface (PES) shown in figure 9.6.

Once again, the activation energies obtained for the three coin metals are higher than those predicted by the Lennard-Jones approximation and even the one-dimensional adiabatic approximation. In order to explain these deviations, let us take the Cu contour plot in figure 9.6 as an example. The Lennard-Jones approximation (the diabatic scenario) is equivalent to determining the energies along two lines perpendicular to the abscissas in the elbow-plot; one at $d_{HH} = 0.75$ Å, which corresponds to the H_2 potential curve; and the other at the hydrogen adsorption equilibrium position on Cu wires $d_{HH} = 2.4$ Å.[1] The activation energy is then obtained by intercrossing these curves. It becomes evident that the resulting E_a is not necessarily equivalent to the saddle point in the elbow plot. Relaxing the hydrogen atoms along their axis at fixed different distances (the adiabatic scenario) does not solve this problem. It is equivalent to finding the energy minimum along lines parallel to the abscissas in the elbow-contour plot. When the location of the activation energy is at relatively long distances from the wire, finding this minimum is trivial. This is the case of H_2 dissociation on Ni, Pd, and Pt wires. However, when the saddle

---

[1]Strictly, the hydrogen atoms should be at infinite distance to each other in their equilibrium position but the latter approximation is valid for illustrative purposes.
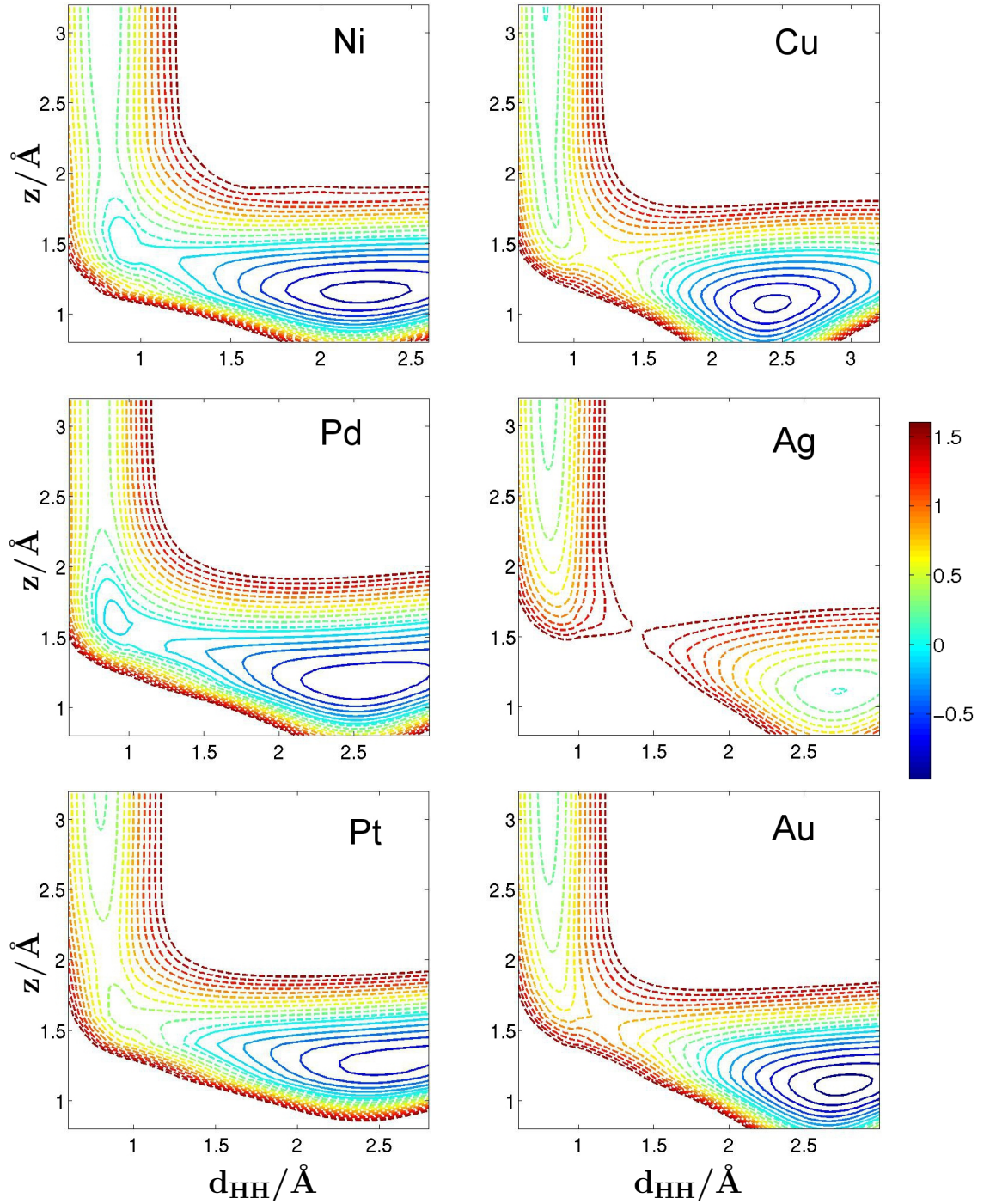
Figure 9.6: Contour plot of the potential energy surfaces (PES) for the dissociation of H_2 on several wires in the b-t-b configuration. The potential energy dependence of the H-H distance (d_{HH} in Å), and the molecule center-of-mass distance from the wire (z in Å) is represented. The contour space between curves is 0.15 eV, dashed lines indicate positive and full lines indicate negative values.

point of the contour curve is close to the elbow, the energy minimum found by the hydrogen bond relaxation can be misleading. Taking the case of Ag as an example, at $z \approx 1.5$ Å the relaxation can lead to minimum energies at the left or the right side of the contourplot, avoiding the saddle point and consequently underestimating the activation energy.

In order to examine the electronic factors that favor Ni, Pd, and Pt against Cu, Ag, and Au towards H_2 dissociation, the DOS projected onto the hydrogen and metal atoms at three stages of the dissociation process are plotted in figure 9.7.

In stage (a), at far distances from the wire, the molecule and the substrate are not interacting. The prominent peak of the DOS projected on H_2 corresponds to the molecule σ state. At stage (b), at distances at which H_2 is about to break, the three coin metals show a significant down-shift of the d band which is not seen in Ni or Pd wires (in Pd this effect is relatively small). This explains why the former wires are more repulsive with respect to H_2 dissociation according to the d band model. Note that in the case of Pd the hydrogen states are in resonance with the d-states of the metal, in agreement with the fact that the dissociation on such a wire is non-activated. At stage (c), where H_2 is dissociated with the hydrogen atoms adsorbed in their equilibrium positions, the states of hydrogen are splitted in bonding and antibonding contributions. As we saw in chapter 7, Ag is the only case in which the antibonding states are occupied, making the hydrogen-wire interaction repulsive.

9.4   Conclusions

In order to obtain the activation energy of a process, several approximations can be used. The dissociation of H_2 on nanowires resulted to be a suitable system to compared them.

There is a general tendency of the activation energy to be smaller for the Ni periodic column than for the three coin metals. While in the first case the barrier occurs when the molecule is at distances larger than 2 Å from the wire, in the three coin metals it appears at distances shorter than 1.4 Å. Pd wires are a particular case since there H_2 dissociation is non-activated. For Ni and Pt the barrier is smaller than 0.4 eV. The process is clearly unfavorable on Ag wires, regardless of the orientation of hydrogen – with an activation energy of the order of 1.5 eV. Cu is an intermediate case, with a barrier of 0.5 eV. Finally, Au is the best coin metal catalyst for the Tafel reaction with a barrier of 0.3 eV.

The most stable path for hydrogen dissociation seems to be the t-b-t configuration for all the metals studied with the exception of Au, for which the b-b-b is the most favorable one.
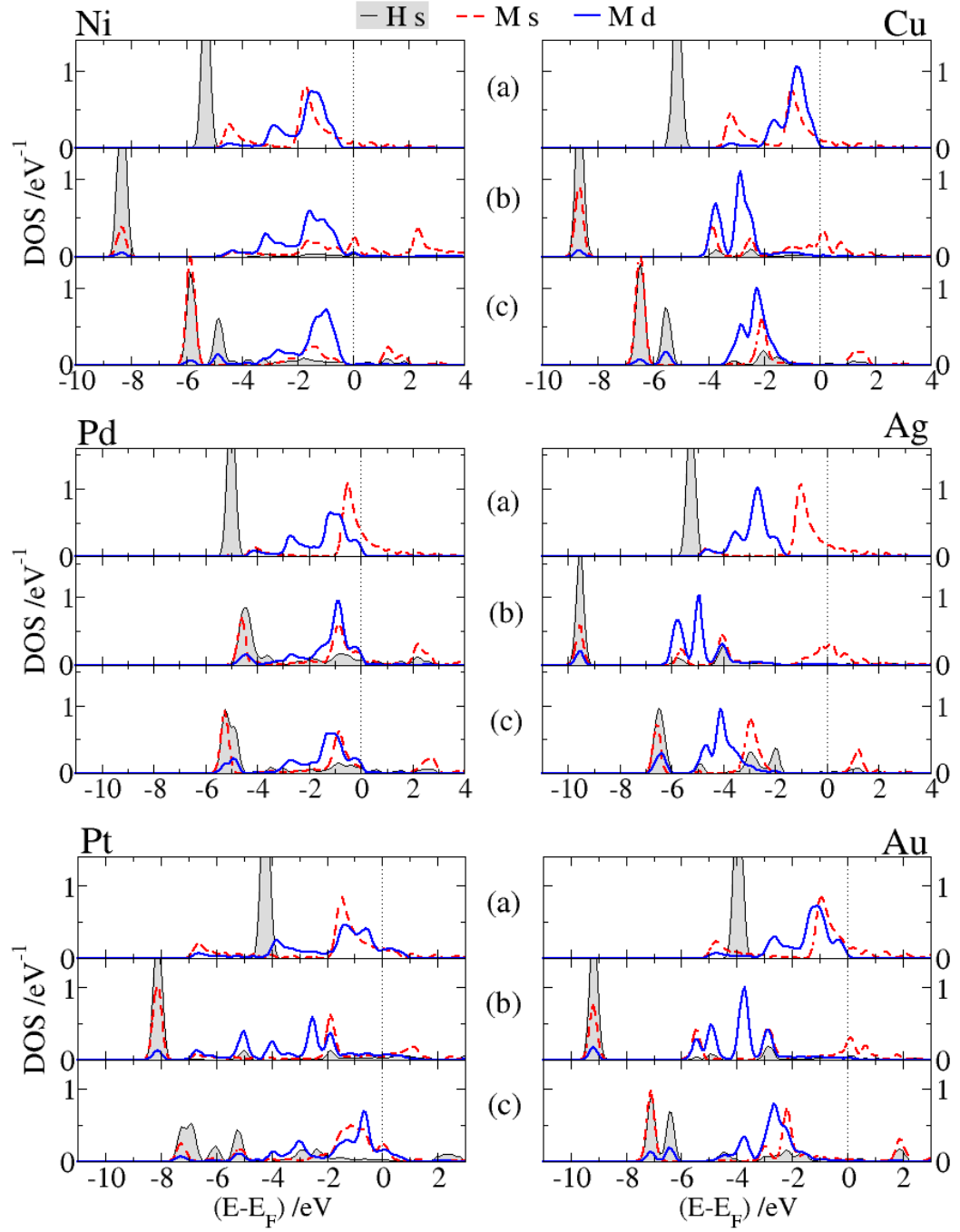
Figure 9.7: Density of states (DOS) projected on the orbital involved in the hydrogen-wire bond. Three stages of the dissociation are evaluated: (a) H$_2$ far away from the wire; (b) H$_2$ close to the hydrogen bond breaking; (c) H$_2$ dissociated with hydrogen atoms adsorbed at the equilibrium position.

10
Atomic oxygen ad/absorption

Although deep in the core nothing is
really clear... the intelligence wags its
tail like a satisfied dog when it
verifies the symmetry of the things.

Julio Cortázar Writer.

We have seen in chapter 7 that gold and copper nanowires are excellent catalysts for the hydrogen evolution reaction (HER). In order to be used in a fuel cell, an ideal catalyst should also catalyze the oxygen reduction reaction (ORR). We start this chapter by analyzing such a possibility. In this case, an oxygen atom is adsorbed at low coverages on several wires. Further on, we explore the chemical and mechanical properties of the so-called oxygenated wires. Two configurations with intercalated oxygen-metal atoms are considered: one in which the atoms are in a linear chain, and another one with the oxygen atoms on both sides of the wire, in a zigzag arrangement. Oxygen adsorption at low coverages and oxygenated wires are schematized in figure 10.1.

Oxygenated wires may be formed as a consequence of the stretching to which the nanowires are subjected in the experimental set-up, where not only oxygen does adsorb *on* the wire but is also *absorbed*. In fact, this phenomenon explains the large Au-Au distance observed by electron microscopy (around 4 Å), for which oxygen atoms are *invisible* [74]. The ad/absorption of oxygen could also explain the striking magnetic behavior of Cu nanowires under an applied magnetic field in

91
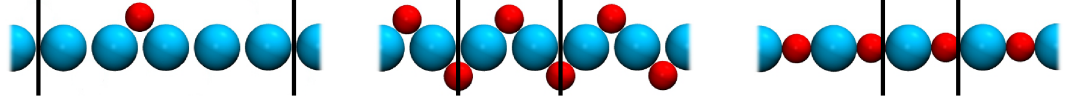
Figure 10.1: Side view of the monoatomic nanowires addressed in this chapter. From left to right: Atomic oxygen adsorbed on a linear wire; zigzag oxygenated wire; linear oxygenated wire. The space between the vertical lines corresponds to the unit cell length – along the wire axis.

air [75]. In agreement, a theoretical work shows that the spin of Cu oxygenated wires is strongly dependent on the interatomic distance [76], however, only the Cu linear oxygenated wire was considered. Studies on Au zigzag oxygenated wires show that an intermetallic stretching of 1 Å from the equilibrium position gives rise to a rather small change in energy, since the chain can adjust the oxygen-gold-oxygen angle during such an elongation [74]. Similar features were obtained for tip-suspended gold chains, where it was also found that the incorporation of oxygen in the metal wire leads to a magnetic behavior [77].

Motivated by these results, we explore the energy, spin, and stress dependence of several oxygenated nanowires with respect to their intermetallic distances.

10.1   Technicalities

Modeling

The same procedure used for atomic hydrogen adsorption (p. 54) was employed here for oxygen. The wire was pre-relaxed and fixed, while oxygen was allowed to relax along the perpendicular axis of the wire at the *bridge* and the *top* sites. In order to optimize the adsorption energy, the number of wire atoms was increased systematically until the change in the binding energy was less than 20 meV. The linear and zigzag oxygenated wires were constructed with one and two metal atoms per unit cell, respectively. In the linear case, no relaxation was needed, the unit cell was increased and the atoms were fixed at equidistant positions along the x axis. In the zigzag case, the metal atoms were fixed equidistantly and the oxygen atoms were allowed to relax along the z axis at both sides of the wire for each unit cell size.

First-principle parameters

The k-points and the plain-wave cutoff energy were taken from the parametrization for monometallic wires (see page 18). Spin considerations were included for some representative systems, but only Pd monometallic wires with and without oxygen

showed a magnetic moment. The energy difference with respect to the non-magnetic systems is -15 meV/atom. Since for oxygen adsorption on Pd eight atoms were used, this energy difference becomes important and therefore calculation for Pd wires were performed considering the spin. For the rest of the cases at this coverage the calculations were performed without spin. In contrast, for oxygenated wires spin was considered for each metal studied and each unit cell size.

10.2   Oxygen adsorption

The adsorption energy of oxygen was calculated according to

$$E_{ads} = E_{wire+O} - (E_{wire} + \frac{1}{2}E_{O2})$$ (10.1)

The adsorption energies E_{ads} and the oxygen distances from the wire axis d_{ow} are summarized in table 10.1.

	E_{ads} [eV]		d_{ow} [Å]	
	top	bridge	top	bridge
Cu	0.19	-1.07	1.70	1.37
Ag	1.21	0.38	1.87	1.51
Au	1.18	0.18	1.87	1.49
Pd	0.04	-0.97	1.87	1.50
Pt	0.36	-0.75	1.83	1.52

Table 10.1: Oxygen adsorption energy (E_{ads}) and oxygen distance from the wire axis (d_{ow}) on mono- and bimetallic nanowires.

It is worth stressing that the absolute values of table 10.1 should be interpreted with care, as we mentioned in the technicalities, the GGA functional overestimates the oxygen-oxygen bond. It is safe, however, to work with the relative energy values, i.e., comparing E_{ads} between different sites for the same metal wire, or among different metal wires for the same site. Oxygen on the bridge site is the most stable configuration for all the cases presented in table 10.1. There is a remarkable difference between the adsorption energy of oxygen at top and bridge sites of around 1 eV, suggesting that oxygen diffusion on the wires is very unlikely to occur.

The oxygen-wire bond

Figure 10.2 shows the DOS projected on to the oxygen atoms and on its nearest metal neighbors. It reveals that the $2p$ orbital of oxygen interacts strongly with the valence d band of the wire. The oxygen $2s$ state, on the other hand, shows almost no interaction with the metals. As shown in the panel of Ag, the peak of the $2s$ state of the oxygen remains narrow and far below the Fermi level (at around -18 eV).
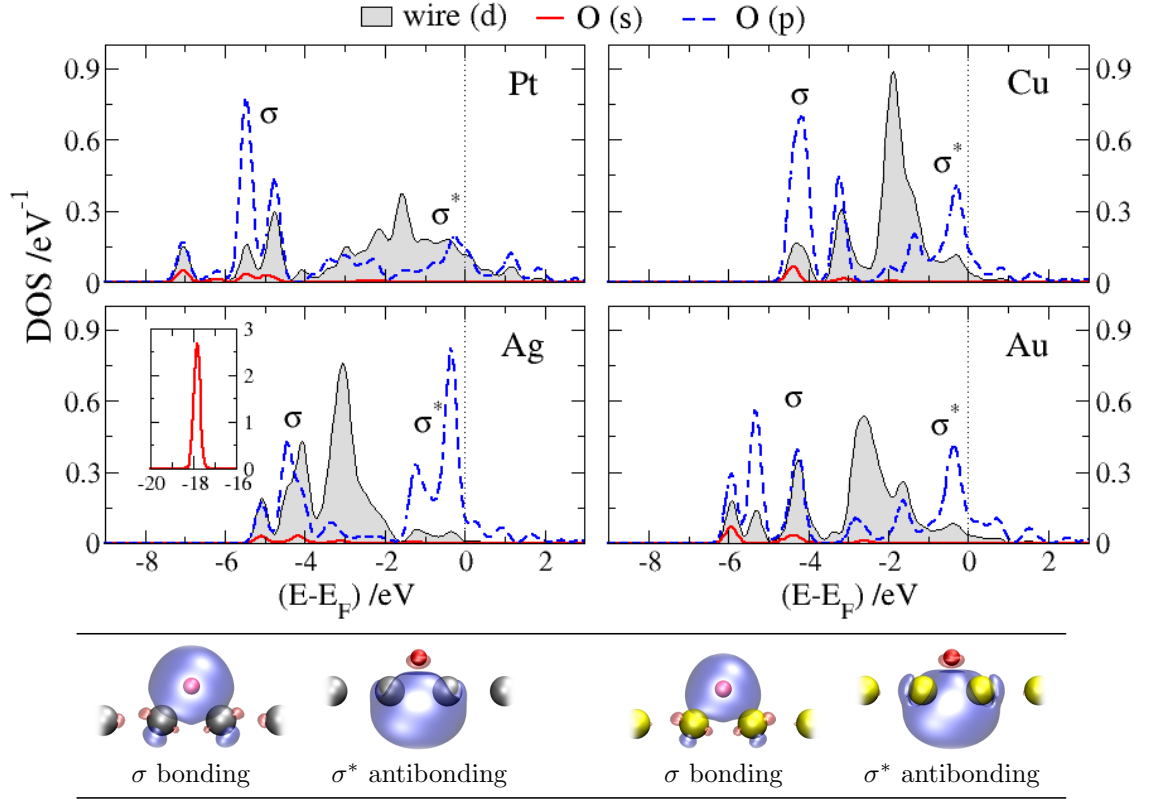
Figure 10.2: Density of states (DOS) projected on the valence d band state of the metal and the $2s$ and $2p$ states of oxygen adsorbed on several wires. The $2s$ state of oxygen shows a sharp peak at around -18 eV in all cases (see inside the panel of Ag). Bonding (σ) and antibonding (σ^*) states are pointed out in the panels.

In order to evaluate whether the different oxygen adsorption energies are reflected in the charge distribution, the charge density difference ($\Delta\rho$) was calculated according to:

$$\Delta\rho = \rho_{wire+O} - (\rho_{wire} + \rho_O) \tag{10.2}$$

For a given position along the z axis (which is the axis that intersects the wire and oxygen), a total sum over $\Delta\rho$ on the xy plane is made and denoted by $\Delta\rho_z$.

Regions with $\Delta\rho_z > 0$ correspond to electron accumulation (bond region) while regions with $\Delta\rho_x < 0$ correspond to electron depletion. Results for oxygen on the top site of Pt, Cu, Ag, and Au wires are shown in figure 10.3.
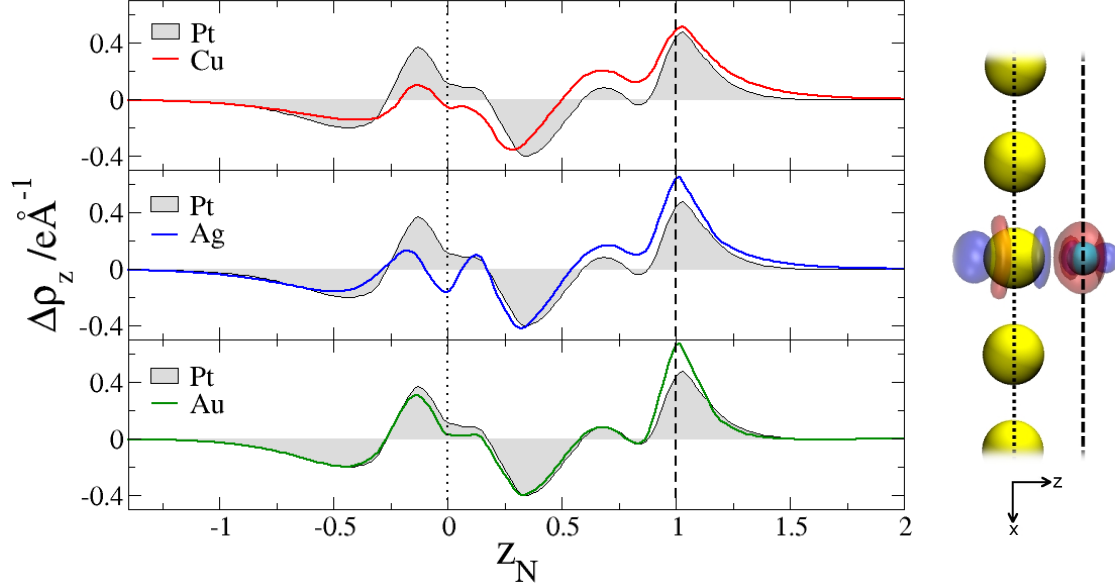
Figure 10.3: Charge density difference sum ($\Delta\rho_z$) over the z axis of some monometallic wires with oxygen on the top site. $\Delta\rho_z$ in each case is contrasted to that of Pt. The distance from the wire axis (z_N) is normalized to the wire-oxygen distance to facilitate the comparison. The dotted line intersects the wire atoms and the dashed line intersects the oxygen atom. As an example, the isosurface of the charge density difference for oxygen on top of a Au wire is plotted on the right. Blue regions correspond to charge depletion and red regions to charge accumulation. Isovalues of ± 0.3 e/Å^3 were used.

Evidence of a wire-oxygen covalent bond is observed at $z \approx 0.7$ Å, where a positive value for $\Delta\rho_z$ is found. The charge accumulation at the bond region seems to be larger for Cu, in agreement with its strong adsorption energy. Since oxygen is more electronegative than the metal wires, a distinct charge depletion is observed in the vicinity of the wire atoms. At the same time, a charge accumulation is observed close to the oxygen atom. By the analysis of figure 10.3 it is not trivial to explain why Pt and Cu adsorption is more favorable than on Ag and Au, i.e., $\Delta\rho_z$ looks rather similar for Au and Pt wires but the corresponding adsorption energies differ by 0.8 eV, being more favorable for Pt. The latter analysis shows the charge distribution induced upon oxygen adsorption in a one-dimensional fashion, however, it is also important to look at $\Delta\rho$ on a plane, as shown in figure 10.4 for oxygen on top and bridge sites.

For oxygen on the bridge site, the charge accumulation in the bond region is

Oxygen top

Pt   **Cu**   **Ag**   **Au**

Oxygen bridge

Pt   **Cu**

Ag   **Au**
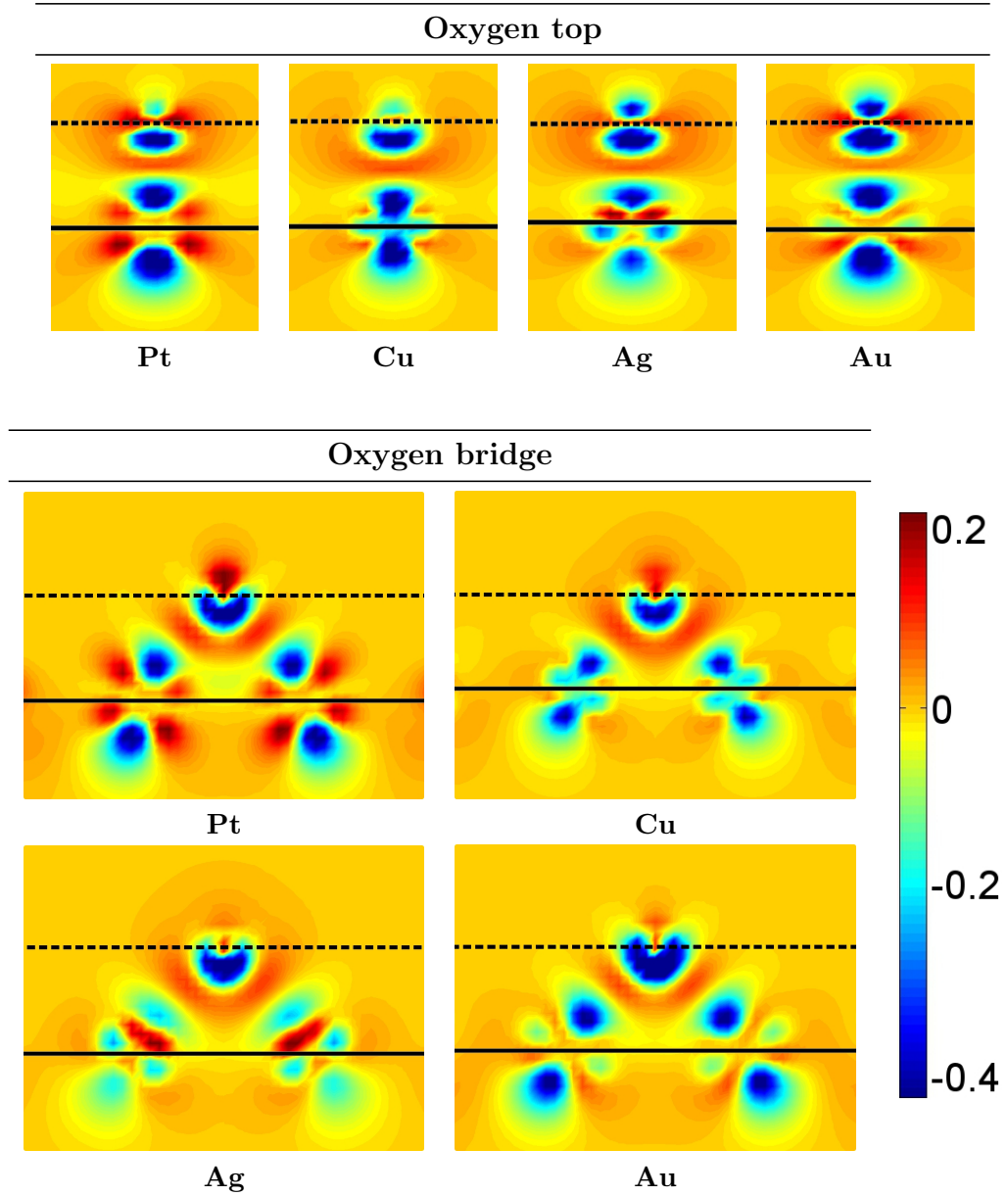
Figure 10.4: Charge density difference in e/Å^3 of oxygen at the top and the bridge site on several nanowires. The full line intersects the wire atoms and the dashed line intersects the oxygen atom.

similar on Pt and Cu wires and larger than on Ag and Au, in agreement with their adsorption energies.

10.3   Oxygen absorption

As described in the introduction, oxygen can actually be part of the metallic chain. In order to study the energetics of the so-called oxygenated wires, the absorption energy of oxygen E_{abs} as a function of the intermetallic distance d_{nn} is shown in figure 10.5 for linear and zigzag oxygenated wires. The terminology E_{abs} is used only to differentiate it from the adsorption energy E_{ads}, but they are both calculated according to equation 10.1.
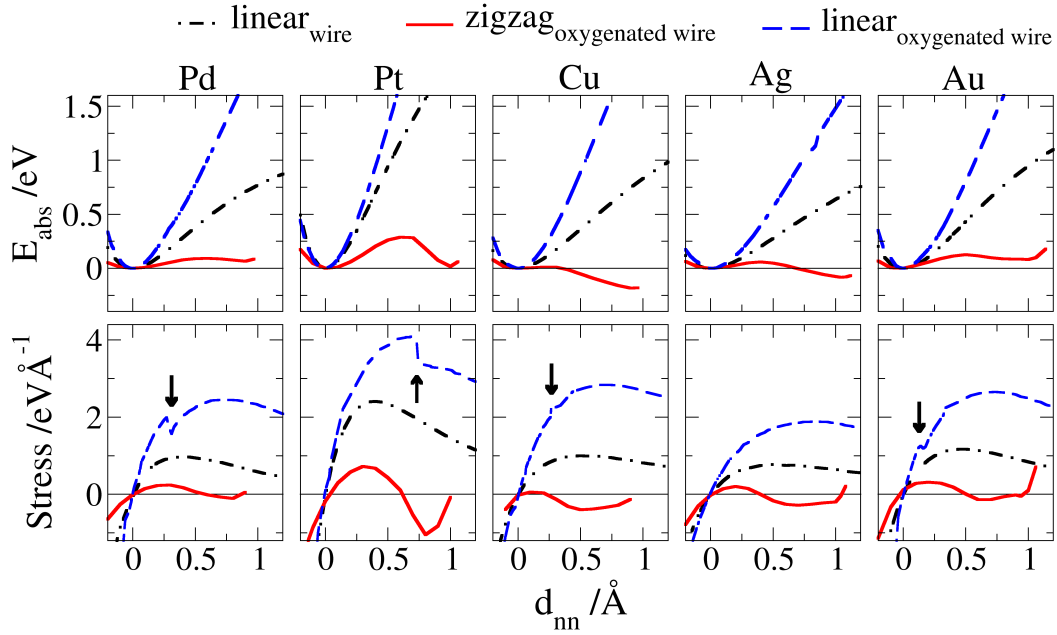
Figure 10.5: Absorption energy of oxygen (E_{abs}) and magnetic moment for oxygenated nanowires as a function of the intermetallic distance (d_{nn}). The dashed lines show the intermetallic equilibrium distance for each wire.

As we can see, there are two minima in the absorption energy of oxygenated wires, one corresponds to the zigzag configuration, and the other to the linear one. Naturally, the elongation of the former gives rise to the latter. The intermetallic distance and absorption energy corresponding to the equilibrium for both configurations are summarized in table 10.2

At the equilibrium position, both configurations are similar in energy. Interestingly, zigzag is not always the most stable configuration, as one could expect. For Cu and Ag the linear arrangement is preferred. In general, the oxygenated wires are very flexible over a large intermetallic distance (around 1 Å), a range in which the energy does not change significantly, as it has been observed on oxygen-gold chains [74]. This is due to the fact that the oxygen-metal distance during the elongation of

			Pd	Pt	Cu	Ag	Au
zigzag	d_{nn}	[Å]	2.9	2.7	2.6	2.8	2.8
	E_{abs}	[eV]	-1.30	-1.64	-1.56	-0.37	-0.59
linear	d_{nn}	[Å]	3.81	3.69	3.52	3.84	3.80
	E_{abs}	[eV]	-1.24	-1.62	-1.75	-0.45	-0.52

Table 10.2: Intermetallic equilibrium distance (d_{nn}) and corresponding absorption energy (E_{abs}) for linear and zigzag oxygenated nanowires.

the zigzag oxygenated wires is rather invariant, only the oxygen-metal-oxygen angle changes. However, for Pt wires, there is a small energetic barrier for the transition of configurations of about 0.3 eV. Atomic oxygen incorporation into the wire is thermodynamically favorable, particularly for Cu, Pt, and Pd. The process is also more favorable than the single atomic adsorption on fixed pre-relaxed wires. This suggests that metallic nanowires cannot be used as catalysts for the ORR since, once absorbed, oxygen will hardly desorb from the wire. Also in figure 10.1 the spin dependence with the intermetallic distance is shown. Just at a first glance it is evident that the spin is strongly dependent on d_{nn}. Only in the case of Pt none of the equilibrium configurations present magnetic behavior. Interestingly, Cu and Ag oxygenated wires are magnetic in all the energy interval between the zigzag and the linear equilibrium states.
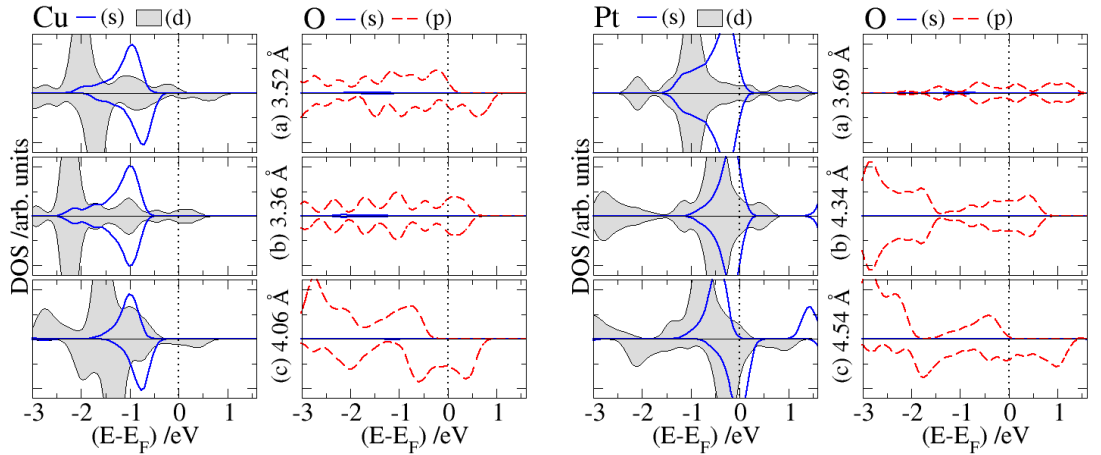
Figure 10.6: Density of states (DOS) of linear oxygenated wires projected on the metals and the oxygen atoms at three interatomic distances: at the equilibrium distance (a), before (b), and after (c) the change of spin. Spin values are shown separately above and below the center of each plot.

At large intermetallic distances the magnetic moment for Pd and Pt is twice as high as for the three coin metals. This is because in the former case both the s and the d states of the metals experience charge depletion in one spin, while in the three coin metals case this depletion occurs only in the d state. Figure 10.6 exemplifies this for Cu and Pt linear oxygenated wires at three intermetallic distances: at the equilibrium, before, and after the change in the spin. Non-polarized wires show symmetric DOS for both spin directions. At intermetallic distances larger than that of the equilibrium, where the spin is observed, the symmetry of the DOS for the two spin directions is broken due to charge accumulation on one spin and charge depletion on the other. The orbitals involved in this charge transfer are not the same for all the metals studied: For the three coin metals, the states at the Fermi level are only the valence d states. This gives rise to a maximum magnetic moment of 1 μ_B. For Pd and Pt on the other hand, the states at the Fermi level are the valence d and s states. This gives rise to a maximum magnetic moment of 2 μ_B. Finally, it is instructive to study what effect oxygen inclusion has on the mechanical properties of the wires.

Figure 10.7 shows the change of potential energy and stress with respect to the intermetallic distance for pure nanowires and both configurations of oxygenated wires. The energies and distances referred to are those corresponding to the equilibrium state for each wire. The discontinuities in the stress curves, readily observed on linear oxygenated wires, are due to the sudden change in the spin.

As remarked earlier, the elongation of zigzag oxygenated wires from their equilibrium distance involves small changes in the energy, and therefore these type of wires have the smallest stress. The linear oxygenated wires are in all cases the most stressed ones. This entails that the corresponding oxygen-metal bond is stronger than the metal-metal bond, which in turn means that larger forces are needed to break the former wires.

10.4   Conclusions

In section 7.2 we found that hydrogen evolution reactions proceeds with a lower activation energy on Cu and Au wires, where hydrogen adsorption is exergonic. In this chapter, we found that oxygen adsorption (E_{ads}) on Cu nanowires is close to 1 eV more favorable than on Au. In general E_{ads} follows the order Cu≈Pd≈Pt<Ag≈Au. The adsorption on Pd and Pt is stronger due to lower occupation of antibonding states that result from combination of the $2p$ of oxygen and the valence d band of the metals in comparison with Ag, Au. According to the density of states projected on oxygen $2p$ states on Cu, the adsorption energy should be similar to the one of other coin metals, however, is remarkably more stable (around 1 eV lower). The charge distribution on Cu induced upon oxygen adsorption on the bridge site is
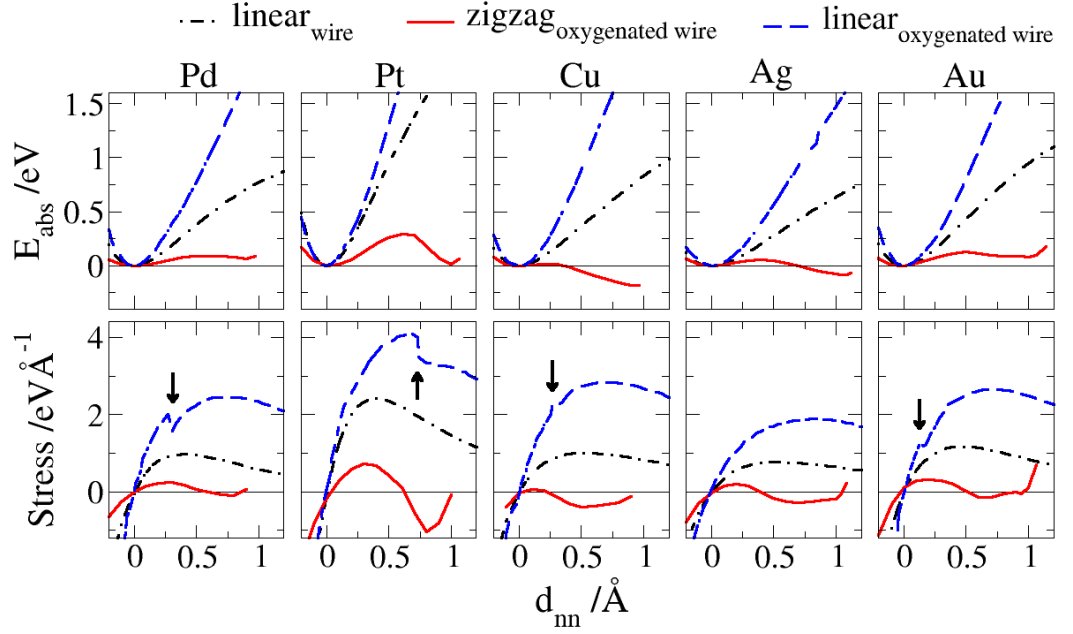
Figure 10.7: Potential energy and stress curves of pure and oxygenated nanowires as a function of the intermetallic distance (d_{nn}). The energies and distances are referred to those of the equilibrium state for each wire. The discontinuities in the stress curves are due to the sudden change in the spin, pointed out with arrows.

more similar to Pt than to Ag and Au. Apparently, the charge distribution explains better the strong oxygen adsorption on the bridge site of Cu wires. The small size of Cu may also play a role since it implies lower Pauli repulsion.

The incorporation of atomic oxygen in the chain leads to stronger interatomic bonds, which strengthens the wire. From the equilibrium state of the zigzag configuration to the equilibrium of the linear one (which implies an elongation of 1 Å approximately), oxygenated wires experience a small change in energy, making them quite flexible to adapt to the mechanical stretching. Only on Pd a barrier of 0.3 eV was found for the latter process. All the systems studied presented strong spin dependence on the intermetallic distance. Oxygenated coinage-metal wires are all spin-polarized in both equilibrium states, oxygenated Pd wires are polarized only in the zigzag equilibrium state, and oxygenated Pt chains are not spin polarized neither in the linear nor in the zigzag equilibrium state.

11

H$_2$O dissociation

What makes the desert beautiful is
that somewhere it hides a well.

Antoine de Saint-Exupery
Writer.

The wealth of water is in your thirst.

Juan Carlos Durilén Writer.

For the systems described so far, the atoms interacting with the nanowires were all strongly adsorbed, i.e. true chemical bonds were created from the atom-wire interaction. The latter are typical *atomic chemisorptions*. In this chapter, we will explore features of a *molecular adsorption*, in particular, water adsorption on Pt wires. In this case, the interaction with the wire is weaker. In the literature we have found neither experimental nor theoretical studies of water on nanowires. However, we could relate the latter to the adsorption of water on Pt(110) surfaces. After the (1×2)-reconstruction, a low-coordinated wire-like disposition of platinum atoms is observed on Pt(110) surfaces as shown in figure 11.1. The most stable adsorption site for 0.5 ML H$_2$O has been found on such platinum atoms [78]. This is due to the narrowing of the d band of the uncoordinated atoms with respect to the more
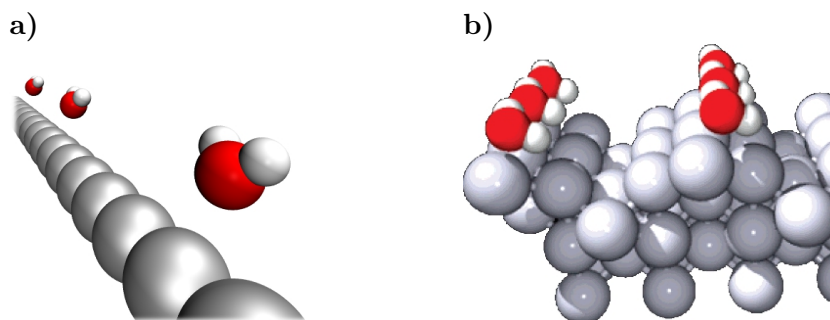
Figure 11.1: a) Perspective view of H_2O on top of a free-standing nanowire at low coverages (θ_{H_2O}=1/6). **b)** Perspective view of the most stable adsorption site of water on (1×2)-reconstructed Pt(110) at half coverage (θ_{H_2O}=1/2) [78]. Water is adsorbed on top of the less coordinated Pt atoms, resembling the adsorption on a nanowire.

coordinated ones (below), which in turn shifts up the d band and strengthens the water-surface interaction. On Pt free-standing nanowires this uncoordination is at its limit, so that the H_2O adsorption is expected to be stronger than on the latter reconstructed surface.

There are many interesting topics to explore concerning the water interaction with Pt wires: its dependence on the coverage, geometrical structures, dynamics, etc. However, the scope of this chapter is to examine a single water molecule adsorption and dissociation on Pt wires, which can serve as a starting point for future work. We start by calculating the adsorption energy of OH on Pt wires. Later, the adsorption and the dissociation of H_2O is addressed, for which two types of nanowire were employed: a monostrand wire (one-atom-thick free-standing wires) and a short monostrand wire between bulk leads. We will refer to them as *nanowires* and *slab-wires*, respectively. The latter was included in the calculations in order to account for the influence of a bulk vicinity. Finally, the results are summarized in the conclusions.

11.1   Technicalities

Modeling

Nanowire: Several geometrical configurations for H_2O and OH were computed on a Pt pre-relaxed wire of six atoms. First, high-symmetry sites were calculated, with oxygen on bridge and top sites, pointing up or down the surface (see H_{up} and O_{up} configurations, respectively in figure 11.1). In this case the relaxations were made in such a way that the molecules keep their orientations towards the surface. Later, H_2O and OH were tilted and fully relaxed (see *tilt* configurations in figure 11.1).

In order to study the isolated adsorption of OH and H_2O on a Pt wire, they were relaxed separately on wires of increasing number of atoms as shown in figure 11.2.
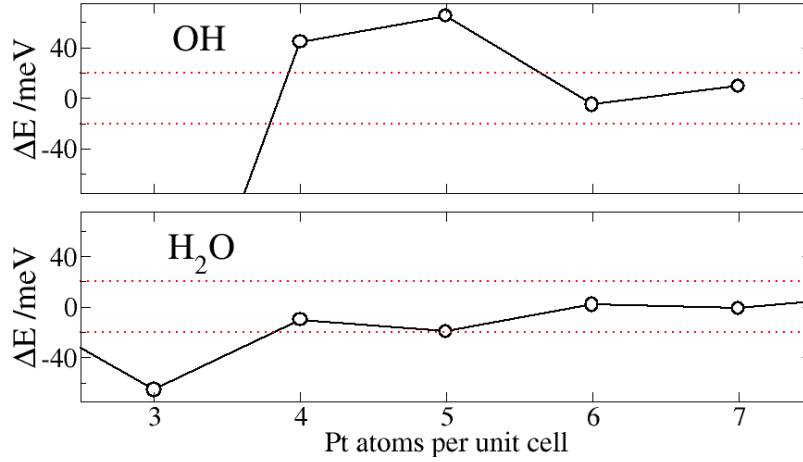
Figure 11.2: Change in energy (ΔE) for the most stable configuration of H_2O and OH on Pt wires as a function of the number of metal atoms per cell.

As it can be seen in the figure, with six Pt atoms per unit cell the convergence for the adsorption of OH and H_2O is achieved.

Slab-wire: The slab consists of a 3×3 fcc(111) supercell with two metal layers. The wire is constructed with five linear Pt atoms perpendicular to the surface on the hollow-fcc site as shown in figure 11.3. Since the periodic cell has no vacuum in the z axis (axis of the wire), the system consists of an infinite set of five-atom wires truncated by two-layers slabs.
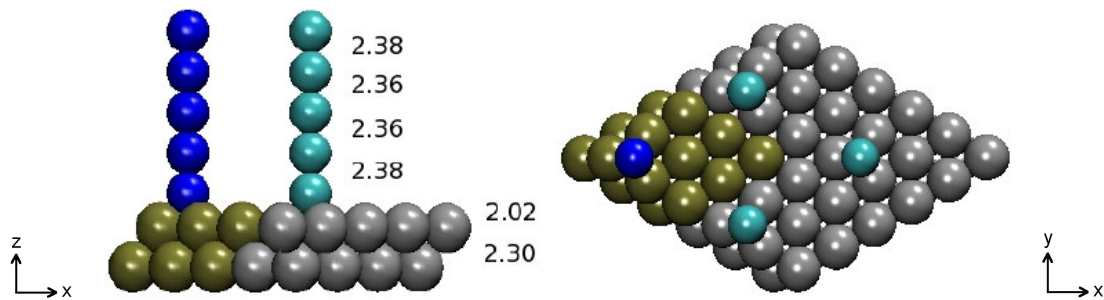
Figure 11.3: Top (left) and side view (right) of a Pt slab-wire. The slab consists of two layers of a 3x3 fcc(111) supercell. For the unit cell the slab is colored ochre and the wire blue.

The lateral dimensions of the surface were fixed from the corresponding bulk distances. The height of the periodic cell (L_z) was changed systematically and the

wire was relaxed perpendicularly to the surface. The wire bond distances (d_{nn}) after relaxation are shown in figure 11.3. These distances are close to those of the monometallic free-standing wire (2.39 Å). Only the most stable configurations of H$_2$O on the free-standing wire were relaxed in this structure by fixing the slab-wire and fully relaxing the adsorbates.

First-principle parameters

Nanowire: For the free standing nanowire, DACAPO [6] and VASP [79–82] DFT packages were used. In both cases the PW91 exchange correlation functional was used. The plane waves implemented were 450 eV, and the *kpts*=22×1×1. Spin considerations were only needed for the calculation of OH in vacuum.
Slab-wire: The slab-wire was only calculated with the VASP code. The same plane wave used for the free standing wire was computed here. The k-points used were integrated in 3-dimensions: *kpts*=4×4×3.

11.2   Adsorption of OH and H$_2$O

Species on the free-standing nanowire: The adsorption energy for OH and H$_2$O on Pt wires was calculated according to

$$
\begin{aligned}
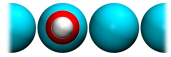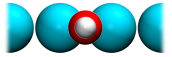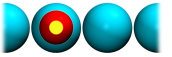E_{ads}^{OH} &= E_{OH+wire} - E_{OH} - E_{wire} & (11.1)\\
E_{ads}^{H_2O} &= E_{H_2O+wire} - E_{H_2O} - E_{wire} & (11.2)
\end{aligned}
$$
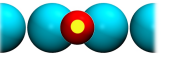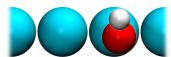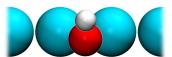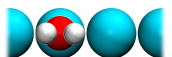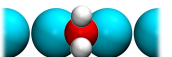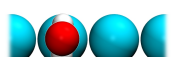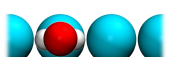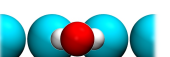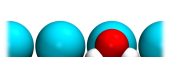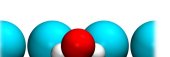
Figure 11.1 shows the different configurations computed for OH and H$_2$O.

The most stable configuration of OH corresponds to oxygen on a *bridge* site and the hydrogen atom tilted and pointed upwards with respect to the wire. The strong adsorption indicates the existence of an oxygen-wire chemical bond, as confirmed by the DOS in figure 11.4: There is a strong interaction of the *s* and *p* states of oxygen with the *d* band of the wire, which are in resonance in the region -9<E<-4 eV.

The most stable adsorption site for H$_2$O on the other hand, corresponds to oxygen on a *bridge* site with the hydrogen atoms parallel to the wire axis, pointing upwards and also tilted. The adsorption energies are rather weak and insensitive to the configurations, suggesting that the H$_2$O-wire interactions are non-bonding, as also confirmed by the DOS in figure 11.4: There are no strong interactions between oxygen-wire states. The small difference in energy between oxygen on *top* and *bridge* configurations indicates that the barrier of water diffusion on Pt wires is negligible (around 0.06 eV).

For the sake of completeness, the bond character of the species was analyzed through charge density differences ($\Delta\rho_e$). Figure 11.5 shows $\Delta\rho_e$ of the adsorbate/wire with respect to the isolated components.

		H$_{up}$ top	**H$_{up}$ brg**	**O$_{up}$ top**	**O$_{up}$ brg**	
OH		-947	-1792	422	287	
	tilt	-2090	-2368			

		t-t-t	**b-t-b**	**b-b-b**	**t-b-t**	
H$_2$O	**H$_{up}$**	-49	-54	-48	-37	
	O$_{up}$	-57	-55	-64	-59	
	tilt	-81	-126	-82	-60	

Table 11.1: Top view of the different orientations of OH and H$_2$O over a Pt wire with their adsorption energy (E_{ads}) in meV. For water, the letters **t** and **b** refer to *bridge* and *top* sites, respectively. The first and third letters correspond to the orientation of hydrogen atoms and the middle one to the orientation of the oxygen atom.

It becomes evident from the figure that OH presents an accumulation of electron charge between the oxygen-wire region and a charge depletion in the vicinity of the atoms, which is characteristic of a covalent bond. Water on the other hand, presents relatively poor charge transfer and no signs of bond formation.

H$_2$O on the slab-wire: The water molecule in the H$_{up}$ b-t-b configuration on the slab-wire presents an adsorption energy of -0.22, being only 0.1 eV more stable than on monostrand free-standing nanowires. Considering the great difference in the calculation time-consumption between these wires, this error is reasonably small. The following calculations were therefore performed on the free-standing wires.

11.3   H$_2$O dissociation

The dissociation energy of a water molecule in vacuum (E_{diss}°) and on the wire (E_{diss}^{wire}) are given in equations 11.3 and 11.4, respectively. For the latter case the following thermodynamic cycle was proposed: H$_2$O desorption from the wire ($-E_{ads}^{H_2O}$), then water dissociation in vacuum (E_{diss}°), and finally OH and atomic hydrogen adsorption on the wire (E_{ads}^{H} and E_{ads}^{OH}, respectively).
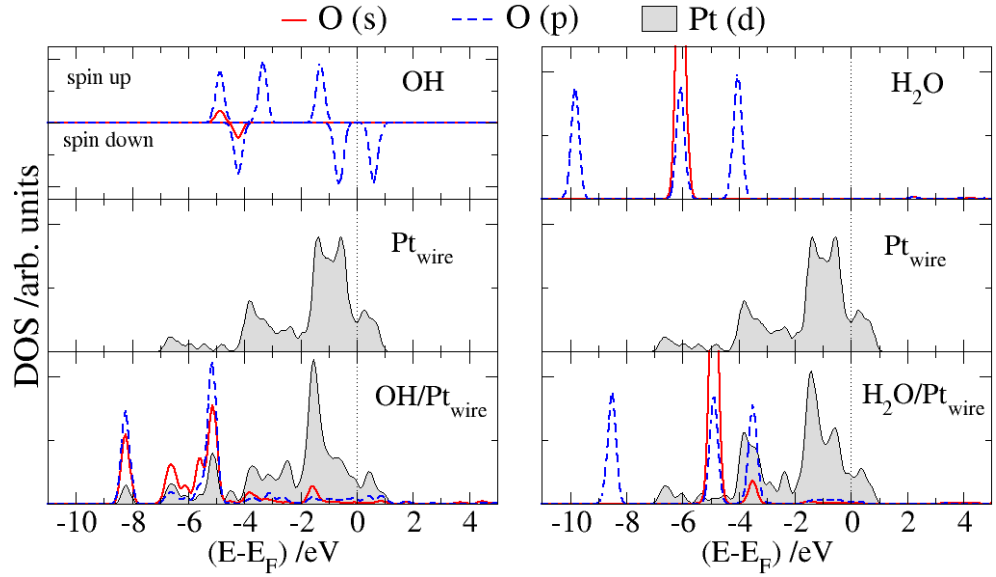
Figure 11.4: Density of states (DOS) projected on oxygen and Pt atoms (in the latter case, reduced by a factor of two). **top)** Isolated OH (left) and isolated H₂O (right). For OH, the DOS for both spins are plotted. **middle)** Isolated Pt wire (left and right). **bottom)** Most stable configuration of OH and H₂O interacting with the Pt wire (left and right, respectively).
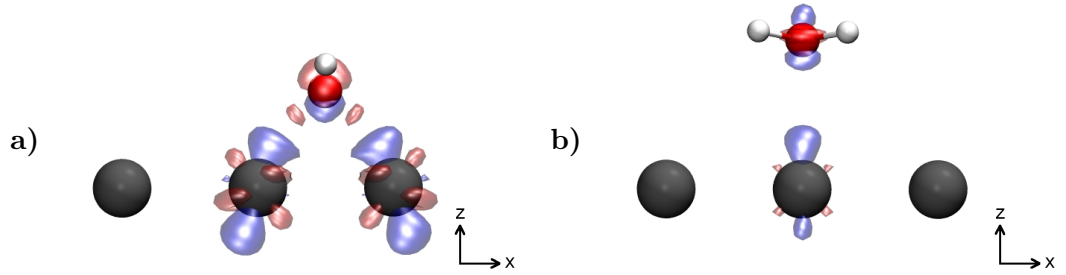
Figure 11.5: Charge density difference of OH and H₂O on the wire with respect to the isolated components. Blue represents electron depletion and red electron accumulation. A charge density of ± 0.08 e/Å^3 is shown in both cases.
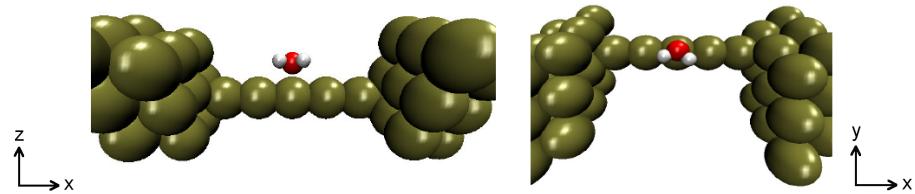
Figure 11.6: Configuration of H_2O adsorbed on Pt slab-wire.

$$E_{diss}^{\circ} \;=\; \frac{E_{H_2}}{2} + E_{OH} - E_{H_2O} \tag{11.3}$$

$$E_{diss}^{wire} \;=\; -E_{ads}^{H_2O} + E_{diss}^{\circ} + E_{ads}^{H} + E_{ads}^{OH} \tag{11.4}$$

The values of all the energetic terms given so far are summarized in table 11.2.

		$E_{ads}^{H_2O}$	E_{ads}^{H}	E_{ads}^{OH}	E_{diss}
Pt(111)[a]		-0.35	-0.47	-2.51	1.15
wire	Dacapo	-0.13	-0.59	-2.37	0.15
	VASP	-0.12	-0.61	-2.35	0.18

	E_{diss}°
Dacapo	2.98
VASP	3.02

Table 11.2: Adsorption energies (E_{ads}) of H$_2$O, H, and OH; and H$_2$O dissociation energy E_{diss} on Pt(111) and on a Pt atomic wire. The dissociation energy of water in vacuum is also given (E_{diss}°). The values are compared through DACAPO and VASP codes. a [83].

As it is evident from table 11.2, both plain-wave packages give almost the same values for the dissociation of a single water molecule on a platinum wire, on an average 0.17 eV. This is remarkably lower than on bulk Pt, where it requires an energy of about 1.15 eV. As we described in the introduction, a system closer in geometry to compare is the reconstructed Pt(110) surface. According to DFT calculations, water dissociation on such a surface takes 0.27 eV to occur [78], which is much closer to our result. Still, the latter case applies for an infinite chain of water molecules on the Pt wire-like surface atoms, not a single molecule. In our case the presence of more water may easily reduce the dissociation energy further and make the process exothermic.

11.4   Conclusions

A single water molecule adsorbs weakly on Pt nanowires. Accordingly, analysis through DOS and charge density difference does not show signs of true chemical bonds between H$_2$O and the wire. As expected, the barrier of diffusion is negligible (around 0.06 eV), so that an adsorbed molecule should diffuse rapidly.

In the experimental setting, nanowires are in contact with a bulk or a cluster structure, which may sufficiently influence the electronic properties of the wire so that a free-standing approximation may not be representative. However, we have found that in comparison with the free-standing wire, the adsorption energy of water on the slab-wire structure is 0.1 eV more stable, a negligible difference in favor of

the monostrand wire approximation, considering the great saving of computational effort.

In contrast to H$_2$O adsorption, the affinity of Pt wires for OH is strong; true chemical bonds are formed in their interaction. Its diffusion on Pt wires is much slower than that of water since the process has a barrier of around 0.3 eV.

Water dissociation on the wire is far more favorable than on Pt bulk, and comparable to Pt(110) reconstructed surfaces (0.17 eV, 1.15 eV, and 0.27 eV, correspondingly). Since water is also weakly adsorbed on Pt surfaces, the main reason for the lower dissociation energy on wires is the stronger adsorption of OH and H on Pt wires in comparison with the surfaces.

12

Conclusions on nanowires

For experimentalists, nanowires are fascinating systems that pushes the capacity of structure manipulation and measurements to the limit. For theoreticians, nanowires are fascinating because we can perform very accurate calculations and explain the experimental results or moreover, make predictions. However, in both fields there is a subjacent intriguing question that motivates the research, and that is more ingrained to human curiosity than to any economical or technological issue. *What happens when the metals become monodimensional? What happens when we reach the atomic limit?*

The most stable configuration for metallic atomic chains is the zigzag one. However, the wires are generally pulled by their bulk sides, adopting a linear arrangement under a typical stress of 1 Å/eV and a strain of at least 0.5 eV. A crucial parameter to examine, in order to predict their stability, is the surface energy σ. For the cases studied here, two groups were distinguished: Ag and Au nanowires, with lower σ, and Cu, Ni, Pd, and Pt nanowires, with a higher one. Accordingly, several experiments from different groups show that the former are intrinsically more stable than the latter. The mono-dimensionality of these systems can lead to striking behaviors,

such as the magnetization of Pd over a certain range of intermetallic distances. In some cases, the combination of metals forming atomic chains leads to stability enhancement. Noteworthy are Au-Cu and Au-Ag bimetallic wires, which were indeed obtained experimentally. We predict that Au-Pd, Ag-Cu, and Au-Ni could also be stable combinations.

The electronic charge distribution of monometallic wires is remarkably similar to that of metal surfaces. Nevertheless, a notable difference in the reactivity was found. The d band of Cu and Au, which lies well below the Fermi level for their surfaces, is shifted upward for nanowires, reaching the Fermi energy. This leads to a remarkable enhancement of the reactivity. Gold is a particular case, the adsorption of hydrogen on this wire is 1 eV more stable than on Au(111). Indeed, the adsorption of hydrogen on Cu and Au becomes exergonic. Using the Schmickler-Santos theory for the proton adsorption in water, we obtained an activation barrier of 0.5 and 0.1 eV, respectively, in comparison with 0.7 eV corresponding to their (111) surface metals. The activation energy required for dissociation of H_2 is 0.3 eV for Au nanowires, 1.5 eV for Ag, 0.5 eV for Cu, below 0.4 eV for Ni and Pt, and negligible for Pd nanowires. These results are in line with the hypothesis that hydrogen adsorption on nanowires triggers the fractional conductance observed experimentally on Cu and Au, but not on Ag.

The enhanced reactivity is also manifested in the great affinity for oxygen. In this case, oxygen adsorption on Pd, Pt, and Cu nanowires is at least 0.5 eV more stable than on Ag and Au chains. It was found that the incorporation or absorption of oxygen is more favorable than the isolated adsorption, which makes these wires bad catalyst for the oxygen reduction reaction. For oxygenated chains (where oxygen and metal atoms are intercalated), the zigzag configuration is generally the most stable one. Interestingly, in contrast to pure zigzag wires, the elongation of the oxygenated chains from the equilibrium distance is almost stress-free for over 1 Å. Also for oxygenated wires, a strong spin dependence of the intermetallic distance was found, even for non-magnetic wires such as Cu. There is experimental evidence of this phenomenon as well.

Water dissociation is an interesting case to examine since the molecule is not specifically adsorbed on the wire, so that the enhanced reactivity should have no major effect. Indeed, the adsorption energy of H_2O on platinum wires was found to be subtly exothermic: -0.1 eV. Still, the dissociation is more favorable than on Pt(111) since hydrogen and OH are more strongly adsorbed on the wire than on the surface. It was also found that the infinite linear chain is an efficient representation of more complex wires, such as atomic chains attached to cluster or bulk metals.

As promising as nanowires may seem for electrocatalysis, they are not suitable for the hydrogen evolution reaction in practical means, principally due to their instability as a chain. In the next part of this thesis we will investigate another type of wire, which is far more stable: graphite-supported wires.

Part III

Graphite-supported wires

13

Introduction

> To say that a man is made up of certain chemical elements is a satisfactory description only for those who intend to use him as a fertilizer.

Hermann Joseph Muller Nobel Prize in medicine 1946.

In section 7.2 we studied the chemical properties of one-atom-thick free-standing wires and predicted that they should be excellent catalysts for the hydrogen evolution reaction [45]. However, free-standing monowires cannot be used as catalysts in practical systems. In this chapter, we focus on a more realistic case, where these nanowires are supported on inert substrates. Promising systems are wires adsorbed at the step edge of highly oriented pyrolytic graphite (HOPG). Ni, Cu, Ag, and Au nanowires with a diameter of 60 to 750 nm and a length that exceed the 100 μm range can be obtained by *electrochemical step edge decoration* (ESED) [84]. The formation of nanowires by ESED occurs in two steps: First, nanoparticles are nucleated on step edges and terraces of HOPG, for which a so-called nucleation potential (E_{nucl}) is applied. Second, these nanoparticles are grown until they coalesce into electrochemically continuous nanowires, for which a so-called grow potential is applied (E_{grow}). For a given nucleation density along the step, the width of the nanowire can be increased by simply increasing the growth time, as exemplified in figure 13.1 with Cu nanowires.
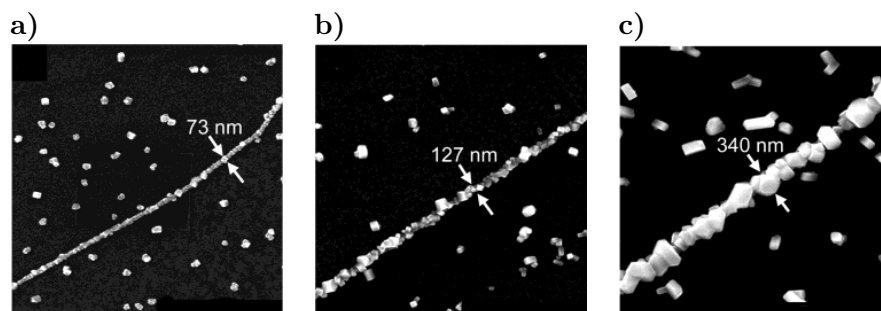
Figure 13.1: Scanning electron micrographs of Cu nanowires obtained by the direct deposition *electrochemical step edge decoration* technique (ESED). These nanowires were electrodeposited from a 2.0 mM $CuSO_45H_2O$ and 0.1 M Na_2SO_4 using E_{nucl}=-800 mV$_{SCE}$ and E_{grow}=-5 mV$_{SCE}$. The growth times in each experiment were: **a)** 120 s; **b)** 600 s; **c)** 2700 s [84].

An alternative technique is to first generate metal nucleation by *physical vapor deposition* (PVD). In this procedure, the metal is deposited by the condensation of the vaporized sample in a vacuum chamber. Ensembles of 2-15 nm diameter nanoparticles nucleated selectively at the linear step edge of HOPG can be synthesized by this procedure [85,85,86]. At this point, the deposition of more metal by PVD does not lead to the formation of continuous nanowires. Instead, these nanoparticles are used as nucleation templates for electrochemically controlled deposition. Nanowires in the diameter interval of at least 70-90 nm can be fabricated by this technique, as shown in figure 13.2.
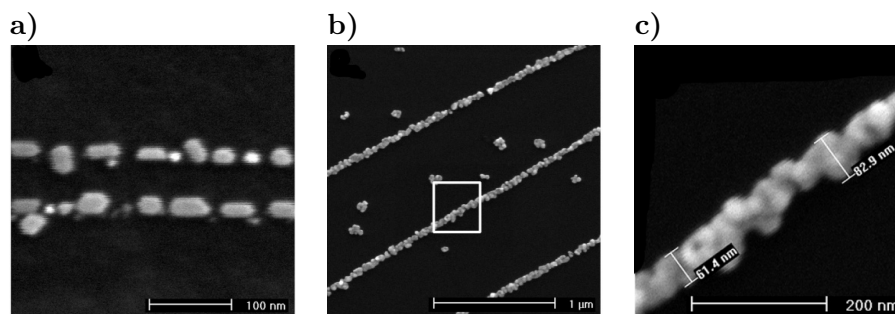
Figure 13.2: Scanning electron micrographs of Au nanostructures obtained by *physical vapor deposition* (PVD) and later electrodeposition. **a)** PVD of Au nanoparticles at 673 K. The particle diameter is in the interval of 2-15 nm; **b-c)** Au nanowire prepared by PVD of Au at 673 K and later electrodeposited at E=612 mV$_{SCE}$ for 15 s [85].

In contrast to free-standing nanowires, these systems are perfectly stable at room temperature and electrically continuous over lengths of 300 μm with a typical resis-

tance of 0.001 to 10^{-5} Ω.

To the best of our knowledge, despite of the vast experimental research in this field, there is no theoretical work closely related to it. To set the stage, in chapter 14 we start with a structural DFT study for nanowires attached to the two most stable step terminations of graphite: zigzag and armchair steps. The chemical interaction between these steps and several transition metals forming one-atom-thick wires is described in detail. In chapter 15, hydrogen adsorption on graphite-supported wires is addressed. A first attempt to predict the catalytic properties of such systems is made through thermodynamics. Do the distinct electronic properties of free-standing nanowires change when they attach to graphite steps?

14

Bare graphite-supported wires

Science fiction writers foresee the
inevitable, and although problems
and catastrophes may be inevitable,
solutions are not.

Isaac Asimov Writer.

14.1 Technicalities

Modeling

Depending on their orientation, graphite steps can expose different numbers of uncoordinated atoms per length. The lower this *uncoordination density* is, the more stable is the graphite step. The two most stable configurations are the so-called *armchair* and *zigzag* configurations, shown in figure 14.1. At the edge of these steps, Ni, Pd, Pt, Cu, Ag, and Au wires were adsorbed. The wire-bond distance imposed by the uncoordinated atoms in the zigzag arrangement is, in some cases, shorter than that of bare wires. Consequently, in these cases the atoms separate along the z axis. This rearrangement of the wire atoms is also seen in the armchair configuration, but the separation takes place *on* the same plane of the step.

Three systems were considered: bare wires, zigzag and armchair bare graphite steps, and zigzag and armchair graphite-supported wires.
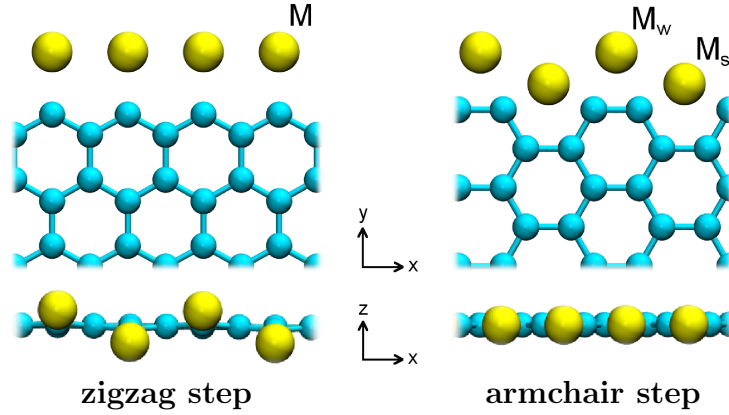
Figure 14.1: Top and side view of zigzag and armchair graphite-supported wire steps.
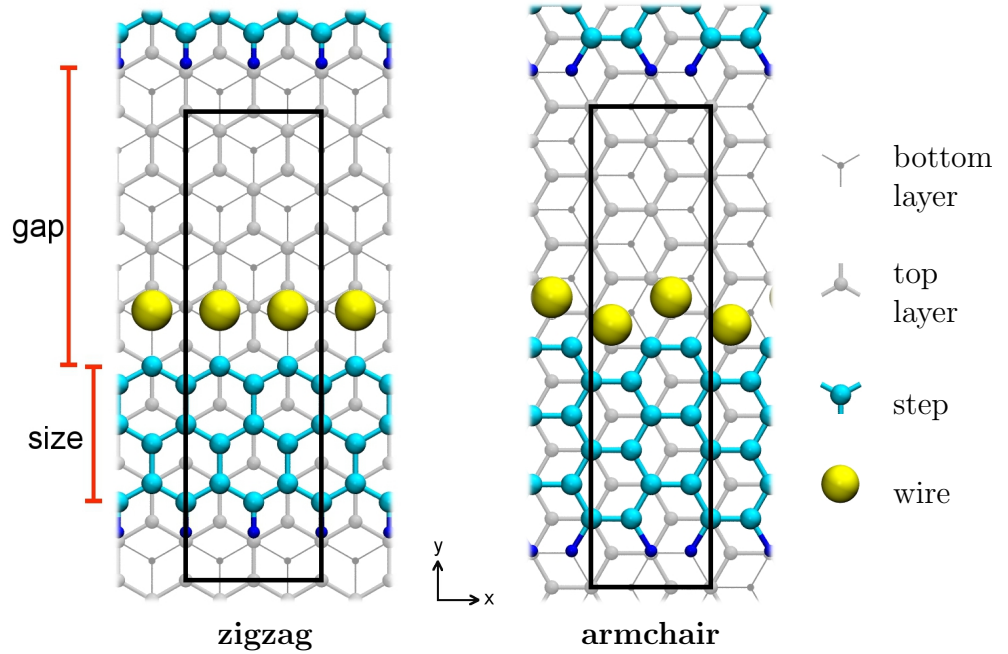
Figure 14.2: Top view of zigzag and armchair graphite-supported wires, the lateral unit cell is sketched with a black rectangle.

The latter are represented by two graphite layers, one graphite step and the metal wire, as shown in figure 14.2. The two layers act as supporting medium for the step at which the adsorption of the wires takes place. For this purpose, two layers are enough. Since DFT does not describe the *van der Waals* interaction correctly, the interlayer distance was fixed at its experimental value (3.35 Å [87]). The surface extends in the xy plane and the edges of the step along the x axis. One

side is closed with hydrogen atoms and the other with the metal wire. The unit cell width (L_x) contains two wire atoms. In the zigzag case this is imposed in order to allow the mentioned corrugation along the z axis. In order to choose the most convenient unit cell length (L_y), two factors had to be considered: the *size* of the step, and the *gap* (see figure 14.2). For the former, the number of carbon atoms was increased until the change in the binding energy was less than 25 meV, as shown in figure 14.3. Steps with six linear carbon atoms along the y axis satisfy the calculation accuracy. The step *gap* was set to be sufficiently large to avoid the interaction of the step images (10.65 Å for zigzag and 7.37 Å for armchair supported wires). The vacuum between surfaces (along the z axis) corresponds to a distance of three graphite interplanes. The final cell dimensions are (4.92×17.04×14.70) Å for zigzag and (4.26×16.82×14.70) Å for armchair supported wires.
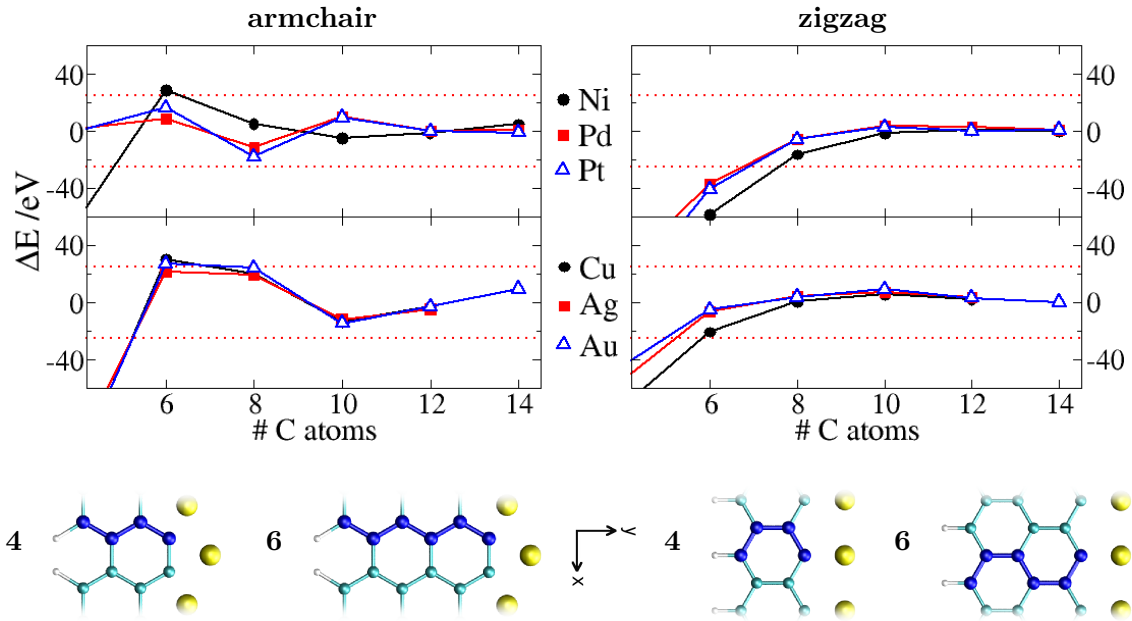
Figure 14.3: Change in the binding energy with respect to the length of the step along the y axis for graphite-supported wires. Values of ±25 meV are captured within red dotted lines.

The bare graphite substrates are just like the corresponding graphite supported-wires but without the wire. Bare wires are infinite free standing one-atom thick wires as described on page 19. The two bottom layers of supported wires and the graphite support were kept fixed, the graphite step was fixed only along the z axis and the rest was fully relaxed.

First-principle calculations

The plane wave cutoff (*pwco*) and the Monkhorst-Pack kpts grid were optimized for each metal and configuration of the graphite-supported wires. The increase by 1 k-point, or by 50 eV in the energy cutoff, led to a negligible change in energy of 5 meV. The parameters computed are summarized in table 14.1.

	config.	Cu	Ag	Au	Ni	Pd	Pt
pwco [eV]	both	450	450	500	450	850	500
dco [eV]	both	500	500	550	500	900	550
kpts	armchair	(16×1×1)					
	zigzag	(24×1×1)					

Table 14.1: Plain wave cutoff (*pwco*), density cutoff (*dco*) and Monkhorst-Pack kpts grids (*kpts*) for zigzag and armchair graphite-supported wires.

As described on page 18, Ni and Pd bare nanowires are spin polarized with a magnetic moment of 1.15 and 0.54 Bohr magnetons (μB) per atom, respectively. However, the spin polarization is lost for both configurations of Pd graphite-supported wires and for Ni W. For zigzag supported wires, Ni shows a magnetic moment of 0.30 μB and the system is only 0.01 eV lower in energy than the non-magnetic one. The rest of the systems studied does not show magnetic behavior.

Relaxation

Relevant bond distances and angles in the supported wires are shown in table 14.2. From this table we can observe:
• The graphite-wire bond distance (d_{GM}) at zigzag and armchair supported wires is larger for Ag and Au, suggesting that the corresponding step-wire bond is weaker for these metals.
• Due to the graphite lattice, the shortest possible metal-metal distance (d_{MM}) for zigzag supported wires is 2.46 Å, which corresponds to a non-corrugated wire. Consequently, if the intermetallic distance of a bare wire is smaller than 2.46 Å (Ni and Cu BW), the corresponding supported wires will not have corrugation; otherwise, the bigger d_{MM} of a bare wires, the more acute will θ be in the corresponding zigzag supported wire.
• For Ni and Cu armchair wires, the weakly adsorbed metal (M_w) is at a smaller distance from the step (d_{GMw}) than for the other metals in table 14.2. In the latter cases M_w is quite far from the step to establish relevant interactions with graphite.
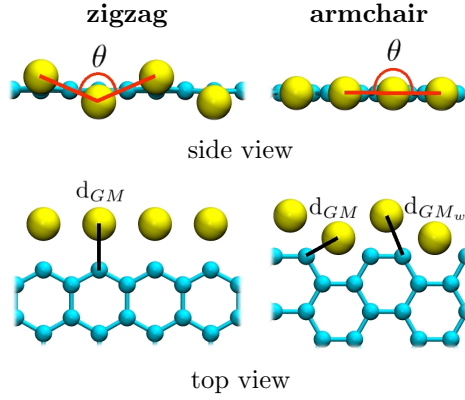
	Ni	Pd	Pt	Cu	Ag	Au
d_{GM}(zz) [Å]	1.80	1.97	1.94	1.92	2.14	2.08
d_{GM}(ac) [Å]	1.93	2.06	2.07	1.96	2.13	2.10
d_{GMw}(ac) [Å]	2.03	3.05	3.05	2.30	3.38	3.29
d_{MM}(wire) [Å]	2.13	2.50	2.39	2.32	2.64	2.61
d_{MM}(zz) [Å]	2.46	2.58	2.54	2.46	2.69	2.67
d_{MM}(ac) [Å]	2.21	2.59	2.58	2.29	2.73	2.71
θ(zz) [^{o}]	180	145	151	180	132	134

Table 14.2: Relevant distances and angles in zigzag (zz) and armchair (ac) graphite-supported wires. The intermetallic distance is compared with that of the free-standing wires (wire). For all the armchair wires studied $\theta=180^o$.

14.2 The graphite-wire bond

The graphite-wire binding energy (E_{bin}) is calculated using the energy of the bare graphite step and the bare wire as reference:

$$E_{bin} = (E_{GSW} - E_{step} - E_{wire})/N \tag{14.1}$$

where N is the number of wire atoms. The binding energy of the nonequivalent metal atoms of the armchair supported wires is distinguished by

$$E_{bin}^{M_s} = E_{BG+M_s} - E_{BG} - E_{BW} \tag{14.2}$$
$$E_{bin}^{M_w} = E_{BG+M_s+M_w} - E_{BG+M_s} - E_{BW}$$
$$E_{bin}^{M_w} = E_{GSW} - E_{BG+M_s} - E_{BW} \tag{14.3}$$
$$\tag{14.4}$$
$$\Delta E = E_{H.wire} - E_{H/.graphite} \tag{14.5}$$

where $E_{bin}^{M_s}$ represents the adsorption energy of M_s without M_w, and $E_{bin}^{M_w}$ is the adsorption energy of M_w with M_s already adsorbed. The results are shown in table 14.3.

Two clear tendencies are observed from table 14.3, the first one is that zigzag are energetically more favored than the armchair supported wires, Au being the only exception, where the energy difference between these structures is smaller than 0.1 eV. Secondly, for zigzag, armchair, and M_s supported wires, the binding energy follows the order Ni≈Pd≈Pt<Cu≈Ag≈Au. These findings are explained by the

supported wires	Ni	Pd	Pt	Cu	Ag	Au
zigzag	-3.00	-3.29	-3.53	-2.27	-1.72	-1.91
armchair	-2.21	-2.28	-2.30	-1.71	-1.41	-1.98
M_s	-3.30	-3.55	-3.81	-2.77	-2.11	-2.33
M_w	-0.93	-0.52	-0.78	-0.63	-0.69	-1.43

Table 14.3: Graphite-wire binding energy E_{bin} in eV. The binding energy of the strongly and weakly adsorbed wire atom (M_s and M_w, respectively) is also shown.

chemical characteristics of the bonds: Two states are particularly involved in the graphite-wire bond, one is the sp_y^2 of the uncoordinated carbon (C_{edge}), and the other one is a d state of the metal ($d_{x^2y^2}$ for zigzag and d_{xy} for armchair supported wires). The combination of both results in bonding and antibonding states shown in figure 14.4.
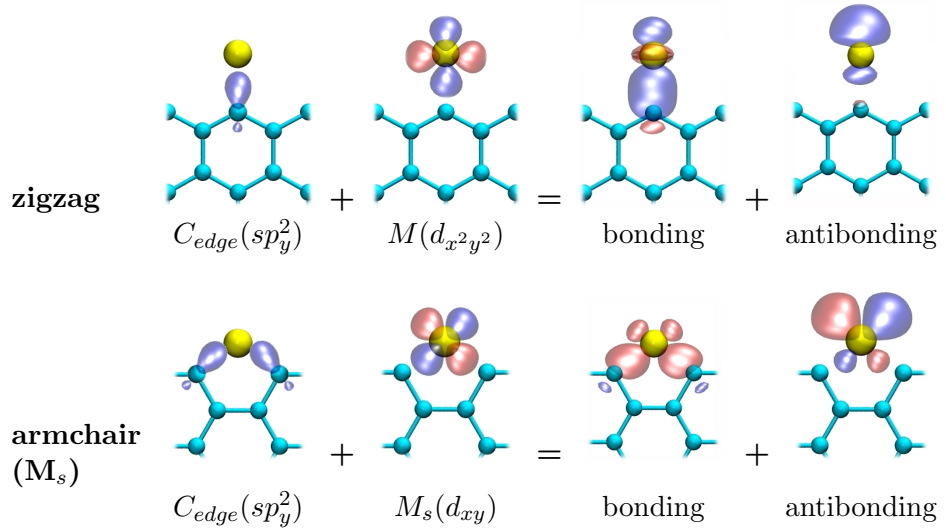
Figure 14.4: Atomic orbital combination of the graphite-wire bond. For the bonding states, the higher probability of finding the electron density is in between C_{edge} and the metal; in the antibonding case, this region is separated by a node.

As an example, the DOS projected on to Au and C_{edge} atoms for the isolated steps, isolated wires and their combination are shown in figure 14.5.

As we can see in the latter figure, there is a strong resonance between the states of the step and the wire. Besides, in their isolated form, wire and graphite-step states are very different. Both observations suggest a strong hybridization of the
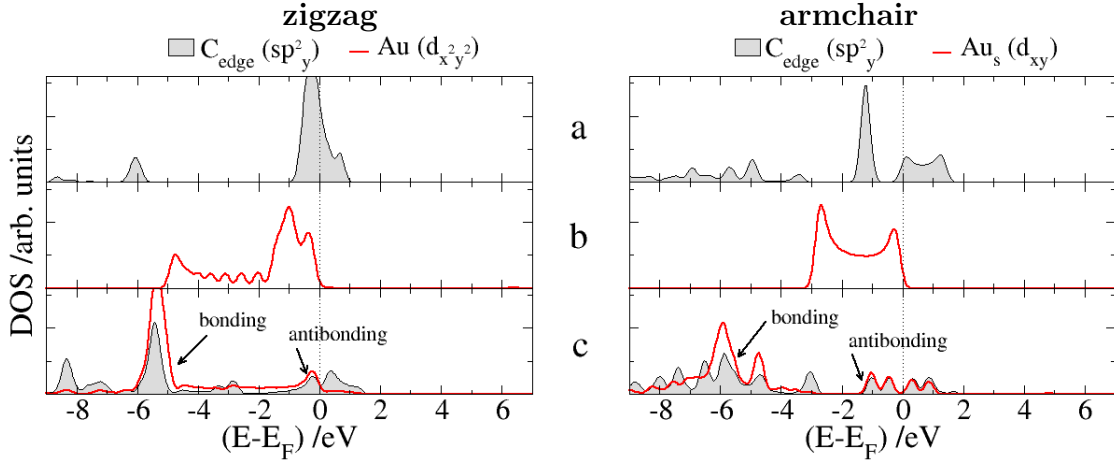
Figure 14.5: Density of states (DOS) projected on to the step edge atoms and the gold atoms for zigzag and armchair (Au_s) supported wires. **a)** sp^2 of the uncoordinated atoms of the isolated graphite step (C_{edge}). **b)** d state of the isolated wire. **c)** sp^2 of the C_{edge} atoms and d state of Au for the supported wires.

states involved in the graphite-wire bond. The antibonding states that result from this interaction are both partially filled in the case of Au. The positions of the antibonding states for all the supported wires studied here are highlighted with arrows in figure 14.6.

It is clear that the antibonding state of Ni, Pd, and Pt zigzag supported wires are empty, which explains their large negative binding energies. In contrast, the antibonding states of Cu, Ag, and Au zigzag supported wires are filled, consequently, their binding energies are higher. The explanation for the differing E_{bin} of armchair supported wires is similar, but here we have to distinguish the strongly from the weakly adsorbed metal wire. The DOS of the armchair supported wires shown in figure 14.6 corresponds to the strongly adsorbed atom, M_s. The position of the antibonding states is similar to that of the zigzag wires, with the difference that for Ni, Pd, and Pt, the antibonding states are *almost* empty. This should make the binding energy of M_s higher than the binding energy of the zigzag supported wires, however, M_s is bonded to two carbon atoms at the edge of the step, while in the zigzag case, each atom is bonded to one only. Still, the binding energies of M_s follows the order Ni≈Pd≈Pt<Cu≈Ag≈Au, like in the zigzag case because Cu, Ag, and Au have the antibonding states *half-filled*. By the reasons given so far, E_{bin} should be stronger for armchair supported wires, however the adsorption of M_w makes the wire adsorption as a whole weaker. The substantially higher binding energy of M_w in comparison with M_s (table 14.3), is due to its weak interaction with the step edge. It is striking that in this case, Au_w adsorbs more strongly than the other M_w atoms studied.
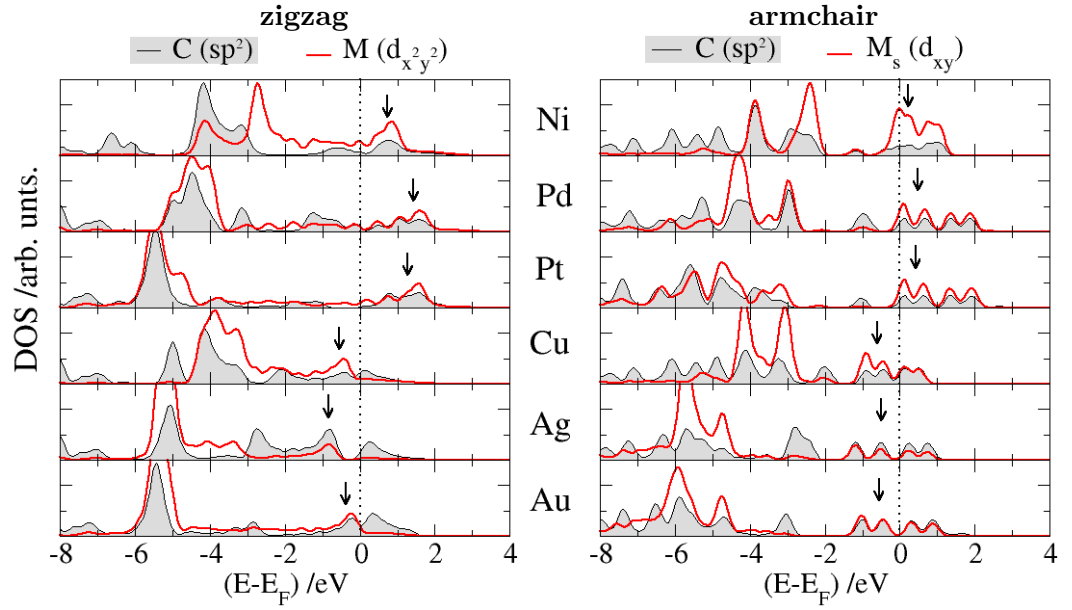
Figure 14.6: DOS projected on to the atomic orbitals shown in figure 14.4. The positions of the antibonding states are highlighted with arrows.
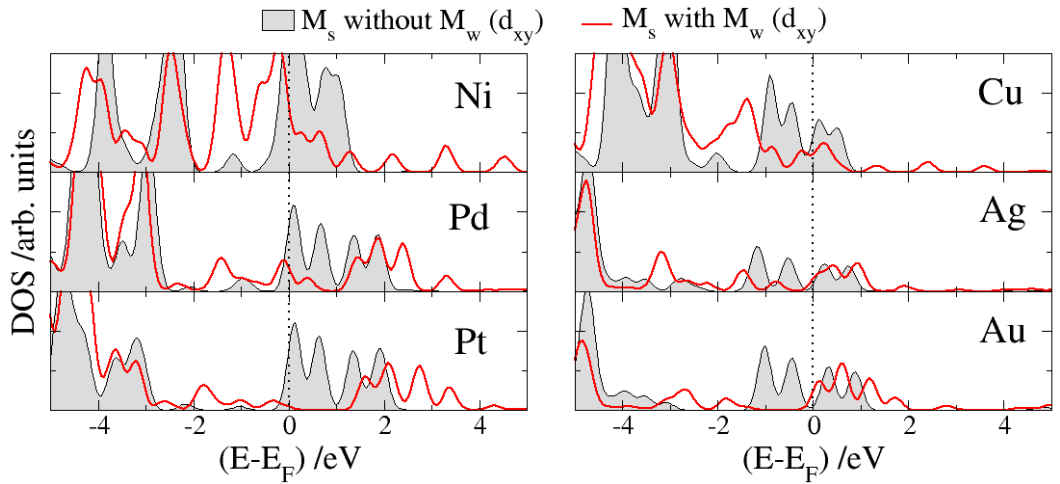
Figure 14.7: Density of the d_{xy} state projected on the strongly adsorbed metal wire (M_s) with and without the weakly adsorbed metal (M_w). Note up-shifting when the adsorption of M_w occurs.

As it is shown in figure 14.7, the DOS projected on Au_s with and without Au_w, reveals that when the latter adsorbs, the antibonding of the former is shifted up. This phenomenon strengthens the wire-step bond in the case of gold, and platinum, but it seems to be less important for the rest of the metal atoms studied.

Another way to compare the bond strength is by looking at the charge density difference distribution. In this case we compare the charge density of supported wires with respect to the charge density of the isolated graphite support and the isolated wire:

$$\Delta\rho = \rho_{GSW} - (\rho_{BG} + \rho_{BW}) \tag{14.6}$$

Figure 14.8a shows the charge density difference of a plane that intersects the step surface and the wire at the armchair supported wires. By comparing the region between the C_{edge} and M_s, it is clear that the electron density in this region is smaller for Au and larger for Pt and Pd, in agreement with the corresponding binding energies. The electron depletion around the atoms and electron accumulation between them is typical of covalent bonds. Carbon is more electronegative than the metal studied, a fact that is reflected in the significant charge transfer from the metals to the step. This charge donation is larger than expected, particularly for Au, whose electronegativity is similar to that of carbon. This is due to the fact that there are actually *two* carbon atoms bonded to M_s. The charge redistribution around M_w for Au, Pt, and Pd is due to the presence of the metal neighbor M_s. Nickel is the only case in which there is a significant charge transfer from M_w towards the step. The charge redistribution deforms the red contours between the carbon atom and M_s, and makes them point also towards M_w. This confirms our assumption concerning the M_w isolation for Au, Pt, and Pd (suggested by their larger distance to the step d_{GM_w} in table 14.2). Note the resemblance of the blue lobes to the d_{xy} orbitals.

The charge density difference of zigzag supported wires is shown in figure 14.8b. In this case, ρ was calculated for a plane that cuts the step surface perpendicularly and intersects a metal atom. Gold shows again the smaller charge accumulation between the step edge and the metal. The charge distribution also indicates the formation of a covalent bond. Since now only *one* carbon atom is bonded to the metal, the accumulation of charge in the bond region follows the prediction made by comparing the corresponding electronegativities.

14.3   Conclusions

The binding energy of Ni, Pd, Pt, Cu, Ag, and Au one-atom-thick wires at the edge of *armchair* and *zigzag* graphite steps was calculated. Two different types of nanowires were obtained, the so-called armchair and zigzag graphite-supported wires. The major difference between them is that in the zigzag case all the metal atoms are equivalent, whereas in the armchair case one type of metal atom is strongly bonded to two carbon atoms (M_s), and the other type is weakly bonded to the graphite step or not bonded to it at all (M_w). In general, zigzag supported wires are substantially

atom	X	Φ [eV]
C	2.55	5.0
Ni	1.91	5.07
Pd	2.20	5.43
Pt	2.28	6.17
Cu	1.90	5.24
Ag	1.93	5.12
Au	2.54	6.43
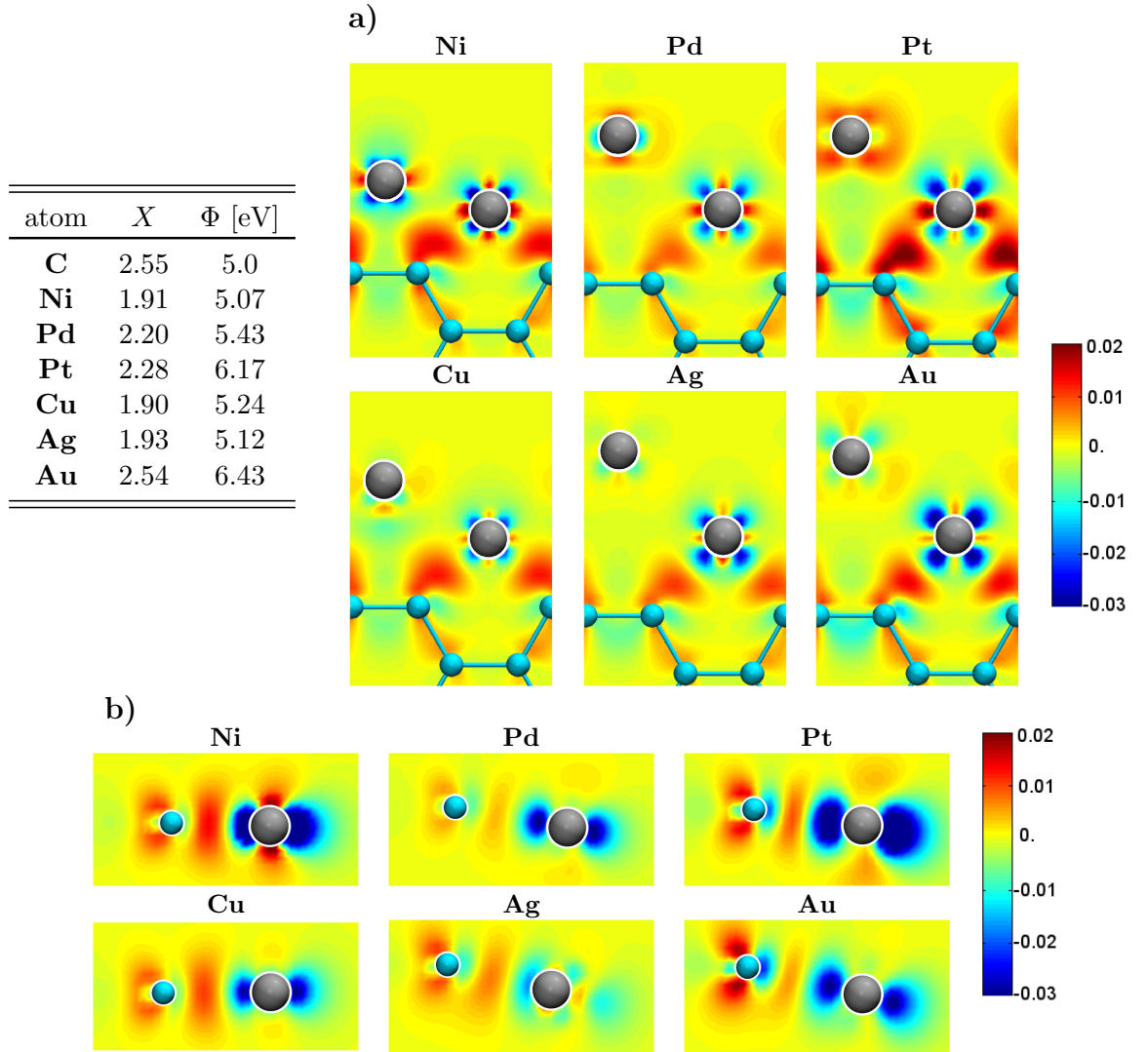
Figure 14.8: Charge density difference (ρ) in e/Å^3 for supported wires. Red represents electron accumulation and blue electron depletion. The Pauling electronegativity scale of the atoms involved is also shown. **a)** Top view of armchair supported wires. **b)** Side view of zigzag supported wires.

more stable than armchair ones, only in the case of Au both configurations are equivalent in energy. Another general trend is that the supported wires of the Ni periodic column are more stable than the supported wires of the Cu periodic column. The occupation of the antibonding states that result from the wire-step interaction, is lower for the Ni periodic column than for the Cu one, which explains their different binding energies. In fact, Ni, Pd, and Pt zigzag supported wires have this antibonding state empty. For armchair supported wires the former state is partially or half-filled,

the reason why the zigzag configuration is more stable than the armchair one.

15

Atomic hydrogen adsorption on graphite-supported wires

15.1 Technicalities

Modeling

Hydrogen was adsorbed on several position sites of zigzag and armchair supported wires. First, the isolated bond between hydrogen and the supported wire was studied. The unit cell (page 118) was systematically replicated in the x dimension (along the wire axis), containing always a single adsorbed hydrogen, until the change in the hydrogen adsorption energy was less than 20 meV. With three replications along the x axis the convergence was achieved, this corresponds to a cell of six wire atoms for zigzag and armchair supported wires. For a hydrogen coverage of $\theta=1$, a single supported wire unit cell was used where two hydrogen atoms were adsorbed. At low

and high hydrogen coverages, the two bottom layers were kept fixed, the step was fixed only along the z axis, and the rest was fully relaxed.

First-principle parameters

The k-points and the plain-wave energy cutoff were taken from the parametrization of the graphite-supported wires (see page 120).

15.2   High hydrogen coverage

Before turning to the description of the hydrogen-wire bond on supported wires, it is instructive to test whether hydrogen adsorption at the step can desorb the wire at a high coverage. The adsorption energies corresponding to the adsorption on the metals of supported wires (E_{ads}^{wire}), and directly at the graphite step (E_{ads}^{step}), are calculated according to

$$E_{ads}^{wire} \quad = \quad \frac{E_{GSWH} - (E_{GSW} + E_{H_2})}{2} \tag{15.1}$$

$$E_{ads}^{step} \quad = \quad \frac{E_{BGH} + E_{wire} - (E_{GSW} + E_{H_2})}{2} \tag{15.2}$$

The energy is divided by a factor of two in order to account for the two hydrogen atoms adsorbed per unit cell. Results are summarized in table 15.1.

The adsorption of hydrogen for Ni, Pd, and Pt zigzag and armchair supported wires is favored on the wire. On the other hand, for the three coin metals, hydrogen adsorption is preferred on the graphite step, indicating that in this case wire desorption is thermodynamically favored. In the light of these findings, we shall focus on the Ni periodic column and Cu, since in the latter case hydrogen does not have a clear energetic preference for the step or the wire. Another tendency observed in table 15.1 is that hydrogen-wire adsorption on armchair supported wires is more stable than on the zigzag ones. This is in line with the fact that the former are more reactive, as we explained in section 14.2.

15.3   Low hydrogen coverage

Since the symmetry of the bare monostrand nanowires is broken at the graphite-supported wires, there are several non-equivalent adsorption sites for hydrogen.

At low coverage, the hydrogen-wire adsorption energy is given by

$$E_{ads} = E_{GSWH} - (E_{GSW} + \frac{E_{H_2}}{2}) \tag{15.3}$$

	zigzag		armchair	
	H-wire	H-step	H-wire	H-step
Ni	-0.22	-0.04	-1.02	-0.27
Pd	-0.06	0.25	-0.49	-0.23
Pt	-0.29	0.48	-0.78	-0.22
Cu	-0.18	-0.78	-0.73	-0.78
Ag	0.00	-1.32	-0.06	-1.08
Au	-0.26	-1.13	-0.15	-0.49

Table 15.1: Top view of hydrogen adsorption at a coverage of $\theta=1$ on the supported wires (H-wire) and directly on the graphite step (H-step), in which case the wire has been desorbed completely and is not interacting with the graphite support. The corresponding adsorption energies are given below. Cases in which the adsorption is favored on the wire are highlighted in red.
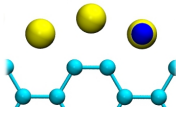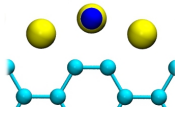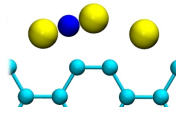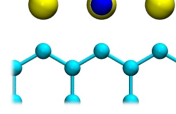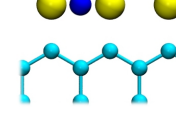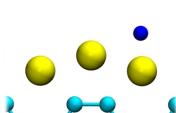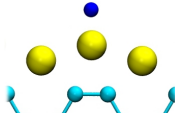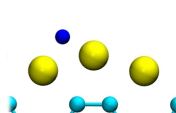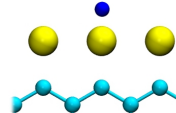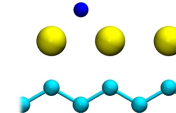
The results for the more relevant configurations computed are presented in table 15.2. Two tendencies are observed. First, there is no common preferable adsorption site, in some cases the bridge position is favored, in others is the top site. Secondly, E_{ads} is rather sensitive to the site at which adsorption takes place, the values change over a range of 1 eV depending on the configuration. Both findings point to the fact that the bonds at the supported wires, in comparison with the free-standing wire, are more localized.

Consistently with the results for a high hydrogen coverage, the adsorption is in general more stable on armchair than on the zigzag supported wires, as we shall explain in the next section.

15.4   The hydrogen-wire bond

The density of states projected on the orbitals involved in the adsorption of hydrogen on armchair supported wires are shown in figure 15.1 and compared with that in the absence of hydrogen.

In agreement with the suggestion that the bond of hydrogen with the graphite-

| | armchair | | | zigzag | |
	top_s	top_w	brg	top	brg
z					
Ni	0.11	0.05	-0.29	0.21	-0.43
Pd	0.12	-0.39	-0.55	1.03	0.24
Pt	-0.48	-1.18	-1.01	0.60	0.22
Cu	1.33	0.47	0.28	1.14	0.62
xy					
Ni	-0.73	-0.67	-1.19	0.08	-0.36
Pd	-0.23	-0.08	0.43	0.93	0.61
Pt	-0.41	-1.17	-0.54	0.17	0.28
Cu	-1.00	-0.89	-0.77	-0.57	-0.85

Table 15.2: Hydrogen adsorption energies in eV for high symmetry sites of supported wires. For armchair supported wires there are two possible top sites: on the strongly adsorbed metal (top_s) and on the weakly adsorbed one (top_w). In each case, hydrogen can be adsorbed *at* the step plane (xy), or *above* the step plane (z). The most stable configurations for zigzag and armchair supported wires are highlighted in red.

supported wires are localized (deduced from table 15.2), the DOS of hydrogen are narrow and sharp, indicating poor delocalization of states. Only in the case of Ni there seems to be a relevant resonance between the hydrogen s state and the metal states. It is also observed in figure 15.1 that the s states of the metal play an important role in the hydrogen-wire bond.

Since hydrogen adsorption becomes localized at the supported wires, it is natural to wonder whether the d band model can still be applied for such systems. The center of the d band of the metals for slabs, free-standing wires, and supported wires is shown in figure 15.2.

Pd and Pt seem to follow the d band model satisfactorily well, while some deviations are observed for Ni. Of the three coin metals, Cu is the one that exhibits a deviation, while Ag and Au are qualitatively well described by the d band model.
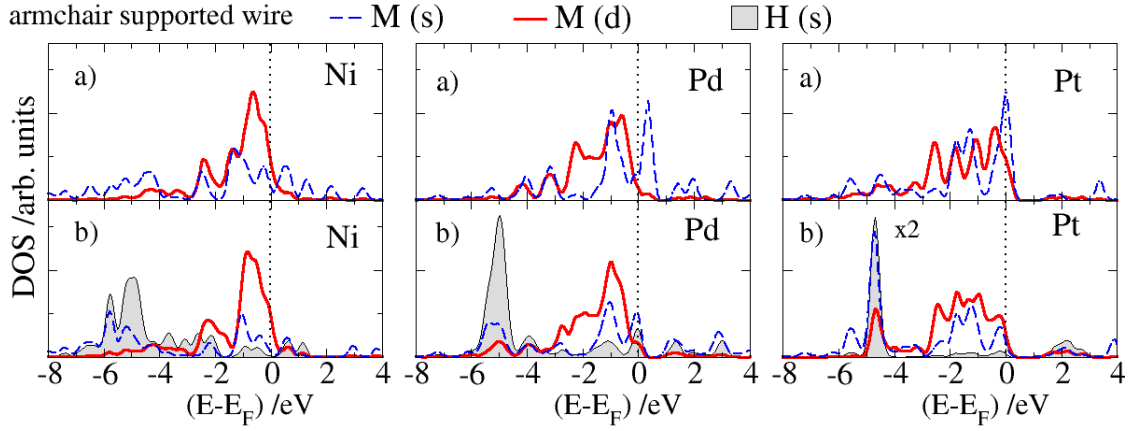
Figure 15.1: Density of states projected on the orbitals involved in the hydrogen-wire bond for armchair graphite-supported wires (W). **a)** Armchair supported wires without hydrogen adsorbed on the wire. **b)** Armchair supported wires with hydrogen adsorbed on the wire at the equilibrium state. The DOS of H $1s$ on Pt armchair supported wires has been compressed by a factor of two in order to fit into the panel.
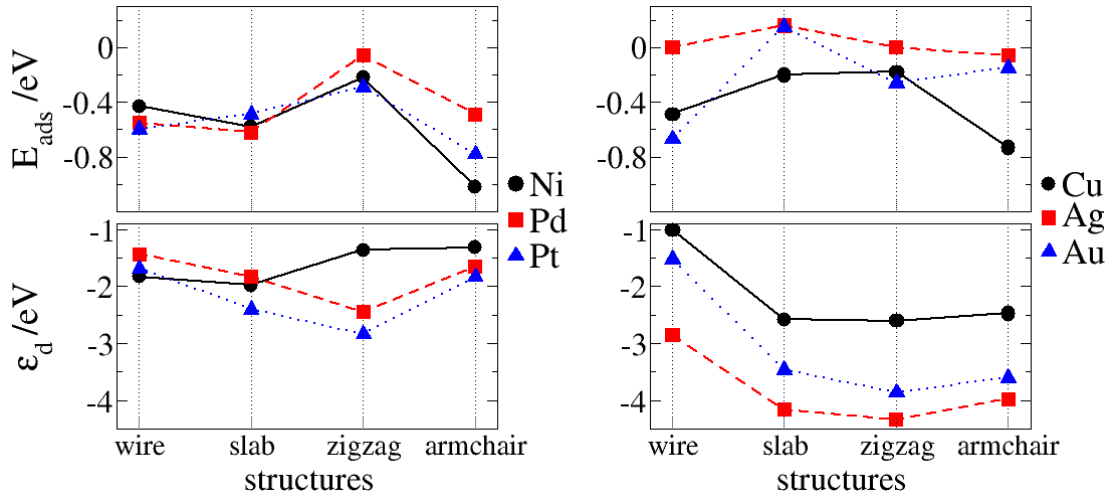
Figure 15.2: Hydrogen adsorption energy (E_{ads}) and position of the d band center (ε_d) at a coverage of $\theta=1$ for free-standing nanowires, fcc(111) surfaces (slab), zigzag, and armchair supported wires. In the ideal case of the d band model, top and bottom panels would be specular images.

The deviation appears only for the armchair wires, in this case hydrogen adsorbs more strongly on Ni and Cu than predicted by the model. This may come from the fact that the valence s state of the metal has also an important overlap with the hydrogen $1s$ state, which in the case of Ni and Cu is more effective due to their

small size (lower Pauli repulsion). With the latter exception, the d band center is higher for the armchair than for the zigzag supported wires, which explains the larger hydrogen affinity of the former.

15.5   Conclusions

As a consequence of their instability, at high hydrogen coverages the three coin metals desorb from the graphite step. Only in the case of Cu this trend is not observed and an equilibrium between hydrogen on the Cu supported wires and at the graphite step can exist. On the other hand, hydrogen adsorption on the metals is favored for Ni, Pd, and Pt supported wires.

At low coverage, the hydrogen adsorption energy is quite site dependent, changing over a range of 1 eV. These results and analysis of the density of states suggest that the projected $1s$ state of hydrogen is more localized on supported wires than on the free-standing wires. The d band model predicts the chemisorption strength of supported wires qualitatively well. Since the d band center is more up-shifted for the armchair supported wires than for the zigzag ones, hydrogen adsorption is stronger on the former case. On Ni and Cu armchair supported wires hydrogen adsorption is stronger than what the d band model predicts, probably due to the strong participation of the valence s states of the metals.

Part IV

Metal surface tuning

16

Rh overlayers on Au and Pd (111) surfaces

> The challenge is not in seeing new places but in having new eyes.

Marcel Proust Writer.

16.1 Introduction

In the search for good and cheap electrocatalysts, much attention has recently been focused on overlayers of metals on a foreign metal substrate. Pseudomorphic overlayers are strained when their lattice constants differ from that of the substrate; the resulting changes in the d band structure can significantly modify the catalytic properties of the layer. In addition, there can be a strong chemical or ligand effect of the substrate on the adsorbate [88]. This combination can result in good catalytic activity, and is also an excellent field to study the relation between the structure and reactivity of metals [89–92].

In electrochemistry palladium monolayers on various substrates have been particularly popular, ever since Pd/Au(111) has shown to be a good catalyst for hydrogen evolution [91–94]. Here we shall investigate theoretically layers of rhodium on Au(111) and Pd(111), and show that they promise to be even better catalysts for this reaction. The formation of these layers has been well investigated experimentally, but so far there have been no kinetic studies. Thus, we make a prediction for

their catalytic properties.

Rhodium on Au(111) grows epitaxially until the second overlayer, afterwards it undergoes cluster growth [95]. In contrast, rhodium deposition on Pd(111) is epitaxial until more than five Rh overlayers have been formed [96–99]. Hydrogen interaction with pure rhodium surfaces has been the topic of several experimental investigations conducted in ultrahigh vacuum. Its adsorption has been studied by high resolution electron energy loss spectra [100], and its diffusion with laser-induced thermal desorption [101]. Hydrogen chemisorption on pure Rh has also been studied theoretically [102], but to our knowledge, not on rhodium overlayers.

In the present work we first examine the stability of Rh/Au(111) and Rh/Pd(111) layers by density-functional theory (DFT). Next, we shall study hydrogen adsorption, which plays an important role in hydrogen evolution, on various sites. Most studies of hydrogen adsorption consider only the most stable species. However, on transition metal surfaces this species is often only a spectator, while the reaction proceeds via more weakly adsorbed atoms. Therefore, we shall distinguish between strongly adsorbed H_s and weakly adsorbed H_w hydrogen. Since the former often adsorbs at potentials above the equilibrium potential for hydrogen evolution, it is sometimes denoted as hydrogen adsorbed at underpotentials H_{upd} [103], while the other form, H_{opd}, is said to form at overpotentials. However, we prefer not to use this terminology, which is incomprehensible to non-electrochemists. Finally, we shall investigate the kinetics of hydrogen evolution on these surfaces, using a theory developed in our group [3,5]. The computational details are given in the appendix.

16.2   Technicalities

Modeling

The lattice constants (a_0) of the surfaces were taken from the calculated equilibrium distances of a periodic fcc bulk: 3.83 Å for Rh, 3.99 Å for Pd and 4.18 Å for Au, which are in agreement with the experimental values [12] (3.80 Å, 3.88 and 4.07, Å respectively). In order to decide the thickness of the monometallic slabs, the surface energy was calculated for several slabs of N layers by $\sigma = (E_{Slab(N)} - NE_{bulk})/2$, where $E_{Slab(N)}$ is the energy of an N-layer slab, and E_{bulk} is the energy per atom of the bulk. The energy criterion of convergence was 0.02 eV which is reached with a slab of four layers (table 16.1).

Only the top two layers of the pure slabs were allowed to relax and the bottom two were kept fixed in their corresponding bulk positions. Additional calculations with an expanded a_0 of pure Rh corresponding to Au ($Rh@Au$) and to Pd ($Rh@Pd$) were calculated in order to study the effect of this expansion separately from the electronic effect induced by the substrates (Au or Pd). For Rh/Au and Rh/Pd slabs

	Pd	**Rh**	**Au**
N	σ/eV	σ/eV	σ/eV
3	0.572	0.812	0.348
4	**0.559**	**0.824**	**0.350**
5	0.558	0.818	0.352
6	0.567	0.817	0.354
7	0.554	0.815	0.351

Table 16.1: Surface energy (σ) with respect to the number of layers for Pd, Rh, and Au slabs.

	Pd	**Au**	**Rh**
a_0 (Å)	3.99	4.18	3.83
Rh expansion	4.8%	9.1%	0 %

the structure was modeled by a four-layer slab of the substrate, on which up to five layers of Rh were deposited. The bottom two layers were kept fixed and the rest were fully relaxed. The same applies for the systems with hydrogen adsorbed at high symmetry sites. Five layers of vacuum were used in all systems. The spin consideration was ruled out since none of the slabs presented spin polarization.

H_2 **dissociation**: For all the types of surfaces over which H_2 dissociation was computed, the molecule was allowed to relax laterally on a plane parallel and at different distances to the surface. The first two bottom layers were fixed and the rest was fully relaxed, independent of the presence of adsorbed hydrogen atoms.

The hydrogen molecule configurations are distinguished by three letters which indicate the position of the first hydrogen atom, the center of mass of the molecule, and the position of the second hydrogen atom, respectively; all with respect to the surface high symmetry sites: hcp-top-fcc (h-t-f), bridge-top-bridge (b-t-b), hcp-bridge-fcc (h-b-f) and top-bridge-top (t-b-t). The f-t-h path on clean surfaces is illustrated in figure 16.9.

First-principle calculations

Special care was taken for the parametrization of the energy cutoff and the k-points sampling of the Brillouin zone based on the Monkhorst-Pack grid [11]. Both parameters were increased systematically until the change in the absolute energy was less than 10 meV. 450 eV energy cutoff and a grid of 8×8×1 is enough to satisfy

the energy accuracy. For the relaxations computed, the convergence criterion was achieved when the total forces were less than 0.01 eV/Å. Spin considerations were included for some representative systems but no magnetic moment was obtained, so it was ruled out from the calculations.

16.3   Stability of Rh/Au(111) and Rh/Pd(111) overlayers

When a monolayer of one metal is deposited epitaxially on another metal substrate with a different lattice constant, a strained overlayer results. Such overlayers can be stable if the inter-metal bonds are stronger than those of the pure metals, and in some cases even epitaxial multilayers can be formed. In order to investigate the stability of rhodium layers on Pd(111) and Au(111) the total and the differential binding energies (E_{bin} and dE_{bin} respectively) have been calculated:

$$
\begin{aligned}
E_{bin} &= E_{Rh(N)/Sub} - NE_{Rh(bulk)} - E_{Sub} & (16.1) \\
dE_{bin} &= E_{Rh(N)/Sub} - E_{Rh(bulk)} - E_{Rh(N-1)/Sub} & (16.2)
\end{aligned}
$$

where $E_{Rh(N)/Sub}$ is the energy of N layers of Rh on the substrate, $E_{Rh(bulk)}$ is the energy of the Rh bulk per atom (with its own lattice constant), and E_{Sub} is the energy of a pure substrate slab. In the thermodynamic limit, the condition $E_{bin} < 0$ corresponds to the familiar condition $\gamma_s > \gamma_a + \gamma_i$ [1] for layer by layer growth, that the surface energy γ_s of the substrate should be larger than the sum of the surface energy γ_a of the adsorbate and the interfacial energy γ_i between the two metals. The surface energy of Rh(111) (2.47 Jm^{-2}) is large compared to that of Au(111) (1.28 Jm^{-2} [?]), and the lattice constant of Rh is expanded by 8% over Au, so we expect E_{bin} to be positive, and this is indeed the case – see Fig. 16.1.

This is in line with the experimental observation, that in the vacuum Rh on Au(111) shows Volmer-Weber cluster growth [104]. In contrast, in an aqueous electrolyte the first two layers of Rh on Au(111) grow epitaxially and are stable [95]. Obviously, the Rh layers are stabilized by the electrolyte. Water adsorption is particularly strong on Rh(111): -0.42 eV per water molecule, compared to -0.13 eV on Au(111) [105] and certainly favours layer by layer growth; in addition, specific adsorption might further stabilize the layers. It is difficult to tell if these layers are absolutely stable or only metastable. In any case, experimentally they are stable, and hydrogen evolution proceeds rapidly.

The surface energy of Pd(111) is 1.92 Jm^{-2} and thus in between those of Rh(111) and Au(111) [106]. In addition, the lattice mismatch between Rh and Pd is only 4%, so we expect monolayers of Rh over Pd(111) to be substantially more stable than
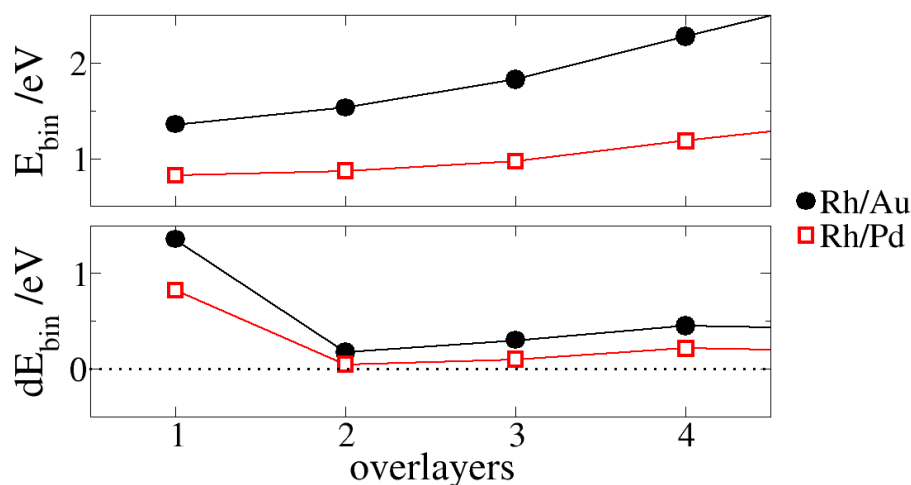
Figure 16.1: Total and differential binding energies (E_{bin} and dE_{bin} respectively) of Rh/Pd and Rh/Au multilayers.

Rh/Au(111), and this is indeed the case – see Fig. 16.1. Nevertheless, our calculations predict cluster growth in the vacuum. There seem to be no experimental data, but the same mechanisms that stabilize Rh/Au(111) in aqueous solutions should also operate for Rh/Pd(111). To shed some light on the possible metastability of such films we investigated the energetics of nucleation by comparing the energies of a four atom island and a four atom cluster (see Fig.16.2).
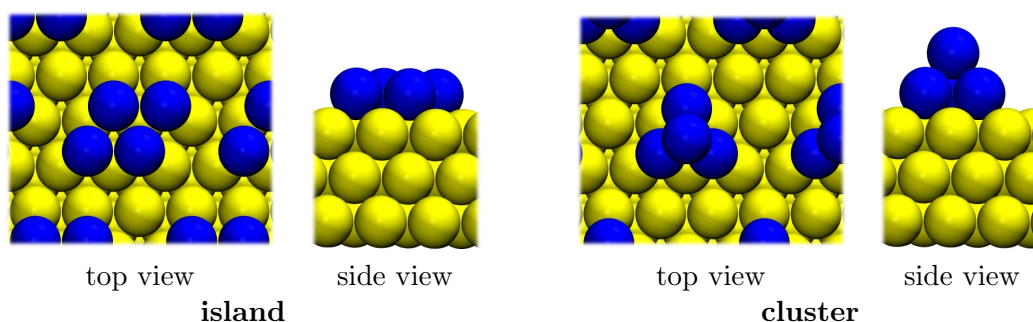
Figure 16.2: Top and side views of 4-atom-clusters on Au(111).

In both cases, the energies of the islands are more favourable than those of the clusters: by 0.09 eV for Rh/Au, and by 0.64 eV for Rh/Pd(111). So at least for small clusters there is a kinetic barrier for the formation of cluster; in electrochemical systems this would be enhanced by the presence of water, which interacts more strongly with Rh than with Au or Pd.

top view   side view
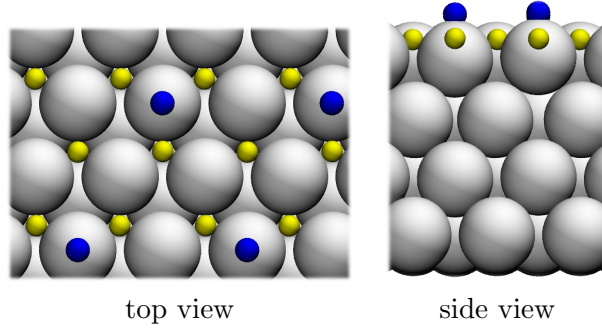
Figure 16.3: Top and side view of the strongly adsorbed hydrogen H_s (yellow) and the weakly adsorbed hydrogen H_w (blue) on Rh(111). H_s is adsorbed on the fcc hollow site, H_w on the top. The diagram is for a full monolayer of H_s and a coverage of $1/4$ for H_w.

16.4   Hydrogen adsorption on Rh(111) surfaces

Adsorbed hydrogen is the intermediate in hydrogen evolution and oxidation, and its energetics have a pronounced influence on the reaction rate. As mentioned in the introduction, on transition metals the first hydrogen atoms are often adsorbed so strongly that they are difficult to desorb in the second step, and hence act like a spectator. Therefore, we have considered two types of hydrogen, a strongly (H_s) and a weakly (H_w) adsorbed species; their adsorption sites on Rh(111) are illustrated in Fig. 16.3. The adsorption energies are obtained from:

$$E_{ads}^s = E(H_s/Sub) - E(Sub) - \frac{E(H_2)}{2} \qquad (16.3)$$

$$E_{ads}^w = E(H_w/H_s/Sub) - E(H_s/Sub) - \frac{E(H_2)}{2} \qquad (16.4)$$

where $E(H_s/Sub)$ is the energy of a Rh(111) substrate fully covered with H_s, $E(H_w/H_s/Sub)$ is the energy of H_w adsorbed on the latter, $E(Subs)$ and $E(H_2)$ are the energies of the clean substrate and of the hydrogen molecule in vacuum, respectively. The adsorption energies for coverages of 1 and 0.25 monolayers (ML) are shown in figure 16.4.

For H_s the most favorable adsorption site is fcc hollow. Its large negative adsorption energy suggests that a monolayer of H_s is formed in such surfaces, as confirmed experimentally [101,107]. The energy decrease from θ=1 to θ=1/4 is due to the decrease of the H_s-H_s repulsion and is of the order of 0.1 eV. On this surface covered with a monolayer of H_s at the fcc hollow sites, the adsorption of H_w takes place. In addition to the repulsion among H_s atoms, there are H_w-H_s repulsions which make $E_{ads}^w > E_{ads}^s$. In this case the top position is the most favorable one, since there the repulsion is lowest.
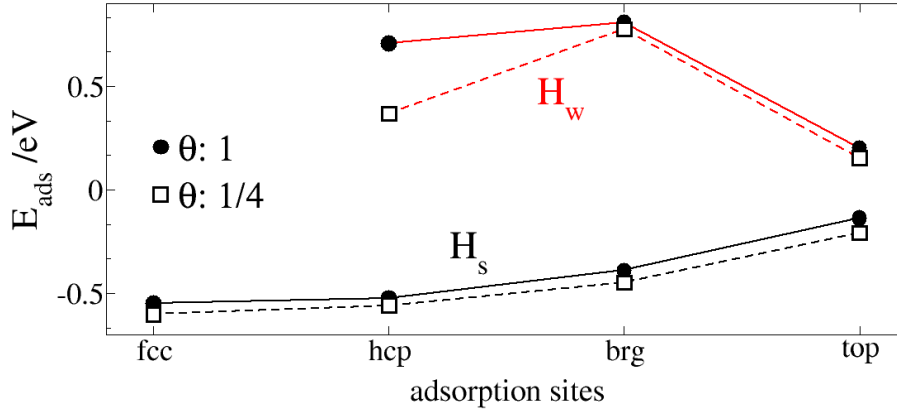
Figure 16.4: Adsorption energies of the strongly and weakly adsorbed hydrogen (H_s and H_w, respectively) on Rh(111) at different adsorption sites and coverages. The data for H_w are for a surface covered by a monolayer of H_s adsorbed in the fcc hollow sites.

Hydrogen adsorption on Rh/Au(111) and Rh/Pd(111) surfaces

The adsorption energies are calculated as in equation 16.3 and 16.4 but now the index *Subs* refers to Rh/Au and Rh/Pd substrates. In Fig. 16.5, hydrogen adsorption energies as a function of the number of Rh overlayers (Rh_n) are presented. In order to determine the chemical effect of the gold or palladium substrates, we have proceeded as in our previous work [88] and also performed calculations for pure rhodium slabs expanded to the lattice constants of gold (Rh@Au) and palladium (Rh@Pd).

For the strongly adsorbed hydrogen, the first Rh overlayer is the most reactive one for both Rh/Pd and Rh/Au. There is still a minor chemical effect for the second layer, but from then on, the adsorption energies are almost the same as on the pure expanded Rh slabs (Rh@Au and Rh@Pd). From the second layer on, the change in the reactivity is mostly attributed to the lattice expansion. The adsorption energy on Rh_1/Au is ~0.42 eV lower than that on pure Rh, and is of the same order as on Pt(111). For Rh_1/Pd the difference is smaller: ~0.18 eV. This suggests that Au induces a larger electronic effect on Rh than Pd, as will be confirmed later with density of states (DOS) studies. The adsorption energy on pure expanded Rh is ~0.16 eV and ~0.09 eV lower than on pure Rh for Rh@Au and Rh@Pd, respectively. This indicates that the geometric effect is also larger for Au than for Pd substrates, which is expected since the lattice constant of Rh is expanded by 8% and 4% correspondingly. The same trends were found for H_s at $\theta=1/4$ (not shown) where an energy decrease of ~0.1 eV was obtained for all the adsorption sites computed.

For the weakly adsorbed hydrogen, and in contrast to the adsorption on pure Rh,

a) H_s adsorption
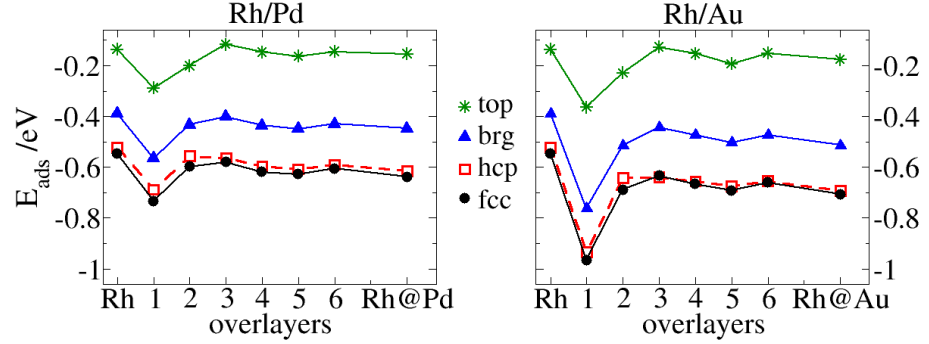
b) H_w adsorption
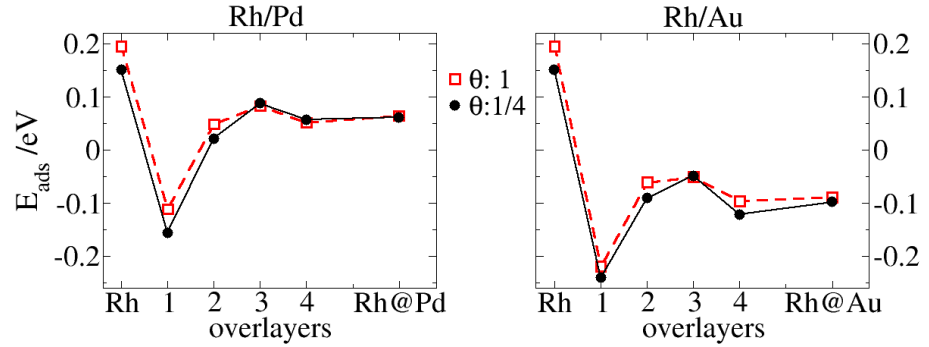
Figure 16.5: a) Adsorption energies (E_{ads}) of H_s at $\theta=1$ on Rh_n/Pd and Rh_n/Au for $n = 1, 2, ...6$. **b)** Adsorption energies of H_w at $\theta=1$ and $\theta=1/4$ on Rh_n/Pd and Rh_n/Au for $n = 1, 2, ...4$. **a-b)** The values are compared with the adsorption energies on clean Rh(111) and on the laterally expanded slabs Rh@Pd and Rh@Au.

E_{ads}^w is exothermic at the first Rh overlayer on both substrates (see figure 16.5b), which suggests that these structures are excellent catalysts for the HER. The electronic effect induced by the substrate extends only to the first Rh overlayer; for higher ones the geometric effect is dominant.

In order to study the electronic effect induced by Pd and Au substrates in greater detail, the DOS of the top Rh layer is illustrated in Fig. 16.6.

Comparing the first Rh overlayer in both substrates, it is clear that the upward shift of the d band is larger on Rh_1/Au than on Rh_1/Pd. Also, a strong chemical effect is involved since the DOS of the overlayers are markedly different from those of the expanded lattices. Here this phenomenon follows the d band model proposed by Hammer and Nørskov [108, 109], since this shift leads to an improvement of the chemisorption, which is bigger for Rh/Au than for Rh/Pd overlayers. In order to make a quantitative comparison, the center of the d band of pure Rh and of up to
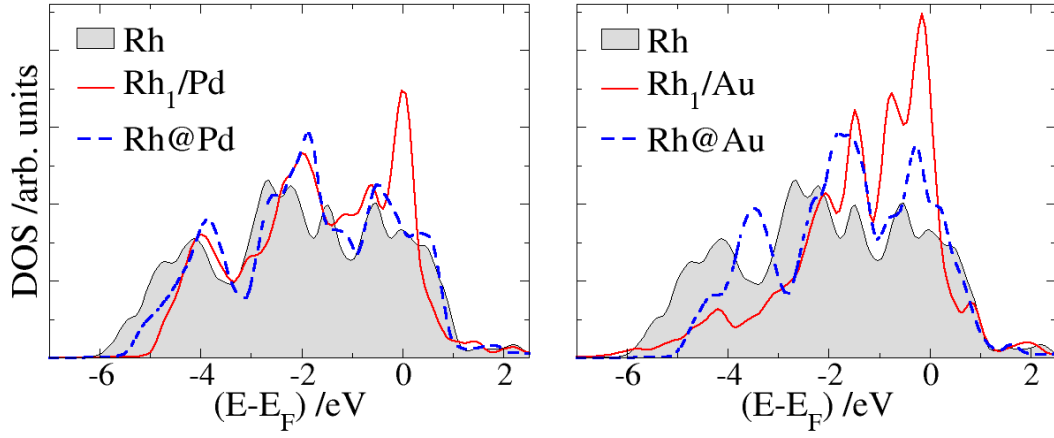
Figure 16.6: Density of states (DOS) projected on the surface atoms of Rh, Rh/Pd, and Rh/Au. The d band states are plotted.

four Rh overlayers was calculated by the means of equation 16.5.

$$\int_{-\infty}^{\infty} \rho_d(\varepsilon)\varepsilon d\varepsilon = \varepsilon_d \tag{16.5}$$

where $\rho_d(\varepsilon)$ is the normalized DOS of the d band as a function of the energy (ε). The results are shown in figure 16.7.
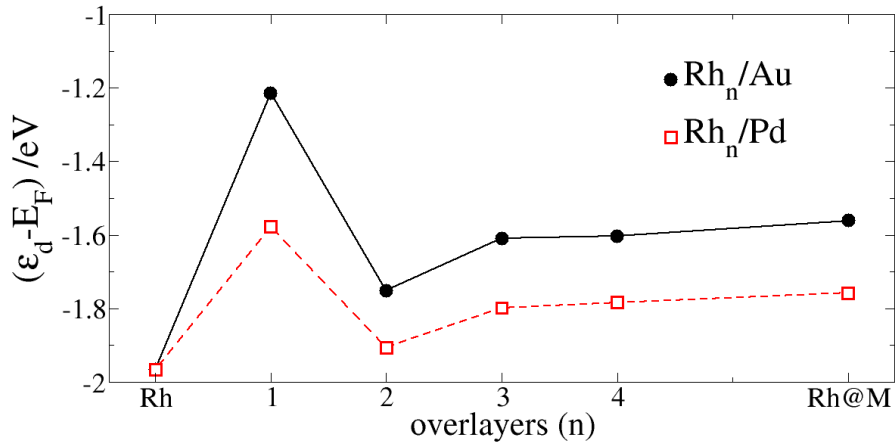
Figure 16.7: Position of the d band center (ε_d) with respect to the Fermi level as a function of the number of Rh overlayers on Au and on Pd substrates. The values are compared with the pure Rh surface (Rh) and the corresponding laterally expanded Rh ($Rh@Sub$).

It becomes evident that the electronic effect induced by the underlying substrate is larger for Au than for Pd. For both, after the second Rh overlayer the electronic effect contributes no longer to the d band shift; it is then solely caused by the lattice expansion.

16.5   Kinetics of the hydrogen reaction

The Volmer reaction

The DFT calculations have shown that the rhodium overlayers, particularly the monolayers, have a strong affinity for hydrogen, which makes them interesting candidates for catalysts. However, reaction rates are determined by activation barriers and only indirectly by thermodynamics. Therefore, we have investigated the Volmer reaction (page 10), by the Schmickler-Santos theory of electrocatalysis. We focus on the activation energy at the standard hydrogen potential NHE, which is a good indicator of the reactivity. At this potential, the free energy for the Volmer reaction is given by the adsorption energies reported above plus an entropy term, which is of the order of 0.2 eV [57]. Thus, to obtain the free energies of adsorption at NHE, a value of 0.2 eV has to be added. For a monolayer of Rh on Au(111) the free energy of adsorption for the weakly adsorbed species is -0.01 eV, and for Rh/Pd(111) it is 0.1 eV. So at NHE the Volmer reaction on both layers is almost isoenergetic, which in view of Sabatier's principle is favorable.
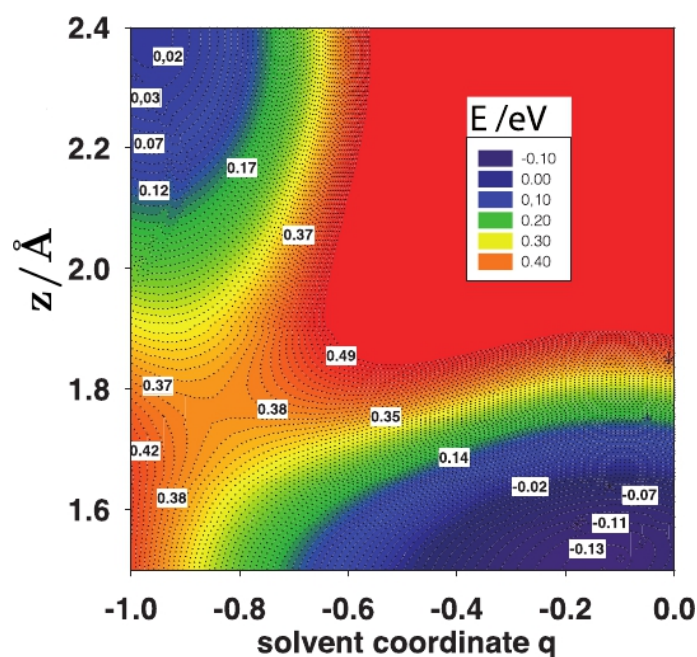
Figure 16.8: Free energy surface for the Volmer reaction on a monolayer of Rh on Au(111).

From our model for hydrogen evolution detailed in [5], we have calculated the free energy surfaces for the Volmer reaction. Figure 16.8 shows the result for Rh/Au(111). This plot shows the free energy of the system as a function of two coordinates: the

solvent coordinate q (page 12) and the distance from the surface. The former is a concept related to the Marcus theory [110] for electron transfer and characterizes the state of the solvent. The transferring proton is strongly solvated, and its discharge requires a reorganization of the solvent. The solvent coordinate is defined in such a way, that a value of q indicates that the solvent would be in equilibrium with a reactant of charge $-q$ [111]. Thus, the initial state is a proton at $q = -1$ and far from the surface, the final state an adsorbed hydrogen atom at $q = 0$ and on top. These two states are separated by an energy barrier of 0.37 eV, which is a very low value and of the same order of magnitude as for Pt(111) [70] – for comparison, for the coinage metals we have obtained barriers of about 0.7 eV. The surface for Rh/Pd(111) is very similar, and the energy of activation about 0.1 eV higher.

The position of the saddle point in Fig. 16.8 is noteworthy. Since the final state is adsorbed on top, the proton can approach the surface losing only a smaller part of its solvation sheath; therefore electron transfer occurs to a solvated state near $q \approx -0.85$. In contrast, when the final state is adsorbed in the fcc hollow site, desolvation is stronger, and the saddle points, at NHE, are closer to $q = -0.5$.

The Tafel reaction

As we mentioned before, the chemical recombination of two adsorbed hydrogen atoms (Tafel reaction) is often the second step in hydrogen evolution; on very active metals like Pt(111) and Re it determines the overall rate. It is simpler to discuss the results for the reverse reaction, the dissociation of H_2, since in this case the initial state is the same on all surfaces – a molecule far from the electrode. We have investigated this step both on pure Rh(111) and on a monolayer of Rh over Au(111), which is the better catalyst of our two monolayer systems. Since it does not involve electron transfer, it can be described by pure DFT.

Two types of surfaces were evaluated: a clean and a H_s-precovered surface. The paths computed are sketched in figure 16.9a (the notation is given in section 16.2).

As shown in figure 16.9b, on clean Rh or Rh_1/Au surfaces there is almost no activation barrier for the dissociation of hydrogen, which indicates that this process occurs instantaneously on these structures. Obviously, this is not the rate determining step for hydrogen evolution. As long as the dissociation proceeds, the surface coverage of H_s increases. Eventually, a hydrogen molecule will have no clean surface left to interact with. When the H_s monolayer is not complete, the dissociation of hydrogen is more favorable, but the barrier increases substantially as the H_s-coverages grows [70]. In order to compare hydrogen dissociation on clean and covered surfaces, we investigated the limiting case, a complete H_s monolayer – see figure 16.10.

At this H_s-covered surface the incoming molecule has to overcome nuclear repulsion, which significantly increases the activation energy. On both substrates the t-b-t path is clearly unfavorable for dissociation (for the f-b-h path we obtained similar
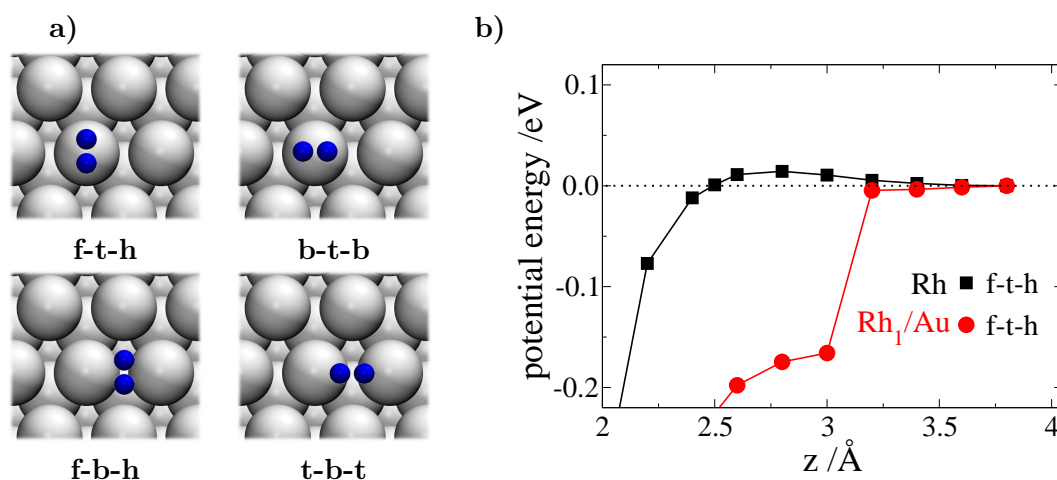
Figure 16.9: Hydrogen dissociation on Rh and Rh_1/Au clean surfaces. **a)** Top view of several paths at the initial state. **b)** Potential energy as a function of the molecule distance from the surface (z).
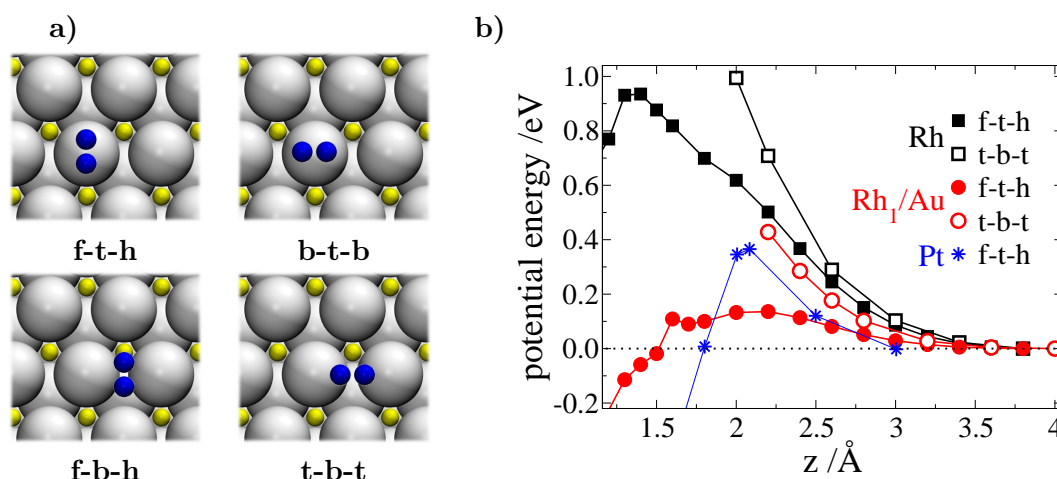
Figure 16.10: Hydrogen dissociation on Rh and Rh_1/Au surfaces covered by a monolayer of the strongly adsorbed hydrogen H_s. **a)** Top view of several paths at the initial state. **b)** Potential energy as a function of the molecule distance from the surface (z).

results). On Rh the f-t-h path leads to a barrier of 0.9 eV, which is a little higher than that on Pt(111) under the same conditions [70]. Surprisingly, on Rh_1/Au the activation energy for the f-t-h path is only 0.16 eV. In the latter case, the barrier is comparable to that on clean Pt and Pd surfaces (0.06 eV [112] and 0.05 eV [113], correspondingly). The same tendency was observed for the b-t-b path on both Rh and Rh_1/Au surfaces. The reasons for this dramatic difference can be explained by

two factors: The *nuclear repulsion* among hydrogen species, and the *affinity* of the precovered surface for hydrogen adsorption. As long as H_2 approaches the surface, the nuclear repulsion between the molecule and the H_s atoms is dominant and increases. This pushes the adsorbed atoms away from their fcc-hollow sites, which also increases the repulsion among H_s neighbors, sketched in figure 16.11a. The distance of two H_s neighbors (d_{Hs}) during the approach of a hydrogen molecule is shown in figure 16.11b.
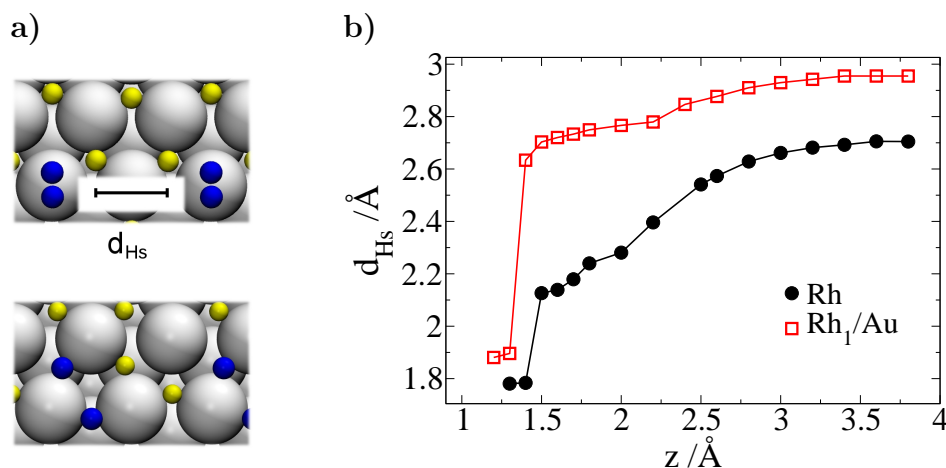
Figure 16.11: a) Top view of a H_s-precovered surface (yellow atoms) on which a H_2 molecule is approaching with the f-t-h configuration (blue atoms). The distance between two H_s atoms (d_{Hs}) is denoted with a segment within the figure. The final state with the dissociated atoms is sketched below. **b)** d_{Hs} as a function of the distance from the hydrogen molecule to the surface (z).

Since the lattice constant of Rh is smaller than that of Au, d_{Hs} is smaller for pure Rh surfaces, making the repulsion stronger than on Rh_1/Au. Indeed, the difference in d_{Hs} on these substrates is around 0.3 Å when H_2 is far from the substrate, and increases during its approach. The total hydrogen repulsion is the dominant force that increases the potential energy at distances larger than 2.5 Å. At closer distances, the molecule interaction with the substrate becomes stronger, the affinity for hydrogen adsorption begins to play a role, and again, is quite different for both substrates. One way to compare them is examining the bond distance of the molecule as it approaches the surface: The more favorable the interaction, the sooner the H_2 bond distance increases.

As shown in figure 16.12, on Rh_1/Au the separation of the hydrogen molecule atoms occurs at larger distances from the surface than on Rh. Moreover, the elongation of the hydrogen bond is smooth on Rh_1/Au, while in the case of Rh there is an abrupt change. At around 2.3 Å from the Rh_1/Au H_s-covered surface the affinity for
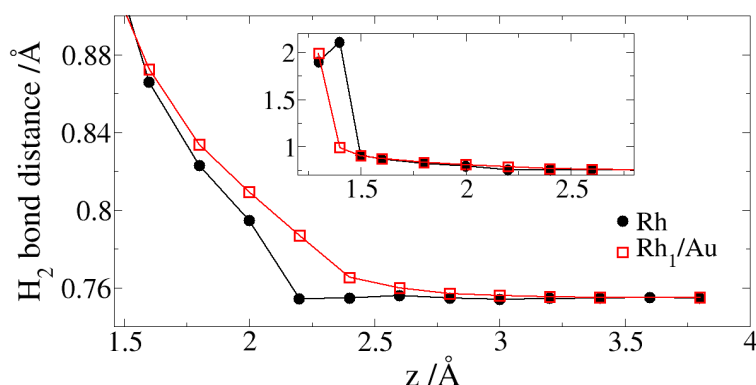
Figure 16.12: H_2 bond distance as a function of the distance from the surface (z). The inset shows a zoomed view at short distances.

H_2 overcompensates hydrogen repulsion and consequently the energy of the system decreases – see figure 16.11b. The Rh H_s-precovered surface on the other hand has a weaker affinity for H_2 so that hydrogen repulsion dominates.
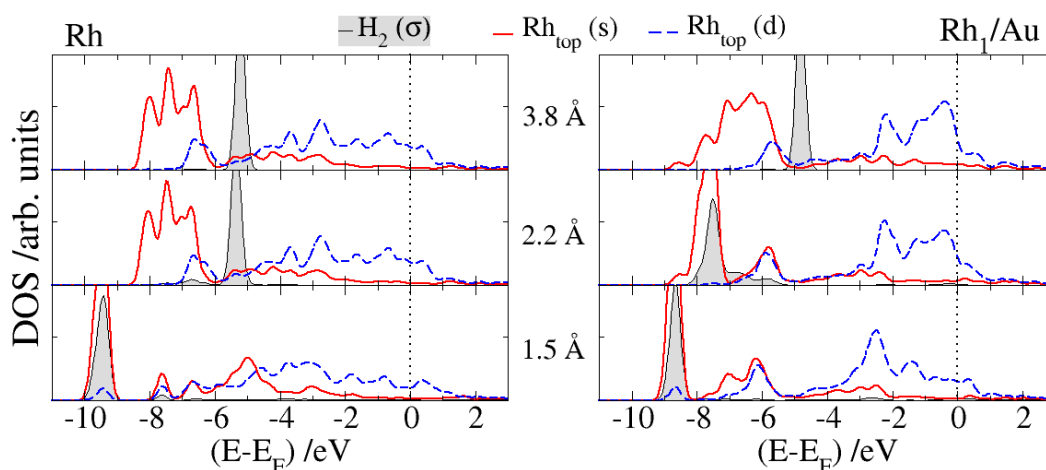
Figure 16.13: Density of states (DOS) projected on the hydrogen molecule and surface metal atom states. Three stages of the H_2 dissociation on H_s-precovered surfaces are compared: H_2 far away from the surface (3.8 Å), closer (2.2 Å), and right before the molecule bond is broken (1.5 Å). The s state of hydrogen and Rh have been reduced by a factor of 4 for clarity.

The differing affinities for H_2 of Rh and Rh_1/Au H_s-precovered surfaces can be analyzed with the aid of the DOS as shown in figure 16.13: At far distances from the surface, H_2 shows a sharp peak which corresponds to the σ bonding state. At 2.2 Å from the surface, only in the case of Rh_1/Au the molecule interacts with the substrate – principally with the s band, which extends further beyond the sur-

face. At closer distances, on both surfaces hydrogen interacts with the s and the d band, both of which undergo significant changes. So, in the case of Rh_1/Au, the electronic interaction with the metal starts at larger distances and helps to reduce the activation barrier.

16.6   Conclusions

Metal monolayers on foreign metal substrates have fascinating catalytic properties. They are only stable if there is a strong chemical bonding between the monolayer and the substrate, so there is always a pronounced chemical or ligand effect. If the lattice constant of the adsorbed metal is smaller than that of the substrate, as is the case for Rh/Au(111) and Rh/Pd(111), the induced strain leads to an upward shift of the d band center of late transition metals, which increases the reactivity.

In the case of Rh/Au(111), the lattice mismatch is particularly large, and the monolayer is only stable because the chemical interaction is so strong. Hence, both the chemical and the d band effect are large, and combine to make this a very promising candidate for hydrogen electrocatalysis. According to our calculations, both hydrogen adsorption and recombination should be extremely fast, even faster than on pure Pt(111).

On Rh/Pd(111) the induced strain is weaker, so its catalytic properties are expected to be not quite as good. However, it can support several commensurate layers, which in itself is an interesting property.

To the best of our knowledge, there are no experimental investigations for hydrogen evolution or oxidation on these systems. Thus, our work is a prediction. This indicates a pronounced change in the relation between theory and experiment that has taken place during the last decade: Previously, theory used to follow the experimentalists trying to explain their data. Nowadays, experiments can be guided by theoretical predictions.

17

CN on Pt(111) surfaces

When we try to pick out anything by itself, we find it is tied to everything else in the universe.

John Muir Naturalist, explorer.

17.1   Introduction

Cyanide adsorbs spontaneously and irreversibly on Pt(111), and adopts an ordered $(2\sqrt{3} \times 2\sqrt{3})\text{R}30^o$ structure, as has been elucidated by low-energy electron diffraction (LEED) [114] and in situ scanning tunnel microscopy (STM) [115, 116]. The cyanide-modified Pt(111) structure (CN-Pt(111) from now on) consists of hexagonally packed hexagons, each containing six CN groups adsorbed on top of Pt atoms surrounding a free Pt atom, as shown in figure 17.1.

As can be observed in the figure, three-fold hollow adsorption sites are not available. Consequently, all the chemical processes that require at least three-fold hollow or trigonal sites are inhibited. As an example, it is well known that the electro-oxidation of small molecules on Pt(111) folllows a dual path mechanism, the direct path competing with a slow reaction path in which CO is adsorbed. This catalyst-poisoning species adsorbs on clean Pt three-fold hollow sites. Since the latter site is
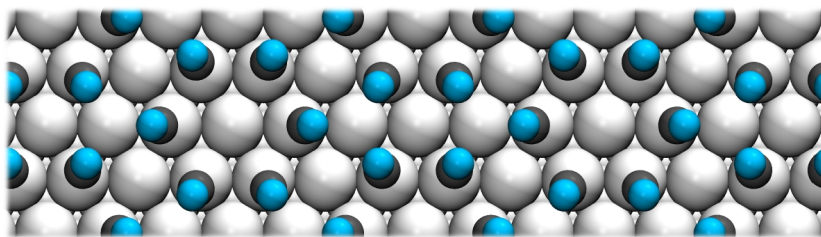
Figure 17.1: Top view of the cyanide-modified Pt fcc(111) surface (CN-Pt(111) surface).

blocked in CN-Pt(111) surfaces, the slow path reaction is inhibited and the electro-oxidation of small organic molecules is channeled through the fast pathway [117,118].

Another very interesting aspect of CN-Pt(111) concerns electrochemical hydrogen adsorption. In comparison with clean Pt(111), on the modified surface the process occurs at 0.2 V higher potentials [119], as shown in figure 17.2. This phenomenon could be ascribed to a reactivity enhancement of the free Pt atoms (non-bonded with CN). However, the density of states of such superficial atoms is almost the same as on clean Pt(111), without any d band shifts that could explain the higher affinity for hydrogen. It has been proposed that the positive shift by 0.2 V in the onset of hydrogen (figure 17.2) is due to the adsorption of hydrogen not on the Pt surface but on the nitrogen atoms of the adsorbed cyanides (CN_{ad}-H) [120].

This could also explain the striking change in the frequency of the carbon-nitrogen stretching mode with respect to the potential [118], also shown in figure 17.2. Due to bond order conservation, the adsorption of hydrogen on CN_{ad} should weaken the carbon-nitrogen bond, consequently the corresponding vibrational frequency should decrease.

One last remarkable feature worth mentioning is the CN-Pt interaction with cations. Surprisingly, this interaction dramatically affects the equilibrium potential of hydrogen adsorption. Moreover, this change corresponds to a Nernstian-like behaviour, i.e., it is proportional to the logarithm of the cations concentration (at relatively high concentrations). This is due to the fact that the cations interact strongly with the negatively charged nitrogen of the CN_{ad}, competing with hydrogen adsorption. The arrangement of CN_{ad} on Pt(111) form cavities at which the cations can adsorb. These cavities are differentiated by their size, given by the number of cyanides: $(CN_{ad})_3$, $(CN_{ad})_4$, and $(CN_{ad})_6$[1], as shown in figure 17.3. STM images and theoretical calculations show that the most stable adsorption site for cations is the $(CN_{ad})_3$ cavity, which leads to the so-called *honeycomb* structure.

In spite of the vast amount of studies on the CN-Pt(111) structure, there is a lack of theoretical work concerning central aspects such as the reason for the $2\sqrt{3} \times 2\sqrt{3}$ structure, the structural and energetic dependence on the cyanide coverage, etc. In

---

[1]This nomenclature does not necessarily respect the stoichiometry
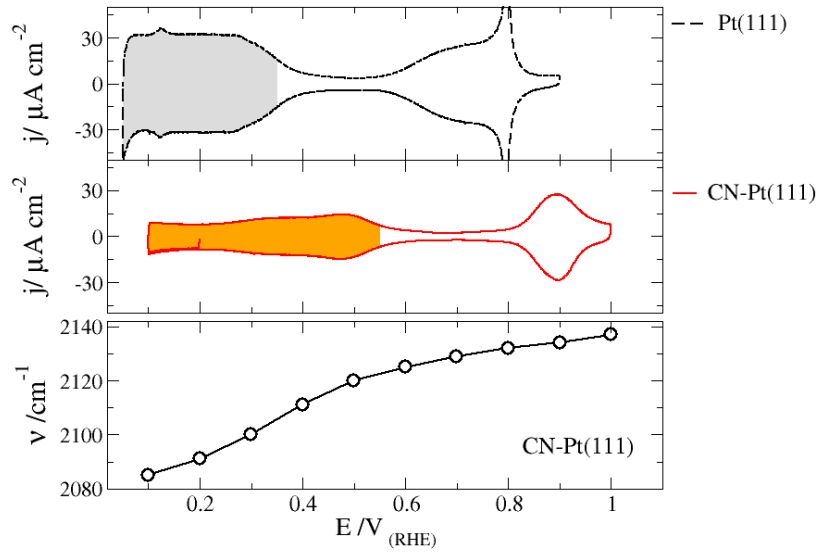
Figure 17.2: Cyclic voltammogram of clean Pt(111) and of CN-Pt(111) in a perchloric acid solution (top two panels) [119]. The potentials at which hydrogen adsorption occurs are colored grey and orange for Pt(111) and CN-Pt(111), respectively. Vibrational frequencies of the carbon-nitrogen stretching for CN-Pt(111) as a function of the potential (RHEA) [118] are shown in the bottom panel.

$(\mathbf{CN_{ad}})_3$ $(\mathbf{CN_{ad}})_4$ $(\mathbf{CN_{ad}})_6$
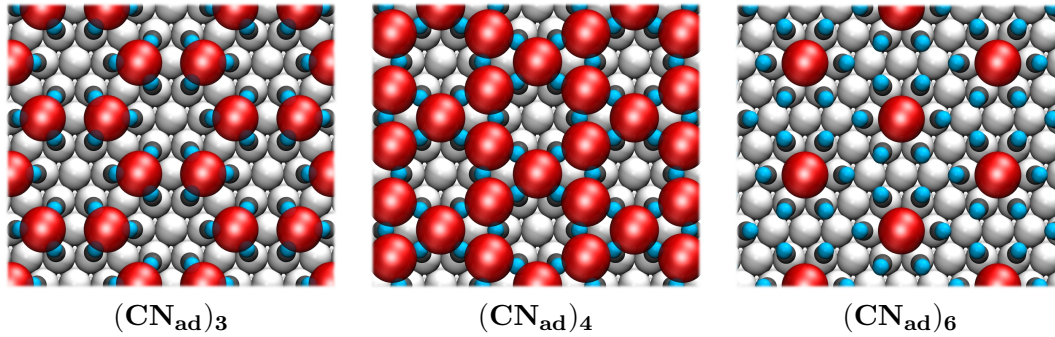
Figure 17.3: Top view of the cavity sites at which cations can adsorb on cyanide-modified Pt(111) surfaces.

this chapter, our aim is to provide a DFT approach that sheds some light on the following questions:

• Why is the $2\sqrt{3} \times 2\sqrt{3}$ structure the preferable one for cyanide on Pt(111)?

• According to experimental infrared spectra, a single vibrational band is observed, corresponding to the C-N stretching mode on a top site [115, 121]. Considering the low barrier for the diffusion of species on Pt(111), why is only the top signal observed?

• How does the coverage of cyanide affect its adsorption energy and localization on platinum?

• What is the reason for the 0.2 V positive shift of the onset of hydrogen adsorption? (see figure 17.2).

17.2   Technicalities

Modeling

The $2\sqrt{3} \times 2\sqrt{3}$ slab consists of three layers, the bottom two were kept fixed at the nearest-neighbor distance corresponding to the Pt bulk (calculated to be 4.00 Å in good agreement with the experimental value, 3.92 Å [12]), and the top layer was allowed to relax. The change in the surface energy σ and the work function Φ between three and four layers is 0.03 eV and 0.06 eV, respectively (table 17.1).

	σ [eV]	Φ [eV]
2	0.65	5.72
3	0.66	5.80
4	0.63	5.74
5	0.64	5.72
6	0.63	5.76

Table 17.1: Surface energy (σ) and work function (Φ) with respect to the number of layers for the Pt fcc(111) surface.

All the structures within this unit cell will be referred to as the *experimental* unit cell. Smaller unit cells were computed for CN coverages between 0.25 and 1 monolayer. Their lateral dimensions will be described in the corresponding section. Hydrogen adsorption was also evaluated on such surfaces. In all cases, the two bottom layers were kept fixed and the rest was fully relaxed. Convergence was achieved when the total forces were less than 0.01 eV/Å. Only the isolated CN radical presented magnetic properties, so only there spin was considered.

First-principle calculations

All calculations were performed with DACAPO [6], a density functional theory (DFT) code. The electron-ion interactions were accounted through ultrasoft pseudopotentials [7], while the valence electrons were treated within the generalized gradient approximation (GGA) in the version of Perdew and Wang [8,9]. Special care was taken for the parametrization of the energy cutoff and the k-points sampling

of the Brillouin zone based on the Monkhorst-Pack grid [11]. Both parameters were increased systematically in a Pt bulk system with the optimized lattice constant until the change in the absolute energy was less than 20 meV. An energy cutoff of 400 eV and a grid of 12×12×12 satisfy the energy accuracy. Consistently, 4×4×1 kpts were used for the CN-Pt surface of the experimental structure.

17.3 CN and CNH adsorption at different coverages

The adsorption energy of cyanide on Pt(111) was calculated by taking the substrate and the radical adsorbate as the reference:

$$E_{ad} = E_{spec-Pt(111)} - (E_{spec} + E_{Pt(111)}) \qquad (17.1)$$
$$\Delta\Phi = \Phi_{spec-Pt(111)} - \Phi_{Pt(111)} \qquad (17.2)$$

where in this case, *spec* refers to CN. As a starting point, we calculate the adsorption energies at different cyanide coverages on small unit cells (2×2 or smaller). We will address the experimental unit cell ($2\sqrt{3} \times 2\sqrt{3}$) and other possible configurations later. The results are shown in figure 17.4. For the sake of simplicity, only the values for cyanide in the hollow-fcc and top sites are shown.

Naturally, the adsorption energy increases with the coverage due to CN-CN repulsion. The major contribution to the repulsion comes from the negatively charged nitrogen. This is in fact the reason for the pseudo-hexagonal arrangement of the nitrogen atoms at a coverage of θ=0.50 monolayer (ML), which introduces some stress to the system, since the adsorbates are not aligned perfectly perpendicular to the metal surface. As we can see, the adsorbate is disposed along interspaced platinum lines, forming a zig-zag structure. By the negligible difference in energy between the hollow-fcc and the top configurations of CN_{ad} at θ=0.50 ML, we cannot explain why the IR spectra for the C-N stretching mode is solely attributed to the top position. The answer may not be in the energetics of the system, but in the surface dipole. Table 17.2 shows the change in the adsorption energies and the change in the work functions with respect to the clean Pt(111) surface ($\Delta\Psi$) for different coverages and adsorption sites of cyanide (for the moment, let us just focus on the results corresponding to CN at θ=0.25 ML and θ=1.00 ML). As we can see, despite a negligible difference in the adsorption energy, the difference in $\Delta\Phi$ is large (1 eV for θ=0.25 ML and 0.5 eV for θ=1.00 ML). In every case, the work function for the top site is higher than for the hollow-fcc site. This entails a larger dipole moment in the former case, which is better solvated by water molecules. This phenomenon could explain the preference for the top site over others with similar energies.
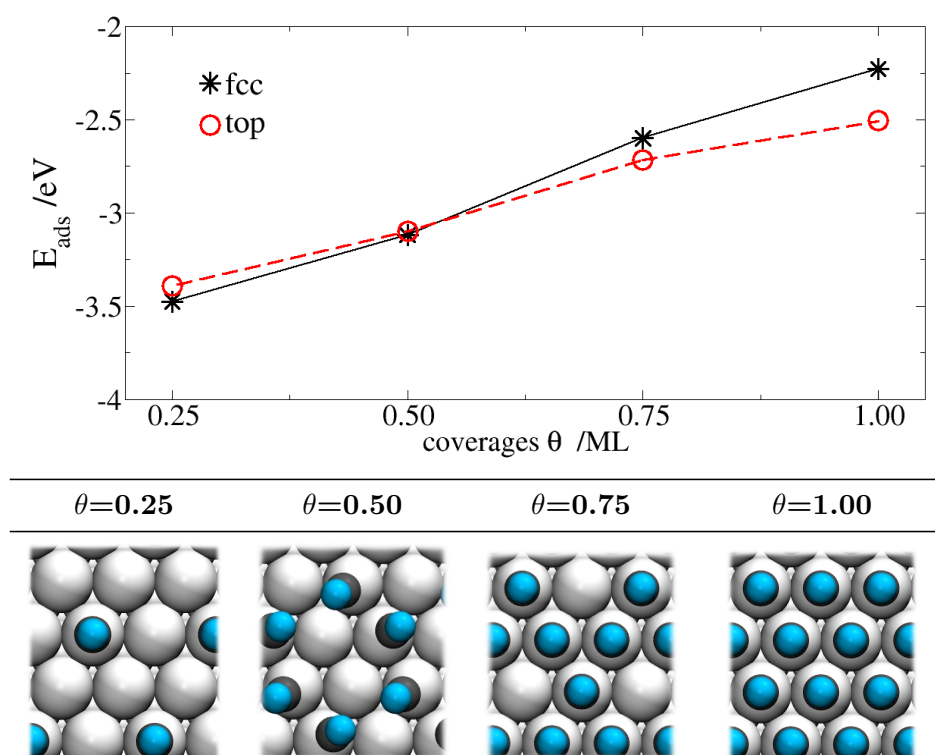
Figure 17.4: Adsorption energy (E_{ad}) of cyanide on Pt(111) at different coverages (θ). Top views of the coverages are also illustrated.

Let us now examine the experimental structure and others with a cyanide half monolayer covering the platinum surface (figure 17.5).
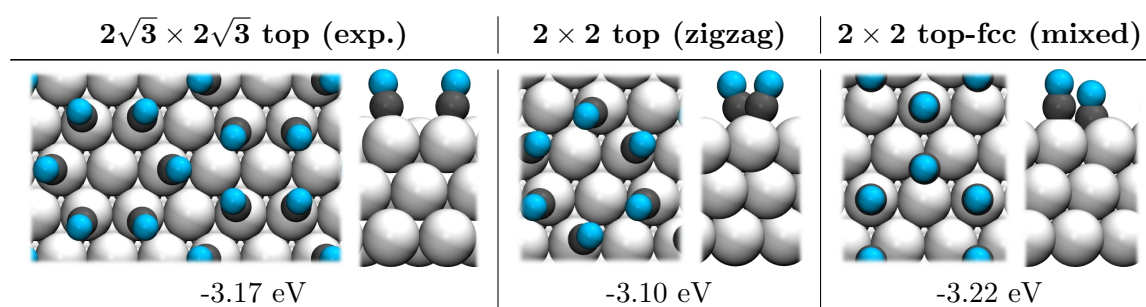
Figure 17.5: Top and side views of different CN arrangements on Pt(111) at a coverage of θ=0.50 ML. The corresponding adsorption energies E_{ad} are also shown.

We have found two configurations almost isoenergetic with respect to the $2\sqrt{3}\times2\sqrt{3}$ structure. One is the already shown zigzag structure, which is slightly higher in energy than the experimental one. The other alternative structure is also close in

energy, but is slightly more stable than the latter. One CN_{ad} is on a top site and the other is in a hollow-fcc site, this is the so-called mixed structure. Here, there are no bond constraints and, more importantly, the N-N repulsion is lowered since the CN are at different heights from the metallic surface. In table 17.2 the E_{ad} and $\Delta\Phi$ of the latter structures are shown (we focus now on the values for CN at θ=0.50 ML). Neither the energy nor the dipole moment of the experimental, zigzag, and mixed structures show a considerable difference that would favor one of them in particular. At least from a pure DFT-thermodynamical point of view, the three structures described above should be in equilibrium. Why is then the $2\sqrt{3}\times2\sqrt{3}$ structure the only one observed experimentally? Our results suggest that the preference for a particular structure may not be directly related to the CN-Pt(111) surface itself, but to its strong interaction with cations. As described in the introduction, the cations prefer $(CN_{ad})_3$ cavities which are not formed in the alternative structures presented here. Instead, the cavities of the alternative structures resemble the $(CN_{ad})_6$ of the experimental one. For the mixed arrangement, the different heights of the adsorbates and the large cavity size immediately ruled them out as stable candidates. For the zigzag case, the $(CN_{ad})_6$ cavity is quite similar to that of the $2\sqrt{3}\times2\sqrt{3}$ structure, but, even if they where identical, the adsorption on $(CN_{ad})_3$ is around 0.6 eV more stable than on $(CN_{ad})_6$ for the experimental structure [120].

Now we would like to concentrate on the stability of a species that may be present on the platinum modified surface *before* hydrogen adsorption on the metal occurs (we shall show the foundations of this assumption in the next section). This species is CNH. Its adsorption energy is also given by equation 17.2, in which the subindex *sec* refers to CNH in this case. Results are summarized in table 17.2.

In comparison with the adsorption of CN, the adsorption of CNH inverts the dipole moment of the surface. Still, large differences in the work function are found in contrast to the small change in the adsorption energy for equal coverages. The zigzag arrangement is among the more stable ones for CN, while the linear configuration is subtly less favorable. However, when hydrogen adsorbs on the nitrogen atoms, the trend is the other way around. This is because the linear configuration presents a hydrogen-bond disposition that lowers the energy, which is not observed in the zigzag case (see figure 17.6). The same pattern has been observed in the experimental structure (but its relaxation has not finished yet).

17.4   Atomic hydrogen adsorption

A very peculiar aspect of the CN-Pt(111) surface is the 0.2 V positive shift of the onset of hydrogen adsorption, as compared with the clean Pt(111) surface, shown in figure 17.2. It is tempting to ascribe this phenomenon to an enhancement of the reactivity of the Pt surface due to the strongly adsorbed CN; however, the density of

θ /ML	**Site**	E_{ad} [eV]		$\Delta\Phi$ [eV]	
		CN	CNH	CN	CNH
0.25	**top**	-3.39	-1.86	2.75	-2.66
	fcc	-3.47	-2.11	1.67	-0.88
0.50	**top** (exp.)	-3.17	-1.64	3.56	-2.49
	top (zigzag)	-3.10	-1.43	3.48	-3.37
	top (linear)	-3.02	-1.60	3.48	-2.23
	fcc (linear)	-3.04	-1.81	2.09	-0.86
	top-fcc (mixed)	-3.23	-1.87	3.24	-2.38
1.00	**top**	-2.51	-1.04	3.82	-2.69
	fcc	-2.23	-0.96	3.33	-1.63

Table 17.2: Adsorption energies (E_{ad}) and work function differences ($\Delta\Phi$) in eV for several CN and CNH configurations and coverages on Pt(111).

zigzag CNH-Pt(111)   linear CNH-Pt(111)   exp. CNH-Pt(111)
-1.43 eV   -1.60 eV   -1.64
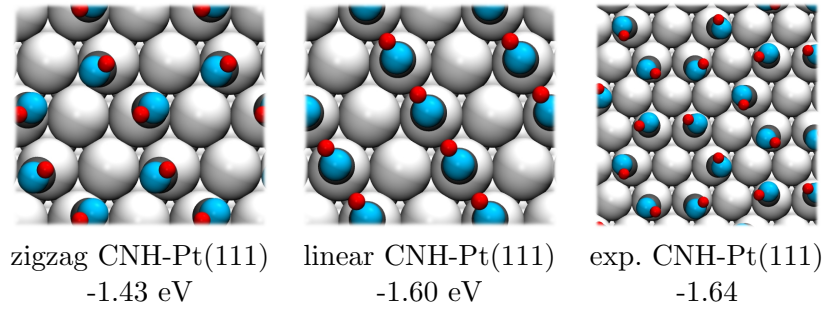
Figure 17.6: From left to right: Zigzag, linear, and experimental configurations of CNH on Pt(111) at a coverage of θ=0.50 ML. The corresponding adsorption energies are given at the bottom.

states shows no sign of such an improvement, as has been pointed out in a previous theoretical work [120].

As we can see in figure 17.7, the DOS projected on to the d band of the Pt atoms non-bonded to CN is nearly identical to that of clean Pt(111). In order to confirm this result, the adsorption energies of hydrogen on CN-Pt(111) were calculated, for which two cases were distinguished: Hydrogen adsorption on the nitrogen atom (E_{ad}^{H-N}), and directly on the metal surface (E_{ad}^{H-Pt}), which are given by
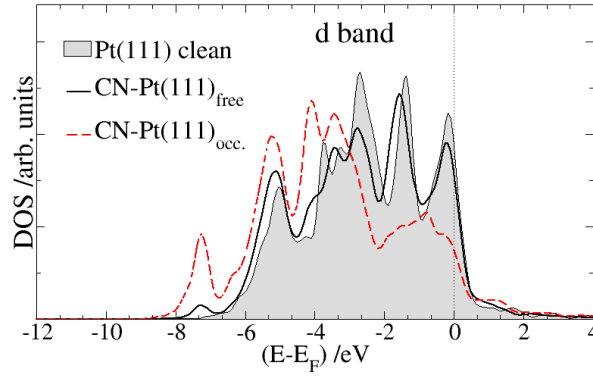
Figure 17.7: Density of states (DOS) projected on d states of clean and CN modified Pt(111) surface atoms. In the latter case, the Pt non-bonded to CN (Pt$_{free}$) are distinguished from those directly bonded to CN (Pt$_{occ}$).
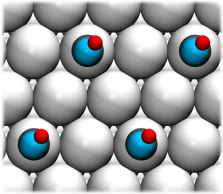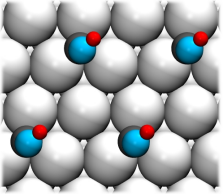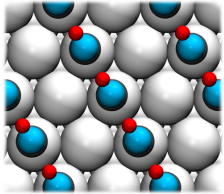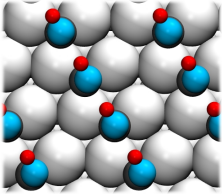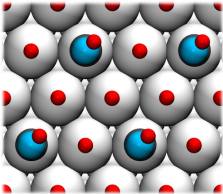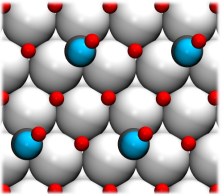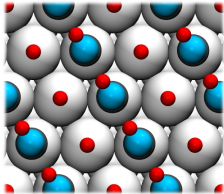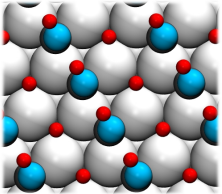
$$E_{ad}^{H-N} = \frac{E_{CNH-Pt(111)} - \left(n_{H_2}\frac{E_{H_2}}{2} + E_{CN-Pt(111)}\right)}{n_{H_2}} \qquad (17.3)$$

$$E_{ad}^{H-Pt} = \frac{E_{CNH-HPt(111)} - \left(n_{H_2}\frac{E_{H_2}}{2} + E_{CNH-Pt(111)}\right)}{n_{H_2}} \qquad (17.4)$$

where n_{H_2} is the number of hydrogen atoms adsorbed with respect to the reference structure. Results are summarized in figure 17.8.

In agreement with the d band model prediction, the adsorption of hydrogen on the metallic surface of CN-Pt(111) is closer in energy with respect to the adsorption on clean Pt(111) (-0.4 eV).[2] The adsorption of hydrogen on the nitrogen atoms is remarkably more stable, in some cases by 1 eV. As expected, hydrogen on the metal increases the magnitude of the work function.

---

[2]Strictly speaking, the values of E_{ad}^{H-Pt} in figure 17.8 correspond to the CNH-Pt(111), where hydrogen is already adsorbed on the nitrogen atoms. However, the difference with respect to E_{ad}^{H-Pt} on CN-Pt(111) clean of hydrogen atoms is negligible (lower than 0.1 eV)

| | θ_{CN}=0.25 | | θ_{CN}=0.50 (linear) | |
	top	fcc	top	fcc
H **|** **N**				
E_{ad}	-1.10 eV	-1.26 eV	-0.95 eV	-1.31 eV
$\Delta\Phi$	-2.66 eV	-0.68 eV	-2.23 eV	-0.86 eV
H **|** **Pt**				
E_{ad}	-0.31 eV	-0.33 eV	-0.23 eV	-0.28 eV
$\Delta\Phi$	-2.84 eV	-1.16 eV	-2.33 eV	-0.90 eV

Figure 17.8: Top view of hydrogen adsorption on CN-Pt(111) and CNH-Pt(111) at different cyanide coverages. The corresponding adsorption energies E_{ads} and delta work functions $\Delta\Phi$ are also given. For hydrogen monolayer on clean Pt(111): E_{ad}^{top}=-0.42 eV, E_{ad}^{fcc}=-0.45 eV, $\Delta\Phi^{top}$=-0.67 eV, $\Delta\Phi^{fcc}$=-0.44 eV. The hydrogen adsorption energy for the experimental structure (see figure 17.6) is close to that of the linear configuration for θ_{CN}=0.50 ML: -1.09 eV.

17.5   Conclusions

Because of its low activation energy for the diffusion of species, the platinum (111) surface is known as a *flat* surface. Our calculations show that this may not be the case at high cyanide coverages. In the ideal case of a complete cyanide monolayer, the top position is favored over the hollow-fcc one by 0.3 eV. On the other hand, at a coverage of θ=0.25 ML, the hollow site is favored by 0.1 eV. This may be due to the repulsion between the large electron density of the nitrogen atoms and that of the metal surface. At low cyanide coverages this repulsion is small and there is not much of a difference between adsorption sites. At one monolayer, however, the repulsion tends to push the adsorbate further from the surface without desorbing CN, and therefore, the top site becomes the most favorable one.

The cyanide coverage corresponding to the experimental structure is θ=0.50 ML. At this coverage, the adsorption energies for different sites are very similar.

This seems to disagree with the results from the IR experiments, where only the top adsorption is observed. The key may not be related to the energy, but to the surface dipole. Due to the large dipole moment of CN, the work functions vary remarkably; the surface dipole for CN on the top site is around 1 eV larger than for CN in the hollow-fcc site. Water interacts stronger with stronger dipoles, which could explain why the top adsorption is favored despite the negligible energetic difference with respect to other sites.

We have performed the adsorption of cyanide on the experimental structure and others of the same coverage. Within the cases analyzed so far, we have not found a substantial difference in energy or in the work function between these structures. We therefore consider the possibility that it is the presence of cations that makes the $2\sqrt{3} \times 2\sqrt{3}$ structure the most favorable one. This is in line with the fact that in the alternative structures discussed here, the cavities do not have the correct geometry to adsorb the cations, as they do in the experimental structure.

Finally, we have confirmed previous results concerning the adsorption of hydrogen. We found that the adsorption energy for hydrogen on the platinum atoms non-bonded to CN is very similar to that on clean Pt(111). However, the adsorption on the nitrogen atoms is favored by at least 0.8 eV. These results support the idea that the 0.2 V positive shift on the onset of the hydrogen adsorption is due to the formation of $CN_{ad}H$.

We obtained some preliminary values for the frequency of vibration corresponding to the C-N stretching mode, which is in line with the experimental results (figure 17.2). The adsorption of hydrogen on both the nitrogen atoms of CN_{ad} and on the platinum surface non-bonded to CN_{ad} decreases the frequency of the C-N vibration. In order to verify the results from this chapter, we shall verify that the tendencies observed also apply to the experimental structure. The corresponding calculations are currently running.

Bibliography

[1] A. Groß, *Theoretical Surface Science: A microscopic perspective*, Springer, Verlag Berlin Heidelberg, second edition, 2009.

[2] M. Gell-Mann, *The Quark and the jaguar: Adventures in the simplex and the complex*, Tusquets, 1995.

[3] W. S. Elizabeth Santos, Angew. Chem. Int. Edit. **46**, 8262 (2007).

[4] E. Santos and W. Schmickler, Chemical Physics **332**, 39 (2007).

[5] E. Santos, A. Lundin, K. Pötting, P. Quaino, and W. Schmickler, Phys. Rev. B **79**, 235436 (2009).

[6] B. Hammer, L. B. Hansen, and J. K. Nørskov, Phys. Rev. B **59**, 7413 (1999).

[7] D. Vanderbilt, "Phys. Rev. B" **41**, 7892 (1990).

[8] Y. Wang and J. P. Perdew, Phys. Rev. B **44**, 13298 (1991).

[9] J. P. Perdew et al., Phys. Rev. B **46**, 6671 (1992).

[10] K. S. Thygesen, L. B. Hansen, and K. W. Jacobsen, Phys. Rev. Lett. **94**, 026405 (2005).

[11] J. H. Monkhorst and D. J. Pack, Phys. Rev. B **13**, 5188 (1976).

[12] C. Kittel, *Introduction to Solid State Physics, Third ed., New York*, Wiley, 1967.

[13] W. Tyson and W. Miller, Surface Science **62**, 267 (1977).

[14] A. Bogozi et al., JACS **123**, 4585 (2001).

[15] C. Z. Li, H. Sha, and N. J. Tao, Phys. Rev. B **58**, 6775 (1998).

[16] H. X. He, C. Shu, C. Z. Li, and N. J. Tao, J. Electroanal. Chem. **522**, 26 (2002).

[17] M. Kiguchi, D. Djukic, and J. M. van Ruitenbeek, Nanotechnol. **18**, 035205 (2007).

[18] P. J. Castle and P. W. Bohn, Anal. Chem. **77**, 243 (2005).

[19] B. J. Murray et al., Analytical Chemistry **77**, 5205 (2005).

[20] J. Hu, T. W. Odom, and C. M. Lieber, Acc. Chem. Res. **32**, 435 (1999).

[21] C. Shu et al., Phys. Rev. Lett. **84**, 5196 (2000).

[22] B. Xu, H. He, S. Boussaad, and N. J. Tao, Electrochim. Acta **48**, 3085 (2003), Electrochemistry in Molecular and Microscopic Dimensions.

[23] N. Garcia, E. V. Ponizowskaya, H. Zhu, J. Q. Xiao, and A. Pons, Appl. Phys. Lett. **82**, 3147 (2003).

[24] J. M. Krans, J. M. van Ruitenbeek, V. Fisun, I. Yanson, and L. J. de Jongh, Nature **375**, 767 (1995).

[25] C. J. Muller, J. M. Krans, T. N. Todorov, and M. A. Reed, Phys. Rev. B **53**, 1022 (1996).

[26] J. M. van Ruitenbeek et al., Review of Scientific Instruments **67**, 108 (1996).

[27] U. Landman, W. D. Luedtke, B. E. Salisbury, and R. L. Whetten, Phys. Rev. Lett. **77**, 1362 (1996).

[28] J. I. Pascual et al., Science **267**, 1793 (1995).

[29] G. Rubio, N. Agraït, and S. Vieira, Phys. Rev. Lett. **76**, 2302 (1996).

[30] E. S. Snow, D. Park, and P. M. Campbell, Applied Physics Letters **69**, 269 (1996).

[31] C. Z. Li and N. J. Tao, Appl. Phys. Lett. **72**, 894 (1998).

[32] C. Z. Li, A. Bogozi, W. Huang, and N. J. Tao, Nanotechnol. **10**, 221 (1999).

[33] N. A. A. L. Yeyati and J. M. van Ruitenbeek, Phys. Rep. **377** (2003).

[34] P. Shi and P. W. Bohn, ACS Nano **2**, 1581 (2008).

[35] P. Shi and P. W. Bohn, ACS Nano **4**, 2946 (2010).

[36] E. P. M. Leiva, C. G. Sánchez, P. Vélez, and W. Schmickler, Phys. Rev. B **74**, 035422 (2006).

[37] S. Frank, C. Hartnig, A. Groß, and W. Schmickler, ChemPhysChem **9**, 1371 (2008).

[38] R. R. Nazmutdinov, M. D. Bronshtein, and W. Schmickler, Electrochim. Acta **55**, 68 (2009).

[39] G. Mészáros, S. Kronholz, S. Karthäuser, D. Mayer, and T. Wandlowski, Appl. Phys. A **87**, 569 (2007).

[40] J. Li, Y. Yamada, K. Murakoshi, and Y. Nakato, Chem. Commun. **21**, 2170 (2001).

[41] L. Jingze, K. Taisuke, M. Kei, and N. Yoshihiro, Appl. Phys. Lett. **81**, 123 (2002).

[42] T. Konishi, M. Kiguchi, and K. Murakoshi, Surf. Sci. **601**, 4122 (2007-09-15).

[43] M. Kiguchi and K. Murakoshi, Appl. Phys. Lett. **88**, 253112 (2006).

[44] J. Li, Y. Nakato, and K. Murakoshi, Chem. Lett. **34**, 374 (2005).

[45] E. Santos, P. Quaino, G. Soldano, and W. Schmickler, Electrochem. Commun. **11**, 1764 (2009).

[46] M. Kiguchi, T. Konishi, K. Hasegawa, S. Shidara, and K. Murakoshi, Phys. Rev. B **77**, 245421 (2008).

[47] W. Liang, M. Zhou, and F. Ke, Nano Letters **5**, 2039 (2005).

[48] P. Vélez, S. Dassie, and E. Leiva, Chem. Phys. Lett. **460**, 261 (2008).

[49] A. Delin, E. Tosatti, and R. Weht, Phys. Rev. Lett. **92**, 057201 (2004).

[50] V. Rodrigues, J. Bettini, P. C. Silva, and D. Ugarte, Phys. Rev. Lett. **91**, 096801 (2003).

[51] J. van Ruitenbeek, Nat Nano **1**, 164 (2006).

[52] J. Bettini et al., Nat Nano **1**, 182 (2006).

[53] A. L. Allred, J. Inorg. Nucl. Chem. **17**, 215 (1961).

[54] L. Pauling, JACS **54**, 3570 (1932).

[55] M. Kiguchi, R. Stadler, I. S. Kristensen, D. Djukic, and J. M. van Ruitenbeek, Phys. Rev. Lett. **98**, 146802 (2007).

[56] M. Kiguchi, T. Konishi, S. Miura, and K. Murakoshi, Nanotechnology **18**, 424011 (2007).

[57] J. K. Nørskov et al., J. Electrochem. Soc. **152**, J23 (2005).

[58] P. W. Atkins, *Physical Chemistry*, Oxford University Press, 6. edition, 1998.

[59] T. Bligaard et al., J. Phys. Chem. B **107**, 9325 (2003).

[60] K. Christmann, R. J. Behm, G. Ertl, M. A. V. Hove, and W. H. Weinberg, J. Chem. Phys. **70**, 4168 (1979).

[61] K. Christmann, G. Ertl, and O. Schober, Surf. Sci. **40**, 61 (1973).

[62] B. E. Spiewak, R. D. Cortright, and J. A. Dumesic, J. Catal. **176**, 405 (1998).

[63] G. Lee, D. B. Poker, D. M. Zehner, and E. W. Plummer, Surf. Sci. **357-358**, 717 (1996).

[64] G. Kresse and J. Hafner, Surf. Sci. **459**, 287 (2000).

[65] W. Dong, V. Ledentu, P. Sautet, A. Eichler, and J. Hafner, Surf. Sci. **411**, 123 (1998).

[66] W. R. P. K. W. D. J. H. G. J. Watson, Graeme W., J. Phys. Chem. B **105**, 4889 (2001).

[67] S. Sakong and A. Groß, Surf. Sci. **525**, 107 (2003).

[68] O. M. Lovvik and R. A. Olsen, J. Chem. Phys. **118**, 3268 (2003).

[69] A. Roudgar and A. Groß, Phys. Rev. B **67**, 033409 (2003).

[70] E. Santos et al., ChemPhysChem **12**, 2274 (2011).

[71] A. Roudgar and A. Groß, J. Electroanal. Chem. **548**, 121 (2003).

[72] Y. Gohda, S. Schnur, and A. Groß, Faraday Discuss. **140**, 233 (2009).

[73] J. Lennard-Jones, Trans. Faraday Soc. **28**, 333 (1932).

[74] S. R. Bahn, N. Lopez, J. K. Nørskov, and K. W. Jacobsen, Phys. Rev. B **66**, 081405 (2002).

[75] D. M. Gillingham, C. Müller, and J. A. C. Bland, Journal of Physics: Condensed Matter **15**, L291 (2003).

[76] J. Hong and R. Q. Wu, JKPS **47**, L553 (205).

[77] C. Zhang, R. N. Barnett, and U. Landman, Phys. Rev. Lett. **100**, 046801 (2008).

[78] M. J. Gladys, O. R. Inderwildi, S. Karakatsani, V. Fiorin, and G. Held, The Journal of Physical Chemistry C **112**, 6422 (2008).

[79] G. Kresse and J. Hafner, Phys. Rev. B **47**, 558 (1993).

[80] G. Kresse and J. Hafner, Phys. Rev. B **49**, 14251 (1994).

[81] G. Kresse and J. Furthmüller, Computational Materials Science **6**, 15 (1996).

[82] G. Kresse and J. Furthmüller, Phys. Rev. B **54**, 11169 (1996).

[83] A. KOverga, M. Koper, W. adsorption, P. dissociation on Pt(111), and P. surfaces: a DFT study, (in preparation) .

[84] E. C. Walter et al., J. Phys. Chem. B **106**, 11407 (2002).

[85] C. E. Cross, J. C. Hemminger, and R. M. Penner, JACS **23**, 10372 (2007).

[86] P. Quaino, M. G. de Chialvo, and M. Vela, J. Argent. Chem. Soc. **93**, 215 (2005).

[87] Y. Baskin and L. Meyer, Phys. Rev. **100**, 544 (1955).

[88] E. Santos, P. Quaino, and W. Schmickler, Electrochimica Acta **55**, 4346 (2010), SENSOR AND SENSOR TECHNOLOGY, Selection of papers from the 1st International Symposium on Electrochemistry; SURFACE IMAGING/SPECTROSCOPY AT THE SOLID/LIQUID INTERFACE, Selection of papers from the 2nd International Symposium.

[89] P. J. M. Gsell and D. Menzel, Science **280**, 5364 (1998).

[90] P. Jakob, M. Gsell, and D. Menzel, The Journal of Chemical Physics **114**, 10075 (2001).

[91] S. Pandelov and U. Stimming, Electrochimica Acta **52**, 5548 (2007), Surface Imaging/Spectroscopy at Solid/Liquid Interface (ISSIS) - Selection of papers from the International Symposium on Surface Imaging/Spectroscopy at Solid/Liquid Interface (ISSIS) , May 28 to June 1, 2006, Krakow, Poland.

[92] C. Köntje, L. Kibler, and D. Kolb, Electrochimica Acta **54**, 3830 (2009).

[93] J. Meier, K. A. Friedrich, and U. Stimming, Faraday Discuss. **121**, 365 (2002).

[94] P. Quaino, E. Santos, H. Wolfschmidt, M. Montero, and U. Stimming, Catalysis Today .

[95] L. A. Kibler, M. Kleinert, and D. M. Kolb, J. Electroanal. Chem. **467**, 249 (1999).

[96] J. Inukai and M. Ito, Journal of Electroanalytical Chemistry **358**, 307 (1993), An International Journal Devoted to all Aspects of Electrode Kinetics, Interfacial Structure, Properties of Electrolytes, Colloid and Biological Electrochemistry.

[97] G. A. Attard, R. Price, and A. Al-Akl, Surface Science **335**, 52 (1995), Proceedings of the IUVSTA Workshop on Surface Science and Electrochemistry.

[98] R. Gómez, A. Rodes, J. M. Pérez, J. M. Feliu, and A. Aldaz, Surface Science **327**, 202 (1995).

[99] R. Gómez, A. Rodes, J. M. Pérez, J. M. Feliu, and A. Aldaz, Surface Science **344**, 85 (1995).

[100] H. Yanagita, H. Fujioka, T. Aruga, N. Takagi, and M. Nishijima, Surface Science **441**, 507 (1999).

[101] S. Mann, T. Seto, C. Barnes, and D. King, Surface Science **261**, 155 (1992).

[102] S. Wilke, V. Natoli, and M. H. Cohen, The Journal of Chemical Physics **112**, 9986 (2000).

[103] G. Jerkiewicz, Progress in Surface Science **57**, 137 (1998).

[104] E. I. Altman and R. J. Colton, Surface Science **304**, L400 (1994).

[105] A. Michaelides and K. Morgenstern, Nat Mater **6** (2007).

[106] L. Vitos, A. V. Ruban, H. L. Skriver, and J. Kollr", Surface Science **411**, 186 (1998).

[107] J. I. Colonell, T. J. Curtiss, and S. J. Sibener, Surface Science **366**, 19 (1996).

[108] B. Hammer and J. K. Nørskov, Surf. Sci. **343**, 211 (1995).

[109] B. Hammer and J. K. Nørskov, Nature **376** (1995).

[110] R. A. Marcus, The Journal of Chemical Physics **24**, 966 (1956).

[111] W. Schmickler and E. Santos, *Interfacial Electrochemistry*, Springer, Heidelberg, second edition, 2010.

[112] N. B. Arboleda and H. Kasai, Surf. Interface Anal. **40**, 1103 (2008).

[113] C. Resch, H. Berger, K. Rendulic, and E. Bertel, Surface Science **316**, L1105 (1994).

[114] J. L. Stickney, S. D. Rosasco, G. N. Salaita, and A. T. Hubbard, Langmuir **1**, 66 (1985).

[115] C. Stuhlmann, I. Villegas, and M. J. Weaver, Chemical Physics Letters **219**, 319 (1994).

[116] Y.-G. Kim, S.-L. Yau, and K. Itaya, Journal of the American Chemical Society **118**, 393 (1996).

[117] A. Cuesta, Journal of the American Chemical Society **128**, 13332 (2006).

[118] A. Cuesta, M. Escudero, B. Lanova, and H. Baltruschat, Langmuir **25**, 6500 (2009).

[119] A. Cuesta and M. Escudero, Phys. Chem. Chem. Phys. **10**, 3628 (2008).

[120] M. Escudero-Escribano et al., ChemPhysChem , n/a (2011).

[121] F. J. Huerta, E. Morallón, J. Vazquez, and A. Aldaz, Surface Science **396**, 400 (1998).

Summary

One of the biggest challenges of this century is to produce sustainable and environmental friendly devices that can cope with the constantly increasing energy demand. Particularly for vehicles, hydrogen-oxygen fuel cells are among the most promising solutions for this issue. The common aim along the different parts of this thesis is to investigate nanostructures as promising catalysts for the hydrogen evolution reaction.

We started by addressing an ultimate case of the nanoscale: **Free-standing monoatomic nanowires**. Several transition metals, such as Au, Ag, Cu, and Pd can be thinned down until the formation of monoatomic chains. The first scientific problem we faced, concerned an intriguing electronic behavior of the nanowires: Fractional conductance. It is well-known that, as the wires get thinner, the conductance drops until it becomes quantized and its value is ideally a multiple of $2e^2/h$ (G_0). Nevertheless, there is a puzzling deviation of this phenomenon. On Ag wires, the conductance is, as expected, a multiple of G_0, regardless of the potential. However, at potentials below the onset of the hydrogen evolution, Cu and Au exhibit *fractional* conductance. The authors ascribed this phenomenon to the adsorption of hydrogen. There is, however, a problem with this idea: at least on the three planar surfaces of the three coin metals, hydrogen does not adsorb. This puzzle motivated our study of the thermodynamics and kinetics of hydrogen adsorption on the wires. Surprisingly, we found that the latter is 1 eV more stable on Au wires than on Au(111) surfaces. Indeed, the adsorption of hydrogen on Cu and Au becomes exergonic on the wire. Using the Schmickler-Santos theory for the proton adsorption in water, we obtained an activation barrier of 0.1 and 0.5 eV, respectively, in comparison with 0.7 eV corresponding to their (111) surface metals. The activation energy required for dissociation of H_2 is 0.3 eV for Au nanowires, 1.5 eV for Ag, 0.5 eV for Cu, below 0.4 eV for Ni and Pt, and negligible for Pd nanowires. These results are in perfect agreement with the hypothesis that hydrogen adsorption on nanowires triggers the fractional conductance observed experimentally on Cu and Au, but not on Ag.

In order to explain this notable enhancement of the reactivity, we investigated the density of states and the charge density distribution on the wires. The electronic charge distribution of monometallic wires is remarkably similar to that of metal surfaces. Nevertheless, a notable difference in the reactivity was found. The d band of

Cu and Au, which lies well below the Fermi level for their surfaces, is shifted upward for nanowires, reaching the Fermi energy. This leads to a remarkable enhancement of the reactivity.

During the research, we found other topics worth investigating, such as mechanical properties. According to DFT calculations, in the equilibrium configuration the atoms should have a zigzag arrangement. However, as it has been experimentally observed, the wires are pulled by their bulk sides, adopting a linear arrangement. In this linear configuration the wires are under a typical stress of 1 Å/eV and a strain of at least 0.5 eV. A crucial parameter to examine, in order to predict their stability, is the surface energy σ. For the cases studied here, two groups were distinguished: Ag and Au nanowires, with lower σ, and Cu, Ni, Pd, and Pt nanowires, with a higher one. Accordingly, several experiments from different groups showed that the former are intrinsically more stable than the latter. The mono-dimensionality of these systems can lead to striking behaviors, such as the magnetization of Pd over a certain range of intermetallic distances. In some cases, the combination of different metals forming atomic chains leads to stability enhancement. Noteworthy are Au-Cu and Au-Ag bimetallic wires, which were indeed obtained experimentally. We predict that Au-Pd, Ag-Cu, and Au-Ni should also form stable combinations.

The enhanced reactivity is also manifested in the great affinity for oxygen. In this case, oxygen adsorption on Pd, Pt, and Cu nanowires is at least 0.5 eV more stable than on Ag and Au chains. It was found that the incorporation or absorption of oxygen is more favorable than the isolated adsorption, which makes these wires bad catalysts for the oxygen reduction reaction. For oxygenated chains (where oxygen and metal atoms are intercalated), the zigzag configuration is generally the most stable one. Interestingly, in contrast to pure zigzag wires, the elongation of the oxygenated chains from the equilibrium distance is almost stress-free for over 1 Å. Also for oxygenated wires, a strong spin dependence of the intermetallic distance was found, even for non-magnetic wires such as Cu. There is experimental evidence of this phenomenon as well.

Water dissociation is an interesting case to examine since the molecule is not specifically adsorbed on the wire, so that the enhanced reactivity should have no major effect. Indeed, the adsorption energy of H_2O on platinum wires was found to be subtly exothermic: -0.1 eV. Still, the dissociation is more favorable than on Pt(111) since hydrogen and OH are more strongly adsorbed on the wire than on the surface. It was also found that the infinite linear chain is an efficient representation of more complex wires, such as atomic chains attached to cluster or bulk metals.

As promising as nanowires may seem for electrocatalysis, they are not suitable for the hydrogen evolution reaction in practical terms, principally due to their instability as a chain. Therefore, we moved on to testing more stable systems: **graphite-supported wires**. The two most stable graphite steps were considered: *armchair*

and *zigzag* steps. Ni, Pd, Pt, Cu, Ag, and Au one-atom-thick wires were adsorbed at the edges of these steps forming the so-called armchair and zigzag graphite-supported wires. The major difference between them is that in the zigzag case all the metal atoms are equivalent, whereas in the armchair case one type of metal atom is strongly bonded to two carbon atoms, and the other type is weakly bonded to the graphite step or not bonded to it at all. In general, these zigzag wires are substantially more stable than the armchair ones, only in the case of Au both configurations are equivalent in energy. Another general trend is that the supported wires of the Ni periodic column are more stable than the supported wires of the Cu periodic column. The occupation of the antibonding states that result from the wire-step interaction is lower for the Ni periodic column than for the Cu one, which explains their different binding energies. In fact, Ni, Pd, and Pt zigzag wires have this antibonding state empty. For the armchair case the former state is partially or half-filled, the reason why the zigzag configuration is more stable than the armchair one.

As a consequence of their instability, at high hydrogen coverages the three coin metals desorb from the graphite step. Only in the case of Cu this trend is not observed and an equilibrium between hydrogen on the Cu supported wire and at the graphite step can exist. On the other hand, hydrogen adsorption on the metals is favored for Ni, Pd, and Pt supported wires.

At low hydrogen coverage, the hydrogen adsorption energy is quite site dependent, changing over a range of 1 eV. These results and analysis of the density of states suggest that the projected $1s$ state of hydrogen is more localized on this supported wires than on the free-standing wires. The d band model predicts the chemisorption strength of supported wires qualitatively well. Since the d band center is more up-shifted for the armchair case than for the zigzag one, hydrogen adsorption is stronger on the former case. On Ni and Cu armchair wires hydrogen adsorption is stronger than what the d band model predicts, probably due to the strong participation of the valence s states of the metals.

In the chapters summarized so far, we studied the influence of the structure *size* on the physical and chemical properties of several metals. In the last part of this thesis we focus on the *structure* of metal surfaces as an essential property for **surface tuning**. Two cases were considered: Rh layers over Au(111) and Pd(111) substrates – Rh/Au(111) and Rh/Pd(111), respectively – and CN-modified Pt(111) surfaces. Metal monolayers on foreign metal substrates have fascinating catalytic properties. They are only stable if there is a strong chemical bonding between the monolayer and the substrate, so there is always a pronounced chemical or ligand effect. If the lattice constant of the adsorbed metal is smaller than that of the substrate, as it is the case for Rh/Au(111) and Rh/Pd(111), the induced strain leads to an upward shift of the d band center of late transition metals, which increases the

reactivity. In the case of Rh/Au(111), the lattice mismatch is particularly large, and the monolayer is only stable because the chemical interaction is so strong. Hence, both the chemical and the d band effect are large, and combine to make this a very promising candidate for hydrogen electrocatalysis. Indeed, both the Volmer and the Tafel reactions (hydrogen adsorption and recombination, respectively) are extremely fast. For comparison, the Volmer reaction rate on Rh/Au(111) is of the same order of magnitude as on pure Pt(111); however, for the Tafel reaction the energy barrier is 0.2 eV lower for Rh/Au(111) than for Pt(111). Since the rate constant depends exponentially on the activation energy by $e^{\Delta E_a/kT}$, a difference of 0.2 eV corresponds to a remarkable change in the overall rate of three orders of magnitude. On Rh/Pd(111) the induced strain is weaker, so its catalytic properties are expected to be not quite as good. However, it can support several commensurate layers, which in itself is an interesting property.

To the best of our knowledge, there are no experimental investigations for hydrogen evolution or oxidation on these systems. Thus, our work is a prediction and an example of the new role theory has taken on during the last decade: Previously, theory used to follow the experimentalists trying to explain their data. Nowadays, experiments can be guided by theoretical predictions.

As we can see, a foreign metal substrate can affect dramatically the electronic features of a metal surface, and therefore its catalytic properties. However, the catalytic improvement cannot only be achieved by this induced electronic effect. In fact, even adsorbates that do not affect the electronic states of a surface can improve a catalyst radically: They can inhibit an undesired reaction by blocking the surface sites at which it occurs, and leave the sites necessary for the reaction of interest available. This is the case of CN-Pt(111), which can catalyse the oxidation of small organic molecules, inhibiting the production of CO – a catalyst poisoning species.

The cyanide coverage corresponding to the experimental structure is $\theta=0.50$ ML. At this coverage, the adsorption energies for different sites are very similar. This seems to disagree with the results from the IR experiments, where only the top adsorption is observed. The key may not be related to the energy, but to the surface dipole. Due to the large dipole moment of CN, the work functions vary remarkably; the surface dipole for CN on the top site is around 1 eV larger than for CN in the hollow-fcc site. Water interacts stronger with stronger dipoles, which could explain why the top adsorption is favored despite the negligible energetic difference with respect to other sites.

We have investigated the adsorption of cyanide on the experimental structure and others of the same coverage. Within the cases analyzed so far, we have not found a substantial difference in energy or in the work function between these structures. We therefore consider the possibility that it is the presence of cations that makes the $2\sqrt{3}\times2\sqrt{3}$ structure the most favorable one. This is in line with the fact that in the alternative structures discussed here the cavities do not have the correct geometry

to adsorb the cations, as they do in the experimental structure.

Finally, we have confirmed previous results concerning the adsorption of hydrogen. We found that the adsorption energy for hydrogen on the platinum atoms non-bonded to CN is very similar to that on clean Pt(111). However, the adsorption on the nitrogen atoms is favored by at least 0.8 eV. These results support the idea that the positive shift on the onset of the hydrogen adsorption is due to the formation of $CN_{ad}H$.

As it has been exemplified very briefly in this work, our understanding of electrocatalysis has improved and enriched over the last 30 years; science has once again broadened our perspective of the universe. The size of the systems that we can work with are experimentally each time smaller, and quantum-theoretically each time bigger. This leads to a fascinating synergy of the fields by which they can test, guide, and feed each other. There is still a lot to discover. There is still a lot to be asked.

Zusammenfassung

Eine der größten Herausforderungen dieses Jahrhunderts ist die Produktion nachhaltiger Resourcen zur Energiegewinnung, die mit dem stetig zunehmenden Energiebedarf mithalten können. Insbesondere für Fahrzeuge ist die Wasserstoffbrennstoffzelle unter den aussichtsreichsten Lösungen für dieses Problem. Die einzelnen Teile dieser Arbeit haben die Untersuchung von Nanostrukturen als viel versprechende Katalysatoren für die Wasserstoff-Entwicklung als gemeinsames Ziel. Am Anfang haben wir uns einem Grenzfall des Nanobereichs zugewandt: **frei stehende, monoatomare Nanodrähte**. Verschiedene Übergangsmetalle wie Au, Ag, Cu und Pd können bis zur Bildung von monoatomaren Ketten verdünnt werden. Das erste wissenschaftliche Problem, das wir in Angriff nahmen, betrifft ein verblüffendes elektronisches Verhalten von Nanodrähten: Fraktionelle Leitfähigkeit. Es ist bekannt, dass, wenn Drähte dünner werden, die Leitfähigkeit abnimmt bis sie gequantelt ist und ihr Wert idealerweise ein Vielfaches von $2e^2/h$ (G_0) beträgt. Eine Abweichung von diesem Phänomen jedoch gibt Rätsel auf: Die Leitfähigkeit von Ag-Drähten ist wie erwartet ein Vielfaches von G_0, unabhängig vom Potential. Cu und Au hingegen weisen fraktionelle Leitfähigkeit auf bei Potentialen im Bereich der Wasserstoff-Entwicklung. Die Autoren schrieben dieses Phänomen der Wasserstoffadsorption zu, aber diese Lösung hat einen Haken: Wasserstoff adsorbiert nicht an den planaren Oberflächen der drei Münzmetalle. Dieses Rätsel war die Motivation für unsere Studie der Thermodynamik und Kinetik der Wasserstoffadsorption an Drähten. Überraschenderweise fanden wir selbige 1 eV energetisch günstiger an Au-Drähten als an Au(111)-Oberflächen. Und in der Tat ist die Adsorption von Wasserstoff an Cu- und Au-Drähten exergonisch. Unter Verwendung der Schmickler-Santos-Theorie für die Protonadsorption in Wasser haben wir eine Aktivierungsbarriere von 0,1 bzw. 0,5 eV ermittelt, im Vergleich zu 0,7 eV für die entsprechenden (111)-Oberflächen der Metalle. Die Aktivierungsenergie für die Dissoziation von H_2 beträgt 0,3 eV für Au-Nanodrähte, 1,5 eV für Ag, 0,5 eV für Cu, weniger als 0,4 eV für Ni und Pt, und ist vernachlässigbar für Pd-Nanodrähte. Diese Ergebnisse sind in sehr guter Übereinstimmung mit der Hypothese, dass Wasserstoffadsorption an Nanodrähten die fraktionelle Leitfähigkeit verursacht, welche experimentell an Cu und Au, aber nicht an Ag beobachtet wurde. Um diese beachtliche Steigerung der Reaktivität zu erklären, untersuchten wir die Zustandsdichte und Elektronen-

dichteverteilung in den Drähten. Die Elektronendichteverteilung in monometallischen Drähten ist der von Metalloberflächen bemerkenswert ähnlich, dennoch fanden wir einen beträchtlichen Unterschied in der Reaktivität. Das d-Band von Cu und Au, welches an Oberflächen weit unter dem Fermi Niveau liegt, ist im Falle von Nanodrähten zu höheren Energien verschoben und erreicht die Fermi-Energie. Dies führt dann zu der beschriebenen höheren Reaktivität. Während unserer Arbeit stießen wir auf weitere Themen, die einer genaueren Betrachtung wert sind, so zum Beispiel die mechanischen Eigenschaften der Nanodrähte. DFT-Berechnungen zufolge sollten die Atome in der Gleichgewichtskonfiguration eine Zickzack-Anordnung einnehmen. Wie jedoch aus Experimenten bekannt ist, werden diese an beiden Seiten in eine lineare Anordnung gezogen. Die Drähte unterliegen in dieser linearen Konfiguration typischerweise einem Stress von 1 Å/eV und sind um mindestens 0,5 eV weniger stabil als die zickzack-Konfiguration. Ein entscheidender Parameter, der zu untersuchen ist, um die Stabilität vorherzusagen, ist die Oberflächenenergie. Die hier betrachteten Systeme wurden in zwei Gruppen unterteilt: Ag und Au-Nanodrähte, die eine niedrigere Oberflächenenergie aufweisen, und Cu, Ni, Pd und Pt-Nanodrähte mit einer höheren. Dementsprechend zeigen mehrere Experimente von verschiedenen Forschungsgruppen, dass erstere an sich stabiler sind als die zuletzt genannten. Die Eindimensionalität dieser Systeme kann zu einem verblüffendem Verhalten führen, wie die Magnetisierung von Pd über einen bestimmten Bereich intermetallischer Abstände. Die Kombination von verschiedenen Metallen, die atomare Ketten bilden, führt in manchen Fällen zu einer erhöhten Stabilität. Erwähnenswert sind hier die bimetallischen Drähten aus Au-Cu und Au-Ag, welche auch schon experimentell hergestellt wurden. Wir prognostizieren, dass auch Au-Pd, Ag-Cu und Au-Ni stabile Kombinationen bilden sollten. Die erhöhte Reaktivität offenbart sich auch in der ausgeprägten Sauerstoffaffinität. In diesem Fall ist die Sauerstoffadsorption an Pd, Pt und Cu-Nanodrähten um mindestens 0,5 eV stabiler als an Ag und Au-Drähten. Die Einbindung oder Absorption von Sauerstoff zeigt sich energetisch günstiger als die isolierte Adsorption, was diese Drähte zu schlechten Katalysatoren für die Sauerstoff-Reduktion macht. Die sauerstoffangereicherten Drähte (in denen Sauerstoff- und Metallatome interkaliert sind) sind am stabilsten in der Zickzack-Konfiguration. Interessanterweise ist die Dehnung der sauerstoffangereicherten Drähte vom Gleichgewichtsabstand, im Gegensatz zu reinen Zickzack-Drähten nahezu stressfrei über mehr als 1 Å. Ebenso beobachtet wurde eine starke Spinabhängigkeit des intermetallischen Abstands in sauerstoffangereicherten Drähten, auch für nichtmagnetische Drähte wie Cu. Für dieses Phänomen gibt es auch experimentelle Belege. Die Dissoziation von Wasser ist ein interessanter Fall, da das Molekül nicht chemisch an dem Draht adsorbiert, so dass die erhöhte Reaktivität keinen besonderen Effekt haben sollte. Tatsächlich wurde eine leicht exotherme Adsorptionsenergie von Wasser an Platindrähten beobachtet: -0,1 eV, was die Dissoziation immer noch energetisch günstiger macht als an Pt(111), da Wasserstoff und OH stärker am

Draht adsorbieren als an der Oberfläche. So viel versprechend Nanodrähte für die Verwendung in der Elektrokatalyse auch erscheinen mögen, für die praktische Anwendung in der Wasserstoff-Entwicklung sind sie nicht geeignet, hauptsächlich aufgrund ihrer Instabilität als Kette. Daher sind wir einen Schritt weitergegangen und haben stabilere Systeme getestet: **Drähte auf Graphitträgern**. Betrachtet wurden die zwei stabilsten Graphitstufen: Sessel- und Zickzack-Stufen. Ni, Pd, Pt, Cu, Ag und Au-Draht von der Dicke eines Atoms wurden an den Kanten dieser Stufen adsorbiert und formten die sogenannten Sessel- und Zickzack-graphitgetragenen Drähte. Der Hauptunterschied zwischen den beiden Formen ist, dass in der Zickzack-Konfiguration alle Metallatome äquivalent sind, wohingegen in der Sessel-Form eine Sorte von Metallatomen stark an zwei Kohlenstoffatome gebunden ist, und die andere Sorte schwach oder nicht an der Graphitstufe gebunden ist. Generell sind die Zickzack-Drähte stabiler als die der Sessel-Form, außer im Fall von Au, für das beide Konfigurationen energetisch äquivalent sind. Ein weiterer allgemeiner Trend ist, dass die an einen Träger gebundenen Drähte der Ni-Gruppe stabiler sind als die der Cu-Gruppe. Die aus der Draht-Stufen-Interaktion resultierende Besetzung der antibindenden Zustände ist niedriger im Fall der Ni- Gruppe als für die Cu-Gruppe, was die verschiedenen Bindungsenergien erklärt. In Ni, Pd und Pt Zickzack-Drähten sind diese antibindenden Zustände unbesetzt, in den entsprechenden Sessel-Formen aber halb oder teilweise besetzt, was die Zickzack- Form stabiler macht als die Sessel-Form. Als eine Konsequenz ihrer Instabilität desorbieren die drei Münzmetalle bei hohen Wasserstoff-Bedeckungsgraden von der Graphitstufe. Im Falle von Cu kann dieser Trend nicht beobachtet werden, und es stellt sich ein Gleichgewicht zwischen Wasserstoff auf der Graphitstufe und dem darauf gebundenen Cu-Draht ein. Wasserstoff-Adsorption am Metall ist hingegen energetisch begünstigt für Ni, Pd und Pt auf Graphit. Für niedrige Bedeckungsgrade ist die Wasserstoff-Adsorptionsenergie abhängig von der Position, die Werte variieren bis zu 1 eV. Diese Ergebnisse und die Betrachtung der Zustandsdichten lassen darauf schließen, dass das 1s Orbital des Wasserstoffs an getragenen Drähten lokalisierter ist als an freistehenden Drähten. Mit dem d-Band-Modell kann die Stärke der Chemisorp- tion von getragenen Drähten qualitativ gut berechnet werden. Nachdem die Mitte des d-Bands bei Drähten der Sessel-Form stärker zu höheren Energien verschoben ist als bei der Zickzack-Form, ist die Wasserstoff-Adsorption an ersteren stärker. An Ni und Cu-Drähten in der Sessel-Form hingegen ist die Wasserstoffadsorption stärker als vom d-Band-Modell vorausgesagt, was wahrscheinlich auf die starke Beteiligung der s-Orbitale der Metalle zurückzuführen ist. In den bis hier zusammengefassten Kapiteln haben wir uns mit dem Einfluss der Strukturgröße auf die physikalischen und chemischen Eigenschaften von verschiedenen Metallen beschäftigt. Im letzten Abschnitt dieser Arbeit konzentrieren wir uns auf die Struktur von Metalloberflächen als einer essentiellen Eigenschaft für **Oberflächentuning**. Zwei Fälle wurden betrachtet: Rh-Schichten auf Au(111)- und Pd(111)-Substraten [im Fol-

genden Rh/Au(111) bzw. Rh/Pd(111)] und CN- modifizierte Pt(111) Oberflächen. Metall-Monoschichten auf Fremdmetallsubstraten haben faszinierende katalytische Eigenschaften. Sie sind nur stabil im Fall einer starken chemischen Bindung zwischen der Monoschicht und dem Substrat, so dass immer ein deutlicher chemischer oder Ligandeneffekt vorliegt. Wenn die Gitterkonstante des adsorbierten Metalls kleiner als die des Substrats ist, wie im Fall von Rh/Au(111) und Rh/Pd(111), führt die induzierte Dehnung zu einer Verschiebung des d-Band Zentrums von späten Übergangsmetall zu höheren Energien, was zu einer erhöhten Reaktivität führt. Im Fall von Rh/Au(111) ist die Gitterfehlanpassung besonders groß, und die Monoschicht ist nur aufgrund der starken chemischen Wechselwirkungen stabil. Dadurch sind der chemische und der d-Band-Effekt groß und machen dieses System zu einem viel versprechenden Kandidaten für die Wasserstof-Elektrokatalyse, und in der Tat sind die Aktivierungsenergien für die Volmer-Reaktion und die Tafel-Reaktion (Wasserstoffadsorption bzw. Rekombination) nach unseren Rechnungen sehr klein. Zum Vergleich, ist die Volmer-Reaktionsgeschwindigkeit für Rh/Au(111) in derselben Größenordnung wie an reinem Pt(111), hingegen ist die Energiebarriere für die Tafel-Reaktion 0,2 eV niedriger für Rh/Au(111) als für Pt(111). Nachdem die Geschwindigkeitskonstante exponentiell von der Aktivierungsenergie abhängt, bedeutet eine Reduktion von 0,2 eV einen signifikanten Unterschied von drei Größenordnungen in der Gesamtrate. An Rh/Pd(111)-Systemen ist die induzierte Dehnung schwächer und die erwartete katalytische Kapazität weniger gut. Es können jedoch mehrere entsprechende Schichten aufgetragen werden, was für sich genommen schon eine interessante Eigenschaft darstellt. Nach unserem Wissen gab es bisher noch keine experimentellen Untersuchungen zur Wasserstoffentwicklung oder Oxidation an diesen Systemen. Demnach ist unsere Arbeit eine Prognose und ein Beispiel für die neue Rolle, die die Theorie im letzten Jahrzehnt eingenommen hat. Ursprünglich wurde in der Elektrochemie die Theorie genutzt, um experimentelle Ergebnisse zu erklären, heute können Experimente mit Hilfe von theoretischen Voraussagen unterstützt und angeleitet werden. Wir haben also gesehen, dass ein Fremdmetallsubstrat den elektronischen Charakter und damit die katalytischen Eigenschaften von Metalloberflächen drastisch beeinflussen kann. Aber eine Verbesserung der katalytischen Eigenschaften kann nicht nur durch diesen induzierten elektronischen Effekt erzielt werden, auch Adsorbate, die die elektronischen Zustände einer Oberfläche nicht beeinflussen, können einen Katalysator radikal verbessern: Sie können eine unerwünschte Reaktion unterbinden, indem sie die Oberfläche an den Stellen blockieren, an denen die Reaktion stattfinden würde und die Stellen unbesetzt lassen, die für die gewünschte Reaktion notwendig sind. Genau das ist der Fall für das System CN-Pt(111), welches die Oxidation von kleinen organischen Molekülen katalysieren kann, während die Produktion von CO, einem Katalysatorgift, unterbunden wird. Der Cyanid-Bedeckungsgrad entsprechend der experimentellen Struktur beträgt 1/2. Bei diesem Bedeckungsgrad sind die Adsorp-

tionsenergien für verschiedene Oberflächenpositionen sehr ähnlich, was den Ergebnissen von IR-Experimenten zu widersprechen scheint, bei denen nur Adsorption an Top-Positionen beobachtet wurde. Der Grund hierfür ist vielleicht nicht begründet in der Energie, sondern dem Oberflächendipol. Aufgrund des großen Dipolmoments von CN variiert die Austrittsarbeit beträchtlich; der Oberflächendipol von CN an einer Top-Position ist etwa 1 eV größer als der von CN in der hollow fcc Position. Wasser wechselwirkt stärker mit stärkeren Dipolen, was erklären könnte, warum die Top-Adsorption trotz des vernachlässigbaren energetischen Unterschieds bevorzugt ist im Vergleich zu anderen Positionen. Wir haben die Adsorption von Cyanid an der experimentellen Struktur und anderen mit gleichem Bedeckungsgrad untersucht. Bei den bisher analysierten Fällen haben wir keinen wesentlichen Unterschied in der Energie gefunden und ziehen daher die Möglichkeit in Betracht, dass die Anwesenheit von Kationen die $2\sqrt{3}\times2\sqrt{3}$ Struktur bevorzugt. Das steht im Einklang mit der Tatsache, dass die Hohlräume in den hier diskutierten alternativen Strukturen nicht die passende Geometrie aufweisen, um die Kationen zu adsorbieren wie es in den experimentellen Strukturen der Fall ist. Schließlich konnten wir bisherige Ergebnisse bezüglich der Adsorption von Wasserstoff bestätigen. Wir fanden die Adsorptionsenergie für Wasserstoff an Platinatomen, die nicht an CN gebunden sind, sehr ähnlich der an einer freien Pt(111)-Oberfläche, wohingegen die Adsorption an Stickstoffatomen um mindestens 0,8 eV bevorzugt ist. Diese Ergebnisse untermauern die Vorstellung, dass die positive Verschiebung am Beginn der Wasserstoffadsorption durch die Bildung von CNad H verursacht wird. Wie exemplarisch in dieser Arbeit dargestellt, hat sich unser Verständnis in der Elektrokatalyse in den letzten 30 Jahren kontinuierlich verbessert und die Forschung bereichert, die Wissenschaft hat wieder einmal unser Blickfeld auf das Universum erweitert. Die Systeme, mit denen wir arbeiten können, werden experimentell immer kleiner und quantentheoretisch immer größer. Das führt zu einer faszinierenden Synergie der Forschungsgebiete, die einander testen, anleiten und fördern. Es gibt noch immer eine Menge zu erforschen. Es gibt noch immer eine Menge zu erfragen.

List of publications

The following articles were published or accepted:

- **1)** Electrochemical reactivity and fractional conductance of nanowires. E. Santos, G. Soldano, P. Quaino, and W. Schmickler. *Electrochem. Comm.* **11**, 1764 (2009).
–Chapter 5 and 7–

- **2)** Some properties of electrochemical nanostructures. E. Santos, G. Soldano, P. Quaino, and W. Schmickler. *J. Chem. Sciences (India)*, special issue to honour the late Prof. S.K. Rangarajan **121**, 575 (2009).
–Chapter 5 and 7–

- **3)** Intrinsic stability and hydrogen affinity of pure and bimetallic nanowires. G. Soldano, E. Santos, and W. Schmickler, *J. Chem. Phys.*, **134**, 174106 (2011).
–Chapter 5-8–

- **4)** Hydrogen electrocatalysis on single crystals and on nanostructured electrodes. E. Santos, P. Hindelang, P. Quaino, E.N. Schulz, G. Soldano, and W. Schmickler. *ChemPhysChem*, in press.
–Chapter 5 and 16–

- **5)** Stability of gold and platinum nanowires on graphite edges. G. Soldano, P. Quaino, E. Santos, and W. Schmickler, *ChemPhysChem*, **11**, 2361 (2010).
–Chapter 14 and 15–

- **6)** Recent progress in hydrogen electrocatalysis. P. Quaino, E. Santos, G. Soldano, and Wolfgang Schmickler, *Advances in Physical Chemistry*, **2011**, 1 (2011).
–Chapter 14 and 15–

- **7)** Hydrogen electrocatalysis on overlayers of rhodium over gold and palladium substrates – more active than platinum? G. Soldano, E. Schulz, E. Santos, and W. Schmickler. *Phys. Chem. Chem. Phys.* (accepted).
–Chapter 16–

The following articles were submited:

- **8)** Oxygen adsorption on pure and bimetallic nanowires, a theoretical study. M. C. Gimenez, and G. Soldano. *ChemPhysChem* (submitted).
–Chapter 10–

Curriculum Vitae

Personal Data

Place and Date of Birth:	Córdoba, Argentina — 16/11/1983
Address:	Albert Einstein Allee 11, PO: 89081 Ulm
Phone and Fax:	+49 731 50-31344 — +49 731 50-22819
Citizenship:	Argentinian and Italian
email:	german.soldano@uni-ulm.de
Civil State:	Single

Education

11/2002	Graduated from the Superior School of Commerce Manuel Belgrano, Córdoba. Title: "Bachelor Orientated in Natural Science and Basic Environmental Problematic"
08/2005 **10/2005**	XII seminary of "Pacific uses of Nuclear Energy". Exact Science Faculty (UNC) and National Commission of Atomic Energy.
12/2007	Licentiate in Chemistry, National University of Córdoba, Argentina. Average mark: 8.84 over 10. Licentiate thesis: Theoretical studies of carbon nanotubes filled with iron"

Languages

English	Speak, read, write (IICANA, "Approved")
Spanish	Native language

Work Experience

04/2008 to date	PhD student of Prof. Schmickler's group (University of Ulm, Germany).
10/2010 11/2010	Integrant of the project *Hydrogen economy: Theoretical and experimental studies of the electrocathalytic activity of materials for fuel cells and other applications.* Program of Scientiffic/Technologycal cooperation between Argentina and Germany under the direction of Dr. A. Chialvo y Dr. W. Schmickler. Project AL0806. (PRELINE, Universidad del Litoral, Santa Fé, Argentina).
10/2009 02/2010	Tutor of "Physical Chemistry for Advanced Materials Students "dictated by E. Santos (University of Ulm, Germany).
06/2008 09/2008	Participant of the Short Term Scientific Mission program -COST D36- under the supervision of Marc Koper. *DFT calculations performing H_2O adsorbance on Pt infinite nanowires.* (Leiden Institute of Chemistry, The Netherlands).
09/2005 04/2008	Undergraduate Teaching Assistance position (Faculty of Chemistry, National University of Córdoba, Argentina).
06/2005 08/2006	Undergraduate researcher position at the department of Organic Chemistry under the supervision of Dr. Mariano Vera and Dr. Adriana Pierini. *Theoretical and experimental studies of organic reactions and synthesis.* (National University of Córdoba, Argentina).

Scientific Meetings

Talks

10/2009	Electrocatalysis at the nanoscale workshop: Theory and Modeling (Reisensburg, Germany). *Concepts for electronic structure, bands in solids, densities of states, d-band model, Wannier orbitals.*
09/2009	ELCAT workshop Training Course on Advanced Instrumental and Spectroscopic Techniques applied to Electrocatalysis (Birminham, United Kingdom). *Properties of bare and graphite-supported nanowires.*

Scientific Meetings

Posters

05/2011   XVII argentinian meeting of physical chemistry and inorganic chemistry. (Córdoba, Argentina). *Theoretical study: Electrocatalytic properties of Rh and Pd monolayers on different surfaces.*

09/2010 61st Annual Meeting of the International Society of Electrochemistry (Nice, France). *Catalytic properties of graphite-supported wires, a DFT study.* G. Soldano, P. Quaino, E. Santos and W. Schmickler.

07/2009 11th International Fischer-Symposium on Microscopy in Electrochemistry (Benedikbeuern, Germany). *Chemical Adsorption at Nanowires.* G. Soldano, P. Quaino, E. Santos and W. Schmickler.

09/2008 59th Annual Meeting of the International Society of Electrochemistry (Sevilla, Spain). *Spiral adsorbate structures on monoatomic nanowire electrodes.* G. Soldano, Stephan Frank, Marc Koper.

03/2007 15th Argentinian Meeting of Chemical-Physics and Organic Chemistry (Tandil Bs.As. Argentina) *Modulating Activity of the Multiple Drugs Resistance (MDR) Related to the Acceptor Capacity of Hydrogen Bond of the Modulator.* G. Soldano, Mariano Vera, Adriana Pierini.

10/2005   Symposium of Physics, (Córdoba, Argentina) *Computational calculations analysis for a protein with several active sites and different substrates.* G. Soldano, Mariano Vera, Adriana Pierini.

Participations

01/2011   ELCAT workshop: Nanoparticles and Nanostructures for electrocatalytic reactions (Prague, Czech Republic).

08/2010 4th ELCAT Network training school and workshop (Leiden, The Netherlands).

05/2007 4th Fourth Latin American Symposium on Scanning Probe Microscopy (Mar del Plata, Argentina).

Other Researcher Activities

2002	Investigation of the nutritional state of the lake "Lago del Parque Sarmiento"realized in the "Superior School of Commerce Manuel Belgrano", Córdoba.

Prices

2008	Price for being among the 100 best academic averages of the National University of Córdoba during the year 2007, given by magazine "Rumbos".

Skills

Programming	FORTRAN90, python, BASH.
Writing	UNIX, Windows OS, Office suite, LaTeX

Science Spreading

2009	BW-Grid Project. *Stability of gold and platinum nanowires on graphite edges.* (Ulm University, Ulm, Germany.) G. Soldano, P. Quaino, E. Santos and W. Schmickler.

Scientific Referees

Prof. Dr. W. Schmickler	Institute of Theoretic Chemistry, Albert-Einstein-Allee 11, 89081 Ulm, Germany. Tel: +49 731 50-31340, Fax: +49 731 50-22819, e-mail: wolfgang.schmickler@uni-ulm.de
Prof. Dr. M.T.M. Koper	Leiden Institute of Chemistry, Leiden University, PO Box 9502, 2300 RA Leiden. Tel: +31-71-5274250, e-mail: m.koper@chem.leidenuniv.nl
Prof. Dr. E.P.M. Leiva	Departamenteo de Matemática y Física, Facultad de Ciencias Químicas - UNC, Edificio Integrador-Subsuelo, Ciudad Universitaria, PO 5000, Córdoba, Argentina. Fax: +54 (351) 4344972, e-mail: eleiva@fcq.unc.edu.ar

Erklärung

Diese Dissertation wurde im Zeitraum März 2008 bis Mai 2011 am Institut für Theoretische Chemie der Universität Ulm unter der Leitung von Professor Wolfgang Schmickler erstellt.

Ehrenwörtliche Erklärung: Ich erkläre ehrenwörtlich, dass die vorliegende wissenschaftliche Arbeit unter Beachtung der Satzung der Universität Ulm zur Sicherung guter wissenschaftlicher Praxis selbständing angefertigt wurde. Alle verwendeten Quellen und Hilfsmittel sind aufgelistet und die wörlich oder inhaltlich übernommenen Stellen sind als solche kenntlich gemacht.

Ulm, den

<div align="right">Germán Soldano</div>

192   Erklärung

Acknowledgments

When a PhD student reaches the acknowledgments part of his thesis, he realizes that it may be the closest thing to acknowledging people in an Oscar ceremony (or even less likely a Nobel prize) that he is ever going to have. A PhD also knows that this is the only part of the thesis that is going to be read by friends and family members. Therefore, I have seriously though in including some conclusions of my thesis here, but in the end I decided not to, so that you also have something to thank me.

I want to start this long list of acknowledgments with Prof Schmickler and Dr Elizabeth Santos, thanks for this journey, for their support, trust, and patience. Thanks also to Prof Ezequiel Leiva, who opened this possibility from Argentina. Thanks to Prof Marcelo Mariscal, for his supervision in my diploma thesis and for the Ulm tips. Thanks to Florian and Kay, who first helped me to accommodate myself in Ulm and in the group. Thanks to Peter Hindelang, the fireman of the binary world, the guy you should call if something is not working.

Thanks to Prof Axel Groß for all the fruitfuls discussions. Prof Marc Koper, I will be always grateful to you for taking me into your group for three months. Thanks to Gonzalo, Stanley, Matteo, François, Steven, Stefan, Alex, Janneka, Jose, thank you guys for such a nice experience; I promise next time I will show you my appreciation in a less energetic manner (bringing the fire department was a bit too much). Andrey, I never thought that Ukrainians and Argentineans could have so much in common, thanks for the night walks, the improvised cinema at home, the cheap philosophy; I am really going to miss your sarcasm; my offer to paying you that tattoo in your back saying *Life is overrated* still stands.

Angelica, my favorite Swedish DJ, thanks for enlighten the office with your humor, and for the babysitting experiences; also thanks to Thomas, thank you guys for adopting me during that ski-trip. Thanks to Tanglaw, Luis, Leandro, Andrés, Markus, Ariel, Anja, Katrin and Daniela, I will miss the topic-discussions in the Mensa with you guys. Anja, the best English/German corrector I have ever met, seriously, Morpheus watching the Matrix is nothing compared to you watching my thesis. Tanglaw, your ability to eat that jelly meal will keep you in my top one list of heroes for a loooong time.

Chris, the man of the infinite to-do list, thanks for the adventures, the talks, the inter-culture exchange, ; when I grow up, I want to be like you.

193

Gracias a la Escuela Superior de Comercio Manuel Belgrano, por enseñarme a dudar. Gracias a las admirables personas que allí me formaron. A Silvana Durilén, por enseñarnos ciencia con poesía.

Gracias totales al Dr. Rafael Fernández, porque queriendo enseñarme a calcular π meadiante métodos estocásticos, me enseñó cuál era mi vocación como científico. Gracias Rafa por contagiarme de fortranitis y por el tiempo compartido.

Gracias a toda la gente de la facu de ciencias químicas, Jime, Carlona, Liz, Ani, Flor, Vicky, Naty, Yami, Fede, Manu, Guguilo, Ger, tanta gente linda con la que puedo estar a gusto con mi locura.

A Noelia, por los sueños que nos hicieron cruzar el charco, gracias por los buenos recuerdos, y por ayudarme a crecer.

A Fernanda, por alegrarme la vista con su sonrisa, las dicusiones científicas y las no tanto.

A Paola, por todas discuciones teóricas optimizadas a 1200 palabras por minuto; y gracias por ampliar mi vocabulario con palabras como *Louis Vuitton, Lafayette, Cartier*, etc. Al trío Lucho/Pao/Manges por el I Simposium of Superficial Talking en Niza, sin duda el mejor simposio al que no he asistido.

A Belén y Sol, por los largos debates sobre el uso y abuso del papel higiénico, por el empuje sobrecargado en el péndulo del parque que dotó de vuelo al susodicho astro por unos instantes que jamás olvidaré.

A Nico, porque en virtud de su excelencia académica, pudimos encontrar al fin un catalizador de hidrógeno como Dios manda!

A Leo, Lucho, Pablo y Juan, los Pseudos. Habría sido un honor escribir esta tesis con ustedes, seguro que las gráficas nos salían más lindas... y más creíbles porque en Alemania no hay tantos feriados...

A la Mely, por visitarme, por Madrid, Vienna, y Ulm.
A Manu, Axel, Gon, Robert, Darío, Fernando, primos y hermanos de sangre y de barro. A todos los caballeros del frontón, gracias por dejarme jugar a ese juego sin luego llevarme al Neuro.

A Geral... detrás de toda tesis hay siempre alguien que sufre la locura de quien la escribe. Esa es Gé. Gracias por aceptarme aquel turrón de Quaker, por traerme los ruidos y los colores de Córdoba por pantalla, por correr 42 km conmigo, por tirar la soga y saltar.

A Dolina y sus secuaces, por todas las noches que me trajeron la patria a mi oficina y a mi Bunker.

A mi familia, a mi tío Ale que cree que vine a buscar el Nobel, a mi mamá que este año seguro que aprende a usar skype, a mi hermano, actual empresario y futuro traficante de animales ilegales, a mi hermana la futura dentista de la familia. A mi papá y a mi mamá de nuevo, por pasarme los genes de superhéroe. A mi abuela, por el aroma de su Lasagna que cruza el océano y me hace apludir desde acá.

A todo mi familia, por el aguante.